UTS UNIVERSITY OF TECHNOLOGY SYDNEY

New Signaling Techniques for Energy and Information Deliveries

by Hongwen Yu

Thesis submitted in fulfilment of the requirements for the degree of

Doctor of Philosophy

under the supervision of Prof. Tuan D. Hoang and Prof. Eryk Dutkiewicz

University of Technology Sydney
Faculty of Faculty of Engineering and Information

November 2021

CERTIFICATE OF ORIGINAL AUTHORSHIP

I, Hongwen Yu declare that this thesis, is submitted in fulfilment of the requirements for the award of Doctor of Philosophy, in the Faculty of Engineering and Information Technology at the University of Technology Sydney.

This thesis is wholly my own work unless otherwise reference or acknowledged. In addition, I certify that all information sources and literature used are indicated in the thesis.

I certify that the work in this thesis has not previously been submitted for a degree nor has it been submitted as part of the requirements for a degree at any other academic institution except as fully acknowledged within the text. This thesis is the result of a Collaborative Doctoral Research Degree program with Shanghai University.

This research is supported by the Australian Government Research Training Program.

Signature: Production Note: Signature removed prior to publication.

Date: 01/11/2021

Acknowledgements

At the time of my doctoral dissertation is about to be completed, there are joy, sadness, and regrets, but most is gratitude.

I would like to express my sincere gratitude to my principle supervisor Prof. Tuan D. Hoang for his continual support, guidance, help and encouragement during my PhD study. Prof. Tuan has brought me into wireless communication optimization theory area, and provided brilliant insights in my research works. It is my honor to have a supervisor who always inspires me to achieve higher targets. His conscientious and meticulous attitude on research has significant influence on my work. Besides serious guidance to my scientific research work, Prof. Tuan also gives me great support to my daily life and mental health.

At the end, I would like to give my deepest gratitude to my parents for their immeasurable support and encouragement throughout my graduate studies.

Publications

The contents of this thesis are based on the following papers that have been published, accepted, or submitted to peer-reviewed journals and conferences.

Journal Papers:

1. H. Yu, H. D. Tuan, A. A. Nasir, T. Q. Duong and H. V. Poor, "Joint Design of Reconfigurable Intelligent Surfaces and Transmit Beamforming under Proper and Improper Gaussian Signaling". *IEEE Journal on Selected Areas in Communications*, 2020, 38(11): 2589-2603.

2. H. Yu, H. D. Tuan, T. Q. Duong, H. V. Poor and Y. Fang, "Optimization for Signal Transmission and Reception in a Macrocell of Heterogeneous Uplinks and Downlinks". *IEEE Transactions on Communications*, 2020, 68(11): 7054-7067.

3. H. Yu, H. D. Tuan, T. Q. Duong, Y. Fang and L. Hanzo, "Improper Gaussian Signaling for Integrated Data and Energy Networking". *IEEE Transactions on Communications*, 2020, 68(6): 3922-3934.

4. H. Yu, H. D. Tuan, A. A. Nasir, T. Q. Duong and L. Hanzo, "Improper Gaussian Signaling for Computationally Tractable Energy and Information Beamforming". *IEEE Transactions on Vehicular Technology*, 2020, 69(11): 13990-13995.

5. H. Yu, H. D. Tuan, E. Dutkiewicz, H. V. Poor and L. Hanzo, "Maximizing the Geometric Mean of User-Rates to Improve Rate-Fairness: Proper vs. Improper Gaussian Signaling". *IEEE Transactions on Wireless Communications*, 2021,21(1):295-309.

6. H. Yu, H. D. Tuan, A. A. Nasir, M. Debbahd and Y. Fang, "New Generalized Zero Forcing Beamforming for Serving More Users in Energy-Harvesting Enabled Networks". *Physical Communication*, 50(2022): 101500.

7. H. Yu, H. D. Tuan, E. Dutkiewicz, H. V. Poor and L. Hanzo, "RIS-aided Zero-Forcing and Regularized Zero-Forcing Beamfoming in Integrated Information and Energy Delivery". *IEEE Transactions on Wireless Communications*, 2021. (Early Access)

8. H. Yu, H. D. Tuan, E. Dutkiewicz, H. V. Poor and L. Hanzo, "Hybrid Beamforming with Analog Finite-Resolution for Millimeter-wave Multi-user Communications". *IEEE Transactions on Communications*, 2021. (Under review)

Conference Papers:

1. H. Yu, H. D. Tuan, A. A. Nasir, M. Debbah and Y. Fang, "Regularized Zero Forcing Beamforming for Serving More Users in Energy-Harvesting Enabled Networks". *Proceedings of 2020 IEEE Tenth International Conference on Communications and Electronics (ICCE)*, Vietnam, 2020: 51-56.

Table of contents

List of figures

List of tables

1 Introduction **3**

1.1 Motivation and Scope 3

1.2 Problems in Next-Generation Wireless Communication Systems 4

1.2.1 Uplink and Downlink Communication 4

1.2.2 Energy Harvesting 5

1.2.3 Reconfigurable Intelligent Surfaces 7

1.3 Dissertation Outline 8

1.4 Notation 12

2 Background **13**

2.1 Improper Gaussian signaling 13

2.2 Optimization Theory 14

2.2.1 Mathematical Optimization 14

2.2.2 Convex Optimization 15

3 Optimization for Signal Transmission and Reception in a Macrocell of Heterogeneous Uplinks and Downlinks **19**

3.1 Introduction 19
3.2 FD-based STR 21
3.3 Time-fraction-wise STR 28
3.4 Bandwidth-fraction-wise STR 36
3.5 Numerical Results 41
3.5.1 Spectral efficiency in terms of max-min throughput 42
3.5.2 EE optimization 46
3.5.3 EE in serving doubled number of users 48
3.6 Conclusions 48

4 Improper Gaussian Signaling for Integrated Data and Energy Networking 51

4.1 Introduction 51
4.2 System Model for improper Gaussian signal processing 54
4.3 Simplified improper Gaussian signaling 61
4.3.1 Path-following iteration 64
4.3.2 Alternating descent iteration 67
4.3.3 Generating a good feasible point for (4.34) 69
4.3.4 Algorithm 70
4.4 Performance results 70
4.4.1 NOMA favored scenario 71
4.4.2 General scenario 75
4.5 Conclusions 77

5 Joint Design of Reconfigurable Intelligent Surfaces and Transmit Beamforming under Proper and Improper Gaussian Signaling 79

5.1 Introduction 79

5.2 Proper Gaussian signaling 82
5.2.1 Alternating descent round 88
5.2.2 Path-following iteration 90
5.2.3 Initialization and penalty parameter 92
5.2.4 Two-phase Algorithm 93
5.3 Improper Gaussian signaling 93
5.3.1 Alternating descent round 95
5.3.2 Path-following round 96
5.3.3 Initialization and penalty parameter 99
5.3.4 Two-phase Algorithm 99
5.4 Performance results 100
5.5 Conclusions 108

6 Maximizing the Geometric Mean of User-Rates to Improve Rate-Fairness: Proper vs. Improper Gaussian Signaling 109

6.1 Introduction 109
6.2 Proper Gaussian signaling 112
6.2.1 Beamforming descent iteration 114
6.2.2 Programmable reflecting elements' descent iteration 116
6.2.3 Proper Gaussian Signaling Geometric Mean Rate Optimization 120
6.3 Improper Gaussian signaling 120
6.3.1 Widely linear beamforming descent iteration 124
6.3.2 Programmable reflecting elements' descent iteration 126
6.3.3 Improper Gaussian Signaling Geometric Mean Rate Optimization 133
6.4 Numerical examples 133
6.5 Conclusions 140

7 RIS-aided Zero-Forcing and Regularized Zero-Forcing Beamfoming in Integrated Information and Energy Delivery 143

7.1 Introduction 143

7.2 RIS-aided zero-forcing beamforming optimization 146

7.2.1 Step descent algorithm 150

7.2.2 Full step descent algorithms 151

7.3 RIS-aided regularized zero-forcing beamforming optimization 155

7.3.1 Trace-maximization based algorithm 156

7.3.2 Determinant-maximization algorithms 156

7.4 ZFB Applications to RIS-aided integrated data and energy delivery . . 158

7.4.1 Energy delivery during $1/t_1$ 159

7.4.2 Information transmission during $1/t_2$ 160

7.4.3 Optimal energy and ZF information beamforming 161

7.5 RZFB applications to RIS-aided integrated data and energy delivery . . 163

7.5.1 The conventional RZFB 163

7.5.2 New RZFB 165

7.5.3 Notices on RZFB for information delivery only 168

7.6 Numerical examples 168

7.6.1 RIS-aided information delivery 169

7.6.2 RIS-aided information and energy delivery 171

7.7 Conclusions 175

8 Conclusions and Future Work 177

8.1 Conclusions 177

8.2 Future work 178

Appendix A Fundamental Inequalities **181**

Appendix B Proof of (6.62) and (6.63) **187**

References **189**

List of figures

3.1 FD-based STR system 21

3.2 TF/BF STR system: (a) Signal transmit during a fraction $\boldsymbol{\tau}$ of time slot/bandwdith; (b) Signal reception during the remaining fraction $1-\boldsymbol{\tau}$ of time slot/bandwidth 29

3.3 e-TF STR system: (a) Signal transmit during a fraction $\boldsymbol{\tau}$ of time slot by all antennas; (b) Signal reception during the remaining fraction $\eta-\boldsymbol{\tau}$ of time slot by the same antennas 30

3.4 Achievable minimum DLU and ULU throughput vs SI σ_{SI}^2 44

3.5 Achievable minimum DLU and ULU throughput vs BS antennas number N_t 45

3.6 Achievable EE by three STRs 47

4.1 Multi-cell energy-harvesting aided system 55

4.2 NOMA favored scenario 71

4.3 Convergence for IGS, s-IGS and NOMA algorithms 72

4.4 Achievable minimum throughput vs number N_t: (a) $K=2$ (18 users); (b) $K=3$ (27 users) 73

4.5 Achievable minimum throughput vs BS transmit power budget P . . . 74

4.6 Achievable minimum throughput vs BS transmit power budget P . . . 75

4.7 OMA favored scenario 75

4.8 Achievable minimum throughput vs BS antennas number N_t: (a) $(K, M) = (2, 4)$; (b) $(K, M) = (3, 6)$ 76

4.9 Achievable minimum throughput vs BS transmit power budget P . . . 77

5.1 System model 83

5.2 Convergence with $P = 20$ dBm, $M = 9$ AP-antennas, and $N = 100$ RIS elements. 102

5.3 Achievable max-min throughput versus the number of antennas at the AP, M, with $P = 20$ dBm and $N = 100$ RIS elements. 102

5.4 Achievable max-min throughput versus the transmit power budget at the AP, P, with $M = 9$ AP-antennas and $N = 100$ RIS elements. . . . 103

5.5 Achievable max-min throughput versus the number of RIS elements, N, with $M = 9$ AP-antennas and $P = 20$ dBm. 103

5.6 Under the setup in Remark 1, achievable max-min throughput versus the number of antennas at the AP with $P = 20$ dBm and $N = 100$ RIS elements. 104

5.7 A simulation setup with the blockage of the direct path between the AP and the UEs. The results for this setup are shown in Figs. 5.8-5.10. . . 104

5.8 Assuming blockage of direct path between AP and UEs $h_{a,k} \equiv 0$, achievable max-min throughput versus the number of antennas at the AP, M, with $P = 26$ dBm and $N = 60$ RIS elements. 105

5.9 Assuming blockage of direct path between AP and UEs $h_{a,k} \equiv 0$, achievable max-min throughput versus transmit power budget at the AP, P, with $M = 8$ AP-antennas and $N = 60$ RIS elements. 106

5.10 Assuming blockage of direct path between AP and UEs $h_{a,k} \equiv 0$, achievable max-min throughput versus the number of RIS elements, N, with $M = 8$ AP-antennas and $P = 26$ dBm. 107

6.1 System model 112

6.2 SR for different the number of antennas M. 135
6.3 Rate distribution for $M = 9$. 135
6.4 Min-rate/max-rate for the different number of antennas M. 136
6.5 Rate-variance for the different of antennas M. 137
6.6 GM for the different number of antennas M. 137
6.7 System model 138
6.8 SR for the different number of antennas M. 138
6.9 User rate distribution for $M = 9$. 139
6.10 Min-rate/max-rate for the different number of antennas M. 140
6.11 Rate-variance for the different number of antennas M. 140
6.12 GM rate for the different number of antennas M. 141

7.1 Chapter organization. 146
7.2 Scenario setup with the blockage of the direct path between the BS and the IUs. 147
7.3 Scenario setup for integrated data and energy networking. 159
7.4 Achievable minimum throughput vs the number of BS antennas M under ZF. 170
7.5 Achievable minimum throughput vs the number of BS antenna M under RZF. 170
7.6 Achievable minimum throughput vs the number of BS antennas M under ZF. 171
7.7 Achievable minimum throughput vs the number of BS antennas M under RZF. 172
7.8 Achievable minimum throughput for $M = 10$ under RZF vs the BS transmit power P. 173

7.9 Achievable minimum throughput for $M = 10$ with energy harvesting under RZF vs RIS for N reflecting elements. 173

7.10 Achievable minimum throughput under RZF vs the number of BS antennas M. 174

7.11 Achievable minimum throughput under RZF for $K = M + 1$ BS antennas. 174

List of tables

1.1 Notation 12

3.1 Simulation Parameters 42

3.2 The rounded average number of iterations for implementing the max-min-throughput Algorithms 45

3.3 Achievable minimum throughput of FD-based STR (bps/Hz) under different δ_2 and σ_{SI}^2 46

3.4 The rounded average number of iterations for the convergence of Algorithms 1-3 48

3.5 Achievable spectral efficiency (SE) in terms of achieved minimum throughput (bps/Hz) and EE (bps/Hz/W) in serving double users vs BS antennas number n 49

4.1 The rounded average number of iterations for the convergence under NOMA favored scenario 74

4.2 The rounded average number of iterations for the convergence under general scenario 77

5.1 The rounded average number of rounds for implementing Algorithms 6-9 in obtaining Fig. 5.3 (direct path between the AP and the UEs) . 108

5.2 The rounded average number of rounds for implementing Algorithms 6-9 in obtaining Fig.5.8 (without direct path between the AP and the UEs) 108

6.1 Major parameters setup 134

6.2 The average number of ZR-UEs versus M 136

6.3 The average number of ZR-UEs versus the number of antennas M . . . 139

7.1 The average number of iterations required for the algorithm's convergence 175

Abstract

The 6th-generation networks aim to further increase the average data rate and the edge rate, decrease in energy consumption and cost, and be able to transfer the energy at the same time. Precoding technology is one of the core technologies to achieve above goals. This thesis conducts in-depth research on uplink and downlink synchronous transmission scenarios, spectrum efficiency in energy-harvesting (EH) communication scenarios and Reconfigurable Intelligent Surfaces (RIS)-aided communication scenarios under precoding optimization methods.

Firstly, we propose a joint design of precoding matrix for base station and uplink users, and optimize the coefficient of time fraction in the same time. We also propose a joint design of precoding matrix for base station and uplink users, and optimize the allocation of downlink and uplink bandwidth in the same time.

Secondly, this dissertation considers multi-cell and multi-user communication scenario with EH, combining the fractional time method and the improper Gaussian signaling (IGS) precoding, an iterative algorithm is designed to optimize the user's max-min throughput in the optimization of spectrum efficiency. Furthermore, a simplified improper Gaussian signaling precoding optimization algorithm is proposed, the algorithm reduces the complexity of the algorithm under improper Gaussian signaling.

Thirdly, in the RIS-aided communication scenario, this dissertation proposes a joint design of RIS and transmit beamforming under proper and improper Gaussian signaling, and introduces the unit-modulus constraints (UMC) of RIS reflection coefficients into the objective function which reduces the complexity of the algorithm.

Fourthly, a joint design of linear transmit beamformers and the programmable reflecting coefficients of an RIS to maximize the geometric mean of the users' rates is

proposed. We also consider the joint design of widely linear transmit beamformers and the programmable reflecting coefficients to further improve the GM of the users' rates.

Finally, this dissertation considers RIS-aided wireless communication system with EH network where the RIS links the connection between the IUs and the BS as there is no direct path between the former and the latter. Joint optimization algorithms for information transfer beamforming, energy transfer beamforming and reflecting coefficients of the RIS based on transmit time-switching approach are developed. The superiority of the proposed algorithm is verified in the simulation section.

In summary, the optimization of precoding for wireless communication systems is studied, and method proposed in this thesis has certain significance for the theoretical research and technical realization of wireless communication systems.

Chapter 1

Introduction

This chapter starts with the motivation and scope of this thesis, then introduces some related research topics, and finally shows outlines of this dissertation.

1.1 Motivation and Scope

With the rapid popularization of mobile smart terminals, the number of mobile terminals has exploded in recent years. The 5th-generation(5G) wireless communication system adopts massive multiple input multiple output (Massive MIMO), millimeter wave (mmWave), full duplex (FD), non-orthogonal multiple access (NOMA),heterogeneous network and other technologies to provide communication with high transmission rate, low delay, high channel capacity, and high spectrum efficiency to meet the exponentially increasing demand for wireless data services. With the commercialization of the 5G wireless communication, researchers also put forward further requirements for wireless communication, such as higher communication quality, faster indoor transmission rate, lower energy consumption, wireless energy harvesting, etc. [1]. The industry and academia have begun to explore the 6th-generation (6G) wireless communication system. 3GPP expects to start the standardization study of 6G wireless communication system in 2023, and realize commercial use in 2028. The goal of the 6G wireless communication system is to interconnect the world and provide everyone with ubiquitous wireless connections [2]. Compared with 5G wireless communication system, 6G wireless

communication system proposes performance requirements such as 1000 times the peak rate, 10 times the regional spectrum efficiency, 10 0 ti mes th e re gional energy efficiency, 10 0 ti mes th e us er ex perience ra te, 10 00 ti mes th e pe ak ac cess density and 1/10 time delay [3]. In the mean time, the system should meet the needs of energy transmission, high physical layer security, fast data analysis, and modular network construction [4, 5]. In order to meet the above performance indicators and functional demand, THz communication, visible light communication, energy harvesting communication [6], intelligent mata-surface communication [7], orthogonal multiple access and other key technology are proposed [8]. Based on the performance indicators and key technologies of 6G proposed recently, this dissertation conducts in-depth research on uplink and downlink communication, energy harvesting (EH), and RIS. Corresponding convex optimization algorithms and closed-form solutions are developed.

1.2 Problems in Next-Generation Wireless Communication Systems

In order to meet the rapid popularization of mobile smart terminals and the consumers' growing demand, many potential technologies are proposed in the next-generation wireless communication systems. In this dissertation, uplink and downlink communication communication, energy harvesting (EH), and RIS aided communication are investigated to improve the quality of service (QoS) of wireless communication systems.

1.2.1 Uplink and Downlink Communication

With the popularization of mobile intelligent terminals, the bandwidth required and the demand for spectrum resources by wireless communication systems is increasing. Uplink and downlink communication provide a solution for alleviating the strained wireless spectrum. However, due to the influence of interference, in general, radio communication cannot be received and transmitted in the same frequency band [9], which means that uplink and downlink wireless communication must work in half-

duplex mode. Some recent work attempts to break this limitation, and various in-band full-duplex wireless communication systems have been designed and proposed [10]. The introduction of full-duplex has a huge impact on the design of communication networks, for example, it can double the spectrum efficiency of cellular networks. Frequency-division duplex (FDD) uses two separate channels to transmit uplink and downlink respectively, so that the communication system can work at full duplex mode. In-band full-duplex can make each individual channel achieve the same performance, saving half of the spectrum resources. The reason why full duplex is difficult to achieve is that part of the energy of the transmission signal will be received by its own receiver and affected by the distance. The power of the self-interference is one billion times stronger than the power of the target received signal (100dB+). This is an unsolved problem. All uplink and downlink communication systems are designed to allocate transmission and reception at different frequencies to avoid self-interference. Recently, self-interference cancellation (SIC) technology has made significant progress. Many research teams have simulated self-interference cancellation wireless communication systems in practical scenarios. The results show that the development of self-interference cancellation technology will gradually satisfy full-duplex communication demand. However, in the long term, the next-generation wireless communication system puts forward higher requirements such as low energy consumption and high speed, and SIC technology is obviously difficult to meet these requirements. [11] and [12] have designed uplink and downlink communication methods based on time slot allocation, which divide the single time slot, so that the uplink and downlink communications are alternately transmitted in the divided time slot. Due to the extremely short alternate transmission interval, this method can meet the current requirements for simultaneous communication on the uplink and downlink. At the same time, since self-interference and inter-link interference are avoided, the spectrum utilization and energy efficiency of the system are greatly improved.

1.2.2 Energy Harvesting

The main methods for energy harvesting communication are simultaneous wireless information and power transfer (SWIPT) [13] and time-fraction-based information and

power transfer (TFIPT) technology [14]. Wireless energy harvesting communication combines wireless information transfer (WIT) and wireless power transfer (WPT), which simultaneous transmit through same wireless media. The energy transfer in the network brings great challenges to the processing of interference, but it also provides the possibility for energy harvesting. Wireless energy transfer communication was first proposed by L.R.Varshney in 2008. The author proposed the concept of "Capacity Energy Function", and aimed at the binary discrete channel and the amplitude-limited additive Gaussian white noise(AWGN) channel scenario, where the energy transmission efficiency and information rate are traded off [15]. Subsequently, the literature [16] studied the application of wireless energy transfer communication in AWGN channel, and designed the simultaneous transmission of short-range wireless information and energy through a coupled inductance circuit, which gives a compromise between information rate and energy efficiency. In addition, for the scenario where the transmitter can obtain channel state information (CSI), literature [17] studied the joint optimization of information and energy processing schemes and receiver power control. The study showed that the best compromise strategy is to allocate all channel gains to energy transfer. After that, a large number of literatures have conducted research on wireless energy transfer communication in various complex system models, mainly including broadcast channel [18], interference channel [19], relay system [20] and so on. Recently, research has proposed energy transmit communication based on time slot allocation [14]. This method uses time slot allocation to use part of the single time slot for information transfer, and then use the remaining time slot for energy transmit, which can avoid the interference to information signals caused by energy signal transmit. In addition, the method can separately perform precoding for energy transfer and information transfer. During information transmission, precoding is used to suppress noise and improve information transmission quality. During energy transmission, precoding is used to amplify signal power to improve energy transmission efficiency.

1.2.3 Reconfigurable Intelligent Surfaces

In order to achieve higher transmission rates, ultra-dense networks (UDN), massive MIMO technology and millimeter wave communication systems have been proposed one after another [21], but these technologies still face severe consumption and hardware consumption issues in practical applications. For example, in an UDN, the energy consumption of circuits and cooling increases almost linearly with newly deployed base stations, while mmWave communication requires a large number of expensive radio frequency (RF) chains and complex signal processing technologies. On the other hand, adding too many active devices, such as micro base stations and relays, to the wireless communication network will cause more serious interference problems. Therefore, researchers are still looking for energy-saving and spectral methods to assist in achieving the requirements of next-generation wireless communication networks [22]. [23] proposed the concept of reconfigurable intelligent reflective surface to meet the above challenges. The reconfigurable intelligent reflective surface is a planar array containing a large number of passive devices (such as low-cost printed oscillators). Each device in the array will be controlled by a small controller to introduce a phase shift for each independent incident electromagnetic wave. As a key component of traditional reflective arrays, passive reflective surfaces are widely used in radar and satellite communications. However, since traditional reflective surfaces have a phase shift determined during manufacture, they cannot meet the dynamics of time-varying channel communication networks. However, the recent development of RF micro electromechanical systems (MEMS) and meta-materials has made it possible to reconfigurable reflective surfaces with real-time phase control [24]. By intelligently adjusting the phases of all components on the reconfigurable intelligent reflective surface, the signals can be coherently superimposed at the target receiving end to increase the power of the received signal, or the signal can be destructively superimposed on the non-target receiving end to avoid interference and strengthen the security and privacy. In [25], Q. Wu compared RIS and related technologies such as amplify-and forward (AF) relay [26], backscatter communication and the active reflection surface intelligence based on massive MIMO [27], the results showed that RIS has the advantages in not requiring a radio frequency chain, lower hardware consumption, and lower energy consumption.

1.3 Dissertation Outline

The outline of the dissertation is as follows:

Chapter 1

This chapter presents the motivation and scope, the research topics and the outline of the dissertation.

Chapter 2

A brief review of proper and improper Gaussian signal. Then, an overview of convex optimization theory is introduced.

Chapter 3

With the goal of improving the spectrum efficiency and energy efficiency of the communication system, chapter 3 studies the uplink and downlink transmission and reception communication scenarios, and discusses full-duplex communication, half-duplex communication, communication based on time slot allocation, and communication methods based on bandwidth allocation, respectively. Corresponding spectrum efficiency and energy efficient optimization algorithms are designed for the above communication methods, which effectively improves the throughput and energy efficiency of the communication network. The simulation results show that the algorithms based on time slot allocation and bandwidth allocation outperform the full-duplex communication and half-duplex communication algorithms, and the joint optimization algorithm based on time slot allocation is better than the joint optimization algorithm based on bandwidth allocation. The work in this chapter has been published in:

- H. Yu, H. D. Tuan, T. Q. Duong, H. V. Poor and Y. Fang, "Optimization for Signal Transmission and Reception in a Macrocell of Heterogeneous Uplinks and Downlinks". *IEEE Transactions on Communications*, 2020, 68(11): 7054-7067.

Chapter 4

Chapter 4 studies the energy harvesting network based on improper Gaussian signaling in the multi-cell and multi-user scenario, which the covariance information of the signal is used in the optimization to obtain the optimal minimum throughput. Compared with the algorithms based on proper Gaussian signals, IGS based algorithms have better spectrum efficiency and information confidentiality, but the algorithm complexity is

also higher. To lower the algorithm complexity, a simplified improper gaussian signaling (s-IGS) algorithm is proposed. Compared with the regular IGS algorithm, s-IGS based algorithm has faster convergence speed and the complexity degree of the algorithm is greatly reduced. The work in this chapter has been published in:

- H. Yu, H. D. Tuan, T. Q. Duong, Y. Fang and L. Hanzo, "Improper Gaussian Signaling for Integrated Data and Energy Networking". *IEEE Transactions on Communications*, 2020, 68(6): 3922-3934.
- H. Yu, H. D. Tuan, A. A. Nasir, T. Q. Duong and L. Hanzo, "Improper Gaussian Signaling for Computationally Tractable Energy and Information Beamforming". *IEEE Transactions on Vehicular Technology*, 2020, 69(11): 13990-13995.
- H. Yu, H. D. Tuan, A. A. Nasir, M. Debbah and Y. Fang, "Regularized Zero Forcing Beamforming for Serving More Users in Energy-Harvesting Enabled Networks". *Proceedings of 2020 IEEE Tenth International Conference on Communications and Electronics (ICCE)*, Vietnam, 2020: 51-56.
- H. Yu, H. D. Tuan, A. A. Nasir, M. Debbahd and Y. Fang, "New Generalized Zero Forcing Beamforming for Serving More Users in Energy-Harvesting Enabled Networks". *Physical Communication*, 50(2022): 101500.

Chapter 5

RIS-aided communication system is studied in this chapter. Aiming at the minimum achievable throughput and spectrum efficiency optimization, a joint optimization algorithm of precoding and PRCs is proposed, which improves users minimum achievable throughput. In the mean time, the design of the optimization algorithm under the IGS is also considered, and the covariance information of the signal is used to further improve the spectrum efficiency of the communication system. The simulation experiment considered two common scenarios: direct channel between the base station and the user and the direct channel between the base station and the user is blocked by obstacles. The results show that optimizing the reflection phase of the reconfigurable intelligent reflector is helpful to the spectrum efficiency of the communication system. The improvement is significant when the direct channel between the base station and the user is blocked by obstacles, and the minimum achievable throughput of IGS based

algorithms outperforms that of PGS based algorithms. The work in this chapter has been published in:

- H. Yu, H. D. Tuan, A. A. Nasir, T. Q. Duong and H. V. Poor, "Joint Design of Reconfigurable Intelligent Surfaces and Transmit Beamforming under Proper and Improper Gaussian Signaling". *IEEE Journal on Selected Areas in Communications*, 2020, 38(11): 2589-2603.

Chapter 6

In this chapter, a RIS-aided network which relies on a multiple antenna array aided base station and a RIS for serving multiple single antenna downlink users is studied. In order to further reduce the complexity of the algorithm, an optimization method based on closed-form solutions is proposed. In the mean time, the geometric mean (GM) rate is set as the optimization target to improve the communication efficiency of the system while ensuring the edge users' rate. Sum rate optimization and GM rate optimization results are compared in the simulation section which demonstrates the superior of the proposed algorithms. The work in this chapter has been published in:

- H. Yu, H. D. Tuan, E. Dutkiewicz, H. V. Poor and L. Hanzo, "Maximizing the Geometric Mean of User-Rates to Improve Rate-Fairness: Proper vs. Improper Gaussian Signaling". *IEEE Transactions on Wireless Communications*, 2021,21(1):295-309.

Chapter 7

A network of a multi-antenna array base station and a RIS to deliver both information to information users and power to energy users is discussed in this chapter. To provide reliable links for all users over the same time-slot, we adopt the transmit time-switching approach, under which information and energy are delivered over different time-slot fractions. This allows us to rely on conjugate beamforming for energy links and zero-forcing/regularized zero-forcing beamforming (ZFB/RZFB) and on the PRCs of the RIS for information links. We show that ZFB/RZFB and PRCs can be still separately optimized in their joint design, where PRC optimization is based on iterative closed-form expressions. We then develop a path-following algorithm for solving our max-min IU throughput optimization problem subject to a realistic constraint on the

quality-of-energy-service in terms of the EUs' harvested energy thresholds. We also propose a new RZFB for substantially improving the IUs' throughput.

- H. Yu, H. D. Tuan, E. Dutkiewicz, H. V. Poor and L. Hanzo, "RIS-aided Zero-Forcing and Regularized Zero-Forcing Beamfoming in Integrated Information and Energy Delivery". *IEEE Transactions on Wireless Communications*, 2021. (Early Access)

Chapter 8

This chapter summarizes the works of this PhD dissertation and presents the future research developments.

1.4 Notation

In this section we describe our notation used in the following chapters.

Table 1.1 Notation

Notations	Description
x	Vector
X	Matrix
$\mathbf{x}$	Vector variable
$\mathbf{X}$	Matrix variable
$(.)^*$	Conjugate operation
$(.)^T$	Transpose operation
$(.)^H$	Conjugate transpose operation
$(.)^{-1}$	Inverse operation
$tr(.)$	Trace operation
$\langle X \rangle$	trace(X)
$\|.\|$	$det(.)$,log-determinate operation
$\mathfrak{Re}$	Real part of a complex variable
$\mathfrak{Im}$	Imaginary part of a complex variable
I_N	Identity matrix of size $N \times N$
$O_{M \times N}$	Zero matrix of size $M \times N$
$\mathsf{diag}(.)$	A diagonal matrix of the size $n \times n$
$[X]^2$	XX^H
$\langle X, Y \rangle$	trace$(X^H Y)$
$\|\|X\|\|$	$\sqrt{\text{trace}(X^H X)}$
$\mathbb{E}(.)$	Expectation opteration
$X \succeq 0$	X is positive semi-definite matrix
$X \succ 0$	X is positive definite matrix
$(X + (*)^H)$	$(X + (X)^H)$
$\mathsf{vec}(X)$	Stack the columns of the matrix X into a single column
$\mathsf{vec}(AXB)$	$(B^T \otimes A)\mathsf{vec}(X)$,where $\otimes$ is the Kronecker product
$x = (x_1, \ldots, x_n)^T \in \mathbb{R}^n$	$e^{\jmath x} = (e^{\jmath x_1}, \ldots, e^{\jmath x_n})^T \in \mathbb{C}^n$
$\angle x$	Argument of a complex number x
$\mathcal{C}(0, a)$	Circular Gaussian random variables

Chapter 2

Background

In this chapter, we briefly describe the improper Gaussian signaling. Then, the optimization theory used in this dissertation is introduced.

2.1 Improper Gaussian signaling

In this section, we will briefly introduce proper Gaussian signal and improper Gaussian signal. To analyze the second-order statistical properties of $x = u + jv$ for $x \in \mathbb{C}^n$, and $u, v \in \mathbb{R}$, integrating its imaginary and real parts a random vector z ($z = \begin{bmatrix} u \\ v \end{bmatrix}$) is considered. Its mathematical expectation value can be expressed as follows [28]:

$$\mu_z = \mathbb{E}z = \begin{bmatrix} \mathbb{E}u \\ \mathbb{E}v \end{bmatrix} = \begin{bmatrix} \mu_u \\ \mu_v \end{bmatrix}, \tag{2.1}$$

and the covariance matrix is then formulated as

$$F_{zz} = \mathbb{E}(z - \mu_z)(z - \mu_z)^T = \begin{bmatrix} F_{uu} & F_{uv} \\ F_{uv}^T & F_{vv} \end{bmatrix}, \tag{2.2}$$

where $F_{uu} = \mathbb{E}(u-\mu_u)(u-\mu_u)^T$, $F_{uv} = \mathbb{E}(u-\mu_u)(v-\mu_v)^T$. The augmented expectation of x can be expressed as:

$$\underline{\mu}_x = \mathbb{E}\underline{x} = T\mu_z = \begin{bmatrix} \mu_x \\ \mu_x^* \end{bmatrix} = \begin{bmatrix} \mu_u + j\mu_v \\ \mu_u - j\mu_v \end{bmatrix}, \tag{2.3}$$

where $\underline{x} = \begin{bmatrix} x \\ x^* \end{bmatrix} = T\mu_z$, $T = \begin{bmatrix} I & jI \\ I & -jI \end{bmatrix} \in \mathbb{C}^{2n\times 2n}$. T represents the real to imaginary transformation, the covariance matrix of x is formulated as:

$$\underline{F}_{xx} = \mathbb{E}(\underline{x} - \underline{\mu}_x)(\underline{x} - \underline{\mu}_x)^H = TF_{zz}T^H = \begin{bmatrix} F_{xx} & \widetilde{F}_{xx} \\ \widetilde{F}_{xx}^* & \widetilde{F}_{xx}^* \end{bmatrix} = \underline{F}_{xx}^H, \tag{2.4}$$

it can observed that $F_{xx} = F_{xx}^H$ and $\widetilde{F}_{xx} = \underline{F}_{xx}^T$:

$$F_{xx} = \mathbb{E}(x-\mu_x)(x-\mu_x)^H = F_{uu} + F_{vv} + j(F_{uv}^T - F_{uv}) = F_{xx}^H, \tag{2.5}$$

$$\widetilde{F}_{xx} = \mathbb{E}(x-\mu_x)(x-\mu_x)^T = F_{uu} - F_{uv} + j(F_{uv}^T + F_{uv}) = \underline{F}_{xx}^T. \tag{2.6}$$

Furthermore, x is a proper Gaussian signal for $\widetilde{F}_{xx} = 0$, or x is a improper Gaussian signal.

2.2 Optimization Theory

In this section, an overview of mathematical optimization and convex optimization are introduced.

2.2.1 Mathematical Optimization

A mathematical optimization problem usually can be expressed as:

$$\begin{aligned} \text{minimize} \quad & f_0(x) \\ \text{s.t.} \quad & f_i(x) \leq b_i,\ i = 1, \ldots, m, \end{aligned} \tag{2.7}$$

where vector $x = (x_1, ..., x_n)$ is the optimization variable of the optimization problem, function f_0 is the objective functions, the functions f_i are constrain functions, and $(b_1, ...b_m)$ are the limits, or bounds for the constraints. The vector x^* reaches its optimal value or solution of (2.7) when f_0 has the smallest value among all vectors satisfy the constraints: for any z with $f_1(z) \leq b_1, ..., f_m(z) \leq b_m$, we have $f_0(z) \leq f_0(x^*)$ [29].

As an important example, if the objective and constraint functions $f_0, ..., f_m$ are linear and satisfy $f_i(\alpha x + \beta y) = \alpha f_i(x) + \beta f_i(y)$ for $x, y \in \mathbb{R}^n$, and $\alpha, \beta \in \mathbb{R}$, then the optimization problem (2.7) is called a linear program. If the optimization problem is not linear, it is called a nonlinear program.

The optimization problem (2.7) is called a linear optimization problem if the objective and constraint functions $(f_0, ..., f_m)$ are linear

$$f_i(\alpha x + \beta y) = \alpha f_i(x) + \beta f_i(y). \tag{2.8}$$

for $x, y \in \mathbb{R}^n$, and $\alpha, \beta \in \mathbb{R}$ [30].

2.2.2 Convex Optimization

A convex optimization problem is a class of optimization problems in which the objective and constraint functions are convex, which means they satisfy the inequality

$$f_i(\alpha x + \beta y) \leq \alpha f_i(x) + \beta f_i(y). \tag{2.9}$$

for $x, y \in \mathbb{R}^n$, and $\alpha, \beta \in \mathbb{R}$ [30].

Comparing (2.8) and (2.9), it can be observed that convexity is more general than linearity: inequality replaces the more restrictive equality. Since any linear program is therefore a special circumstance of convex optimization problem, we can consider convex optimization to be a generalization of linear programming [29].

Fundamental definitions in convex optimization are given as follows

Definition 1 *[30] Let a, b be two points of $\mathbb{R}^n$. The set of all $x \in \mathbb{R}^n$ of the form*

$$\begin{aligned} x &= (1-\lambda)a + \lambda b \\ &= a + \lambda(b-a), \quad \lambda \in \mathbb{R} \end{aligned} \tag{2.10}$$

is called the line through a and b. A subset M of $\mathbb{R}^n$ is callsed an affine set if it contains every line through two points of it, i.e., if $(1-\lambda)a + \lambda b \in M$ for every $a \in M$, $b \in M$, and every $\lambda \in \mathbb{R}$.

Definition 2 *[30] Given two points $a, b \in \mathbb{R}^n$, the set of all points $x = (1-\lambda)a + \lambda b$ such that $0 \leq \lambda \leq 1$ is called the (closed) line segment between a and b and denoted by $[a, b]$. A set $C \subset \mathbb{R}^n$ is called convex if it contains any line segment between two points of it; in other words, if $(1-\lambda)a + \lambda b \in C$ whenever $a, b \in C$, $0 \leq \lambda \leq 1$.*

Definition 3 *[30] A function $f(x)$ is convex, if x is on a convex domain C, for all $x, y \in C$ and $0 \leq \lambda \leq 1$, it is true that*

$$f(\lambda x + (1-\lambda)y) \leq \lambda f(x) + (1-\lambda)f(y). \tag{2.11}$$

Definition 4 *[30] A function $f(x)$ is concave, if x is on a convex domain C, for all $x, y \in C$ and $0 \leq \lambda \leq 1$, it is true that*

$$f(\lambda x + (1-\lambda)y) \geq \lambda f(x) + (1-\lambda)f(y). \tag{2.12}$$

Definition 5 *[30] To the problem $\min\{f(x)|x \in D\}$, a point $x^* \in D$ such that*

$$f(x^*) \leq f(x), \ \forall x \in D, \tag{2.13}$$

is called a global minimizer. A point $x' \in D$ such that there exists a neighborhood W of x' satisfying

$$f(x') \leq f(x), \ \forall x \in D \cap W, \tag{2.14}$$

is called a local minimizer.

A convex optimization problem is represented by

$$\begin{aligned} \min \quad & f_0(x) \\ \text{s.t.} \quad & f_i(x) \leq 0, \ i = 1, \ldots, m, \end{aligned} \tag{2.15}$$

where $f_i(\cdot), i = 0, \ldots, m$ are convex functions. The most important characteristics of such a convex optimization problem are

- Any local minimizer of (2.15) is also its global minimizer;
- (2.15) is computationally tractable for very wide classes of convex functions $f_i(\cdot)$ is the sense there are algorithms of polynomial complexity for its computation.

Chapter 3

Optimization for Signal Transmission and Reception in a Macrocell of Heterogeneous Uplinks and Downlinks

3.1 Introduction

The Internet-of-things (IoT) is characterized by massive wireless connectivity of low latency, which means that the future wireless communication must be cost-efficient and environment-friendly in accommodating a plethora of wireless downlinks and uplinks over the same time slot within a constrained communication bandwidth [31]. One of the first and perhaps the most natural answers is the full-duplexing (FD) exploitation, which provides means for simultaneous signal transmission and reception (STR) over the same frequency band/bandwidth by the same base station (BS) of co-located transmit and receive antennas [32–34]. However, the FD exploitation suffers its self-interference (SI) bottleneck as the interference to the receive signal from the transmit signal is expected very strong [10, 35]. Even for microcells, it is impossible to control SI under a level so that the FD-based STR is more spectral-efficient or energy-efficient than the conventional half-duplexing (HD)-based transmission and reception, which transmit

and receive signal in two separated time-slots, even by using the advanced techniques of signal processing [36–48]. Motivated by this unsolved issue of the FD exploitation, and also originated from [14], where the information and energy are proposed to be transferred separately over the same wireless channels within a time-slot instead of their simultaneous transfer, it was suggested in [48, 12, 49] to use a fraction of a time-slot to transmit signals to the relays and then the remaining complementary time-fraction to forward the received signals at the relays to the destination end. Such time-fraction-wise half-duplexing (HD) relaying is not only much easier implemented but is much better than that using the FD-based relaying. Additionally, unlike FD-based relaying, which must use a half of the relays' antennas for receiving signals and another half of relays' antennas for forwarding them, the time-fraction-wise HD relaying can use all available antennas for receiving and then forwarding signals to enjoy multi-antenna diversity in both signal transmission and reception. Time-fraction-wise based communication is capable of improving the SISO system's communication capacity [50, 51]. Another approach to STR within a time-slot, which can also avoid the SI, is to transmit signal and receive signal at the same time-slot using separated communication bandwidths, i.e. the whole bandwidth is divided into two parts, one is used for signal transmission and the remaining complementary one is used for signal reception. This bandwidth-fraction-wise STR must still use a half of antennas for signal transmission and another half of antennas for signal reception. Moreover, it can be practically implemented only when the bandwidth parts are fixed beforehand.

The present chapter examines the three aforementioned approaches to serve a macrocell of heterogeneous downlinks and uplinks within a time-slot. Under the FD-based STR, the focus is to design the transmit beamformers at the BS and uplink users. Under the time-fraction-wise STR, the focus is to jointly design the time-fraction-wise beamformers at the BS and uplink users and time-fraction allocation, while the focus under the bandwidth-fraction-wise STR is to jointly design the bandwidth-fraction-wise beamformers at the BS and uplink users and bandwidth-fraction allocation. Motivated by saving energy to control the negative impact of wireless communication in global warming [22, 52], all these design problems aim to maximize the network energy-efficiency (EE) under the quality-of-service (QoS) constraints for downlink and uplink throughput. While the spectral efficiency (SE) of (microcell) FD transceivers has

been considered previously (see e.g. [39] and references therein), its EE subject to the downlink and uplink QoS constraints was not appropriately considered. This chapter is the first work to consider STR over macrocell, which exploits time-fraction-wise and bandwidth-fraction-wise beamforming. All the problems of beamforming design are formulated as nonconcave objective function optimization subject to nonconvex constraints, which are computationally challenging. Our further contributions are developments of tailored path-following algorithms for their computation.

The rest of the chapter is organized as follows. Section II is devoted to the problem of EE maximization under FD-based STR, where in the end the FD-based STR's drawbacks are analysed in depth. Sections III and IV then are devoted to the problem of EE maximization under time-fraction-wise STR and bandwidth-fraction-wise STR, which provide remedy means for the FD-based STR. Simulations are provided in Section V to substantiate the analytical development of the previous sections, where the SE of STR is also additionally revealed. The appendix provides some fundamental inequalities used for deriving the equations in Sections II-IV.

3.2 FD-based STR

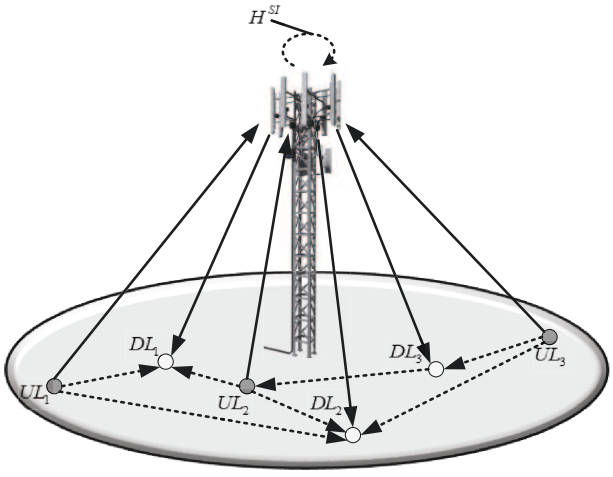

Fig. 3.1 FD-based STR system

Consider a macrocell of a BS serving d downlink single-antenna users termed by DL_j, $j = 1, \ldots, d$, and u uplink single-antenna users termed by UL_i, $i = 1, \ldots, u$, as

illustrated by Fig. 3.1. The BS is equipped with n antennas. Under the FD-based STR, n_1 antennas are used for signal transmission to serve the downlinks and other $n_2 = n - n_1$ antennas are used for signal reception to serve the uplinks. Usually, $n_1 \geq d$ and $n_2 \geq u$ are required for practical implementation. Let $s_j^{\mathsf{d}} \in \mathbb{C}$ with $|s_j^{\mathsf{d}}| = 1$ be the information intended for DL_j, which is beamformed by $\boldsymbol{v}_j \in \mathbb{C}^{n_1}$ before the BS's transmission. Let $s_i^{\mathsf{u}} \in \mathbb{C}$ with $|s_i^{\mathsf{u}}| = 1$ be the information UL_i intends to send to the BS, which is allocated by power $\boldsymbol{p}_i^2$ before the uplinks' transmission. For notational convenience, define

$$\begin{aligned} \boldsymbol{v} &\triangleq \{\boldsymbol{v}_j \ : \ j = 1, \ldots, d\}, \\ \boldsymbol{p} &\triangleq \{\boldsymbol{p}_i \ : \ i = 1, \ldots, u\}, \ \mathcal{D} = \{1, \ldots, d\}. \end{aligned}$$

The received signal at DL_j is

$$y_j \triangleq \underbrace{h_{j,\mathsf{bs}}^H \boldsymbol{v}_j s_j^{\mathsf{d}}}_{\text{desired signal}} + \underbrace{\sum_{\ell \in \mathcal{D} \setminus \{j\}} h_{j,\mathsf{bs}}^H \boldsymbol{v}_\ell s_\ell^{\mathsf{d}}}_{\text{DL interference}} + \underbrace{\sum_{i=1}^{u} h_{j,i} \boldsymbol{p}_i s_i^{\mathsf{u}}}_{\text{UL interference}} + n_j, \quad j = 1, \ldots, d, \tag{3.1}$$

where $h_{j,\mathsf{bs}} \in \mathbb{C}^{n_1}$ and $h_{j,i} \in \mathbb{C}$ are the channels from the BS to DL_j and from UL_i to DL_j, respectively, and n_j is the background white Gaussian noise with the variance σ_{d}^2.

The throughput at DL_j is

$$r_j^{\mathsf{d}}(\boldsymbol{v}, \boldsymbol{p}) \triangleq \ln\left(1 + \frac{|\lambda_j(\boldsymbol{v}_j)|^2}{\psi_j(\boldsymbol{v}, \boldsymbol{p})}\right), \tag{3.2}$$

where $\lambda_j(\boldsymbol{v}_j) \triangleq h_{j,\mathsf{bs}}^H \boldsymbol{v}_j$, and $\psi_j(\boldsymbol{v}, \boldsymbol{p}) \triangleq \sum_{\ell \in \mathcal{D} \setminus \{j\}} |h_{j,\mathsf{bs}}^H \boldsymbol{v}_\ell|^2 + \sum_{i=1}^{u} \boldsymbol{p}_i^2 |h_{j,i}|^2 + \sigma_{\mathsf{d}}^2$, which is a convex quadratic function. At the same time, the received signal at the BS is

$$y_{bs} \triangleq \underbrace{\sum_{i=1}^{u} h_{\mathsf{bs},i} \boldsymbol{p}_i s_i^{\mathsf{u}}}_{\text{desired signal}} + \underbrace{H^{\mathcal{SI}} \sum_{j=1}^{d} \boldsymbol{v}_j \tilde{s}_j}_{\text{residual SI}} + n_{\mathsf{bs}} \tag{3.3}$$

$$= \begin{bmatrix} h_{\mathsf{bs},1} & h_{\mathsf{bs},2} & \ldots & h_{\mathsf{bs},u} \end{bmatrix} \begin{bmatrix} \boldsymbol{p}_1 s_1^{\mathsf{u}} \\ \boldsymbol{p}_2 s_2^{\mathsf{u}} \\ \ldots \\ \boldsymbol{p}_u s_u^{\mathsf{u}} \end{bmatrix} + \tilde{n}_{\mathsf{bs}}, \tag{3.4}$$

where $h_{\mathsf{bs},i} \in \mathbb{C}^{n_2}$ is the channel vector from UL_i to the BS, n_{bs} is the background white Gaussian noise with the variance $\sigma^2_{\mathsf{bs}} I_{n_2}$. Furthermore, $H^{\mathcal{SI}} \in \mathbb{C}^{n_2 \times n_1}$ is the residual self-loop channel from the transmit antennas to the receive antennas at the BS after all real-time cancelation in both analog and digital domains [53, 54]. $\tilde{s}_j$ is the additive Gaussian noise with $\mathbb{E}\left[|\tilde{s}_j|^2\right] = \sigma^2_{SI}$ and the SI level σ^2_{SI} is the ratio of the average SI powers before and after the SI cancelation process [55, 10, 53, 56]. The term $\tilde{n}_{\mathsf{bs}} \triangleq H^{\mathcal{SI}} \sum_{j=1}^{d} \boldsymbol{v}_j \tilde{s}_j + n_{\mathsf{bs}}$ in (3.4) represents the self-loop interference plus noise. By assuming that the entries of the self-loop channel $H^{\mathcal{SI}}$ in (3.3) are treated as independent circularly symmetric complex Gaussian random variables with zero mean and unit variance, $\tilde{n}_{\mathsf{bs}}$ can be assumed white noise with the covariance

$$\left(\sigma^2_{SI} \sum_{j=1}^{d} ||\boldsymbol{v}_j||^2 + \sigma^2_{\mathsf{bs}}\right) I_{n_2}, \tag{3.5}$$

which only depends on the BS transmit power and thus cannot be mitigated by the transmit beamformer $\boldsymbol{v}$.

Make QR decomposition

$$\begin{bmatrix} h_{\mathsf{bs},1} & h_{\mathsf{bs},2} & \dots & h_{\mathsf{bs},u} \end{bmatrix} = Q_{\mathsf{bs}} R_{\mathsf{bs}} \in \mathbb{C}^{n_2 \times u}, \tag{3.6}$$

where $Q_{\mathsf{bs}} \triangleq \begin{bmatrix} q_{\mathsf{bs},1} & q_{\mathsf{bs},2} & \dots & q_{\mathsf{bs},n_2} \end{bmatrix} \in \mathbb{C}^{n_2 \times n_2}$ is an unitary matrix and $R_{\mathsf{bs}} \in \mathbb{C}^{n_2 \times u}$ is an upper rectangular matrix. It follows from (3.4) that

$$Q^H_{\mathsf{bs}} y_{\mathsf{bs}} = R_{\mathsf{bs}} \begin{bmatrix} \boldsymbol{p}_1 s^{\mathsf{u}}_1 \\ \boldsymbol{p}_2 s^{\mathsf{u}}_2 \\ \dots \\ \boldsymbol{p}_u s^{\mathsf{u}}_u \end{bmatrix} + Q^H_{\mathsf{bs}} \tilde{n}_{\mathsf{bs}}. \tag{3.7}$$

Upon successive interference cancellation (SIC) decoding, the throughput of s^{u}_i at the BS is

$$r^{\mathsf{u}}_i(\boldsymbol{v}, \boldsymbol{p}_i) = \ln\left(1 + \frac{\boldsymbol{p}^2_i |R_{\mathsf{bs}}(i,i)|^2}{\psi_{\mathsf{bs}}(\boldsymbol{v})}\right), \quad i = 1, \dots, u, \tag{3.8}$$

where $\psi_{\mathsf{bs}}(\boldsymbol{v}) \triangleq \sigma^2_{SI} \sum_{j \in \mathcal{D}} ||\boldsymbol{v}_j||^2 + \sigma^2_{\mathsf{bs}}$.

Following e.g. [57], the consumed power P^{tot} for the STR is modelled by the following convex quadratic function

$$P^{tot}(\boldsymbol{v},\boldsymbol{p}) = \zeta P^{t}(\boldsymbol{v},\boldsymbol{p}) + P_{BS} + P_{UE}, \tag{3.9}$$

where $P^{t}(\boldsymbol{v},\boldsymbol{p}) \triangleq \sum\limits_{j\in\mathcal{D}} ||\boldsymbol{v}_j||^2 + \sum\limits_{i=1}^{u} \boldsymbol{p}_i^2$ is the total transmit power of the BS and UEs, and ζ is the reciprocal of drain efficiency of power amplifier, P_{BS} and P_{UE} are the circuit power of the BS and UEs, respectively.

We consider the following design problem of downlink beamforming and uplink power allocation to maximize the FD-based STR's EE:

$$\max_{\boldsymbol{v},\boldsymbol{p}} \quad \frac{\sum\limits_{j=1}^{d} r_j^{\mathsf{d}}(\boldsymbol{v},\boldsymbol{p}) + \sum\limits_{i=1}^{u} r_i^{\mathsf{u}}(\boldsymbol{v},\boldsymbol{p}_i)}{P^{tot}(\boldsymbol{v},\boldsymbol{p})} \tag{3.10a}$$

$$\text{s.t.} \qquad \sum_{j=1}^{d} ||\boldsymbol{v}_j||^2 \le P_{\text{BS}}^{\max}, \tag{3.10b}$$

$$0 < \boldsymbol{p}_i \le \sqrt{P_{\text{UE}}^{\max}}, \quad i = 1,\ldots,u, \tag{3.10c}$$

$$r_j^{\mathsf{d}}(\boldsymbol{v},\boldsymbol{p}) \ge r_{\mathsf{d}}, \quad j = 1,\ldots,d, \tag{3.10d}$$

$$r_i^{\mathsf{u}}(\boldsymbol{v},\boldsymbol{p}_i) \ge r_{\mathsf{u}}, \quad i = 1,\ldots,u, \tag{3.10e}$$

where (3.10b)-(3.10c) cap the transmit power constraints, while (3.10d)-(3.10e) cap the QoS constraints for both downlink and uplink transmission because r_{d} and r_{u} are throughput thresholds. $P_{\text{BS}}^{\max}$ and $P_{\text{UE}}^{\max}$ are the power budget for the BS and UL_i, respectively.

By changing variable if necessary one can replace $|\lambda_j(\boldsymbol{v}_j)|^2$ by $(\bar{\lambda}_j(\boldsymbol{v}_j))^2$ for $\bar{\lambda}_j(\boldsymbol{v}_j) = \Re\{\lambda_j(\boldsymbol{v}_j)\}$ in (3.2), so

$$r_j^{\mathsf{d}}(\boldsymbol{v},\boldsymbol{p}) = \ln\left(1 + \frac{(\bar{\lambda}_j(\boldsymbol{v}_j))^2}{\psi_j(\boldsymbol{v},\boldsymbol{p})}\right),$$

and the downlink QoS constraint (3.10d) is equivalent to the second-order cone (SOC) constraint

$$\begin{aligned}\bar{\lambda}_j(\boldsymbol{v}_j) &\geq \sqrt{e^{r_{\mathsf{d}}}-1}\sqrt{\psi_j(\boldsymbol{v},\boldsymbol{p})} \\ &= \sqrt{e^{r_{\mathsf{d}}}-1}\left\|\begin{matrix}(h_{j,\mathsf{bs}}^H\boldsymbol{v}_\ell)_{\ell\in\mathcal{D}\setminus\{j\}} \\ (\boldsymbol{p}_i|h_{j,i}|)_{i=1}^u \\ \sigma_{\mathsf{d}}\end{matrix}\right\|_2, j=1,\ldots,d, \end{aligned} \tag{3.11}$$

while the uplink QoS constraint (3.10e) is also equivalent to the following SOC constraint

$$\begin{aligned}\boldsymbol{p}_i|R_{\mathsf{bs}}(i,i)| &\geq \sqrt{e^{r_{\mathsf{u}}}-1}\sqrt{\psi_{\mathsf{bs}}(\boldsymbol{v})} \\ &= \sigma_{SI}\sqrt{e^{r_{\mathsf{u}}}-1}\left\|\begin{matrix}(\boldsymbol{v}_i)_{i=1}^d \\ \sigma_{\mathsf{bs}}/\sigma_{SI}\end{matrix}\right\|_2, i=1,\ldots,u. \end{aligned} \tag{3.12}$$

Therefore, the problem (3.10) is equivalent to the following convex constrained optimization problem

$$\begin{aligned}\max_{\boldsymbol{v},\boldsymbol{p}}\ \Phi(\boldsymbol{v},\boldsymbol{p}) &\triangleq \frac{\sum_{j=1}^d r_j^{\mathsf{d}}(\boldsymbol{v},\boldsymbol{p})+\sum_{i=1}^u r_i^{\mathsf{u}}(\boldsymbol{v},\boldsymbol{p}_i)}{P^{tot}(\boldsymbol{v},\boldsymbol{p})} \\ \text{s.t.}\quad & (3.10b),(3.10c),(3.11),(3.12),\end{aligned} \tag{3.13}$$

where the computational difficulty is concentrated at its objective function $\Phi(\boldsymbol{v},\boldsymbol{p})$, which is not concave, making (3.13) a nonconvex problem. Usually, this objective is handled by fractional programming. Let $(v^{(\kappa)},p^{(\kappa)})$ be a feasible point for (3.10) found from the $(\kappa-1)$th iteration. Then the so called Dinkelbach's iteration [58] invokes the following optimization problem to generate $(v^{(\kappa+1)},p^{(\kappa+1)})$ at the κ-th iteration: $(v^{(\kappa+1)},p^{(\kappa+1)})$ at the κ-th iteration:

$$\begin{aligned}\max_{\boldsymbol{v},\boldsymbol{p}}\ & \sum_{j=1}^d r_j^{\mathsf{d}}(\boldsymbol{v},\boldsymbol{p})+\sum_{i=1}^u r_i^{\mathsf{u}}(\boldsymbol{v},\boldsymbol{p}_i)-\Phi(v^{(\kappa)},p^{(\kappa)})P^{tot}(\boldsymbol{v},\boldsymbol{p}) \\ \text{s.t.}\quad & (3.10b),(3.10c),(3.11),(3.12).\end{aligned} \tag{3.14}$$

However, this problem is still nonconvex and thus computationally intractable as the first two terms in its objective function, which constitute the numerator of the objective function $\Phi(\boldsymbol{v},\boldsymbol{p})$ in (3.13) are not concave. Our previous works [48, 59] have proposed to optimize the fractional objective function $f(\boldsymbol{v},\boldsymbol{p})$ in (3.12), avoiding the computational intractable iteration (3.14). We now develop another path-following iterations, which like (3.14) generate a sequence $\{f(v^{(\kappa)},p^{(\kappa)})\}$ of improved values of the objective in (3.12) but in contrast to (3.14) invoke a simple quadratic optimization problem at each iteration and thus are very computationally efficient.

Applying the inequality (A.12) in the appendix for $\boldsymbol{x}=\bar{\lambda}_j(\boldsymbol{v}_j)$, $\boldsymbol{y}=\psi_j^{\mathsf{d}}(\boldsymbol{v},\boldsymbol{p})$ and $\bar{x}=\bar{\lambda}_j(v_j^{(\kappa)})$, $\bar{y}=\psi_j^{\mathsf{d}}(v^{(\kappa)},p^{(\kappa)})$ yields

$$\begin{aligned} r_j^{\mathsf{d}}(\boldsymbol{v},\boldsymbol{p}) \geq & r_j^{\mathsf{d},(\kappa)}(\boldsymbol{v},\boldsymbol{p}) \\ \triangleq & a_j^{\mathsf{d},(\kappa)} - b_j^{\mathsf{d},(\kappa)} \left(\frac{(\bar{\lambda}_j(v_j^{(\kappa)}))^2}{2\bar{\lambda}_j(v_j^{(\kappa)})\bar{\lambda}_j(\boldsymbol{v}_j) - (\bar{\lambda}_j(v_j^{(\kappa)}))^2} + \frac{\psi_j^{\mathsf{d}}(\boldsymbol{v},\boldsymbol{p})}{\psi_j^{\mathsf{d}}(v^{(\kappa)},p^{(\kappa)})} \right), \end{aligned} \tag{3.15}$$

over the trust region

$$2\bar{\lambda}_j(v_j^{(\kappa)})\bar{\lambda}_j(\boldsymbol{v}_j) - (\bar{\lambda}_j(v_j^{(\kappa)}))^2 > 0, \quad j=1,\ldots,d, \tag{3.16}$$

where $0 < a_j^{\mathsf{d},(\kappa)} \triangleq r_j^{\mathsf{d}}(v^{(\kappa)},p^{(\kappa)}) + 2b_j^{\mathsf{d},(\kappa)}$, and $0 < b_j^{\mathsf{d},(\kappa)} \triangleq \frac{(\bar{\lambda}_j(v_j^{(\kappa)}))^2}{\psi_j^{\mathsf{d}}(v^{(\kappa)},p^{(\kappa)})+(\bar{\lambda}_j(v_j^{(\kappa)}))^2}$.

Analogously, applying the inequality (A.12) in the appendix for $\boldsymbol{x}=\boldsymbol{p}_i|R_{\mathsf{bs}}(i,i)|$, $\boldsymbol{y}=\psi_{\mathsf{bs}}(\boldsymbol{v})$ and $\bar{x}=p_i^{(\kappa)}|R_{\mathsf{bs}}(i,i)|$, $\bar{y}=\psi_{\mathsf{bs}}(v^{(\kappa)})$ yields

$$\begin{aligned} r_i^{\mathsf{u}}(\boldsymbol{v},\boldsymbol{p}_i) \geq & r_i^{\mathsf{u},(\kappa)}(\boldsymbol{v},\boldsymbol{p}_i) \\ \triangleq & a_i^{\mathsf{u},(\kappa)} - b_i^{\mathsf{u},(\kappa)} \left(\frac{(p_i^{(\kappa)})^2}{2p_i^{(\kappa)}\boldsymbol{p}_i - (p_i^{(\kappa)})^2} + \frac{\psi_{\mathsf{bs}}(\boldsymbol{v})}{\psi_{\mathsf{bs}}(v^{(\kappa)})} \right), \end{aligned} \tag{3.17}$$

over the trust region

$$2p_i^{(\kappa)}\boldsymbol{p}_i - (p_i^{(\kappa)})^2 > 0, \quad i=1,\ldots,u, \tag{3.18}$$

where $0 < a_i^{\mathsf{u},(\kappa)} = r_i^{\mathsf{u}}(v^{(\kappa)},p^{(\kappa)}) + 2b_i^{\mathsf{u},(\kappa)}$ and $b_i^{\mathsf{u},(\kappa)} = \frac{(p_i^{(\kappa)}|R_{\mathsf{bs}}(i,i)|)^2}{\psi_{\mathsf{bs}}(v^{(\kappa)})+(p_i^{(\kappa)}|R_{\mathsf{bs}}(i,i)|)^2}$.

To generate the next iterative point $(v^{(\kappa+1)}, p^{(\kappa+1)})$ at the κth iteration, we solve the following convex problem :

$$\max_{\boldsymbol{v},\boldsymbol{p}} \; L^{(\kappa)}(\boldsymbol{v},\boldsymbol{p}) \triangleq \sum_{j=1}^{d} r_j^{\mathsf{d},(\kappa)}(\boldsymbol{v},\boldsymbol{p}) + \sum_{i=1}^{u} r_i^{\mathsf{u},(\kappa)}(\boldsymbol{v},\boldsymbol{p}_i) - f(v^{(\kappa)}, p^{(\kappa)}) P^{tot}(\boldsymbol{v},\boldsymbol{p})$$

$$\text{s.t.} \quad (3.10b), (3.10c), (3.11), (3.12), (3.16), (3.18). \tag{3.19}$$

Note that $L^{(\kappa)}(v^{(\kappa)}, p^{(\kappa)}) = 0$ so $L^{(\kappa)}(v^{(\kappa+1)}, p^{(\kappa+1)}) > 0$ because $(v^{(\kappa+1)}, p^{(\kappa+1)})$ is the optimal solution of (3.19). This means

$$\begin{aligned}
& \sum_{j=1}^{d} r_j^{\mathsf{d},(\kappa)}(v^{(\kappa+1)}, p^{(\kappa+1)}) + \sum_{i=1}^{u} r_i^{\mathsf{u},(\kappa)}(v^{(\kappa+1)}, p_i^{(\kappa+1)}) \\
& -\Phi(v^{(\kappa)}, p^{(\kappa)}) P^{tot}(v^{(\kappa+1)}, p^{(\kappa+1)}) > 0 \\
\Leftrightarrow \quad & \frac{\sum_{j=1}^{d} r_j^{\mathsf{d}}(v^{(\kappa+1)}, p^{(\kappa+1)}) + \sum_{i=1}^{u} r_i^{\mathsf{u}}(v^{(\kappa+1)}, p_i^{(\kappa+1)})}{P^{tot}(v^{(\kappa+1)}, p^{(\kappa+1)})} > \Phi(v^{(\kappa)}, p^{(\kappa)}) \\
\Leftrightarrow \quad & \Phi(v^{(\kappa+1)}, p^{(\kappa+1)}) > \Phi(v^{(\kappa)}, p^{(\kappa)}),
\end{aligned} \tag{3.20}$$

i.e. $(p^{(\kappa+1)}, v^{(\kappa+1)})$ can archive better results than $(p^{(\kappa)}, v^{(\kappa)})$ for the nonconvex optimization problem (3.13). Then it is easy to show that the sequence $\{(p^{(\kappa)}, v^{(\kappa)})\}$ converges at least to a locally optimal solution of (3.13)/(3.10) [60]. It has been shown e.g. in [14] that such a locally optimal solution often turns out to be the global one. A pseudo-code of the proposed iterative process is given by Algorithm 1.

Algorithm 1 Full-duplex EE Optimization Algorithm

1: **Initialization:** Set $\kappa = 0$. Calculate the initial point $(v^{(0)}, p^{(0)})$ by: $\min_{\boldsymbol{v},\boldsymbol{p}} \; \sum_{j=1}^{d} ||\boldsymbol{v}_j||^2 + \sum_{i=1}^{u} \boldsymbol{p}_i^2$ subject to (3.10b), (3.10c), (3.11), (3.12).
2: **Repeat:** Generate the next feasible point $(v^{(\kappa+1)}, p^{(\kappa+1)})$ for (3.10) by solving the convex problem (3.19). Set $\kappa := \kappa + 1$.
3: **Output** $(v^{(\kappa)}, p^{(\kappa)})$.

Although Algorithm 1 provides means for efficient computation of the FD-based STR's EE optimization problem (3.10), one can see the following inherent drawbacks of FD-based STR preventing it from achieving high EE or providing high QoS:

- The DL throughput defined by (3.2) is UL interference-limited: the UL interference in (3.1) can be strong and uncontrolled whenever there is a UL near to a DL.

- The UL throughput defined by (3.8) is SI-limited: the SI in (3.3), which is proportional to the BS transmit power as (3.5) shows, is very strong due to the co-location of BS transmit and receive antennas. It is technologically impossible to suppress it to the background noise level even for microcells with much weaker transmit signals.

- Only n_1 antennas are used for signal transmission and n_2 antennas are used for signal reception, restricting the number of served downlinks and uplinks up to n_1 and n_2 respectively.

The next two sections provide quite different STRs to resolve these drawbacks.

3.3 Time-fraction-wise STR

We now propose the first alternative approach, which not only resolves all the above issues of (micro) FD-based STR but also works for macrocells. Still within a single time slot, the BS uses n_1 antennas to transmit signal during a fraction $0 < \boldsymbol{\tau} < 1$ of the time-slot to serve DLs as illustrated by Fig. 3.2(a) and then users the remaining n_2 antennas in the remaining fraction $1 - \boldsymbol{\tau}$ to receive signal from ULs, who are kept silent during the first $\boldsymbol{\tau}$ fraction, as illustrated by Fig. 3.2(b). Inter-link interference and SI are thus completely avoided.

Moreover, as illustrated by Fig. 3.3, all n antennas can be used to transmit signal during a fraction $0 < \boldsymbol{\tau} < 1$ of the time-slot to serve DLs, which are then switched in a fraction ϵ of the time-slot to receive signal from ULs in the remaining fraction $1 - \epsilon - \boldsymbol{\tau}$. Thus, the full number of antennas is utilized for transmission and reception with is no inter-link interference and SI. We refer the first option as TF while the second option as e-TF to distinguish them.

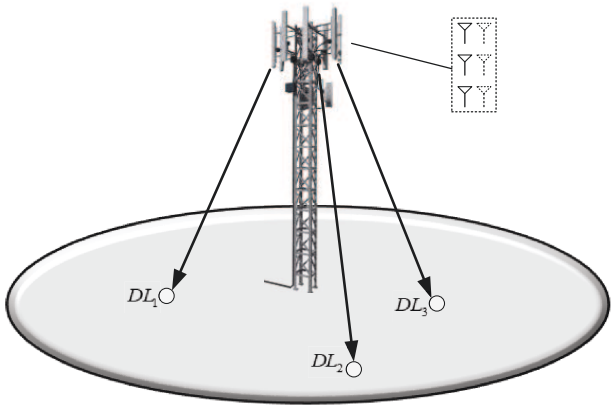

(a)

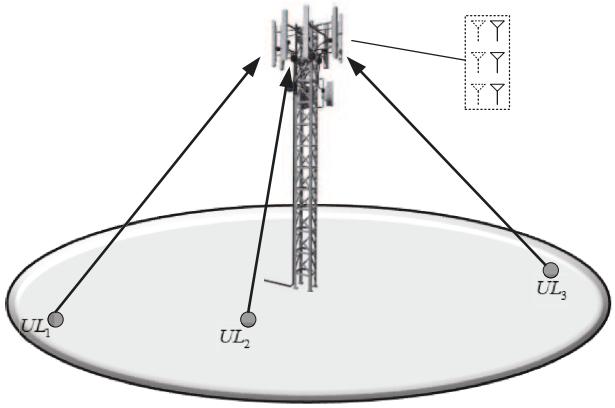

(b)

Fig. 3.2 TF/BF STR system: (a) Signal transmit during a fraction $\boldsymbol{\tau}$ of time slot/bandwdith; (b) Signal reception during the remaining fraction $1-\boldsymbol{\tau}$ of time slot/bandwidth

Now, let $\widetilde{\boldsymbol{v}}_j \in \mathbb{C}^{n_t \times d_1}$ be the beamforming vector for DL_j, so $n_t = n_1$ for TF while $n_t = n$ for e-TF. For computational tractability, the power allocated to s_i^{u} is defined by $1/\boldsymbol{p}_i$ instead of $\boldsymbol{p}_i^2$ in the previous section.

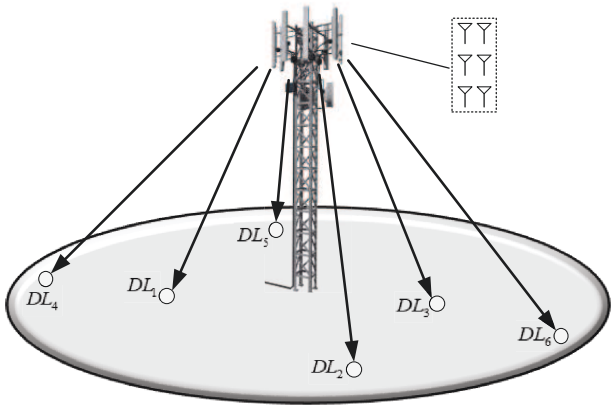

(a)

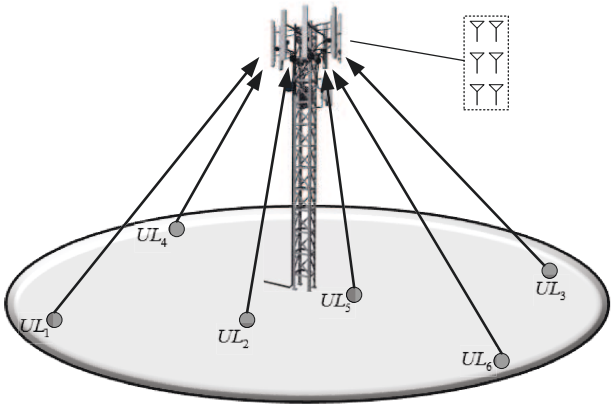

(b)

Fig. 3.3 e-TF STR system: (a) Signal transmit during a fraction $\boldsymbol{\tau}$ of time slot by all antennas; (b) Signal reception during the remaining fraction $\eta - \boldsymbol{\tau}$ of time slot by the same antennas

The received signal at DLU j is now:

$$\tilde{y}_j \triangleq \underbrace{\tilde{h}_{j,\mathsf{bs}}^H \widetilde{\boldsymbol{v}}_j s_j^{\mathsf{d}}}_{\text{desired signal}} + \underbrace{\sum_{\ell \in \mathcal{D}\setminus\{j\}} \tilde{h}_{j,\mathsf{bs}}^H \widetilde{\boldsymbol{v}}_\ell s_\ell^{\mathsf{d}}}_{\text{DL interference}} + n_j, j = 1, \ldots, d, \tag{3.21}$$

where $\tilde{h}_{j,\mathsf{bs}} \in \mathbb{C}^{n_t}$ is the downlink channel from the BS to DL_j.

For $\widetilde{\boldsymbol{v}} \triangleq \{\widetilde{\boldsymbol{v}}_j, j = 1, \ldots, d\}$, the throughput at DL_j is $\boldsymbol{\tau}\rho_j^{\mathsf{d}}(\widetilde{\boldsymbol{v}})$ with

$$\rho_j^{\mathsf{d}}(\widetilde{\boldsymbol{v}}) \triangleq \ln\left(1 + \frac{|\widetilde{\lambda}_j(\widetilde{\boldsymbol{v}}_j)|^2}{\phi_j^{\mathsf{d}}(\widetilde{\boldsymbol{v}})}\right), \tag{3.22}$$

where $\widetilde{\lambda}_j(\widetilde{\boldsymbol{v}}_j) \triangleq \tilde{h}_{j,\mathsf{bs}}^H \widetilde{\boldsymbol{v}}_j$ and $\phi_j^{\mathsf{d}}(\widetilde{\boldsymbol{v}}) \triangleq \sum_{\ell \in \mathcal{D}\setminus\{j\}} |\tilde{h}_{j,\mathsf{bs}}^H \widetilde{\boldsymbol{v}}_\ell|^2 + \sigma_{\mathsf{d}}^2$.

The received signal at the BS is now

$$\widetilde{y}_{\mathsf{bs}} \triangleq \sum_{i=1}^{u} \tilde{h}_{\mathsf{bs},i} s_i^{\mathsf{u}} / \sqrt{\boldsymbol{p}_i} + \widetilde{n}_{\mathsf{bs}}, \tag{3.23}$$

where $\tilde{h}_{\mathsf{bs},i} \in \mathbb{C}^{n_r}$ is the uplink channel from UL_i to the BS ($n_r = n_2$ for TF and $n_r = n$ for e-TF), and $\widetilde{n}_{\mathsf{bs}}$ is the additive white Gaussian noise with variance $\sigma_{\mathsf{bs}}^2 I_{n_r}$. Again, making QR decomposition

$$\begin{bmatrix} \tilde{h}_{\mathsf{bs},1} & \tilde{h}_{\mathsf{bs},2} & \ldots & \tilde{h}_{\mathsf{bs},u} \end{bmatrix} = \tilde{Q}_{\mathsf{bs}} \tilde{R}_{\mathsf{bs}}$$

with an unitary matrix $\tilde{Q}_{\mathsf{bs}}$ of size $n_r \times n_r$ and an upper rectangular matrix $\tilde{R}_{\mathsf{bs}}$ of size $n_r \times u$, the uplink throughput of s_i^{u} at the BS is $(\eta - \boldsymbol{\tau})\rho_i^{\mathsf{u}}(\boldsymbol{p}_i)$ with $\eta = 1$ for TF and $\eta = 1 - \epsilon$ for e-FT, and

$$\rho_i^{\mathsf{u}}(\boldsymbol{p}_i) \triangleq \ln\left(1 + |\tilde{R}_{\mathsf{bs}}(i,i)|^2 / \sigma_{\mathsf{bs}}^2 \boldsymbol{p}_i\right). \tag{3.24}$$

For $\boldsymbol{p} \triangleq \{\boldsymbol{p}_i, i = 1, \ldots, u\}$, instead of (3.9), the consumed power is modelled as

$$P^{tot}(\widetilde{\boldsymbol{v}}, \boldsymbol{p}, \boldsymbol{\tau}) = \zeta P_i^t(\widetilde{\boldsymbol{v}}, \boldsymbol{p}, \boldsymbol{\tau}) + P_{BS} + P_{UE}, \tag{3.25}$$

where $P_i^t(\widetilde{\boldsymbol{v}}, \boldsymbol{p}, \boldsymbol{\tau}) \triangleq \boldsymbol{\tau} \sum_{j=1}^{d} ||\widetilde{\boldsymbol{v}}_j||^2 + (\eta - \boldsymbol{\tau}) \sum_{i=1}^{u} 1/\boldsymbol{p}_i$ is the total transmit power of the BS and UEs, which is no longer a convex function. The time-fraction-wise (TF-wise)

STR's EE optimization problem is now formulated as

$$\max_{0<\boldsymbol{\tau}<1,\widetilde{\boldsymbol{v}},\boldsymbol{p}} \frac{\boldsymbol{\tau}\sum_{j=1}^{d}\rho_j^{\mathsf{d}}(\widetilde{\boldsymbol{v}})+(\eta-\boldsymbol{\tau})\sum_{i=1}^{u}\rho_i^{\mathsf{u}}(\boldsymbol{p}_i)}{P^{tot}(\widetilde{\boldsymbol{v}},\boldsymbol{p},\boldsymbol{\tau})} \quad \text{s.t.} \tag{3.26a}$$

$$\boldsymbol{\tau}\sum_{j=1}^{d}||\widetilde{\boldsymbol{v}}_j||^2 \le P_{\mathrm{BS}}^{\max}, \tag{3.26b}$$

$$(\eta-\boldsymbol{\tau})/\boldsymbol{p}_i \le P_{\mathrm{UE}}^{\max}, \quad i=1,\ldots,u, \tag{3.26c}$$

$$\boldsymbol{\tau}\rho_j^{\mathsf{d}}(\widetilde{\boldsymbol{v}}) \ge r_{\mathsf{d}}, \quad j=1,\ldots,d, \tag{3.26d}$$

$$(\eta-\boldsymbol{\tau})\rho_i^{\mathsf{u}}(\boldsymbol{p}_i) \ge r_{\mathsf{u}}, \quad i=1,\ldots,u, \tag{3.26e}$$

$$||\widetilde{\boldsymbol{v}}_j||^2 \le P_{\mathsf{D}}^{\max}, \quad j=1,\ldots,d, \tag{3.26f}$$

$$1/P_{\mathsf{U}}^{\max} \le \boldsymbol{p}_i, \quad i=1,\ldots,u, \tag{3.26g}$$

where (3.26f) and (3.26g) caps the physical limit of transmit power rates for the BS and ULs. Compared to the EE optimization problem (3.13) for the FD-based STR, the problem (3.26) is more computationally difficult because not only the objective function in (3.26) exhibits a more complex structure but all constraints (3.26b)-(3.26e) are no longer computationally tractable because the presence of variable $\boldsymbol{\tau}$. By introducing the variable $\boldsymbol{\theta}=(\boldsymbol{\theta}_1,\boldsymbol{\theta}_2)$, which satisfies the convex constraint

$$\boldsymbol{\tau} \ge 1/\boldsymbol{\theta}_1 > 0, \quad \eta-\boldsymbol{\tau} \ge 1/\boldsymbol{\theta}_2 > 0, \tag{3.27}$$

the problem (3.26) is equivalently expressed by

$$\max_{\boldsymbol{\tau},\boldsymbol{\theta},\widetilde{\boldsymbol{v}},\boldsymbol{p}} \tilde{\Phi}(\widetilde{\boldsymbol{v}},\boldsymbol{p},\boldsymbol{\theta}) \triangleq \frac{\sum_{j=1}^{d}\rho_j^{\mathsf{d}}(\widetilde{\boldsymbol{v}})/\boldsymbol{\theta}_1+\sum_{i=1}^{u}\rho_i^{\mathsf{u}}(\boldsymbol{p}_i)/\boldsymbol{\theta}_2}{\tilde{P}^{tot}(\widetilde{\boldsymbol{v}},\boldsymbol{x},\boldsymbol{\theta})} \tag{3.28a}$$

$$\text{s.t.}(3.26f),(3.26g),(3.27),$$

$$\sum_{j=1}^{d}||\widetilde{\boldsymbol{v}}_j||^2 \le P_{\mathrm{BS}}^{\max}\boldsymbol{\theta}_1, \tag{3.28b}$$

$$1/\boldsymbol{p}_i \le P_{\mathrm{UE}}^{\max}\boldsymbol{\theta}_2, \quad i=1,\ldots,u, \tag{3.28c}$$

$$\rho_j^{\mathsf{d}}(\widetilde{\boldsymbol{v}}) \ge \boldsymbol{\theta}_1 r_{\mathsf{d}}, \quad j=1,\ldots,d, \tag{3.28d}$$

$$\rho_i^{\mathsf{u}}(\boldsymbol{p}_i) \ge \boldsymbol{\theta}_2 r_{\mathsf{u}}, \quad i=1,\ldots,u, \tag{3.28e}$$

for

$$\tilde{P}^{tot}(\widetilde{\boldsymbol{v}},\boldsymbol{x},\boldsymbol{\theta}) \triangleq \zeta\left(\sum_{j=1}^{d}\frac{||\widetilde{\boldsymbol{v}}_j||^2}{\boldsymbol{\theta}_1}+\sum_{i=1}^{u}\frac{1}{\boldsymbol{x}_i\boldsymbol{\theta}_2}\right)+P^{BS}+UP^{UE}, \tag{3.29}$$

which becomes a convex function. Note that the constraints and (3.26f), (3.26g), (3.27), (3.28b), and (3.28c) in (3.28) are now convex, while the constraints (3.28d) and (3.28e) are nonconvex. Let $(\tilde{v}^{(\kappa)}, p^{(\kappa)}, \theta^{(\kappa)})$ be a feasible point for (3.28) found from the $(\kappa-1)$th iteration.

Applying the inequalities (A.12) and (A.11) for $\boldsymbol{x}=\widetilde{\lambda}_j(\widetilde{\boldsymbol{v}}_j)$, $\boldsymbol{y}=\phi_j^{\mathsf{d}}(\widetilde{\boldsymbol{v}})$, $\boldsymbol{t}=\boldsymbol{\theta}_1$ and $\bar{x}=\widetilde{\lambda}_j(\tilde{v}_j^{(\kappa)})$, $\bar{y}=\phi_j^{\mathsf{d}}(\tilde{v}^{(\kappa)})$, $\bar{t}=\theta_1^{(\kappa)}$ yields

$$\begin{aligned}\rho_j^{\mathsf{d}}(\widetilde{\boldsymbol{v}}) &\geq \rho^{\mathsf{d},(\kappa)}(\widetilde{\boldsymbol{v}})\\ &\triangleq \tilde{a}_j^{\mathsf{d},(\kappa)}-\tilde{b}_j^{\mathsf{d},(\kappa)}\left(\frac{|\widetilde{\lambda}_j(\tilde{v}_j^{(\kappa)})|^2}{2\Re\{(\widetilde{\lambda}_j(\tilde{v}_j^{(\kappa)}))^*\widetilde{\lambda}_j(\widetilde{\boldsymbol{v}}_j)\}-|\widetilde{\lambda}_j(\tilde{v}_j^{(\kappa)})|^2}+\frac{\phi_j^{\mathsf{d}}(\widetilde{\boldsymbol{v}})}{\phi_j^{\mathsf{d}}(\tilde{v}^{(\kappa)})}\right)\end{aligned} \tag{3.30}$$

and

$$\begin{aligned}\frac{\rho_j^{\mathsf{d}}(\widetilde{\boldsymbol{v}})}{\boldsymbol{\theta}_1} &\geq \tilde{f}_j^{\mathsf{d},(\kappa)}(\widetilde{\boldsymbol{v}},\boldsymbol{\theta}_1)\\ &\triangleq \tilde{\tilde{a}}_j^{\mathsf{d},(\kappa)}-\tilde{\tilde{b}}_j^{\mathsf{d},(\kappa)}\left(\frac{|\widetilde{\lambda}_j(\tilde{v}_j^{(\kappa)})|^2}{2\Re\{(\widetilde{\lambda}_j(\tilde{v}_j^{(\kappa)}))^*\widetilde{\lambda}_j(\widetilde{\boldsymbol{v}}_j)\}-|\widetilde{\lambda}_j(\tilde{v}_j^{(\kappa)})|^2}+\frac{\phi_j^{\mathsf{d}}(\widetilde{\boldsymbol{v}})}{\phi_j^{\mathsf{d}}(\tilde{v}^{(\kappa)})}\right)\\ &\quad -\tilde{\tilde{c}}_j^{\mathsf{d},(\kappa)}\boldsymbol{\theta}_1\end{aligned} \tag{3.31}$$

over the trust region

$$2\Re\{(\widetilde{\lambda}_j(\tilde{v}_j^{(\kappa)}))^*\widetilde{\lambda}_j(\widetilde{\boldsymbol{v}}_j)\}-|\widetilde{\lambda}_j(\tilde{v}_j^{(\kappa)})|^2>0, \quad j=1,\ldots,d, \tag{3.32}$$

where

$$0<\tilde{a}_j^{\mathsf{d},(\kappa)}=\rho_j^{\mathsf{d}}(\tilde{v}^{(\kappa)})+2\tilde{b}_j^{\mathsf{d},(\kappa)}, 0<\tilde{b}_j^{\mathsf{d},(\kappa)}=\frac{|\widetilde{\lambda}_j(\tilde{v}_j^{(\kappa)})|^2}{\phi_j^{\mathsf{d}}(\tilde{v}^{(\kappa)})+|\widetilde{\lambda}_j(\tilde{v}_j^{(\kappa)})|^2},$$

and

$$0 < \tilde{\tilde{a}}_j^{\mathsf{d},(\kappa)} = 2\frac{\rho_j^{\mathsf{d}}(\tilde{v}^{(\kappa)})}{\theta_1^{(\kappa)}} + 2\tilde{\tilde{b}}_j^{\mathsf{d},(\kappa)},$$
$$0 < \tilde{\tilde{b}}_j^{\mathsf{d},(\kappa)} = \frac{|\widetilde{\lambda}_j(\tilde{v}_j^{(\kappa)})|^2}{(\phi_j^{\mathsf{d}}(\tilde{v}^{(\kappa)}) + |\widetilde{\lambda}_j(\tilde{v}_j^{(\kappa)})|^2)\theta_1^{(\kappa)}},$$
$$0 < \tilde{\tilde{c}}_j^{\mathsf{d},(\kappa)} = \frac{\rho_j^{\mathsf{d}}(\tilde{v}^{(\kappa)})}{(\theta_1^{(\kappa)})^2}.$$

The nonconvex constraint (3.28d) is innerly approximated by the following convex constraint

$$\rho^{\mathsf{d},(\kappa)}(\widetilde{\boldsymbol{v}}) \geq \boldsymbol{\theta}_1 r_{\mathsf{d}}, \quad j = 1, \ldots, d, \tag{3.33}$$

i.e. any feasible point for (3.33) is also feasible for (3.28d).

Applying the inequalities (A.4) and (A.3) in the appendix for $\boldsymbol{x} = \boldsymbol{p}_i\sigma_{\mathsf{bs}}^2/|\tilde{R}_{\mathsf{bs}}(i,i)|^2$, $\boldsymbol{t} = \boldsymbol{\theta}_2$, and $\bar{x} = p_i^{(\kappa)}\sigma_{\mathsf{bs}}^2/|\tilde{R}_{\mathsf{bs}}(i,i)|^2$, $\bar{t} = \theta_2^{(\kappa)}$ yields

$$\rho_i^{\mathsf{u}}(\boldsymbol{p}_i) \geq \rho_i^{\mathsf{u},(\kappa)}(\boldsymbol{p}_i) \triangleq a_i^{\mathsf{u},(\kappa)} - b_i^{\mathsf{u},(\kappa)}\frac{\boldsymbol{p}_i}{p_i^{(\kappa)}} \tag{3.34}$$

and

$$\frac{\rho_i^{\mathsf{u}}(\boldsymbol{p}_i)}{\boldsymbol{\theta}_2} \geq \tilde{f}_i^{\mathsf{u},(\kappa)}(\boldsymbol{p}_i, \boldsymbol{\theta}_2) \triangleq \tilde{a}_i^{\mathsf{u},(\kappa)} - \tilde{b}_i^{\mathsf{u},(\kappa)}\frac{\boldsymbol{p}_i}{p_i^{(\kappa)}} - \tilde{c}_i^{\mathsf{u},(\kappa)}\boldsymbol{\theta}_2, \tag{3.35}$$

where

$$0 < a_i^{\mathsf{u},(\kappa)} = \rho_i^{\mathsf{u}}(p_i^{(\kappa)}) + b_i^{\mathsf{u},(\kappa)}, b_i^{\mathsf{u},(\kappa)} = \frac{|\tilde{R}_{\mathsf{bs}}(i,i)|^2}{p_i^{(\kappa)}\sigma_{\mathsf{bs}}^2 + |\tilde{R}_{\mathsf{bs}}(i,i)|^2}, \tag{3.36}$$

and

$$0 < \tilde{a}_i^{\mathsf{u},(\kappa)} = 2\frac{\rho_i^{\mathsf{u}}(p_i^{(\kappa)})}{\theta_2^{(\kappa)}} + \tilde{b}_i^{\mathsf{u},(\kappa)},$$
$$\tilde{b}_i^{\mathsf{u},(\kappa)} = \frac{|\tilde{R}_{\mathsf{bs}}(i,i)|^2}{(p_i^{(\kappa)}\sigma_{\mathsf{bs}}^2 + |\tilde{R}_{\mathsf{bs}}(i,i)|^2)\theta_2^{(\kappa)}},$$
$$\tilde{c}_i^{\mathsf{u},(\kappa)} = \frac{\rho_i^{\mathsf{u}}(p_i^{(\kappa)})}{(\theta_2^{(\kappa)})^2}.$$

The nonconvex constraint (3.28e) is innerly approximated by the following convex constraint

$$\rho_i^{\mathsf{u},(\kappa)}(\boldsymbol{p}_i) \geq \boldsymbol{\theta}_2 r_{\mathsf{u}}, \quad i = 1, \ldots, u. \tag{3.37}$$

To generate the next feasible point $(\tilde{v}^{(\kappa+1)}, p^{(\kappa+1)}, \theta^{(\kappa+1)})$ at the κth iteration, we solve the following convex problem t:

$$\begin{aligned}\max_{\tilde{\boldsymbol{v}},\boldsymbol{p},\boldsymbol{\theta},\boldsymbol{\tau}} \ \tilde{L}^{(\kappa)}(\tilde{\boldsymbol{v}},\boldsymbol{p},\boldsymbol{\theta}) \triangleq \sum_{j=1}^{d} \tilde{f}_j^{\mathsf{d},(\kappa)}(\tilde{\boldsymbol{v}},\boldsymbol{\theta}_1) + \sum_{i=1}^{u} \tilde{f}_i^{\mathsf{u},(\kappa)}(\boldsymbol{x}_i,\boldsymbol{\theta}_2) - \tilde{\Phi}(\tilde{v}^{(\kappa)}, x^{(\kappa)}, \theta^{(\kappa)})\tilde{P}^{tot}(\tilde{\boldsymbol{v}},\boldsymbol{p},\boldsymbol{\theta}) \\ \text{s.t.}(3.26f), (3.26g), (3.27), (3.28b), (3.32), (3.33), (3.37). \end{aligned} \tag{3.38}$$

Note that any feasible point for the convex problem (3.38) is also feasible for the nonconvex problem (3.28). Also, $\tilde{L}^{(\kappa)}(\tilde{v}^{(\kappa)}, p^{(\kappa)}, \theta^{(\kappa)}) = 0$ so $\tilde{L}^{(\kappa)}(\tilde{v}^{(\kappa+1)}, p^{(\kappa+1)}, \theta^{(\kappa+1)}) > 0$ at the optimal solution of (3.38) as far as $(\tilde{v}^{(\kappa)}, p^{(\kappa)}, \theta^{(\kappa)}) \neq (\tilde{v}^{(\kappa+1)}, p^{(\kappa+1)}, \theta^{(\kappa+1)})$. Like (3.20),we then have

$$\tilde{\Phi}(\tilde{v}^{(\kappa+1)}, p^{(\kappa+1)}, \theta^{(\kappa+1)}) > \tilde{\Phi}(\tilde{v}^{(\kappa)}, p^{(\kappa)}, \theta^{(\kappa)}), \tag{3.39}$$

i.e. $(\tilde{v}^{(\kappa+1)}, p^{(\kappa+1)}, \theta^{(\kappa+1)})$ is a better feasible for (3.28) than $(\tilde{v}^{(\kappa)}, p^{(\kappa)}, \theta^{(\kappa)})$. As such, the sequence $\{(\tilde{v}^{(\kappa)}, p^{(\kappa)}, \theta^{(\kappa)})\}$ converges at least to a locally optimal solution of (3.28).

It is important to locate a feasible point $(\tilde{v}^{(0)}, p^{(0)}, \theta^{(0)})$ for (3.28) for initialization as follows: under fixed $\tau^{(0)}$ and $(\theta_1^{(0)}, \theta_2^{(0)}) = (1/\tau^{(0)}, 1/(\eta - \tau^{(0)}))$, by changing variable if necessary one can replace $|\tilde{\lambda}_j(\tilde{\boldsymbol{v}}_j)|^2$ by $(\bar{\lambda}_j(\tilde{\boldsymbol{v}}_j))^2$ for $\bar{\lambda}_j(\tilde{\boldsymbol{v}}_j) = \Re\{\tilde{\lambda}_j(\tilde{\boldsymbol{v}}_j)\}$ in (3.22), so

$$\rho_j^{\mathsf{d}}(\tilde{\boldsymbol{v}}) = \ln\left(1 + \frac{(\bar{\lambda}_j(\tilde{\boldsymbol{v}}_j))^2}{\phi_j(\tilde{\boldsymbol{v}})}\right),$$

and (3.26d) is equivalent to the SOC constraint

$$\begin{aligned}\bar{\lambda}_j(\tilde{\boldsymbol{v}}_j) &\geq \sqrt{e^{r_{\mathsf{d}}/\tau^{(0)}} - 1}\sqrt{\phi_j(\tilde{\boldsymbol{v}})} \\ &= \sqrt{e^{r_{\mathsf{d}}/\tau^{(0)}} - 1}\left\|\begin{matrix}(\tilde{h}_{j,\mathsf{bs}}^H \tilde{\boldsymbol{v}}_\ell)_{\ell\in\mathcal{D}\setminus\{j\}} \\ \sigma_{\mathsf{d}}\end{matrix}\right\|_2, j = 1, \ldots, d,\end{aligned}$$

while (3.26e) is also equivalent to the following linear constraint

$$|\tilde{R}_{\mathsf{bs}}(i,i)| \geq \boldsymbol{p}_i\sqrt{e^{r_{\mathsf{u}}/(\eta-\tau^{(0)})}-1}\sigma_{\mathsf{bs}}, \quad i=1,\ldots,u. \tag{3.40}$$

We then solve the following convex problem to generate $(\tilde{v}^{(0)}, p^{(0)})$

$$\min_{\widetilde{\boldsymbol{v}},\boldsymbol{p}} \sum_{j=1}^{d}||\widetilde{\boldsymbol{v}}_j||^2+\sum_{i=1}^{u}\frac{1}{\boldsymbol{p}_i} \quad \text{s.t.} \quad (3.40),(3.40), \tag{3.41a}$$

$$\sum_{j=1}^{d}||\widetilde{\boldsymbol{v}}_j||^2 \leq \frac{P_{\mathrm{BS}}^{\max}}{\tau^{(0)}}, ||\widetilde{\boldsymbol{v}}_j||^2 \leq P_{\mathsf{D}}^{\max}, \quad j=1,\ldots,d, \tag{3.41b}$$

$$1 \leq \frac{P_{\mathrm{UE}}^{\max}}{\eta-\tau^{(0)}}\boldsymbol{p}_i, 1/P_{\mathsf{U}}^{\max} \leq \boldsymbol{p}_i, \quad i=1,\ldots,u. \tag{3.41c}$$

Algorithm 2 summarizes our proposed computational procedure for solving (3.28).

Algorithm 2 TF-wise EE Optimization Algorithm

1: Set $\kappa=0$. For a fixed $0<\tau^{(0)}<1$ solve (3.41) for a feasible point $(\tilde{v}^{(0)}, p^{(0)})$ for (3.26) and then set $\theta_1^{(0)}=1/\tau^{(0)}$ and $\theta_2^{(0)}=1/(\eta-\tau^{(0)})$.
2: **Repeat:** Generate the next feasible point $(\tilde{v}^{(k)}, p^{(\kappa)}, \theta^{(\kappa)})$ for (3.28) by solving the convex problem (3.38). Set $\kappa:=\kappa+1$.
3: **Output** $(\tilde{v}^{(k)}, p^{(\kappa)}, \theta^{(\kappa)})$ and $\tau^{(\kappa)}=1/\theta_1^{(\kappa)}$ as the optimal solution of (3.26).

3.4 Bandwidth-fraction-wise STR

Instead of time-fraction allocation for serving uplinks and downlinks, we now consider a bandwidth allocation for their service, i.e. a portion $0<\boldsymbol{\tau}<1$ of the whole normalized bandwidth is allocated to the downlink service, the portion ϵ for guarding and the remaining complementary portion $(\eta-\boldsymbol{\tau})$ with $\eta=1-\epsilon$ is allocated to the uplink service. Unlike two approaches presented in the previous section, this bandwidth-fraction-wise STR can be practically implemented only when the portion τ is determined and fixed beforehand. In simulation, we also provide numerical for $\tau=1/2$, i.e. a half of the bandwidth is used for serving the uplinks and another half of the bandwidth is used for serving downlinks.

As in (3.1), let $h_{j,\mathsf{bs}} \in \mathbb{C}^{n_1}$ be the channel vector from the BS to DL_j and $\boldsymbol{v}_j$ be the beamformer for the information s_j^{d} intended for DL_j. The received signal at DL_j is

$$\hat{y}_j \triangleq \underbrace{h_{j,\mathsf{bs}}^H \boldsymbol{v}_j s_j^{\mathsf{d}}}_{\text{desired signal}} + \underbrace{\sum_{\ell \in \mathcal{D}\setminus\{j\}} h_{j,\mathsf{bs}}^H \boldsymbol{v}_\ell s_\ell^{\mathsf{d}}}_{\text{DL interference}} + n_j(\boldsymbol{\tau}), j = 1, \ldots, d, \tag{3.42}$$

where $n_j(\boldsymbol{\tau})$ is the additive white circularly symmetric complex Gaussian noise with the variance $\boldsymbol{\tau}\sigma_{\mathsf{d}}^2$. Unlike (3.1), the received signal y_j is now free from the UL interference as the BS's broadcast and ULs' transmit are implemented in orthogonal frequency bands.

The throughput at DL_j is $\boldsymbol{\tau}\varphi_j^{\mathsf{d}}(\boldsymbol{v}, \boldsymbol{\tau})$ with

$$\varphi_j^{\mathsf{d}}(\boldsymbol{v}, \boldsymbol{\tau}) \triangleq \ln\left(1 + \frac{|\tilde{\lambda}_j(\boldsymbol{v}_j)|^2}{\upsilon_j(\boldsymbol{v}, \boldsymbol{\tau})}\right), \tag{3.43}$$

where $\tilde{\lambda}_j(\boldsymbol{v}_j) \triangleq h_{j,\mathsf{bs}}^H \widetilde{\boldsymbol{v}}_j$ as in (3.2), and $\upsilon_j(\boldsymbol{v}, \boldsymbol{\tau}) \triangleq \sum_{\ell \in \mathcal{D}\setminus\{j\}} |h_{j,\mathsf{bs}}^H \boldsymbol{v}_\ell|^2 + \boldsymbol{\tau}\sigma_{\mathsf{d}}^2$.

As in (3.4), let $h_{\mathsf{bs},i} \in \mathbb{C}^{n_2}$ be the channel vector from UL_i to the BS, and s_i^{u} be the information UL_i intends to send to the BS. The received signal at the BS is

$$\hat{y}_{\mathsf{bs}} \triangleq \sum_{i=1}^{u} h_{\mathsf{bs},i}\sqrt{\boldsymbol{p}_i} s_i^{\mathsf{u}} + n_{\mathsf{bs}}(\boldsymbol{\tau}), \tag{3.44}$$

where $\boldsymbol{p}_i$ is the UL_i' transmit power, and $n_{\mathsf{bs}}(\boldsymbol{\tau})$ is the additive white circularly symmetric Gaussian noise with variance $(\eta - \boldsymbol{\tau})\sigma_{\mathsf{bs}}^2 I_{N_2}$. The achievable uplink throughput for s_i^{u} at the BS is $(\eta - \boldsymbol{\tau})\varphi_i^{\mathsf{u}}(\boldsymbol{p}_i, \boldsymbol{\tau})$ with

$$\varphi_i^{\mathsf{u}}(\boldsymbol{p}, \boldsymbol{\tau}) \triangleq \ln\left(1 + \frac{\boldsymbol{p}_i |\tilde{R}_{\mathsf{bs}}(i,i)|^2}{(\eta - \boldsymbol{\tau})\sigma_{\mathsf{bs}}^2}\right). \tag{3.45}$$

The consumed power P^{tot} is modelled by the following convex quadratic function

$$P^{tot}(\boldsymbol{v}, \boldsymbol{p}) = \zeta P_i^t(\boldsymbol{v}, \boldsymbol{p}) + P^{BS} + UP^{UE}, \tag{3.46}$$

where $P^t(\boldsymbol{v}, \boldsymbol{p}) \triangleq \sum_{j=1}^{d} ||\boldsymbol{v}_j||^2 + \sum_{i=1}^{u} \boldsymbol{p}_i$.

The bandwidth-fraction-wise (BF-wise) STR's EE optimization problem is formulated as

$$\max_{0<\boldsymbol{\tau}<1,\boldsymbol{v},\boldsymbol{p}} \ \hat{\Phi}(\boldsymbol{v},\boldsymbol{p},\boldsymbol{\tau}) \triangleq$$

$$\frac{\boldsymbol{\tau}\sum_{j=1}^{d}\varphi_j^{\mathsf{d}}(\boldsymbol{v},\boldsymbol{\tau})+(\eta-\boldsymbol{\tau})\sum_{i=1}^{u}\varphi_i^{\mathsf{u}}(\boldsymbol{p}_i,\boldsymbol{\tau})}{P^{tot}(\boldsymbol{v},\boldsymbol{p})} \quad \text{s.t.} \tag{3.47a}$$

$$\sum_{j=1}^{d}||\boldsymbol{v}_j||^2 \le P_{\mathrm{BS}}^{\max}, \tag{3.47b}$$

$$\boldsymbol{p}_i \le P_{\mathrm{UE}}^{\max}, \quad i=1,\ldots,u, \tag{3.47c}$$

$$\boldsymbol{\tau}\varphi_j^{\mathsf{d}}(\boldsymbol{v},\boldsymbol{\tau}) \ge r_{\mathsf{d}}, \quad j=1,\ldots,d, \tag{3.47d}$$

$$(\eta-\boldsymbol{\tau})\varphi_i^{\mathsf{u}}(\boldsymbol{p}_i,\boldsymbol{\tau}) \ge r_{\mathsf{u}}, \quad i=1,\ldots,u, \tag{3.47e}$$

which a nonconvex problem as the objective function is nonconcave while the downlink and uplink QoS constraints (3.47d) and (3.47e) are nonconvex. Like the computational approach presented in the previous sections, we now develop a lower-bounding concave approximation for the numerator of its objective function and inner convex approximations for its nonconvex constraints.

Let $(v^{(\kappa)},p^{(\kappa)},\tau^{(\kappa)})$ be a feasible point for (3.47) at $(\kappa-1)$th iteration. Applying the inequalities (A.12) and (A.13) for

$$\begin{aligned}\varphi_j^{\mathsf{d}}(\boldsymbol{v},\boldsymbol{\tau}) &\ge \varphi_j^{\mathsf{d},(\kappa)}(\boldsymbol{v},\boldsymbol{\tau})\\ &\triangleq \hat{a}_j^{\mathsf{d},(\kappa)}-\hat{b}_j^{\mathsf{d},(\kappa)}\left(\frac{|\widetilde{\lambda}_j(v_j^{(\kappa)})|^2}{2\Re\{(\widetilde{\lambda}_j(v_j^{(\kappa)}))^*\widetilde{\lambda}_j(\boldsymbol{v}_j)\}-|\widetilde{\lambda}_j(v_j^{(\kappa)})|^2}+\frac{\upsilon_j(\boldsymbol{v},\boldsymbol{\tau})}{\upsilon_j(v^{(\kappa)},\tau^{(\kappa)})}\right),\end{aligned} \tag{3.48}$$

and

$$\begin{aligned}\boldsymbol{\tau}\varphi_j^{\mathsf{d}}(\boldsymbol{v},\boldsymbol{\tau}) \ge \hat{f}_j^{\mathsf{d},(\kappa)}(\boldsymbol{v},\boldsymbol{\tau})\hat{a}_j^{\mathsf{d},(\kappa)}-\hat{b}_j^{\mathsf{d},(\kappa)}&\left(\frac{|\widetilde{\lambda}_j(v_j^{(\kappa)})|^2}{2\Re\{(\widetilde{\lambda}_j(v_j^{(\kappa)}))^*\widetilde{\lambda}_j(\boldsymbol{v}_j)\}-|\widetilde{\lambda}_j(v_j^{(\kappa)})|^2}\right.\\ &\left.+\frac{\upsilon_j(\boldsymbol{v},\boldsymbol{\tau})}{\upsilon_j(v^{(\kappa)},\tau^{(\kappa)})}\right)-\frac{\hat{\hat{c}}_j^{\mathsf{d},(\kappa)}}{\boldsymbol{\tau}},\end{aligned} \tag{3.49}$$

over the trust region (3.32), where

$$0 < \hat{a}_j^{\mathsf{d},(\kappa)} = \varphi_j^{\mathsf{d}}(v^{(\kappa)}, \tau^{(\kappa)}) + 2\hat{b}_j^{\mathsf{d},(\kappa)}, 0 < \hat{b}_j^{\mathsf{d},(\kappa)} = \frac{|\widetilde{\lambda}_j(v_j^{(\kappa)})|^2}{\upsilon_j(v^{(\kappa)}, \tau^{(\kappa)}) + |\widetilde{\lambda}_j(v_j^{(\kappa)})|^2}, \quad (3.50)$$

and

$$\begin{aligned} 0 < \hat{\hat{a}}_j^{\mathsf{d},(\kappa)} &= 2\tau^{(\kappa)}\varphi_j^{\mathsf{d}}(v^{(\kappa)}, \tau^{(\kappa)}) + 2\hat{\hat{b}}_j^{\mathsf{d},(\kappa)}, \\ 0 < \hat{\hat{b}}_j^{\mathsf{d},(\kappa)} &= \frac{\tau^{(\kappa)}|\widetilde{\lambda}_j(v_j^{(\kappa)})|^2}{\upsilon_j(v^{(\kappa)}, \tau^{(\kappa)}) + |\widetilde{\lambda}_j(v_j^{(\kappa)})|^2}, \\ 0 < \hat{\hat{c}}_j^{\mathsf{d},(\kappa)} &= (\tau^{(\kappa)})^2\varphi_j^{\mathsf{d}}(v^{(\kappa)}, \tau^{(\kappa)}). \end{aligned}$$

Applying the inequalities (A.7) and (A.10) in the appendix for $\boldsymbol{x} = \boldsymbol{p}_i|\tilde{R}_{\mathsf{bs}}(i,i)|^2$, $\boldsymbol{y} = (\eta - \boldsymbol{\tau})\sigma_{\mathsf{bs}}^2$ and $\bar{x} = p_i^{(\kappa)}|\tilde{R}_{\mathsf{bs}}(i,i)|^2$, $\bar{y} = (\eta - \tau^{(\kappa)})\sigma_{\mathsf{bs}}^2$ yields

$$\begin{aligned} \varphi_i^{\mathsf{u}}(\boldsymbol{p}, \boldsymbol{\tau}) &\geq \varphi_i^{\mathsf{u},(\kappa)}(\boldsymbol{p}, \boldsymbol{\tau}) \\ &\triangleq \hat{a}_i^{\mathsf{u},(\kappa)} - \hat{b}_i^{\mathsf{u},(\kappa)} \left(\frac{p_i^{(\kappa)}}{\boldsymbol{p}_i} + \frac{\eta - \boldsymbol{\tau}}{\eta - \tau^{(\kappa)}} \right), \end{aligned} \quad (3.51)$$

and

$$\begin{aligned} (\eta - \boldsymbol{\tau})\varphi_i^{\mathsf{u}}(\boldsymbol{p}, \boldsymbol{\tau}) &\geq \hat{f}_i^{\mathsf{u},(\kappa)}(\boldsymbol{p}, \boldsymbol{\tau}) \\ &\triangleq \hat{\hat{a}}_i^{\mathsf{u},(\kappa)} - \hat{\hat{b}}_i^{\mathsf{u},(\kappa)} \left(\frac{p_i^{(\kappa)}}{\boldsymbol{p}_i} + \frac{\eta - \boldsymbol{\tau}}{\eta - \tau^{(\kappa)}} \right) - \frac{\hat{\hat{c}}_i^{\mathsf{u},(\kappa)}}{\eta - \boldsymbol{\tau}}, \end{aligned} \quad (3.52)$$

where

$$0 < \hat{a}_i^{\mathsf{u},(\kappa)} = \varphi_i^{\mathsf{u}}(p^{(\kappa)}, \tau^{(\kappa)}) + 2\hat{b}_i^{\mathsf{u},(\kappa)}, 0 < \hat{b}_i^{\mathsf{u},(\kappa)} = \frac{p_i^{(\kappa)}|\tilde{R}_{\mathsf{bs}}(i,i)|^2}{(\eta - \tau^{(\kappa)})\sigma_{\mathsf{bs}}^2 + p_i^{(\kappa)}|\tilde{R}_{\mathsf{bs}}(i,i)|^2}, \quad (3.53)$$

and

$$\begin{aligned} 0 < \hat{\hat{a}}_i^{\mathsf{u},(\kappa)} &= 2(\eta - \tau^{(\kappa)})\varphi_i^{\mathsf{u}}(p^{(\kappa)}, \tau^{(\kappa)}) + 2\hat{\hat{b}}_i^{\mathsf{u},(\kappa)}, \\ 0 < \hat{\hat{b}}_i^{\mathsf{u},(\kappa)} &= \frac{(\eta - \tau^{(\kappa)})p_i^{(\kappa)}|\tilde{R}_{\mathsf{bs}}(i,i)|^2}{(\eta - \tau^{(\kappa)})\sigma_{\mathsf{bs}}^2 + p_i^{(\kappa)}|\tilde{R}_{\mathsf{bs}}(i,i)|^2}, \end{aligned}$$

$$0 < \hat{c}_i^{\mathsf{u},(\kappa)} = (\eta - \tau^{(\kappa)})^2 \varphi_i^{\mathsf{u}}(p^{(\kappa)}, \tau^{(\kappa)}).$$

We thus solve the following convex problem to generate the next feasible point $(v^{(\kappa+1)}, p^{(\kappa+1)}, \tau^{(\kappa+1)})$ for (3.47):

$$\max_{0<\boldsymbol{\tau}<1, \boldsymbol{v}, \boldsymbol{p}} \ \hat{L}^{(\kappa)}(\boldsymbol{v}, \boldsymbol{p}, \boldsymbol{\tau}) \triangleq$$

$$\sum_{j=1}^{d} \hat{f}_j^{\mathsf{d},(\kappa)}(\boldsymbol{v}, \boldsymbol{\tau}) + \sum_{i=1}^{u} \hat{f}_i^{\mathsf{u},(\kappa)}(\boldsymbol{p}, \boldsymbol{\tau}) - \hat{\Phi}(v^{(\kappa)}, p^{(\kappa)}, \tau^{(\kappa)}) P^{tot}(\boldsymbol{v}, \boldsymbol{p})$$

$$\text{s.t.} \quad (3.32), (3.47b), (3.47c), \tag{3.54a}$$

$$\varphi_j^{\mathsf{d},(\kappa)}(\boldsymbol{v}, \boldsymbol{\tau}) \geq r_{\mathsf{d}}/\boldsymbol{\tau}, \quad j = 1, \ldots, d, \tag{3.54b}$$

$$\varphi_i^{\mathsf{u},(\kappa)}(\boldsymbol{p}_i, \boldsymbol{\tau}) \geq r_{\mathsf{u}}/(\eta - \boldsymbol{\tau}), \quad i = 1, \ldots, u, \tag{3.54c}$$

where by (3.49) and (3.52), a lower-bounding concave expression for the numerator of the objective function in (3.47a) is provided by the first two terms in (3.54a), while by (3.48) and (3.51) the convex constraints (3.54b) and (3.54c) provides an inner convex expression for the nonconvex constraint (3.47d) and (3.47e), respectively. Similarly to (3.39), it is easy to show that

$$\hat{\Phi}(v^{(\kappa+1)}, p^{(\kappa+1)}, \tau^{(\kappa+1)}) > \hat{\Phi}(v^{(\kappa)}, p^{(\kappa)}, \tau^{(\kappa)}),$$

as far as $(v^{(\kappa+1)}, p^{(\kappa+1)}, \tau^{(\kappa+1)}) \neq (v^{(\kappa)}, p^{(\kappa)}, \tau^{(\kappa)})$, i.e. $(v^{(\kappa+1)}, p^{(\kappa+1)}, \tau^{(\kappa+1)})$ is a better feasible point than $(v^{(\kappa)}, p^{(\kappa)}, \tau^{(\kappa)})$ for the nonconvex optimization problem (3.47). The sequence $\{(v^{(\kappa)}, p^{(\kappa)}, \tau^{(\kappa)})\}$ thus converges at least to a locally optimal solution of (3.47).

To locate an initial feasible point $(v^{(0)}, p^{(0)}, \tau^{(0)})$ for (3.47) we fix $\tau^{(0)}$ and replace $|\tilde{\lambda}_j(\boldsymbol{v}_j)|^2$ by $(\bar{\lambda}_j(\boldsymbol{v}_j))^2$ for $\bar{\lambda}_j(\boldsymbol{v}_j) = \Re\{\tilde{\lambda}_j(\boldsymbol{v}_j)\}$ in (3.43), to make

$$\varphi_j^{\mathsf{d}}(\boldsymbol{v}, \boldsymbol{\tau}) = \ln\left(1 + \frac{(\bar{\lambda}_j(\boldsymbol{v}_j))^2}{v_j(\boldsymbol{v}, \boldsymbol{\tau})}\right),$$

so the nonconvex downlink QoS constraint (3.47d) is equivalent to the SOC constraint

$$\begin{aligned}\bar{\lambda}_j(\boldsymbol{v}_j) &\geq \sqrt{e^{r_j^{\min}/\tau^{(0)}}-1}\sqrt{v_j(\boldsymbol{v},\boldsymbol{\tau})} \\ &= \sqrt{e^{r_j^{\min}/\tau^{(0)}}-1}\left\|\begin{matrix}(h_{j,\mathsf{bs}}^H\boldsymbol{v}_\ell)_{\ell\in\mathcal{D}\setminus\{j\}} \\ \tau_0\sigma_{\mathsf{d}}\end{matrix}\right\|_2, \end{aligned} \tag{3.55}$$

while the nonconvex uplink QoS constraint (3.47e) is also equivalent to the following SOC constraint

$$\sqrt{\boldsymbol{p}_i}|\tilde{R}_{\mathsf{bs}}(i,i)| \geq \sqrt{e^{r_{\mathsf{bs}}^{\min}/(\eta-\tau^{(0)})}-1}\sqrt{(\eta-\tau^{(0)})}\sigma_{\mathsf{bs}},\ i=1,\ldots,u.$$

We then solve the convex problem

$$\min_{\boldsymbol{v},\boldsymbol{p}} \sum_{j=1}^{d}||\boldsymbol{v}_j||^2+\sum_{i=1}^{u}\boldsymbol{p}_i \quad \text{s.t.} \quad (3.47b),(3.47c),(3.55),(3.56) \tag{3.56}$$

to obtain a feasible point $(v^{(0)},p^{(0)},\tau^{(0)})$ for (3.47).

Algorithm 3 summarizes our proposed computational procedure for solving (3.47).

Algorithm 3 BF-wise EE Optimization Algorithm

1: Set $\kappa=0$. For a fixed $0<\tau^{(0)}<1$ solve (3.56) for a feasible point $(v^{(0)},p^{(0)},\tau^{(0)})$ for (3.47).
2: **Repeat** Generate the next feasible point $(v^{(\kappa+1)},p^{(\kappa+1)},\tau^{(\kappa+1)})$ for (3.47) by solving the convex problem (3.54). Set $\kappa:=\kappa+1$.
3: **Output** $(v^{(\kappa+1)},p^{(\kappa+1)},\tau^{(\kappa+1)})$.

3.5 Numerical Results

The data of wireless communications in a macrocell environment is used to weight the pros and con of the proposed STRs. Table I taken from [61] lists important parameters used in all simulations. The number of served downlink users and uplink users are $d=u=n/2$, which also means $n_1=n_2=n/2$. For e-FT and FB, set $\epsilon=0.1$. [1] The

[1] According [62], the one time slot is 0.667ms and the antennas switching time is 0.02ms while the guard band is also about 10% of the available bandwidth.

channel vector between the BS and an user follows the line for sight (LOS) path loss model as $10^{-PL_{\text{LOS}}/20}\tilde{h}$ with $PL_{\text{LOS}} = 103.4 + 24.2\log_{10}\delta_1$, where the entries of $\tilde{h}$ are independent circularly-symmetric Gaussian random variables with zero means and unit variance and δ_1 (km) is their distance. The interfering channel from an UL to a DL follows the non-line-of-sight (NLOS) path loss model as $10^{-PL_{\text{NLOS}}/20}\tilde{h}_{uu}$ with $PL_{\text{NLOS}} = 131.1 + 42.8\log_{10}\delta_2$, where $\tilde{h}_{uu}$ is circular-symmetric random variable with zero means and unit variance, and δ_2 is their distance. If not specially specified, DL and UL users are uniformly distributed in the cell so that $\delta_1 = 0.25$ km and $\delta_2 = 0.1$ km, respectively.

Table 3.1 Simulation Parameters

Parameter	Value
Carrier frequency	2 GHz
System bandwidth	10 MHz
Maximum BS transmit power ($P_{\text{BS}}^{\max}$)	46 dBm
Maximum user transmit power ($P_{\text{UE}}^{\max}$)	23 dBm
Dynamic circuit power of the BS (P_c^{BS})	6.31 W
Static circuit power of the BS (P_s^{BS})	0.5012 W
Dynamic circuit power of a UE (P_c^{UE})	4.417 W
Static circuit power of the UEs (P_s^{UE})	0.1 W
Noise power density	-174dBm/Hz

The tolerance for the algorithm convergence is set to 10^{-4}. In arriving at the final figures, the results of 1000 Monte-Carlo runs are averaged.

3.5.1 Spectral efficiency in terms of max-min throughput

Although the chapter is mainly focused on EE optimization subject to downlink and uplink QoS constraints, it is still of interest to know how the spectral efficiency of the three STRs by considering the following max-min throughput optimization problem

$$\max_{\boldsymbol{v},\boldsymbol{p}} \ \min\{\min_{j=1,\ldots,d} r_j^{\mathsf{d}}(\boldsymbol{v},\boldsymbol{p}), \min_{i=1,\ldots,u} r_i^{\mathsf{u}}(\boldsymbol{v},\boldsymbol{p}_i)\} \quad \text{s.t.} \quad (3.10b), (3.10c) \tag{3.57}$$

for the FD-based STR, and

$$\max_{0<\boldsymbol{\tau}<1,\widetilde{\boldsymbol{v}},\boldsymbol{p}} \min\{\min_{j=1,\ldots,d} \boldsymbol{\tau}\rho_j^{\mathsf{d}}(\widetilde{\boldsymbol{v}}), \min_{i=1,\ldots,u}(\eta-\boldsymbol{\tau})\rho_i^{\mathsf{u}}(\boldsymbol{p}_i)\} \quad \text{s.t.} \quad (3.26b),(3.26c),(3.26f),(3.26g) \tag{3.58}$$

for the TF-wise STR, and

$$\max_{0<\boldsymbol{\tau}<1,\boldsymbol{v},\boldsymbol{p}} \min\{\min_{j=1,\ldots,d} \boldsymbol{\tau}\sum_{j=1}^{d}\varphi_j^{\mathsf{d}}(\boldsymbol{v},\boldsymbol{\tau}), \min_{i=1,\ldots,u}(\eta-\boldsymbol{\tau})\varphi_i^{\mathsf{u}}(\boldsymbol{p}_i,\boldsymbol{\tau})\}\text{s.t.}(3.47b),(3.47c), \tag{3.59}$$

for the BF-wise STR. Obviously, these nonsmooth nonconvex optimization problems can be solved by the Algorithms that are similar to Algorithms 1-3, which at the κth iteration compute the following convex problem

$$\max_{\boldsymbol{v},\boldsymbol{p}} \min\{\min_{j=1,\ldots,d} r_j^{\mathsf{d},(\kappa)}(\boldsymbol{v},\boldsymbol{p}), \min_{i=1,\ldots,u} r_i^{\mathsf{u},(\kappa)}(\boldsymbol{v},\boldsymbol{p}_i)\} \quad \text{s.t.} \quad (3.10b),(3.10c),(3.16),(3.18), \tag{3.60}$$

with $r_j^{\mathsf{d},(\kappa)}$ and $r_i^{\mathsf{u},(\kappa)}$ defined from (3.15) and (3.17) to generate a better feasible point $(v^{(\kappa+1)},p^{(\kappa+1)})$ for (3.57), and

$$\max_{\widetilde{\boldsymbol{v}},\boldsymbol{p},\boldsymbol{\theta},\boldsymbol{\tau}} \min\{\min_{j=1,\ldots,d} \tilde{f}_j^{\mathsf{d},(\kappa)}(\widetilde{\boldsymbol{v}},\boldsymbol{\theta}_1), \min_{i=1,\ldots,u} \tilde{f}_i^{\mathsf{u},(\kappa)}(\boldsymbol{x}_i,\boldsymbol{\theta}_2)\} \quad \text{s.t.} \quad (3.26f),(3.26g),(3.27),(3.28b),(3.32), \tag{3.61}$$

with $\tilde{f}_j^{\mathsf{d},(\kappa)}$ and $\tilde{f}_i^{\mathsf{u},(\kappa)}$ defined from (3.31) and (3.35) to generate a better feasible point $(v^{(\kappa+1)},p^{(\kappa+1)},\theta^{(\kappa+1)},\tau^{(\kappa+1)})$ for (3.58), and

$$\max_{0<\boldsymbol{\tau}<1,\boldsymbol{v},\boldsymbol{p}} \min\{\min_{j=1,\ldots,d} \hat{f}_j^{\mathsf{d},(\kappa)}(\boldsymbol{v},\boldsymbol{\tau}), \min_{i=1,\ldots,u} \hat{f}_i^{\mathsf{u},(\kappa)}(\boldsymbol{p},\boldsymbol{\tau})\}\text{s.t.} \quad (3.32),(3.47b),(3.47c) \tag{3.62}$$

with $\hat{f}_j^{\mathsf{d},(\kappa)}$ and $\hat{f}_i^{\mathsf{u},(\kappa)}$ defined from (3.49) and (3.52) to generate a better feasible point $(v^{(\kappa+1)},p^{(\kappa+1)},\tau^{(\kappa+1)})$ for (3.59).

Fig. 3.4 plots the achievable minimum throughput under different n. Only the achievable max-min throughput of the FD based STR is severely downgraded when the SI σ_{SI}^2 increases, which is especially low for the practical range $[-120,-90]$ dB

of σ_{SI}^2. Both TF and BF outperform FD for $\sigma_{SI}^2 \geq -110$ dB. At $\sigma_{SI}^2 = -90$ dB, the achievable minimum throughput by the formers is actually twice of that achievable by the latter. The gap is wider by increasing the number of transmit antennas, which leads to more downlink interference to uplinks under FD.

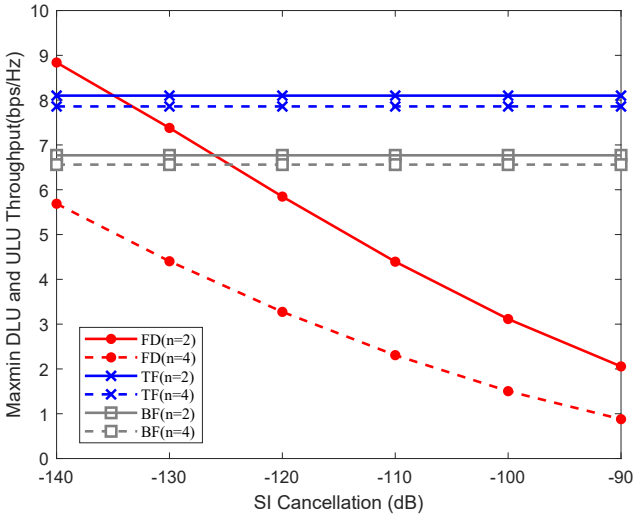

(a)

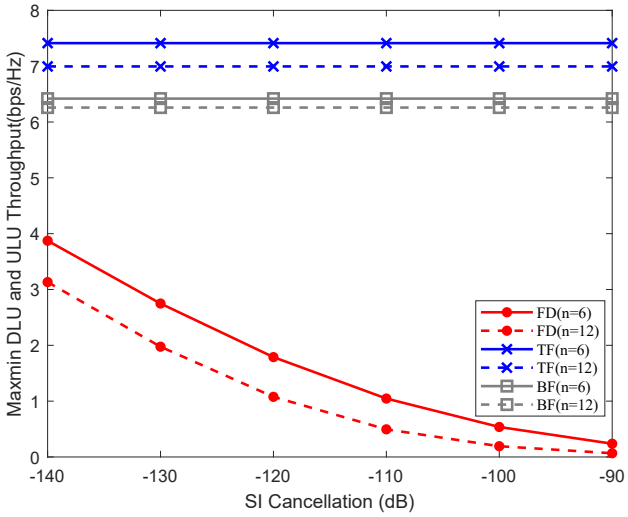

(b)

Fig. 3.4 Achievable minimum DLU and ULU throughput vs SI σ_{SI}^2

Fig. 3.5 shows the effectiveness of the optimal time fraction as e-TF clearly outperforms the half-duplex (HD) TDD, which use all n antennas and $(1-\eta)/2$

fraction of the time slot for each downlink and uplink service. It also shows the benefit of employing all antennas for both downlink and uplink services, as TF is not only consistently outperformed by e-TF but it is also outperformed by HD TDD with $n \geq 6$. It is not surprised that the HD FDD, which allocates $(1-\eta)/2$ bandwidth' portion for each downlink and uplink service, is the worst performer.

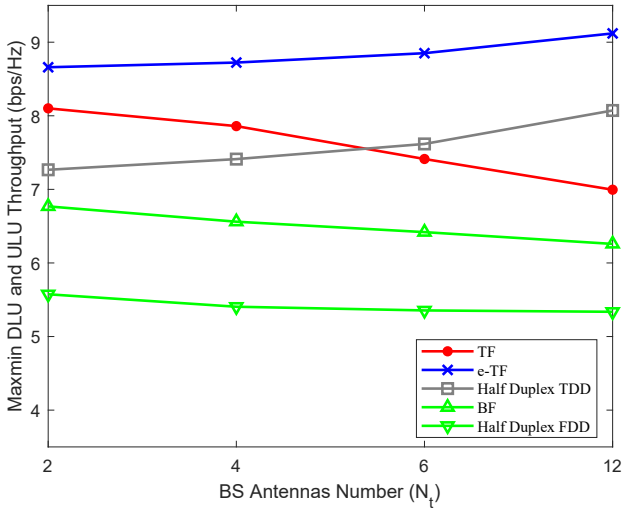

Fig. 3.5 Achievable minimum DLU and ULU throughput vs BS antennas number N_t

Table 3.2 provides the rounded average number of iterations for the results in Fig. 3.4, which particularly shows that all the three algorithms converge within 25 iterations.

Table 3.2 The rounded average number of iterations for implementing the max-min-throughput Algorithms

	$n=2$	$n=4$	$n=6$	$n=12$
FD-based STR($\delta_{SI}^2 = -140$dB)	6	8	10	14
FD-based STR($\delta_{SI}^2 = -130$dB)	7	9	11	15
FD-based STR($\delta_{SI}^2 = -120$dB)	7	10	15	16
FD-based STR($\delta_{SI}^2 = -110$dB)	8	11	17	17
FD-based STR($\delta_{SI}^2 = -100$dB)	10	12	18	20
FD-based STR($\delta_{SI}^2 = -90$dB)	11	12	21	22
TF-wise STR	5	7	12	12
e-TF-wise STR	6	7	11	12
BF-wise STR	4	10	12	16

Furthermore, to examine the impact of UL users to DL users in the FD-based STR we also simulate the following scenario: DL users are still uniformly distributed over the macrocell but there is one UL user in proximity of each DL user. Table 3.3 shows the achievable minimum throughput by the FD-based STRs for $n = 6$, which is very sensitive to the distance δ_2 between a DL user and its nearest UL user. The ratio of that between that achieved for $\delta_2 = 0.05$ km and that achieved for $\delta_2 = 0.005$ km is more than ten and increases as the SI σ_{SI}^2 increases.

Table 3.3 Achievable minimum throughput of FD-based STR (bps/Hz) under different δ_2 and σ_{SI}^2

δ_{SI}^2 \ δ_2	0.05 km	0.03 km	0.01 km	0.005 km
−140 dB	3.1125	2.3542	0.9213	0.3214
−130 dB	2.0376	1.6678	0.5033	0.2392
−120 dB	1.4424	0.9874	0.1779	0.0884
−110 dB	0.8431	0.4879	0.0621	0.0297
−100 dB	0.4101	0.1892	0.0203	0.0096
−90 dB	0.1740	0.0676	0.0065	0.0031

3.5.2 EE optimization

The downlink and uplink throughput thresholds for the QoS are set as $r_{\mathtt{d}} = 0.4$ bps/Hz and $r_{\mathtt{u}} = 1$ bps/Hz, while the circuit power at the BS and ULs are $P_{\text{BS}} = nP_c^{BS} + P_s^{BS}$ W and $P_{\text{UE}} = uP_c^{UE} + P_s^{UE}$ W, and the drain efficiency of power amplifier is $\zeta = 20\%$[63].

Fig. 3.6 shows the achievable EE by Algorithms 1-3 under various numbers (n) of BS antennas. As expected, the achievable EE by the FD-based STR is quickly dropped when the SI level σ_{SI}^2 raises up. At $\sigma_{SI}^2 = -90$ dB, the achievable EE by the latter becomes double of that by the former. TF and e-TF are seen more efficient than BF. Furthermore, e-TF outperforms TF thanks to its its exploitation of all available antennas for its STR. As it happens to the spectral efficiency, using more antennas in serving more users makes the FD's EE deteriorated but improves the EE of other STRs. They perform similarly at low SI level $\sigma_{SI}^2 \in [-140, -120]$ dB but the FD is quickly outperformed by others for $\sigma_{SI}^2 \geq -110$ dB.

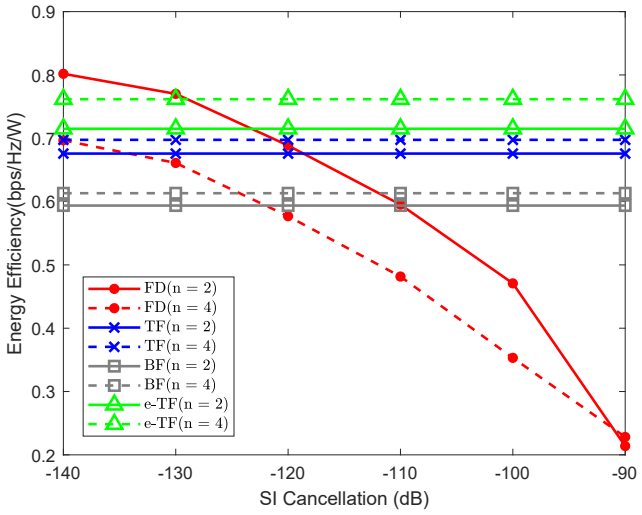

(a)

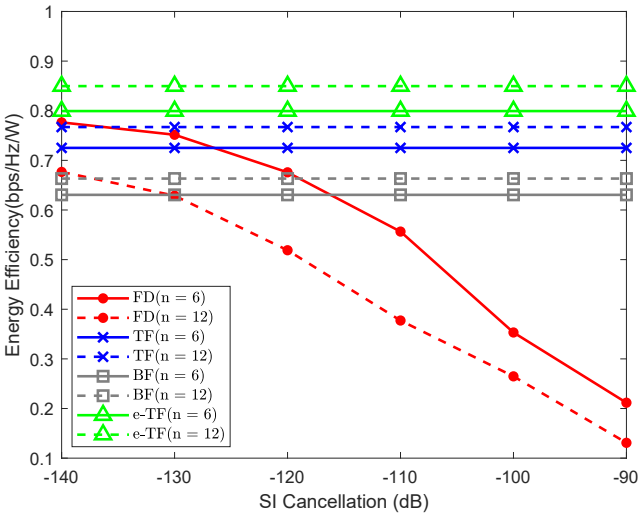

(b)

Fig. 3.6 Achievable EE by three STRs

The rounded average number of algorithm iterations to output Fig. 3.6 is given by Table 3.4. All the proposed algorithms are seen convergent within 45 iterations. Compared to Table 3.2, a few more iterations are needed, which are quite expected because the EE optimization problem is seen more complex than the spectral efficiency optimization problem. Both Algorithms 2 and 3 exploit well the fractional structure of the objective function without its direct approximation. All the percentage number in

the tables represent the probability of obtaining a valid result in all Monte-Carlo runs. The success percentage of the FD-based STR is extremely low for $\sigma_{SI}^2 \in [-100, -90]$ dB as it hardly provides the required QoS. In contrast, the other STRs always perform well with hundred percentage of success as they can avoid the FD inherent self-interference.

Table 3.4 The rounded average number of iterations for the convergence of Algorithms 1-3

	$n = 2$	$n = 4$	$n = 6$	$n = 12$
FD-based STR ($\sigma_{SI}^2 = -140$ dB)	16 (100%)	19 (100%)	16 (100%)	27 (100%)
FD-based STR ($\sigma_{SI}^2 = -130$ dB)	17 (100%)	20 (100%)	22 (100%)	22 (100%)
FD-based STR ($\sigma_{SI}^2 = -120$ dB)	19 (99%)	23 (100%)	27 (94%)	34 (100%)
FD-based STR ($\sigma_{SI}^2 = -110$ dB)	20 (99%)	28 (96%)	34 (88%)	40 (75%)
FD-based STR ($\sigma_{SI}^2 = -100$ dB)	22 (66%)	35 (75%)	35 (69%)	38 (50%)
FD-based STR ($\sigma_{SI}^2 = -90$ dB)	25 (2%)	35 (17%)	38 (3%)	44 (6%)
TF-wise STR	14 (100%)	11 (100%)	10 (100%)	10 (100%)
e-TF-wise STR	12 (100%)	9 (100%)	10 (100%)	9 (100%)
BF-wise STR	19 (100%)	10 (100%)	22 (100%)	18 (100%)
e-TF-wise STR (double users)	13 (100%)	11 (100%)	12 (100%)	11 (100%)

3.5.3 EE in serving doubled number of users

Until now, the e-TF and HD-TDD are purposely allowed to serve $n/2$ downlink users and $n/2$ uplink users to accommodate comparison with other STRs. Table 3.5 provides their achievable spectral efficiency and EE in serving double numbers of both downlink and uplink users (n downlink users and n uplink users). The rounded averaged number of iterations to output the EE of e-TF is given by the last row of Table 3.4. It is reasonable to expect that their achievable EE is higher compared to that achievable by serving $n/2$ donwlink users and $n/2$ uplink users under the same power constraints.

3.6 Conclusions

The chapter has proposed three possible techniques for implementing heterogeneous macrocell downlink and uplink communications within one time-slot, which are the

Table 3.5 Achievable spectral efficiency (SE) in terms of achieved minimum throughput (bps/Hz) and EE (bps/Hz/W) in serving double users vs BS antennas number n

	$n = 2$	$n = 4$	$n = 6$	$n = 12$
e-TF STR's SE	7.6310	6.9935	6.7696	6.7040
HD TDD's SE	6.3821	5.9489	5.8242	5.5425
e-TF STR's EE	1.0232	1.0996	1.1352	1.1996
HD TDD's EE	0.9393	0.9964	0.9996	1.0711

FD-based STR, fraction-time-wise STR, and bandwidth-fraction-wise STR. The three optimization algorithms have been developed to compute the energy efficiency by joint downlink beamforming and uplink power allocation under these STRs. As expected, the FD hardly suitable as its inherent self-interference is not expected to be suppressed to the level for proper implementation. Being free from the mutual interference between downlinks and uplinks, other two techniques have been shown to be effective for STR. Especially, the fraction-time-wise STR is very efficient and can serve many more downlinks and uplinks as it can exploit the full number of the BS antennas for STR. Both the fraction-time base STR and fraction-bandwidth STR for multi-cell result in separated down-link multi-cell systems and uplink multi-cell systems, so they can be used in realistic cellular networks.

Chapter 4

Improper Gaussian Signaling for Integrated Data and Energy Networking

4.1 Introduction

The Internet-of-things (IoT) further broadens the challenges imposed on wireless communications by demanding wireless access for not only information but also for energy [64]. An access point may provide an information service or energy service, or both. In terms of base stations (BSs), it is expected that they are able to transfer not only information but also energy, requiring both high information throughput and substantial harvested energy. In fact, signal processing conceived for high information throughput aims for mitigating the interference at the receiver end, whilst interference actually can be beneficial for harvesting energy.

At the time of writing, there are two popular techniques of transfering information and energy over the same wireless medium within a time slot. The first one is the so-called simultaneous wireless information and power transfer (SWIPT) [65–69], which splits the received signal into two components, namely one for energy-harvesting (EH) and one for information decoding (ID) either by power splitting or time-switching (TS). Its practical implementation requires a sophisticated variable power-splitter [67]. From

a signal processing perspective, it would be counterproductive to design a common beamformer to optimize the conflicting targets of information and energy beamforming at the same time. The second approach is the so-called time-fraction-based information and power transfer (TFIPT) relying on separate fractions of the time-slot [40, 70, 71],[1] which may be conveniently implemented in practice and it is capable of outperforming SWIPT. Under this approach, the EH is improved by energy beamformers, while the information throughput is improved by information beamformers.

To improve the information throughput, which suffers from the network's ambition to provide EH service, we may invoke non-orthogonal multiple access (NOMA) (see e.g. [72, 73]), in order to compensate for the EH-induced throughput loss, when supporting multiple users. It was also shown in [73] that NOMA-based TFIPT outperforms its SWIPT counterpart. Since the main factor limiting the network throughput is multi-user interference, under NOMA the users of better channel conditions access and decode the information intended for users of poorer channel conditions to subtract it from their received signal before decoding their own information. However, this procedure degrades the secrecy of the users of poorer channel conditions. Moreover, the information throughput gain by NOMA is only substantial enough when the users channel conditions are strongly differentiated. Otherwise, conventional orthogonal multi-access (OMA) is still preferred in terms of both its information throughput and user secrecy.

Proper Gaussian signaling (PGS) relies on proper signals is popular owing to its ease of analysis and design, but it requires the multi-user interference (MUI) to be completely suppressed [74]. This requirement may be eliminated by Improper Gaussian signaling (IGS) [75, 76], which was shown to exhibit supremacy over PGS in diverse practical scenarios, for example in single-input single-output (SISO) networks [77–84] or in MIMO interference networks [85–89] of multiple unicast transmitter-receiver pairs, as well as in broadcast networks [90–92] and in cognitive networks [93–95] relying on PGS for the primary users and IGS for the secondary users. Most recently, NOMA-PGS and NOMA-IGS was designed for multi-user multi-cell networks in [96]. In contrast to proper Gaussian signals having arbitrary covariance, improper Gaussian signals are characterized by the so-called augmented covariance of double size associated

[1] One should not confuse this with SWIPT, which splits the received signal using time-switching.

with a special structure involving its covariance and pseudo-covariance [75]. As such, in contrast to PGSs which are generated by linearly beamforming proper Gaussian sources, IGSs are generated by the widely linear beamforming of Gaussian sources, which are determined by a pair of correlated beamforming vectors. The design of beamforming vectors for IGS is more complex than for PGS not only because it involves twice the number of decision variables, but more importantly, the throughput functions are log-determinant $\log\det(.)$ even for multi-input single output (MISO) networks. Hence their optimization problem is facing large challenging on commutating than that the optimization of the logarithmic PGS throughput. However, as mentioned above, NOMA PGS requires additional processing at the users of better channel conditions to decode the information intended for the users of poorer channel conditions, and thus jeopardizes the secrecy of weaker users. By contrast, IGS improves the users' throughput without the above-mentioned extra NOMA-processing at the receiver end.

Against the above background, this chapter proposes IGS for energy-harvesting aided networks with the following main contributions:

- We conceive and generate improper Gaussian signals by applying widely linear beamforming to proper Gaussian sources to improve the information throughput subject to EH constraints. The corresponding beamforming optimization problem becomes nonconvex, which involves log determinant functions, and thus it is computationally challenging. Hence a path-following computational procedure is proposed for this nonconvex problem, which iterates between improved feasible points and converges at least to a locally optimal solution.

- Additionally, we then develop a simplified IGS (s-IGS), which still improves the information throughput by applying linear beamforming to improper Gaussian sources. The resultant reduced-complexity beamforming optimization problem is then solved by a new path-following procedure.

- The simulation results provided demonstrate that both IGS and s-IGS outperform NOMA PGS. Hence,the information throughput can be improved without any additional signal processing at the user end and yet the user secrecy is preserved.

The chapter is organized as follows. Beamforming optimization problems for IGS and s-IGS are addressed in Sections II and Section III, respectively, while the simulations demonstrating their advantage over NOMA are provided in Section IV. Section V concludes the chapter, which is followed by the Appendix. The Appendix develops new fundamental matrix inequalities, which were used for developing the path-following algorithms in Sections II and III.

4.2 System Model for improper Gaussian signal processing

Fig. 4.1 illustrates the downlink (DL) of a N cells system, where the all the BSs are equipped with N_t-transmit antennas (TAs) serving multiple single-antenna-aided users. In the i-th cell, there are K energy-harvesting (EH) users (EU) indexed by $(i, e_1), \ldots, (i, e_K)$, who harvest energy transferred by the BS through the wireless channels and thus have to be located sufficiently near to their BS. There are M information-receiving users (IUs) indexed by $(i, d_1), \ldots, (i, d_M)$, who receive and decode information transmitted by the BS through the wireless DL channels. Note that there is a potential overlap between the sets of EUs and IUs, whenever there are users, who receive both energy and information from the BS through the same wireless channels. Then

$$\mathcal{S}_E \triangleq \{(s, e_\ell) \ : \ s = 1, \ldots, N; \ell = 1, \ldots, K\}$$

and

$$\mathcal{S}_I \triangleq \{(s, d_\ell) \ : \ s = 1, \ldots, N; \ell = 1, \ldots, M\}$$

respectively represent the set of EUs and IUs. Under time-fraction-based information and energy transfer [40, 70, 71], we use the specific fraction of time $0 < 1/\mathbf{t}_1 < 1$ for power delivery, and use the remaining fraction of $0 < 1/\mathbf{t}_2 < 1$ is used for information transmit. Let $h_{s,i,e_j} \in \mathbb{C}^{1\times N_t}$ be the channel spanning from the BS s to the EU (i, e_j), $\mathbf{x}^E_{s,e_\ell} = \boldsymbol{v}_{s,e_\ell}\tilde{s}_{s,e_\ell} \in \mathbb{C}^{N_t\times 1}$ be the beamformed energy signal intended for the EU (s, e_ℓ), where $\boldsymbol{v}_{s,e_\ell} \in \mathbb{C}^{N_t\times 1}$ is the energy beamformer and $\tilde{s}_{s,e_\ell} \in \mathbb{C}$ is the energy symbol with $\mathbb{E}(|\tilde{s}_{s,e_\ell}|^2) = 1$. All $\tilde{s}_{s,e_\ell}$, $s = 1, \ldots, N; \ell = 1, \ldots, K$ are independent. The signal

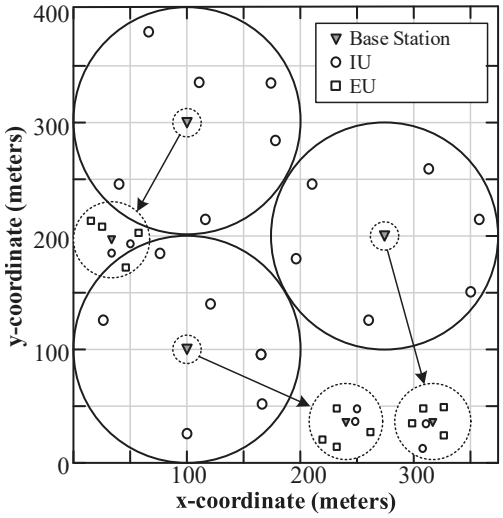

Fig. 4.1 Multi-cell energy-harvesting aided system

received by the EU (i, e_j) is

$$y_{i,e_j} = \sum_{(s,e_\ell)\in\mathcal{S}_E} h_{s,i,e_j}\mathbf{x}^E_{s,e_\ell} + n_{i,e_j}, \tag{4.1}$$

where $n_{i,e_j} \in \mathbb{C}$ is the background noise, which is proper Gaussian with zero mean and variance σ^2. Given the energy conversion efficiency $0 < \zeta < 1$, the energy harvested by the EU $(i, e_j) \in \mathcal{S}_E$ is $(1/\mathbf{t}_1)\zeta\mathbb{E}(|y_{i,e_j}|^2)$, which is[2]

$$(1/\mathbf{t}_1)\zeta\pi_{i,e_j}(\boldsymbol{v}_{\mathcal{S}_E}), \tag{4.2}$$

where

$$\pi_{i,e_j}(\boldsymbol{v}_{\mathcal{S}_E}) = \sum_{\ell=1}^{K} |h_{i,i,e_j}\boldsymbol{v}_{i,e_\ell}|^2. \tag{4.3}$$

In (4.3), the energy of the background noise n_{i,e_j} and the interference from the BSs of the other cells are low for EH and thus are ignored.

Let $n_{i,d_j} \in \mathbb{C}$ be the background noise at IU (i, d_j), which is proper Gaussian with zero mean and variance σ^2. For the information transfer during the remaining $1/\mathbf{t}_2$

[2]The RF-to-harvested energy conversion function is in practice non-linear. However, there is no generally agreed accurate function at the time of writing. Hence, to avoid obfuscating the salient IGS-related trends, we have opted for this simple linear model.

fraction of time, the signal received by the IU (i, d_j) is

$$y_{i,d_j} = \sum_{(s,d_\ell)\in\mathcal{S}_I} h_{s,i,d_j}\mathbf{x}^I_{s,d_\ell} + n_{i,d_j}, \tag{4.4}$$

where in general, the beamformed information signal intended for the IU (s, d_ℓ) is denoted as $\mathbf{x}^I_{s,d_\ell} \in \mathbb{C}^{N_t\times 1}$ in (4.4), which is improper Gaussian, i.e. $\mathbb{E}\left((\mathbf{x}^I_{s,d_\ell})^2\right) \neq 0$, and it is generated by widely linear beamforming of a normalized proper Gaussian source s_{s,d_ℓ} ($\mathbb{E}(|s_{s,d_\ell}|^2) = 1$ and $\mathbb{E}((s_{s,d_\ell})^2) = 0$) as [96]

$$\mathbf{x}^I_{s,d_\ell} \;=\; \boldsymbol{w}_{1,s,d_\ell}s_{s,d_\ell} + \boldsymbol{w}_{2,s,d_\ell}s^*_{s,d_\ell} \tag{4.5}$$

with the aid of the beamformers $\boldsymbol{w}_{1,s,d_\ell} \in \mathbb{C}^{N_t\times 1}$ and $\boldsymbol{w}_{2,s,d_\ell} \in \mathbb{C}^{N_t\times 1}$. Then, the signal received in (4.4) at the IU (i, d_j) is rewritten as

$$y_{i,d_j} = \sum_{(s,d_\ell)\in\mathcal{S}_I} h_{s,i,d_j}(\boldsymbol{w}_{1,s,d_\ell}s_{s,d_\ell} + \boldsymbol{w}_{2,s,d_\ell}s^*_{s,d_\ell}) + n_{i,d_j}. \tag{4.6}$$

By writing

$$(\mathbf{x}^I_{s,d_\ell})^* = \begin{bmatrix}\boldsymbol{w}^*_{2,s,d_\ell} & \boldsymbol{w}^*_{1,s,d_\ell}\end{bmatrix}\begin{bmatrix}s_{s,d_\ell}\\ s^*_{s,d_\ell}\end{bmatrix}$$

and defining $\boldsymbol{w}_{s,d_\ell} = \{\boldsymbol{w}_{j,s,d_\ell}, j = 1, 2\}$, we can express the augmented equation of (4.6) as

$$\begin{aligned}
\bar{\mathbf{y}}_{i,d_j} \;&\triangleq\; \begin{bmatrix}y_{i,d_j}\\ y^*_{i,d_j}\end{bmatrix}\\
&= \sum_{(s,d_\ell)\in\mathcal{S}_I}\begin{bmatrix}h_{s,i,d_j}\boldsymbol{w}_{1,s,d_\ell} & h_{s,i,d_j}\boldsymbol{w}_{2,s,d_\ell}\\ h^*_{s,i,d_j}\boldsymbol{w}^*_{2,s,d_\ell} & h^*_{s,i,d_j}\boldsymbol{w}^*_{1,s,d_\ell}\end{bmatrix}\begin{bmatrix}s_{s,d_\ell}\\ s^*_{s,d_\ell}\end{bmatrix} + \begin{bmatrix}n_{i,d_j}\\ n^*_{i,d_j}\end{bmatrix}\\
&= \Lambda_{i,i,d_j}(\boldsymbol{w}_{i,d_j})\bar{\mathsf{bs}}_{i,d_j} + \sum_{(s,d_\ell)\in\mathcal{S}_I\setminus\{i,d_j\}}\Lambda_{s,i,d_j}(\boldsymbol{w}_{s,d_\ell})\bar{\mathsf{bs}}_{s,d_\ell} + \bar{\mathbf{n}}_{i,d_j}
\end{aligned} \tag{4.7}$$

for

$$\Lambda_{s,i,d_j}(\boldsymbol{w}_{s,d_\ell}) \triangleq \begin{bmatrix}h_{s,i,d_j}\boldsymbol{w}_{1,s,d_\ell} & h_{s,i,d_j}\boldsymbol{w}_{2,s,d_\ell}\\ h^*_{s,i,d_j}\boldsymbol{w}^*_{2,s,d_\ell} & h^*_{s,i,d_j}\boldsymbol{w}^*_{1,s,d_\ell}\end{bmatrix}, \tag{4.8}$$

which represents a linear mapping from $\mathbb{C}^{(2N_t)\times 1}$ to $\mathbb{C}^{2\times 2}$, and

$$\bar{\mathsf{bs}}_{s,d_\ell} \triangleq \begin{bmatrix} s_{s,d_\ell} \\ s^*_{s,d_\ell} \end{bmatrix} \in \mathbb{C}^2, \bar{\mathbf{n}}_{i,d_j} \triangleq \begin{bmatrix} n_{i,d_j} \\ n^*_{i,d_j} \end{bmatrix} \in \mathbb{C}^2. \tag{4.9}$$

It may be readily shown that

$$\mathbb{E}\{[\bar{\mathsf{bs}}_{i,d_\ell}]^2\} = I_2, \mathbb{E}\{[\bar{\mathbf{n}}_{i,d_j}]^2\} = \sigma^2 I_2, \tag{4.10}$$

and

$$\mathbb{E}\{[\Lambda_{s,i,d_j}(\boldsymbol{w}_{s,d_\ell})\bar{\mathsf{bs}}_{i,d_j}]^2\} = [\Lambda_{s,i,d_j}(\boldsymbol{w}_{s,d_\ell})]^2. \tag{4.11}$$

The throughput at the IU (i, d_j) expressed in nats/sec/Hz is given by the mutual information (MI) between $\bar{y}_{i,d_j}$ and $\bar{s}_{i,d_j}$ computed as [97]

$$\frac{1}{2\mathbf{t}_2} r_{i,d_j}(\boldsymbol{w}_{\mathcal{S}_I}) \tag{4.12}$$

for

$$r_{i,d_j}(\boldsymbol{w}_{\mathcal{S}_I}) = \ln \left| I_2 + [\Lambda_{i,i,d_j}(\boldsymbol{w}_{i,d_j})]^2 \left(\Psi_{i,d_j}(\boldsymbol{w}_{\mathcal{S}_I})\right)^{-1} \right|, \tag{4.13}$$

and

$$\Psi_{i,d_j}(\boldsymbol{w}_{\mathcal{S}_I}) \triangleq \sum_{(s,d_\ell)\in\mathcal{S}_I\setminus\{(i,d_j)\}} [\Lambda_{s,i,d_j}(\boldsymbol{w}_{s,d_\ell})]^2 + \sigma^2 I_2. \tag{4.14}$$

Based on (4.2) and (4.12), we consider the following problem of max-min throughput optimization

$$\max_{\boldsymbol{v}_{\mathcal{S}_E},\boldsymbol{w}_{\mathcal{S}_I},\mathbf{t}=(\mathbf{t}_1,\mathbf{t}_2)^T\in\mathbb{R}_+^2,\boldsymbol{\gamma}} \boldsymbol{\gamma} \quad \text{s.t.} \tag{4.15a}$$

$$r_{i,d_j}(\boldsymbol{w}_{\mathcal{S}_I}) \geq 2\boldsymbol{\gamma}\mathbf{t}_2, (i,d_j)\in\mathcal{S}_I, \tag{4.15b}$$

$$\pi_{i,e_j}(\boldsymbol{v}_{\mathcal{S}_E}) \geq \frac{e_{\min}}{\zeta}\mathbf{t}_1, (i,e_j)\in\mathcal{S}_E, \tag{4.15c}$$

$$\frac{1}{\mathbf{t}_1}+\frac{1}{\mathbf{t}_2}\leq 1, \tag{4.15d}$$

$$\frac{1}{\mathbf{t}_1}\sum_{j=1}^{K}||\boldsymbol{v}_{i,e_j}||^2+\frac{\sum_{j=1}^{M}||\boldsymbol{w}_{i,d_j}||^2}{\mathbf{t}_2}\leq P, i=1,\ldots,N, \tag{4.15e}$$

$$||\boldsymbol{v}_{i,e_j}||^2\leq P, (i,e_j)\in\mathcal{S}_E; ||\boldsymbol{w}_{i,d_j}||^2\leq P, (i,d_j)\in\mathcal{S}_I, \tag{4.15f}$$

where P is the power budget granted for each BS and we have

$$||\boldsymbol{w}_{i,d_j}||^2=||\boldsymbol{w}_{1,i,d_j}||^2+||\boldsymbol{w}_{2,i,d_j}||^2,$$

which is the power of the widely linear beamformer in (4.5). Note that by (4.15b), $\boldsymbol{\gamma}$ in (4.15a) represents $\min_{(i,d_j)\in\mathcal{S}_I}(1/2\mathbf{t}_2)r_{i,d_j}(\boldsymbol{w}_{\mathcal{S}_I})$, i.e. it is the minimal value among the IUs' throughput $(1/2\mathbf{t}_2)r_{i,d_j}(\boldsymbol{w}_{\mathcal{S}_I})$, $(i,d_j)\in\mathcal{S}_I$. Furthermore, $e_{\min}$ in (4.15c) is the threshold of EH, so the constraint (4.15c) sets the threshold in serving the EUs. The constraint (4.15d) restricts the fractional-time-based implementation within a single time slot, and (4.15e) is a typical sum-power constraint, while (4.15f) is the physical transmission power constraint. The last three constraints (4.15d)-(4.15f) in (4.15) are convex.

The problem (4.15) is nonconvex because the pair of constraints (4.15b) and (4.15c) representing the information throughput and EH power are nonconvex. To develop a path-following algorithm for its computation, which improves its feasible value in each iteration, we have to develop an inner convex approximation of these nonconvex constraints.

Let $(v_{\mathcal{S}_E}^{(\kappa)}, w_{\mathcal{S}_I}^{(\kappa)}, t^{(\kappa)}, \gamma^{(\kappa)})$ be the feasible point for (4.15) found from the $(\kappa-1)$th iteration.

To obtain an inner convex approximation of (4.15b) we have to derive a concave upper bounding function approximation of its left-hand-side (LHS) and a convex lower bounding function approximation of its right-hand-side (RHS). Applying the inequality (A.15) in the Appendix yields the following concave upper bounding approximation of the LHS of (4.15b):

$$\begin{aligned} r_{i,d_j}(\boldsymbol{w}_{\mathcal{S}_I}) &\geq a_{i,d_j}^{(\kappa)} + 2\langle B_{i,d_j}^{(\kappa)} \Lambda_{i,i,d_j}(\boldsymbol{w}_{i,d_j})\rangle - \langle C_{i,d_j}^{(\kappa)}, [\Lambda_{i,i,d_j}(\boldsymbol{w}_{i,d_j})]^2 + \Psi_{i,d_j}(\boldsymbol{w}_{\mathcal{S}_I})\rangle \\ &= a_{i,d_j}^{(\kappa)} - \sigma^2\langle C_{i,d_j}^{(\kappa)}\rangle + 2\langle B_{i,d_j}^{(\kappa)} \Lambda_{i,i,d_j}(\boldsymbol{w}_{i,d_j})\rangle - \langle C_{i,d_j}^{(\kappa)}, \sum_{(s,d_\ell)\in\mathcal{S}_I} [\Lambda_{s,i,d_j}(\boldsymbol{w}_{s,d_\ell})]^2\rangle \\ &= a_{i,d_j}^{(\kappa)} - \sigma^2\langle C_{i,d_j}^{(\kappa)}\rangle + 2\langle B_{i,d_j}^{(\kappa)} \Lambda_{i,i,d_j}(\boldsymbol{w}_{i,d_j})\rangle \\ &\quad - \sum_{(s,d_\ell)\in\mathcal{S}_I} \langle \Lambda_{s,i,d_j}^H(\boldsymbol{w}_{s,d_\ell}) C_{i,d_j}^{(\kappa)} \Lambda_{s,i,d_j}(\boldsymbol{w}_{s,d_\ell})\rangle \\ &= a_{i,d_j}^{(\kappa)} - \sigma^2\langle C_{i,d_j}^{(\kappa)}\rangle + 2\langle B_{i,d_j}^{(\kappa)} \Lambda_{i,i,d_j}(\boldsymbol{w}_{i,d_j})\rangle - \sum_{(s,d_\ell)\in\mathcal{S}} ||(C_{i,d_j}^{(\kappa)})^{1/2} \Lambda_{s,i,d_j}(\boldsymbol{w}_{s,d_\ell})||_F^2 \\ &\triangleq r_{i,d_j}^{(\kappa)}(\boldsymbol{w}_{\mathcal{S}_I}), \end{aligned}$$

where we have

$$a_{i,d_j}^{(\kappa)} = r_{i,d_j}(w_{\mathcal{S}_I}^{(\kappa)}) - \langle [\Lambda_{i,i,d_j}(w_{i,d_j}^{(\kappa)})]^2 \left(\Psi_{i,d_j}(w_{\mathcal{S}_I}^{(\kappa)})\right)^{-1}\rangle, \tag{4.16a}$$

$$B_{i,d_j}^{(\kappa)} = (\Lambda_{i,i,d_j}(w_{i,d_j}^{(\kappa)}))^H \left(\Psi_{i,d_j}(w_{\mathcal{S}_I}^{(\kappa)})\right)^{-1}, \tag{4.16b}$$

$$0 \preceq C_{i,d_j}^{(\kappa)} = \left(\Psi_{i,d_j}(w_{\mathcal{S}_I}^{(\kappa)})\right)^{-1} - \left([\Lambda_{i,i,d_j}(w_{i,d_j}^{(\kappa)})]^2 + \Psi_{i,d_j}(w_{\mathcal{S}_I}^{(\kappa)})\right)^{-1}. \tag{4.16c}$$

Meanwhile, the RHS of (4.15b) is upper bounded as follows:

$$2\boldsymbol{\gamma}\mathbf{t}_2 \leq \frac{\gamma^{(\kappa)} t_2^{(\kappa)}}{2} \left(\frac{\boldsymbol{\gamma}}{\gamma^{(\kappa)}} + \frac{\mathbf{t}_2}{t_2^{(\kappa)}}\right)^2. \tag{4.17}$$

Using (4.16) and (4.17), the nonconvex constraint (4.15b) is innerly approximated by the following convex constraint in the sense that any feasible point for the latter is also feasible for the former:

$$r_{i,d_j}^{(\kappa)}(\boldsymbol{w}_{\mathcal{S}}) \geq \frac{\gamma^{(\kappa)} t_2^{(\kappa)}}{2} \left(\frac{\boldsymbol{\gamma}}{\gamma^{(\kappa)}} + \frac{\mathbf{t}_2}{t_2^{(\kappa)}}\right)^2, (i,d_j) \in \mathcal{S}_I. \tag{4.18}$$

From (4.3), the LHS of (4.15c) is seen to be convex quadratic, hence the nonconvex constraint (4.15c) is said to be reverse convex and can be innerly approximated by a convex constraint by linearizing its LHS at $v_{\mathcal{S}_e}^{(\kappa)}$ [30]

$$\sum_{\ell=1}^{K}[2\Re\{(v_{i,e_\ell}^{(\kappa)})^H h_{i,i,e_j}^H h_{i,i,e_j}\boldsymbol{v}_{i,e_\ell}\} - |h_{i,i,e_j}v_{i,e_\ell}^{(\kappa)}|^2] \geq \frac{e_{\min}}{\zeta}\mathbf{t}_1, \quad (i,e_j)\in\mathcal{S}_E, \tag{4.19}$$

which was used in the previous treatises of [40, 70, 71] handling EH constraints.

We solve the following convex problem at its κth iteration, which provides a feasible value for (4.15),the next feasible point $(v_{\mathcal{S}_E}^{(\kappa+1)}, w_{\mathcal{S}_I}^{(\kappa+1)}, t^{(\kappa+1)}, \gamma^{(\kappa+1)})$ for (4.15) is generated by:

$$\max_{\boldsymbol{v}_{\mathcal{S}_E},\boldsymbol{w}_{\mathcal{S}_I},\mathbf{t}=(\mathbf{t}_1,\mathbf{t}_2)^T\in\mathbb{R}_+^2,\boldsymbol{\gamma}} \boldsymbol{\gamma} \quad \text{s.t.} \quad (4.15d)-(4.15f),(4.18),(4.19). \tag{4.20}$$

This convex problem involves $n_v = NN_t(K+2M)+3$ decision variables and $m_c = 1+N(K+M+1)$ quadratic constraints, hence its computational complexity is [98]

$$\mathcal{O}(m_c^{2.5}(n_v^2+m_c)). \tag{4.21}$$

Note that we have $\gamma^{(\kappa+1)} > \gamma^{(\kappa)}$ as long as $(v_{\mathcal{S}_E}^{(\kappa+1)}, w_{\mathcal{S}_I}^{(\kappa+1)}, t^{(\kappa+1)}, \gamma^{(\kappa+1)}) \neq (v_{\mathcal{S}_E}^{(\kappa)}, w_{\mathcal{S}_I}^{(\kappa)}, t^{(\kappa)}, \gamma^{(\kappa)})$, because they respectively are the optimal solution and a feasible point for (4.20). This means that $(v_{\mathcal{S}_E}^{(\kappa+1)}, w_{\mathcal{S}_I}^{(\kappa+1)}, t^{(\kappa+1)}, \gamma^{(\kappa+1)})$ is a better feasible point than $(v_{\mathcal{S}_E}^{(\kappa)}, w_{\mathcal{S}_I}^{(\kappa)}, t^{(\kappa)}, \gamma^{(\kappa)})$ for (4.15). As such, the sequence $\{(v_{\mathcal{S}_E}^{(\kappa)}, w_{\mathcal{S}_I}^{(\kappa)}, t^{(\kappa)}, \gamma^{(\kappa)})\}$ of feasible points for (4.15) converges at least to a point satisfying the Karush-Kuh-Tucker (KKT) condition of optimality [60]. Our previous result (see e.g. [71]) shows that such a point often turns out to be the globally optimal solution of (4.15).

It is important to locate a feasible point $(v_{\mathcal{S}_E}^{(0)}, w_{\mathcal{S}_I}^{(0)}, t^{(0)}, \gamma^{(0)})$ for (4.15) for initializing the path-following procedure. Let us fix $t^{(0)} = (t_1^{(0)}, t_2^{(0)})$ and good $\gamma^{(0)}$ and randomly

generate $(v_{\mathcal{S}_E}^{(0)}, w_{\mathcal{S}_I}^{(0)})$ feasible for (4.15e)-(4.15f). Then iterate as follows

$$\max_{\boldsymbol{v}_{\mathcal{S}_E}, \boldsymbol{w}_{\mathcal{S}_I}, \boldsymbol{\eta}} \ \boldsymbol{\eta} \quad \text{s.t.} \quad (4.15f) \tag{4.22a}$$

$$r_{i,d_j}^{(\kappa)}(\boldsymbol{w}_{\mathcal{S}_I}) \geq 2\gamma^{(0)} t_2^{(0)} \boldsymbol{\eta}, (i, d_j) \in \mathcal{S}_I, \tag{4.22b}$$

$$\sum_{\ell=1}^{K} [2\Re\{(v_{i,e_\ell}^{(\kappa)})^H h_{i,i,e_j} h_{i,i,e_j}^H \boldsymbol{v}_{i,e_\ell}\} - |h_{i,i,e_j}^H v_{i,e_\ell}^{(\kappa)}|^2] \geq \frac{e_{\min}}{\zeta} t_1^{(0)} \boldsymbol{\eta}, (i, e_j) \in \mathcal{S}_E, \tag{4.22c}$$

$$\frac{1}{t_1^{(0)}} \sum_{j=1}^{K} ||\boldsymbol{v}_{i,e_j}||^2 + \frac{\sum_{j=1}^{M} ||\boldsymbol{w}_{i,d_j}||^2}{2t_2^{(0)}} \leq P, i = 1, \ldots, N, \tag{4.22d}$$

until reaching $\boldsymbol{\eta} \geq 1$ at $(v_{\mathcal{S}_E}^{(0)}, w_{\mathcal{S}_I}^{(0)})$ in order to guarantee that $(t^{(0)}, \gamma^{(0)}\boldsymbol{\eta}, w_{\mathcal{S}_I}^{(\kappa)}, v_{\mathcal{S}_E}^{(\kappa)})$ is feasible for (4.15).

Algorithm 4 represents the formal pseudo code of the above computational procedure.

Algorithm 4 IGS algorithm for (4.15)

1: **Initialization:** Set $\kappa := 0$ and iterate (4.22) for finding a good initial feasible point $(v_{\mathcal{S}_E}^{(0)}, w_{\mathcal{S}_I}^{(0)}, t^{(0)})$ for (4.15)
2: **Repeat until** (4.15) **is reached:** Generate the feasible point $(v_{\mathcal{S}_E}^{(\kappa+1)}, w_{\mathcal{S}_I}^{(\kappa+1)}, t^{(\kappa+1)})$ for (4.15) by solving the convex optimization problem (4.20); Reset $\kappa := \kappa + 1$.
3: **Output** $\mathbf{t} = t^{(\kappa)}$, $\boldsymbol{v}_{\mathcal{S}_E} = v_{\mathcal{S}_E}^{(\kappa)}$, and $\boldsymbol{w}_{\mathcal{S}_E} = w_{\mathcal{S}_E}^{(\kappa)}$.

4.3 Simplified improper Gaussian signaling

In (4.5), the improper Gaussian signal $\mathbf{x}_{s,d_\ell}^I$ is generated as a widely linear transform of a proper Gaussian source s_{s,d_ℓ}. By contrast, in this section, the improper Gaussian signal $\mathbf{x}_{s,d_\ell}^I$ in (4.4) is generated as a linear transform of an improper Gaussian source as follows

$$\mathbf{x}_{s,d_\ell}^I = \boldsymbol{w}_{s,d_\ell} s_{s,d_\ell}, \boldsymbol{w}_{s,d_\ell} \in \mathbb{C}^{N_t \times 1}, \tag{4.23}$$

where s_{s,d_ℓ} is a normalized improper Gaussian random variable ($\mathbb{E}(|s_{s,d_\ell}|^2)=1$), which is fully characterized by the augmented covariance defined in [75]:

$$\begin{aligned}\mathbf{P}_{s,d_\ell} &= \begin{bmatrix}\mathbb{E}(|s_{s,d_\ell}|^2) & \mathbb{E}(s_{s,d_\ell}^2)\\ (\mathbb{E}(s_{s,d_\ell}^2))^* & \mathbb{E}(|s_{s,d_\ell}|^2)\end{bmatrix}\\ &= \mathbb{E}\left\{\begin{bmatrix}s_{s,d_\ell}\\ s_{s,d_\ell}^*\end{bmatrix}\begin{bmatrix}s_{s,d_\ell}\\ s_{s,d_\ell}^*\end{bmatrix}^H\right\}\\ &= \begin{bmatrix}1 & \mathbf{q}_{s,d_\ell}\\ \mathbf{q}_{s,d_\ell}^* & 1\end{bmatrix}\end{aligned} \tag{4.24}$$

with $\mathbf{q}_{s,d_\ell}\in\mathbb{C}$ satisfying the following convex quadratic constraint to make it qualified as a pseudo-covariance of s_{s,d_ℓ}

$$|\mathbf{q}_{s,d_\ell}|^2<1,(s,d_\ell)\in\mathcal{S}_I, \tag{4.25}$$

which makes $\mathbf{P}_{s,d_\ell}$ positive definite. Note that $\mathbf{q}_{s,d_\ell}=0$ in (4.24) means $\mathbb{E}(s_{s,d_\ell}^2)=0$, i.e. s_{s,d_ℓ} becomes proper.

By taking the square root according to

$$\mathbf{P}_{s,d_\ell}^{1/2}=\begin{bmatrix}\alpha_{s,d_\ell} & \beta_{s,d_\ell}\\ \beta_{s,d_\ell}^* & \alpha_{s,d_\ell}\end{bmatrix}\succeq 0,$$

in conjunction with

$$\begin{aligned}\alpha_{s,d_\ell}&=\frac{(1+\sqrt{1-|\mathbf{q}_{s,d_\ell}|^2})^{1/2}}{\sqrt{2}},\\ \beta_{s,d_\ell}&=\frac{\mathbf{q}_{s,d_\ell}}{\sqrt{2}(1+\sqrt{1-|\mathbf{q}_{s,d_\ell}|^2})^{1/2}},\end{aligned}$$

it can be readily shown that

$$s_{s,d_\ell}=\alpha_{s,d_\ell}\tilde{s}_{s,d_\ell}+\beta_{s,d_\ell}\tilde{s}_{s,d_\ell}^*$$

for a normalized proper Gaussian $\tilde{s}_{s,d_\ell}$. Therefore (4.23) can be written in the widely linear form

$$\mathbf{x}_{s,d_\ell}^I=\boldsymbol{w}_{s,d_\ell}\alpha_{s,d_\ell}\tilde{s}_{s,d_\ell}+\boldsymbol{w}_{s,d_\ell}\beta_{s,d_\ell}\tilde{s}_{s,d_\ell}^*, \tag{4.26}$$

which a particular class of (4.5) associated with

$$\boldsymbol{w}_{1,s,d_\ell} = \alpha_{s,d_\ell}\boldsymbol{w}_{s,d_\ell} \quad \& \quad \boldsymbol{w}_{2,s,d_\ell} = \beta_{s,d_\ell}\boldsymbol{w}_{s,d_\ell}. \tag{4.27}$$

The advantage of (4.23) over (4.5) is that for each (s, d_ℓ), the former involves only $N_t + 1$ complex decision variables for information beamforming ($\boldsymbol{w}_{s,d_\ell}$ of dimension N_t plus the complex variable $\mathbf{q}_{s,d_\ell}$), while the latter involves $2N_t$ complex decision variables ($\boldsymbol{w}_{j,d_\ell}$, $j = 1, 2$, each of dimension N_t).

For the information transfer during the remaining $1/\mathbf{t}_2$ fractional time, the signal (4.4) received at the IU (i, d_j) is now specified as

$$y_{i,d_j} = \sum_{(s,d_\ell)\in\mathcal{S}_I} h_{s,i,d_j}\boldsymbol{w}_{s,d_\ell}s_{s,d_\ell} + n_{i,d_j}. \tag{4.28}$$

By writing down its augmented form:

$$\begin{bmatrix} y_{i,d_j} \\ y^*_{i,d_j} \end{bmatrix} = \sum_{(s,d_\ell)\in\mathcal{S}_I} \mathcal{L}_{s,i,d_j}(\boldsymbol{w}_{s,d_\ell}) \begin{bmatrix} s_{s,d_\ell} \\ s^*_{s,d_\ell} \end{bmatrix} + \begin{bmatrix} n_{i,d_j} \\ n^*_{i,d_j} \end{bmatrix}, \tag{4.29}$$

for

$$\mathcal{L}_{s,i,d_j}(\boldsymbol{w}_{s,d_\ell}) \triangleq \begin{bmatrix} h_{s,i,d_j}\boldsymbol{w}_{s,d_\ell} & 0 \\ 0 & h^*_{s,i,d_j}\boldsymbol{w}^*_{s,d_\ell} \end{bmatrix} \in \mathbb{C}^{2\times 2},$$

which is a linear operator from $\mathbb{C}^{N_t\times 1}$ to $\mathbb{C}^{2\times 2}$, we can readily determine the augmented covariance of the signal of interest in (4.28) as

$$\Phi_{i,d_j}(\boldsymbol{w}_{i,d_j}, \mathbf{q}_{i,d_j}) = \mathcal{L}_{i,i,d_j}(\boldsymbol{w}_{i,d_j})\mathbf{P}_{i,d_j}\mathcal{L}^H_{i,i,d_j}(\boldsymbol{w}_{i,d_j}) \tag{4.30}$$

and interference-plus-noise of (4.28) can be expressed in augmented covariance form as

$$\Gamma_{i,d_j}(\boldsymbol{w}_{\mathcal{S}_I}, \mathbf{q}_{\mathcal{S}_I}) = \sum_{(s,d_\ell)\in\mathcal{S}_I\setminus(i,d_j)} \mathcal{L}_{s,i,d_j}(\boldsymbol{w}_{s,d_\ell})\mathbf{P}_{s,d_\ell}\mathcal{L}^H_{s,i,d_j}(\boldsymbol{w}_{s,d_\ell}) + \sigma^2 I_2. \tag{4.31}$$

The information throughput at user (i, d_j) is then expressed as [74]

$$\frac{1}{2\mathbf{t}_2} r_{i,d_j}(\boldsymbol{w}_{\mathcal{S}_I}, \mathbf{q}_{\mathcal{S}_I}), \tag{4.32}$$

where

$$r_{i,d_j}(\boldsymbol{w}_{\mathcal{S}_I}, \mathbf{q}_{\mathcal{S}_I}) = \ln \left| I_2 + \Phi_{i,d_j}(\boldsymbol{w}_{i,d_j}, \mathbf{q}_{i,d_j}) \left(\Gamma_{i,d_j}(\boldsymbol{w}_{\mathcal{S}_I}, \mathbf{q}_{\mathcal{S}_I}) \right)^{-1} \right|. \tag{4.33}$$

With $\mathbf{x}^I_{s,d_\ell}$ defined by (4.23), the problem of max-min information throughput optimization subject to the EUs' harvested energy and power constraints is formulated as follows instead of (4.15):

$$\max_{\mathbf{t}=(\mathbf{t}_1,\mathbf{t}_2)\in\mathbb{R}^2_+, \boldsymbol{v}_{\mathcal{S}_E}, \boldsymbol{w}_{\mathcal{S}_I}, \mathbf{q}_{\mathcal{S}_I}, \boldsymbol{\gamma}} \quad \boldsymbol{\gamma} \quad \text{s.t.} \quad (4.15c), (4.15d), (4.25), \tag{4.34a}$$

$$r_{i,d_j}(\boldsymbol{w}_{\mathcal{S}_I}, \mathbf{q}_{\mathcal{S}_I}) \geq 2\boldsymbol{\gamma}\mathbf{t}_2, (i,d_j) \in \mathcal{S}_I, \tag{4.34b}$$

$$\frac{\sum_{j=1}^K ||\boldsymbol{v}_{i,e_j}||^2}{\mathbf{t}_1} + \frac{\sum_{j=1}^M ||\boldsymbol{w}_{i,d_j}||^2}{\mathbf{t}_2} \leq P, i = 1, \ldots, N, \tag{4.34c}$$

$$||\boldsymbol{v}_{i,e_j}||^2 \leq P_{\max}, (i,e_j) \in \mathcal{S}_E, \tag{4.34d}$$

$$||\boldsymbol{w}_{i,d_j}||^2 \leq P_{\max}, (i,d_j) \in \mathcal{S}_I, \tag{4.34e}$$

where (4.34b) is the counterpart of (4.15b) for maximizing the IUs' minimal throughput, while (4.34c) and (4.34d)-(4.34e) correspond to the power constraints (4.15e) and (4.15f), respectively. In (4.34), the constraint (4.25) is obviously convex, and the constraints (4.15c), (4.34c) and (4.34d)-(4.34e) are also convex just like their counterparts in (4.15).

The nonconvex constraint (4.34b) involves much fewer decision variables than its counterpart (4.15b) but the former also contains many crossed terms between beamformers and pseudo-covariances that require a different approximation technique.

Let $(t^{(\kappa)}, \gamma^{(\kappa)}, w^{(\kappa)}_{\mathcal{S}_I}, v^{(\kappa)}_{\mathcal{S}_E}, q^{(\kappa)}_{\mathcal{S}_I})$ be the feasible point for (4.34) found from the $(\kappa-1)$th iteration. The nonconvex constraint (4.15d) in (4.34a) is innerly approximated by the convex constraint (4.19). However, we still have to develop an inner convex approximation of the nonconvex constraint (4.34b).

4.3.1 Path-following iteration

Use the equivalent representation

$$r_{i,d_j}(\boldsymbol{w}_{\mathcal{S}_I}, \mathbf{q}_{\mathcal{S}_I}) = f_{i,d_j}(\boldsymbol{w}_{i,d_j}, \mathbf{P}_{i,d_j}) + g_{i,d_j}(\boldsymbol{w}_{\mathcal{S}_I}, \mathbf{q}_{\mathcal{S}_I}), \tag{4.35}$$

in conjunction with

$$f_{i,d_j}(\boldsymbol{w}_{i,d_j}, \mathbf{P}_{i,d_j}) \triangleq \ln \left| \Phi_{i,d_j}(\boldsymbol{w}_{i,d_j}, \mathbf{q}_{i,d_j}) \right| = 2 \ln |h_{i,i,d_j} \boldsymbol{w}_{i,d_j}|^2 + \ln |\mathbf{P}_{i,d_j}|, \tag{4.36}$$

and

$$g_{i,d_j}(\boldsymbol{w}_{\mathcal{S}_I}, \mathbf{q}_{\mathcal{S}_I}) \triangleq \ln \left| \Big(\Phi_{i,d_j}(\boldsymbol{w}_{i,d_j}, \mathbf{q}_{i,d_j}) \Big)^{-1} + \Big(\Gamma_{i,d_j}(\boldsymbol{w}_{\mathcal{S}_I}, \mathbf{q}_{\mathcal{S}_I}) \Big)^{-1} \right|. \tag{4.37}$$

Using the inequality (A.18) yields

$$\begin{aligned} f_{i,d_j}(\boldsymbol{w}_{i,d_j}, \mathbf{P}_{i,d_j}) &\geq \\ f_{i,d_j}(w_{i,d_j}^{(\kappa)}, P_{i,d_j}^{(\kappa)}) + 4 - \frac{2|h_{i,i,d_j} w_{i,d_j}^{(\kappa)}|^2}{|h_{i,i,d_j} \boldsymbol{w}_{i,d_j}|^2} - \langle P_{i,d_j}^{(\kappa)}, \mathbf{P}_{i,d_j}^{-1} \rangle &\geq \\ f_{i,d_j}(w_{i,d_j}^{(\kappa)}, P_{i,d_j}^{(\kappa)}) + 4 - \langle P_{i,d_j}^{(\kappa)}, \mathbf{P}_{i,d_j}^{-1} \rangle & \\ - \frac{2|h_{i,i,d_j} w_{i,d_j}^{(\kappa)}|^2}{2\Re\{(w_{i,d_j}^{(\kappa)})^H h_{i,i,d_j} h_{i,i,d_j} \boldsymbol{w}_{i,d_j}\} - |h_{i,i,d_j} w_{i,d_j}^{(\kappa)}|^2} &\triangleq \\ f_{i,d_j}^{(\kappa)}(\boldsymbol{w}_{i,d_j}, \mathbf{P}_{i,d_j}) & \end{aligned} \tag{4.38}$$

over the trust region

$$2\Re\{(w_{i,d_j}^{(\kappa)})^H h_{i,i,d_j}^H h_{i,i,d_j} \boldsymbol{w}_{i,d_j}\} - |h_{i,i,d_j} w_{i,d_j}^{(\kappa)}|^2 > 0. \tag{4.39}$$

Furthermore, using the inequality (A.17) in the Appendix yields

$$\begin{aligned} g_{i,d_j}(\boldsymbol{w}_{\mathcal{S}_I}, \mathbf{q}_{\mathcal{S}_I}) &\geq \\ g_{i,d_j}(w_{\mathcal{S}_I}^{(\kappa)}, q_{\mathcal{S}_I}^{(\kappa)}) + 2 - \langle B_{i,d_j}^{(\kappa)}, \Phi_{i,d_j}(\boldsymbol{w}_{i,d_j}, \mathbf{q}_{i,d_j}) \rangle - \langle C_{i,d_j}^{(\kappa)}, \Gamma_{i,d_j}(\boldsymbol{w}_{\mathcal{S}_I}, \mathbf{q}_{\mathcal{S}_I}) \rangle &= \\ g_{i,d_j}(w_{\mathcal{S}_I}^{(\kappa)}, q_{\mathcal{S}_I}^{(\kappa)}) + 2 - \sigma^2 \langle C_{i,d_j}^{(\kappa)} \rangle - \sum_{(s,d_\ell) \in \mathcal{S}_I} \langle [\chi_{i,d_j,s,d_\ell}(\boldsymbol{w}_{s,d_\ell})]^2, \mathbf{P}_{s,d_\ell} \rangle, & \end{aligned} \tag{4.40}$$

where

$$\begin{aligned} 0 \prec B_{i,d_j}^{(\kappa)} &\triangleq \Big(\Phi_{i,d_j}(w_{i,d_j}^{(\kappa)}, q_{i,d_j}^{(\kappa)}) \Big)^{-1} - \Big(\Phi_{i,d_j}(w_{i,d_j}^{(\kappa)}, q_{i,d_j}^{(\kappa)}) + \Gamma_{i,d_j}(w_{\mathcal{S}_I}^{(\kappa)}, q_{\mathcal{S}_I}^{(\kappa)}) \Big)^{-1}, \\ 0 \prec C_{i,d_j}^{(\kappa)} &\triangleq \Big(\Gamma_{i,d_j}(w_{\mathcal{S}_I}^{(\kappa)}, q_{\mathcal{S}_I}^{(\kappa)}) \Big)^{-1} - \Big(\Phi_{i,d_j}(w_{i,d_j}^{(\kappa)}, q_{i,d_j}^{(\kappa)}) + \Gamma_{i,d_j}(w_{\mathcal{S}_I}^{(\kappa)}, q_{\mathcal{S}_I}^{(\kappa)}) \Big)^{-1}, \end{aligned} \tag{4.41}$$

and

$$\begin{aligned}\chi_{i,d_j,i,d_j}(\boldsymbol{w}_{i,d_j}) &\triangleq \mathcal{L}^{*}_{i,i,d_j}(\boldsymbol{w}_{i,d_j})(B^{(\kappa)}_{i,d_j})^{1/2},\\ \chi_{i,d_j,s,d_\ell}(\boldsymbol{w}_{s,d_\ell}) &= \mathcal{L}^{*}_{s,i,d_j}(\boldsymbol{w}_{s,d_\ell})(C^{(\kappa)}_{i,d_j})^{1/2}, (s,d_\ell)\in\mathcal{S}_I\setminus(i,d_j).\end{aligned} \tag{4.42}$$

Let us introduce the positive definite matrix variables $\mathbf{X}_{i,d_j,s,d_\ell}$ of size 2×2 satisfying the semi-definite constraints of

$$\left[\chi_{i,d_j,s,d_\ell}(\boldsymbol{w}_{s,d_\ell})\right]^2 \preceq \mathbf{X}_{i,d_j,s,d_\ell}, (s,d_\ell)\in\mathcal{S}_I \tag{4.43}$$

$$\Leftrightarrow \quad \begin{bmatrix} \mathbf{X}_{i,d_j,s,d_\ell} & \chi_{i,d_j,s,d_\ell}(\boldsymbol{w}_{s,d_\ell}) \\ \left(\chi_{i,d_j,s,d_\ell}(\boldsymbol{w}_{s,d_\ell})\right)^H & I_2 \end{bmatrix} \succeq 0, (s,d_\ell)\in\mathcal{S}_I. \tag{4.44}$$

Then, by using the inequality (A.18), we arrive at:

$$\begin{aligned}\langle[\chi_{i,d_j,s,d_\ell}(\boldsymbol{w}_{s,d_\ell})]^2, \mathbf{P}_{s,d_\ell}\rangle &\leq\\ \langle\mathbf{X}_{i,d_j,s,d_\ell}, \mathbf{P}_{s,d_\ell}\rangle &\leq\\ \frac{1}{4}||(X^{(\kappa)}_{i,d_j,s,d_\ell})^{-1/2}\left(\mathbf{X}_{i,d_j,s,d_\ell}P^{(\kappa)}_{s,d_\ell} + X^{(\kappa)}_{i,d_j,s,d_\ell}\mathbf{P}_{s,d_\ell}\right)(P^{(\kappa)}_{s,d_\ell})^{-1/2}||^2, (s,d_\ell)\in\mathcal{S}_I,\end{aligned} \tag{4.45}$$

for

$$X^{(\kappa)}_{i,d_j,s,d_\ell} = \left[\chi_{i,d_j,s,d_\ell}(w^{(\kappa)}_{s,d_\ell})\right]^2, (s,d_\ell)\in\mathcal{S}_I. \tag{4.46}$$

Hence,

$$g_{i,d_j}(\boldsymbol{w}_{\mathcal{S}_I}, \mathbf{q}_{\mathcal{S}_I}) \geq g^{(\kappa)}_{i,d_j}(\mathbf{X}_{\mathcal{S}_I}, \mathbf{q}_{\mathcal{S}_I}) \tag{4.47}$$

for

$$\begin{aligned}g^{(\kappa)}_{i,d_j}(\mathbf{X}_{\mathcal{S}_I}, \mathbf{q}_{\mathcal{S}_I}) \triangleq\ & -\frac{1}{4}\sum_{(s,d_\ell)\in\mathcal{S}_I}||(X^{(\kappa)}_{i,d_j,s,d_\ell})^{-1/2}\left(\mathbf{X}_{i,d_j,s,d_\ell}P^{(\kappa)}_{s,d_\ell} + X^{(\kappa)}_{i,d_j,s,d_\ell}\mathbf{P}_{s,d_\ell}\right)\\ & (P^{(\kappa)}_{s,d_\ell})^{-1/2}||^2_F + g_{i,d_j}(w^{(\kappa)}_{\mathcal{S}_I}, q^{(\kappa)}_{\mathcal{S}_I}) + 2.\end{aligned} \tag{4.48}$$

To generate the next iterative point $(t^{(\kappa+1)}, \gamma^{(\kappa+1)}, w_{\mathcal{S}_I}^{(\kappa+1)}, v_{\mathcal{S}_E}^{(\kappa+1)}, q_{\mathcal{S}}^{(\kappa+1)})$ at the κth iteration, we solve the following convex optimization problem t

$$\max_{\mathbf{t},\boldsymbol{w}_{\mathcal{S}_I},q_{\mathcal{S}_I},\boldsymbol{v}_{\mathcal{S}_E},\boldsymbol{\gamma},\mathbf{X}_{\mathcal{S}_I}} \ \boldsymbol{\gamma} \quad \text{s.t.} \quad (4.15d), (4.19), (4.25), (4.34c), (4.34d)-(4.34e), (4.39), (4.44), \tag{4.49a}$$

$$f_{i,d_j}^{(\kappa)}(\boldsymbol{w}_{i,d_j}, \mathbf{P}_{i,d_j}) + g_{i,d_j}^{(\kappa)}(\mathbf{X}_{\mathcal{S}_I}, \mathbf{q}_{\mathcal{S}_I}) \geq \frac{\gamma^{(\kappa)} t_2^{(\kappa)}}{2} \left(\frac{\boldsymbol{\gamma}}{\gamma^{(\kappa)}} + \frac{\mathbf{t}_2}{t_2^{(\kappa)}} \right)^2, (i, d_j) \in \mathcal{S}_I, \tag{4.49b}$$

The computational complexity of this convex problem is (4.21) is determined by $n_v = 3 + N[M(N + t + 1 + 3M) + K]$ and $m_c = 1 + N(2K + 4M + 1)$.

Note by observing (4.38) and (4.47) that the LHS of (4.49b) is a concave lower bounding approximation of the LHS of (4.34b), while by (4.17), the RHS of (4.49b) is a convex upper-bounding approximation of the RHS of (4.34b). Hence in fact the convex constraint (4.49b) is an inner approximation of the nonconvex constraint (4.34b). The convex problem (4.49) is then seen as an inner approximation of the nonconvex problem (4.34). Then $\gamma^{(\kappa+1)} > \gamma^{(\kappa)}$ as far as $\gamma^{(\kappa+1)} \neq \gamma^{(\kappa)}$ because $(t^{(\kappa+1)}, \gamma^{(\kappa+1)}, w_{\mathcal{S}_I}^{(\kappa+1)}, v_{\mathcal{S}_E}^{(\kappa+1)}, q_{\mathcal{S}}^{(\kappa+1)})$ and $(t^{(\kappa)}, \gamma^{(\kappa)}, w_{\mathcal{S}_I}^{(\kappa)}, v_{\mathcal{S}_E}^{(\kappa)}, q_{\mathcal{S}_I}^{(\kappa)})$ are the optimal solution and a feasible point for (4.49). As such, the sequence $\{(t^{(\kappa)}, \gamma^{(\kappa)}, w_{\mathcal{S}_I}^{(\kappa)}, v_{\mathcal{S}_E}^{(\kappa)}, q_{\mathcal{S}_I}^{(\kappa)})\}$ generated by (4.49) is of improved feasible points for the nonconvex problem (4.34) and it converges at least to a point satisfying the KKT condition of optimality [60].

4.3.2 Alternating descent iteration

One can see that the function $r_{i,d_j}(\boldsymbol{w}_{\mathcal{S}_I}, \mathbf{q}_{\mathcal{S}_I})$ defined by (4.33) is complex. We therefore develop an alternating procedure for its more efficient computation.

Alternating optimization in $\boldsymbol{w}_{\mathcal{S}}$

By fixing $\mathbf{q}_{\mathcal{S}_I} = q_{\mathcal{S}_I}^{(\kappa)}$, we address the problem

$$\max_{\mathbf{t},\boldsymbol{w}_{\mathcal{S}_I},\boldsymbol{v}_{\mathcal{S}_E},\boldsymbol{\gamma}} \ \boldsymbol{\gamma} \quad \text{s.t.} \quad (4.15c), (4.15d), (4.34c), (4.34d)-(4.34e), \tag{4.50a}$$

$$r_{i,d_j}(\boldsymbol{w}_{\mathcal{S}_I}, q_{\mathcal{S}_I}^{(\kappa)}) \geq 2\boldsymbol{\gamma}\mathbf{t}_2, (i, d_j) \in \mathcal{S}_I. \tag{4.50b}$$

Using the inequality (A.15) in the Appendix yields

$$\begin{aligned} r_{i,d_j}(\boldsymbol{w}_{\mathcal{S}_I}, q_{\mathcal{S}_I}^{(\kappa)}) \quad &\geq \\ r_{i,d_j}(w_{\mathcal{S}_I}^{(\kappa)}, q_{\mathcal{S}_I}^{(\kappa)}) - \langle \Phi_{i,d_j}(w_{i,d_j}^{(\kappa)}, q_{i,d_j}^{(\kappa)}), \left(\Gamma_{i,d_j}(w_{\mathcal{S}_I}^{(\kappa)}, q_{\mathcal{S}_I}^{(\kappa)})\right)^{-1} \rangle & \\ +2\Re\{\langle \mathcal{L}_{i,i,d_j}(\boldsymbol{w}_{i,d_j}) P_{i,d_j}^{(\kappa)} \mathcal{L}_{i,i,d_j}^H(w_{i,d_j}^{(\kappa)}) \times \left(\Gamma_{i,d_j}(w_{\mathcal{S}_I}^{(\kappa)}, q_{\mathcal{S}_I}^{(\kappa)})\right)^{-1} \rangle\} & \\ -\langle \left(\Gamma_{i,d_j}(w_{\mathcal{S}_I}^{(\kappa)}, q_{\mathcal{S}_I}^{(\kappa)})\right)^{-1} - \left(\Phi_{i,d_j}(w_{i,d_j}^{(\kappa)}, q_{i,d_j}^{(\kappa)}) + \Gamma_{i,d_j}(w_{\mathcal{S}_I}^{(\kappa)}, q_{\mathcal{S}_I}^{(\kappa)})\right)^{-1}, & \\ \Phi_{i,d_j}(\boldsymbol{w}_{i,d_j}, q_{i,d_j}^{(\kappa)}) + \Gamma_{i,d_j}(\boldsymbol{w}_{\mathcal{S}_I}, q_{\mathcal{S}_I}^{(\kappa)}) \rangle \quad &\triangleq \\ \tilde{r}_{i,d_j}^{(\kappa)}(\boldsymbol{w}_{\mathcal{S}_I}). \qquad (4.51) & \end{aligned}$$

To generate the next feasible point $(t^{(\kappa+1)}, \bar{\gamma}^{(\kappa+1)}, w_{\mathcal{S}_I}^{(\kappa+1)}, v_{\mathcal{S}_E}^{(\kappa+1)})$ for (4.34), we solve the following convex problem for:

$$\max_{\mathbf{t}, \boldsymbol{w}_{\mathcal{S}_I}, \boldsymbol{v}_{\mathcal{S}_E}, \boldsymbol{\gamma}} \ \boldsymbol{\gamma} \quad \text{s.t.} \quad (4.15c), (4.19), (4.34c), (4.34d) - (4.34e), \qquad (4.52a)$$

$$\tilde{r}_{i,d_j}^{(\kappa)}(\boldsymbol{w}_{\mathcal{S}_I}) \geq \frac{\gamma^{(\kappa)} t_2^{(\kappa)}}{2} \left(\frac{\boldsymbol{\gamma}}{\gamma^{(\kappa)}} + \frac{\mathbf{t}_2}{t_2^{(\kappa)}} \right)^2, (i, d_j) \in \mathcal{S}_I. \qquad (4.52b)$$

The computational complexity of this convex problem is (4.21) determined by $n_v = 3 + NN_t(M + K)$ and $m_c = N(3K + 2M + 1)$.

Since the convex constraint (4.52b) is an inner approximation of the nonconvex constraint (4.50b), the convex problem (4.52) is seen as an inner approximation of the nonconvex problem (4.50). We then have

$$\bar{\gamma}^{(\kappa+1)} \geq \gamma^{(\kappa)}, \qquad (4.53)$$

because they are the optimal and a feasible value for (4.52).

Alternating optimization in $\mathbf{q}_{\mathcal{S}_I}$

By fixing $(\mathbf{t}, \boldsymbol{w}_{\mathcal{S}_I}, \boldsymbol{v}_{\mathcal{S}_E}) = (t^{(\kappa+1)}, w_{\mathcal{S}_I}^{(\kappa+1)}, v_{\mathcal{S}_E}^{(\kappa+1)})$, we address the problem

$$\max_{\mathbf{q}_{\mathcal{S}_I}, \boldsymbol{\gamma}} \ \boldsymbol{\gamma} \quad \text{s.t.} \quad (4.25), \qquad (4.54a)$$

$$r_{i,d_j}(w_{\mathcal{S}_I}^{(\kappa+1)}, \mathbf{q}_{\mathcal{S}_I}) \geq 2\boldsymbol{\gamma} \mathbf{t}_2^{(\kappa+1)}, (i, d_j) \in \mathcal{S}_I. \qquad (4.54b)$$

Using the inequality (A.16) in the Appendix yields

$$\begin{aligned} r_{i,d_j}(w_{\mathcal{S}_I}^{(\kappa+1)}, \mathbf{q}_{\mathcal{S}_I}) \;&\geq \\ r_{i,d_j}(w_{\mathcal{S}_I}^{(\kappa+1)}, q_{\mathcal{S}_I}^{(\kappa)}) + 4 - \langle \Big(\Gamma_{i,d_j}(w_{\mathcal{S}_I}^{(\kappa+1)}, q_{\mathcal{S}_I}^{(\kappa)})\Big)^{-1}, \Gamma_{i,d_j}(w_{\mathcal{S}_I}^{(\kappa+1)}, \mathbf{q}_{\mathcal{S}_I})\rangle \\ -\langle \Phi_{i,d_j}(w_{i,d_j}^{(\kappa+1)}, q_{i,d_j}^{(\kappa)}) + \Gamma_{i,d_j}(w_{\mathcal{S}_I}^{(\kappa+1)}, q_{\mathcal{S}_I}^{(\kappa)}), \\ \Big(\Phi_{i,d_j}(w_{i,d_j}^{(\kappa+1)}, \mathbf{q}_{i,d_j}) + \Gamma_{i,d_j}(w_{\mathcal{S}_I}^{(\kappa+1)}, \mathbf{q}_{\mathcal{S}_I})\Big)^{-1}\rangle \;&\triangleq \\ \hat{r}_{i,d_j}^{(\kappa)}(\mathbf{q}_{\mathcal{S}_I}). \end{aligned} \tag{4.55}$$

To generate the next feasible point $(q_{\mathcal{S}}^{(\kappa+1)}, \gamma^{(\kappa+1)})$ for (4.34), we then solve the following convex optimization problem:

$$\begin{aligned} &\max_{q_{\mathcal{S}_I}, \boldsymbol{\gamma}} \; \boldsymbol{\gamma} \quad \text{s.t.} \quad (4.25), \\ &\hat{r}_{i,d_j}^{(\kappa)}(\mathbf{q}_{\mathcal{S}_I}) \geq 2\boldsymbol{\gamma} t_2^{(\kappa+1)}, (i,d_j) \in \mathcal{S}_I. \end{aligned} \tag{4.56}$$

The computational complexity of this convex problem is (4.21) determined by $n_v = 1 + NM$ and $m_c = 3NM$.

Note that we have $\gamma^{(\kappa+1)} > \bar{\gamma}^{(\kappa+1)} \geq \gamma^{(\kappa)}$ provided that $\gamma^{(\kappa+1)} > \bar{\gamma}^{(\kappa+1)}$, hence the sequence $\{(t^{(\kappa)}, \gamma^{(\kappa)}, w_{\mathcal{S}_I}^{(\kappa)}, v_{\mathcal{S}_E}^{(\kappa)}, q_{\mathcal{S}_I}^{(\kappa)})\}$ is of feasible points for the nonconvex problem (4.34), which converges to a feasible point satisfying the KKT conditions for one of two variable sets $(\mathbf{t}, \boldsymbol{v}_{\mathcal{S}_E}, \boldsymbol{w}_{\mathcal{S}_I})$ and $\mathbf{q}_{\mathcal{S}_I}$, when the other is held fixed.

4.3.3 Generating a good feasible point for (4.34)

It is important to generate a good feasible point for (4.34). For this we fix $\mathbf{t}^{(0)}$ to satisfy (4.15d) and $q_{\mathcal{S}_I}^{(0)}$ (for instance $q_{s,d_\ell}^{(0)} \equiv 0.2$) and reasonable $\gamma^{(0)}$. We then randomly generate $w_{\mathcal{S}_I}^{(0)}$ and $v_{\mathcal{S}_E}^{(0)}$ satisfying the convex constraints (4.34c)-(4.34e). Let us set

$$P_{i,d_j}^{(\kappa)} \equiv \begin{bmatrix} 1 & q_{i,d_j}^{(0)} \\ (q_{i,d_j}^{(0)})^* & 1 \end{bmatrix}.$$

We then iterate

$$\max_{\boldsymbol{v}_{\mathcal{S}_E},\boldsymbol{w}_{\mathcal{S}_I},\boldsymbol{\eta}} \ \boldsymbol{\eta} \quad \text{s.t.} \quad (4.22d), (4.34d) - (4.34e), \tag{4.57a}$$

$$\tilde{r}_{i,d_j}^{(\kappa)}(\boldsymbol{w}_{\mathcal{S}_I}) \geq 2\gamma_0 t_2^{(0)}\boldsymbol{\eta}, (i,d_j) \in \mathcal{S}_I, \tag{4.57b}$$

$$\frac{\sum_{j=1}^{K}||\boldsymbol{v}_{i,e_j}||^2}{t_1^{(0)}} + \frac{\sum_{j=1}^{M}||\boldsymbol{w}_{i,d_j}||^2}{t_2^{(0)}} \leq P, i = 1,\ldots,N, \tag{4.57c}$$

until we have $\boldsymbol{\eta} \geq 1$ for guaranteeing that $(t^{(0)}, \gamma^{(0)}\boldsymbol{\eta}, w_{\mathcal{S}_I}^{(\kappa)}, v_{\mathcal{S}_E}^{(\kappa)}, q_{\mathcal{S}_I}^{(\kappa)})$ is feasible for (4.34).

4.3.4 Algorithm

For optimizing a trade-off between the convergence speed and the solution optimality we propose Algorithm 5, which uses the alternating optimization until its convergence and then switches to the path-following optimization in order to converge at least to a locally optimal solution.

Algorithm 5 s-IGS algorithm for (4.34)

1: **Initialization:** Fix $q_{\mathcal{S}_I}^{(0)}$. Set $\kappa := 0$ and then iterate (4.57) for finding a good initial feasible point $(v_{\mathcal{S}_E}^{(0)}, w_{\mathcal{S}_I}^{(0)}, t^{(0)})$ for (4.34)
2: **Repeat until** (4.34) **is reached:** Generate the feasible point $(v_{\mathcal{S}_E}^{(\kappa+1)}, w_{\mathcal{S}_I}^{(\kappa+1)}, t^{(\kappa+1)})$ for (4.34) by solving the convex optimization problems (4.52) and (4.56) of alternating optimization to ; Reset $\kappa := \kappa + 1$.
3: **Repeat until convergence of the objective in** (4.34)**:** Solve the convex optimization problem (4.49) of path-following optimization to generate the feasible point $(v_{\mathcal{S}_E}^{(\kappa+1)}, w_{\mathcal{S}_I}^{(\kappa+1)}, t^{(\kappa+1)})$ for (4.34); Reset $\kappa := \kappa + 1$.
4: **Output** $\mathbf{t} = t^{(\kappa)}$, $\boldsymbol{v}_{\mathcal{S}_E} = v_{\mathcal{S}_E}^{(\kappa)}$, and $\boldsymbol{w}_{\mathcal{S}_I} = w_{\mathcal{S}_I}^{(\kappa)}$.

4.4 Performance results

In all our simulations we consider networks of three cells ($N = 3$). The channel spanning from a BS to a user at a distance of d meters is expressed as $\sqrt{10^{-\sigma_{\text{PL}}/10}}\tilde{h}$, where $\sigma_{\text{PL}} = 30 + 10\beta\log_{10}(d)$ is the path-loss in dB, and $\tilde{h}$ is the Rician fading channel

gain associated with a Rician factor of 10 dB for the EUs served by that BS only. Otherwise, $\tilde{h}$ is the normalized Rayleigh fading channel gain. The path-loss exponent β is set to 3 for the Rician channels and to 2 for the Rayleigh channels. The power of the signal received by the UEs must exceed the threshold of -21 dBm with 13 nm CMOS technology [67] to facilitate EH. We set $e_{\min} = -20$ dBm, $\zeta = 0.5$, $P = 35$ dBm. The bandwidth is set to $B = 20$ MHz, the power spectral density of noise is -174 dBm/Hz.

4.4.1 NOMA favored scenario

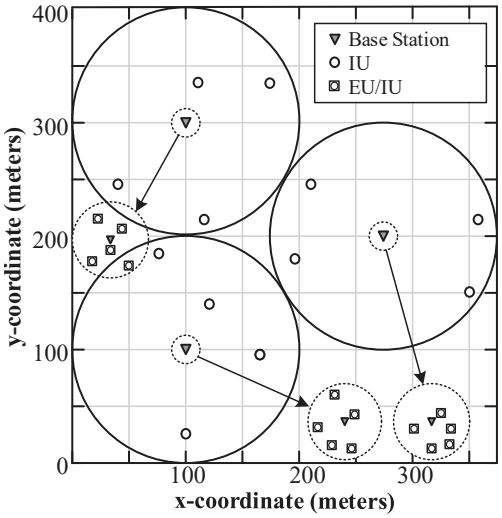

Fig. 4.2 NOMA favored scenario

Fig. 4.2 illustrates a scenario, where K EUs (i, e_j), $j = 1, \ldots, K$ also act as the first K IUs. The other K IUs (i, d_{K+j}), $j = 1, \ldots, K$ in each cells are distributed near the cell boundary. Those IUs which are located near the cell-boundary, are not only in poorer channel conditions than the IUs (i, d_j), $j = 1, \ldots, K$ but are then subject to intercell-interference. By bringing about the differentiated channel conditions between the near IUs (i, d_j), $j = 1, \ldots, K$ and far IUs (i, d_{K+j}), $j = 1, \ldots, K$, such scenario favours NOMA, helping it to perform better than the conventional OMA. Both NOMA and OMA use proper Gaussian signal for carrying information, i.e. $q_{s,d_\ell} \equiv 0$ in (4.24) so the information signal $\mathbf{x}^I_{s,d_\ell}$ defined by (4.23) or (4.5) for $\boldsymbol{w}_{2,s,d_\ell} \equiv 0$ is generated by linearly beamforming of a normalized proper Gaussian source s_{s,d_ℓ}. Under OMA, each IU (i, d_j), $j = 1, \ldots, 2K$ decodes its own information s_{i,d_j} while under NOMA each

pair of IUs (i, d_j) and (i, d_{K+j}), $j = 1, \ldots, K$ decode the information $s_{i,d_{K+j}}$ for the IU (i, d_{K+j}) and then the IU (i, d_j) subtracts $s_{i,d_{K+j}}$ from its interference in decoding its own information s_{i,d_j}.

Fig. 4.3 characterizes the convergence behaviour of the proposed Algorithms for $N_t = 6$ and $K = 3$, i.e. each BS is equipped with $N_t = 6$ DL TAs and there are a total of 27 users served by the network. The NOMA PGS algorithm [73] converges rapidly as a benefit of the efficient approximation of the logarithmic functions. The convergence rate of the IGS and s-IGS algorithms is similar, but the computational complexity of the latter is significantly lower.

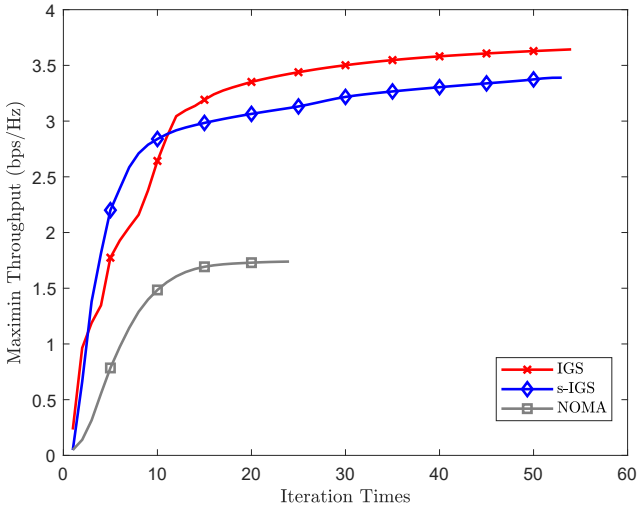

Fig. 4.3 Convergence for IGS, s-IGS and NOMA algorithms

Fig. 4.4 plots the achievable minimum throughput under different numbers N_t of DL TAs for $K = 2$ (18 users in total) and $K = 3$ (27 users in total). Both the IGS and s-IGS outperform NOMA [73]. IGS outperforms s-IGS since the latter is a particular class of the former. All of them still benefit from the spatial diversity associated with the number N_t of BS TAs. This figure also shows the efficiency of the time fraction optimization as IGS, s-IGS and NOMA outperform their counter parts IGS ($\mathbf{t}_1 = \mathbf{t}_2 = 2$), s-IGS($\mathbf{t}_1 = \mathbf{t}_2 = 2$) and NOMA ($\mathbf{t}_1 = \mathbf{t}_2 = 2$), respectively, which use the half of the time-slot for power transfer and the remaining half for information transfer.

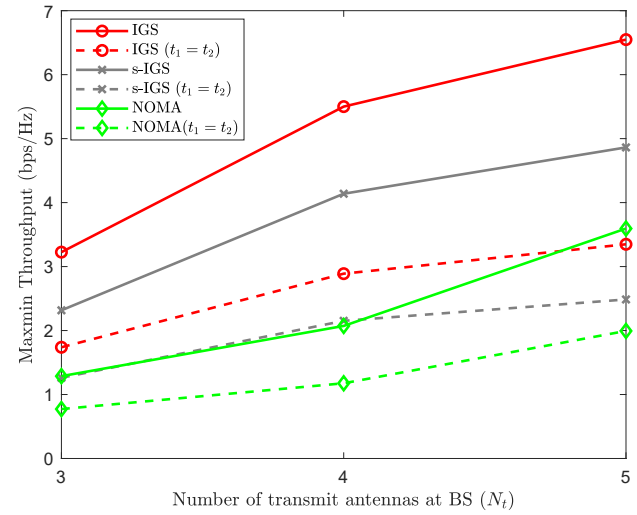

(a)

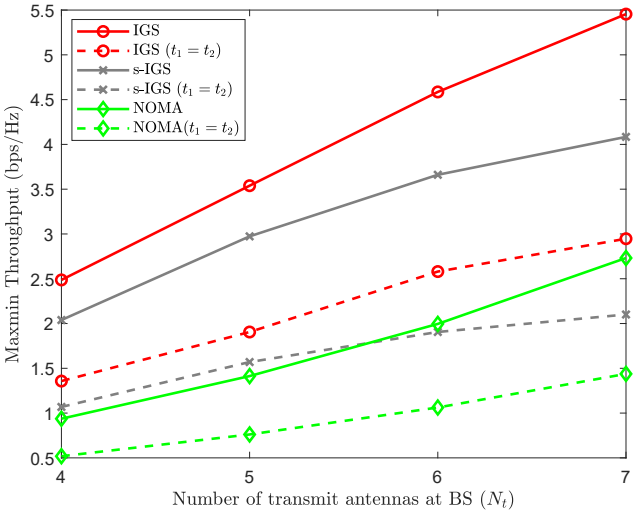

(b)

Fig. 4.4 Achievable minimum throughput vs number N_t: (a) $K = 2$ (18 users); (b) $K = 3$ (27 users)

We now examine the achievable minimum throughput upon varying the BS transmit power budget P in Fig. 4.5 under $(N_t, K) = (6, 3)$. Both the IGS and s-IGA exploit the available transmit power much better than NOMA since the latter cannot use the total affordable power budget because its achievable minimum throughput is not sensitive to $P \geq 33$ dBm. By contrast, by employing additional beamformers $\boldsymbol{w}_{2,s,d_\ell}$ for the conjugate proper Gaussian information source s^*_{s,d_ℓ} in (4.5) or optimizing the

pseudo-covariance $\mathbf{q}_{s,d_\ell}$ in (4.24), IGS allows the total power budget be exploited for improving its throughput. Naturally, beyond a certain threshold, namely $P = 41$ dBm in Fig. 4.5, its performance also becomes saturated. This should not be a surprise for interference-limited networks.

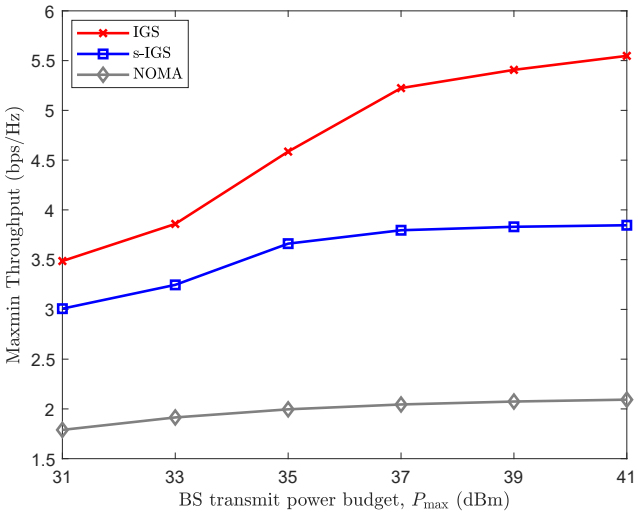

Fig. 4.5 Achievable minimum throughput vs BS transmit power budget P

Fig. 4.6 portrays the users' max-min throughput under $(N_t, K) = (6, 3)$ upon varying the EH threshold $e_{\min}$ to show the impact of the latter imposed on the former. As expected, the increase of the latter degrades the performance of the former.

Table 4.1 provides the rounded average number of iterations required required for the convergence of the three algorithms for $K = 3$ under different number of BS TAs N_t. For lower N_t the feasibility set becomes narrower, which forces all algorithms to converge slower.

Table 4.1 The rounded average number of iterations for the convergence under NOMA favored scenario

	$N_t = 4$	$N_t = 5$	$N_t = 6$	$N_t = 7$
IGS	30	31	20	20
S-IGS	25	28	31	18
NOMA	24	22	15	18

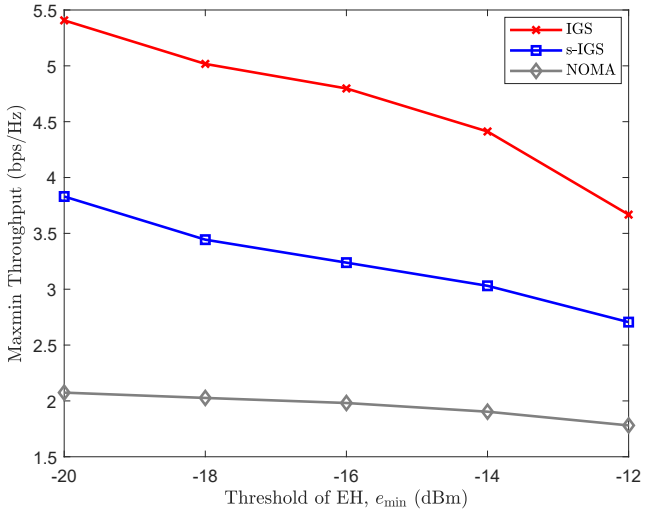

Fig. 4.6 Achievable minimum throughput vs BS transmit power budget P

4.4.2 General scenario

Fig. 4.7 illustrates a general scenario, where M IUs are located outside the EH zone, hence they cannot act as EUs. The IUs' channel conditions are not differentiated, therefore NOMA is inefficient. We thus compare IGS and s-IGS to the conventional PGS orthogonal multiple access (OMA), in which IU decodes its own message only.

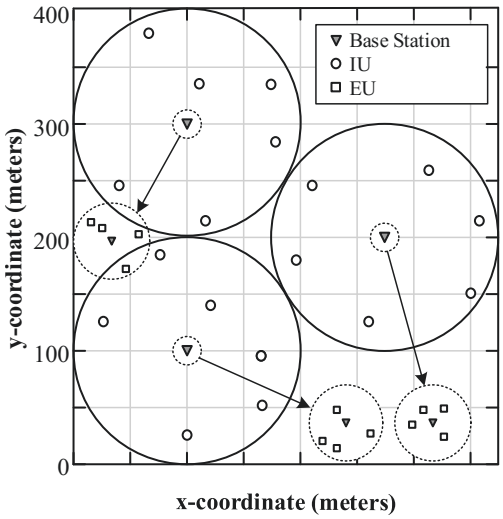

Fig. 4.7 OMA favored scenario

Fig 4.8 shows the achievable minimum throughput for IGS, s-IGS and PGS OMA for different values of N_t. There are $K = 2$ EUs and $M = 4$ IUs for simulating Fig. 4.8(a), and $K = 3$ EUs and $M = 6$ IUs for simulating Fig. 4.8(b). As expected, IGS is the best performer, followed by s-IGS, while PGS OMA is the worst performer. Similarly to Fig. 4.4, this figure also includes the performance of IGS, s-IGS and PGS OMA at $\mathbf{t}_1 = \mathbf{t}_2 = 2$ to show the efficiency of the time fraction optimization.

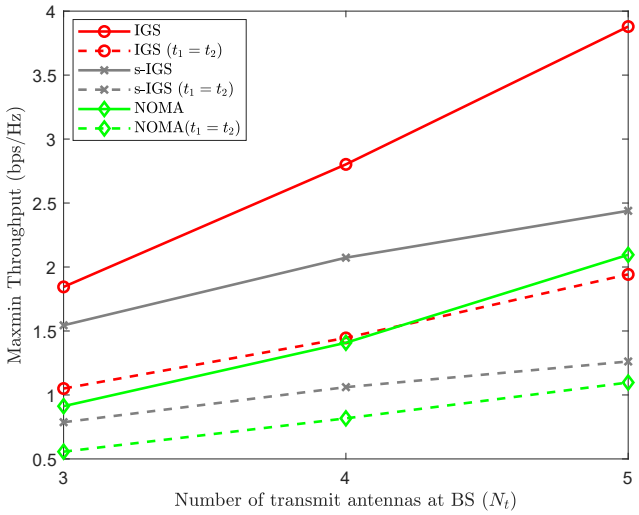

(a)

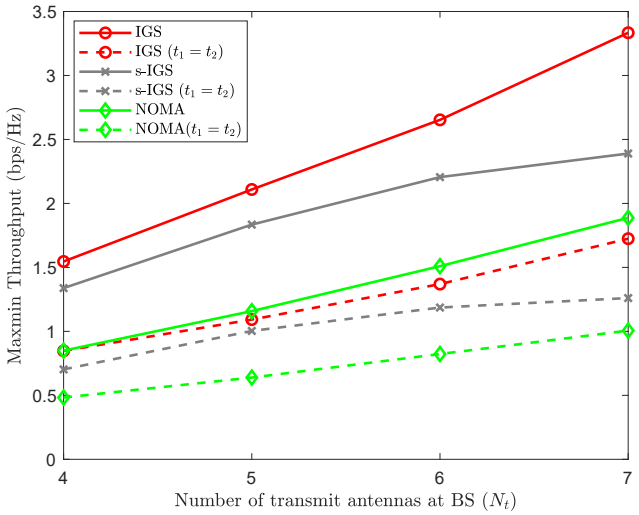

(b)

Fig. 4.8 Achievable minimum throughput vs BS antennas number N_t: (a) $(K, M) = (2, 4)$; (b) $(K, M) = (3, 6)$

Fig. 4.9 provides the achievable minimum throughput for varying values of the BS transmit power budget P. All three algorithms are capable of exploiting the affordable power budget to compensate for the increased distance from the BS to the IUs that makes the pathloss higher.

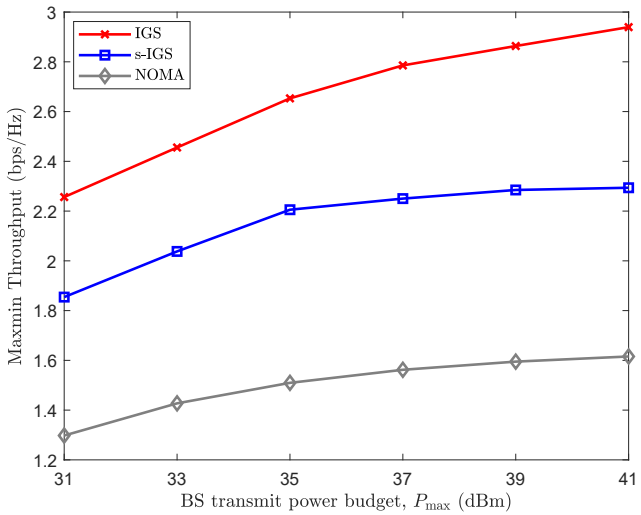

Fig. 4.9 Achievable minimum throughput vs BS transmit power budget P

Finally, Table 4.2 provides the rounded average number of iterations for the convergence of IGS, s-IGS and PGS OMA for $(K, M) = (3, 6)$ and different values of N_t.

Table 4.2 The rounded average number of iterations for the convergence under general scenario

	$N_t = 4$	$N_t = 5$	$N_t = 6$	$N_t = 7$
IGS	17	16	19	18
S-IGS	16	20	21	19
PGS OMA	6	8	10	11

4.5 Conclusions

We have applied improper Gaussian signaling (IGS), in both general format and a particular format (s-IGS), for improving the information throughput of a multi-cell

energy-harvesting enabled network, which aims for transferring both information and energy over the same wireless channels within a time slot. In contrast to NOMA, which improves the network throughput by allowing the users of better channel condition to access and decode the information of the users of poorer channel condition, IGS is capable of improving the network throughput more substantially than NOMA, maintaining the users' secrecy under OMA. Although the problem of max-min information user throughput subject to the EH thresholds and power budget is much more computationally challenging than its NOMA counterpart, the chapter has developed path-following algorithms for its computation, which converge at least to a locally optimal solution. The numerical examples provided for networks serving 18 users and 27 users have confirmed the advantages of IGS over NOMA and OMA proper Gaussian signaling.

Chapter 5

Joint Design of Reconfigurable Intelligent Surfaces and Transmit Beamforming under Proper and Improper Gaussian Signaling

5.1 Introduction

The next-generation networks aim to increase 1000-fold in the average data rate, 100× improvement in the edge rate (worst data rate that a user can reasonably expect), and at least 100× decrease in energy consumption and cost compared to that offered by presently commercialized ones [99]. Though recently proposed technologies, e.g., massive multiple-input multiple-output (MIMO) and millimeter wave (mmWave) communication systems, have the potential to meet data rate requirements [21], they fail to address the target of low energy consumption and hardware cost [100]. Particularly, efficient communication by these technologies require large number of costly and power-hungry radio frequency (RF) chains (depending on the number of antennas), where each comprises several active components. Therefore, researchers are still hunting for an energy efficient as well as spectral efficient solution to assist the realization of futuristic networks [101, 22].

Recently, the use of reconfigurable intelligent surface (RIS) has been identified as a low-energy consumption and spectral efficient solution [64, 102, 6]. RIS is a planar array of a large number of low-cost and nearly-passive reflecting elements with reconfigurable parameters. Each reflecting element on RIS can introduce an independent phase shift on the incident electromagnetic wave (from the acesss points (AP) or transmitter) [103]. The phase shifts induced by the passive elements can be programmed to ensure that reflected signals from the RIS elements coherently add, together or also with other direct-path signals, if available, at the user end [102, 104, 105]. More importantly, RIS can be installed in such places such as buildings which block the direct transmission from the AP to its users [106]. RIS technology is quite different with several distinct positives when compared with the other existing technologies such as backscatter communication [107, 108], amplify-and forward (AF) relaying, and intelligent surface based massive MIMO [109]. A detailed comparison among these technologies is provided in [6, 110]. The work [23] shows that a particular RIS-aided MIMO system can achieve the same rate performance as that achieved by massive MIMO system without using RIS, but the former option is energy-and cost-efficient with significantly reduced active antennas/RF chains.

Naturally, RIS-aided systems need to be optimized in terms of transmit beamformers and RIS reflecting coefficients for delivering high rates. Optimization of RIS-aided systems looks computationally intractable because of two reasons: (i) both rate and transmit power become very complex functions in the beamformers and RIS reflecting coefficients; (ii) The RIS reflecting coefficients are constrained by the nonconvex unit-modulus constraint (UMC). Alternating optimization between the beamformers and the RIS reflecting coefficients is often applied. Each round of alternating optimization consists of optimization in the beamformers with the reflecting coefficients held fixed and optimization in the reflecting coefficients with the beamformers held fixed. These optimization problems are still nonconvex and thus still computationally challenging. The authors in [64] and [111] use general-purpose gradient/projected gradient algorithms for their computation, which do not necessarily converge. The authors in [23] reformulate alternating optimization in the reflecting coefficients as a matrix rank-one constrained optimization problem. The matrix rank-one constraint is then dropped for convex relaxation. The reader is also referred to [112] for computa-

tional efficiency of this convex relaxation. At each round of alternating optimization, the objective function is replaced by a surrogate function in [113–115], and then the nonconvex unit-modulus constraint on the reflecting coefficients is relaxed to the convex bounded-by-unit-modulus constraint for alternating optimization in the reflecting coefficients, while the minimum-mean-square-error (MMSE) algorithm is used for alternating optimization in the beamformers. Alternating optimization does not seem to be computationally efficient if each round still invokes two nonconvex problems, which are still computationally challenging. Theoretically, its found solution is not even locally optimal as it is only optimal in one set of variables with other set of variables held fixed.

It should be emphasized that all the aforementioned works are based on the conventional proper Gaussian signaling (PGS), which is induced by linearly beamforming proper Gaussian source. Recently, it has been shown e.g. in [90, 91, 88, 92, 96, 116–118] that improper Gaussian signaling (IGS), which is induced by widely linearly beamforming proper Gaussian source [75], outperforms PGS clearly in interference-limited networks. Under PGS, the transmit signal is still proper Gaussian and completely characterized by its covariance. In contrast, the transmit signal under IGS is improper Gaussian and is characterized by the so-called augmented covariance of double size with a special structure, which involves both the covariance and the pseudo-covariance information [75]. As such, in contrast to PGS, which is induced by single beamformers, IGS is induced by pairs of correlated beamformers. The design of beamforming vectors for IGS is more complex than for PGS because it involves twice the number of decision variables, and more importantly, the rate functions are log-determinant $\log\det(.)$ even for multi-input single output (MISO) networks. Their optimization is much more computationally challenging than that for PGS, which involves logarithmic functions only.

Against the above background, this chapter investigates the joint design of transmit beamformers and RIS reflecting coefficient in networks of a multiple antenna array AP serving multiple single-antenna users with the aid of an RIS, under both PGS and IGS. The contributions of the chapter are following:

- Under PGS, based on the exactly penalized optimization reformulation, which incorporates the computationally intractable unit-modulus constraint on the reflecting coefficients into the optimization objective, we develop an algorithm of low computational complexity, each iteration of which invokes up to two convex problems. Moreover, it rapidly converges at least to a locally optimal solution.
- This is the first work to use IGS for RIS-aided communication networks. Again, based on the exactly penalized optimization reformulation, we develop another algorithm of low computational complexity, which rapidly converges at least to a locally optimal solution.
- IGS bases algorithms clearly outperforms PGS bases algorithms in severely interference-limited scenarios when the number of transmit antennas is less than the number of served users.

The chapter is organized as follows. The joint design of beamformers and RIS reflecting coefficients to maximize the worst users' rate under PGS and RIS are addressed in Sections II and Section III, respectively. The simulations to demonstrate the advantage of RIS over PGS are provided in Section IV, which is followed by Section V for concluding the chapter. The Appendix provides fundamental matrix inequalities, which were used for developing the algorithms in Sections II and III.

5.2 Proper Gaussian signaling

Consider a RIS-aided network as illustrated by Fig. 5.1, where a RIS of N reflecting units assists the downlink from an M-antenna array AP to K single-antenna users (UEs). Let x be the transmit signal from the AP. The received signal at UE k can be expressed as

$$y_k = \left(\sqrt{\beta_{\text{AP-RIS}}}\sqrt{\beta_{\text{RIS-k}}}h_{r,k}\mathbf{R}_{\text{RIS-k}}^{1/2}\boldsymbol{\Theta}H_{AR} + \sqrt{\beta_{\text{AP-k}}}h_{a,k}\right)x + n_k, \tag{5.1}$$

where $\sqrt{\beta_{\text{AP-RIS}}}$ and $\sqrt{\beta_{\text{RIS-k}}}$ model the path-loss and large-scale fading of the AP-to-RIS link and from the RIS-to-UE k link, respectively [119, 111], $\sqrt{\beta_{\text{AP-k}}}$ models the path-loss and large-scale fading of the direct path between the AP and the UE

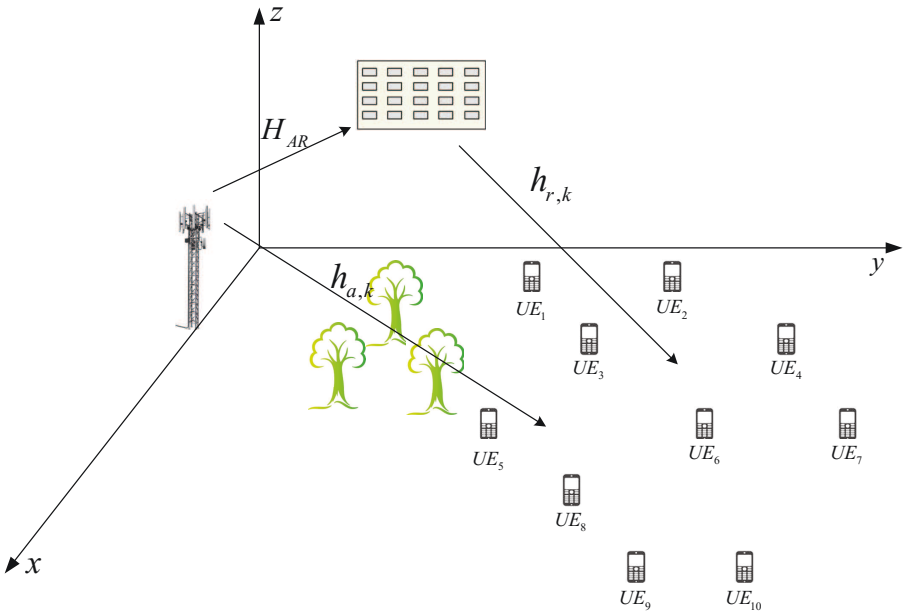

Fig. 5.1 System model

k, $H_{AR} \in \mathbb{C}^{N\times M}$ is the line-of-sight (LoS) channel matrix between the AP and RIS, $h_{r,k} \in \mathbb{C}^{1\times N}$ and $h_{a,k} \in \mathbb{C}^{1\times M}$,[1] respectively, denote the small-scale fading channels from the RIS and the AP to UE k, $\mathbf{R}_{\text{RIS-k}} \in \mathbb{C}^{N\times N}$ represents the spatial correlation matrix for the RIS elements with respect to the user k [111, 120], $n_k \in \mathcal{C}(0,\sigma)$ is the background noise at UE k, and for $\boldsymbol{\theta} \triangleq (\theta_1,\ldots,\theta_N) \in \mathbb{C}^N$ with

$$|\theta_n| = 1, n = 1,\ldots,N, \tag{5.2}$$

which denotes the vector of the RIS's reflecting-coefficients, the matrix of reflection-coefficients of the RIS is

$$\boldsymbol{\Theta} = \begin{bmatrix} \theta_1 & 0 & \ldots & 0 \\ 0 & \theta_2 & \ldots & 0 \\ 0 & 0 & \ldots & \theta_N \end{bmatrix} \in \mathbb{C}^{N\times N}.$$

Since the RIS is usually deployed on the facade of high-rise building [106] and the AP is usually deployed at a certain height it is justified to assume LoS communication between the AP and RIS [111]. The communication channel between the AP and UEs

[1] In Section IV, we also consider particular cases of no direct path between the AP and UEs, i.e. $h_{a,k} \equiv 0$

$h_{a,k}$ is non-LOS (NLoS) and thus modeled by Rayleigh fading, while the presence of LoS link is assumed between the RIS and UEs and thus the corresponding channel $h_{r,k}$ is modeled by Rician fading [121]. The NLoS communication between the AP and UEs motivates the use of an RIS to support the transmission. To focus on the design of beamforming vectors and reflection-coefficients of the RIS, the chapter assumes that the channel state information is perfectly available at the AP, which is responsible for calculating the reflection-coefficients of the RIS and feeding them back to the RIS controller through dedicated control channels. This assumption is in line with the existing relevant research in the literature [113–115]. Under this assumption, the results of the chapter will represent an upper bound on the practical achievable performance.

Let $s_k \in \mathcal{C}(0,1)$ be the information intended for UE k. Under PGS, the proper Gaussian source s_k is linearly beamformed by the beamformer $\boldsymbol{w}_k \in \mathbb{C}^M$. Therefore, the transmit signal x, which is given by

$$x = \sum_{k=1}^{K} \boldsymbol{w}_k s_k, \tag{5.3}$$

is also proper Gaussian. Using (5.3), the equation (5.1) is written by

$$y_k = \mathcal{H}_k(\boldsymbol{\theta}) \sum_{k=1}^{K} \boldsymbol{w}_k s_k + n_k, \tag{5.4}$$

for

$$\mathcal{H}_k(\boldsymbol{\theta}) \triangleq \sqrt{\beta_{\text{AP-RIS}}}\sqrt{\beta_{\text{RIS-k}}} h_{r,k} \mathbf{R}_{\text{RIS-k}}^{1/2} \boldsymbol{\Theta} H_{AR} + \sqrt{\beta_{\text{AP-k}}} h_{a,k} \in \mathbb{C}^{1\times M}. \tag{5.5}$$

Let $\boldsymbol{w} \triangleq \{\boldsymbol{w}_k, k \in \mathcal{K}\}$. Based on the signal-to-interference-plus-noise (SINR) defined by

$$\rho_k(\boldsymbol{\theta}, \boldsymbol{w}) \triangleq \frac{|\mathcal{H}_k(\boldsymbol{\theta})\boldsymbol{w}_k|^2}{\sum_{j\in\mathcal{K}\setminus\{k\}} |\mathcal{H}_k(\boldsymbol{\theta})\boldsymbol{w}_j|^2 + \sigma}, \tag{5.6}$$

the rate in nats at UE k is calculated by

$$r_k(\boldsymbol{\theta}, \boldsymbol{w}) = \ln\left(1 + \rho_k(\boldsymbol{\theta}, \boldsymbol{w})\right). \tag{5.7}$$

Given a power budget P, the max-min rate optimization problem can be formulated as

$$\max_{\boldsymbol{\theta},\boldsymbol{w}} \min_{k=1,\ldots,K} r_k(\boldsymbol{\theta},\boldsymbol{w}) \quad \text{s.t.} \quad (5.2), \tag{5.8a}$$

$$\sum_{k=1}^{K} ||\boldsymbol{w}_k||^2 \leq P, \tag{5.8b}$$

which is equivalent to max-min SINR optimization:

$$\max_{\boldsymbol{\theta},\boldsymbol{w}} f(\boldsymbol{\theta},\boldsymbol{w}) \triangleq \min_{k=1,\ldots,K} \rho_k(\boldsymbol{\theta},\boldsymbol{w}) \quad \text{s.t.} \quad (5.2), (5.8b). \tag{5.9}$$

This optimization problem is nonconvex because its objective function is nonconcave and the unit-modulus constraint (UMC) (5.2) is obviously nonconvex. To the authors' best knowledge, there is no efficient method to handle the UMC (5.2), which is often relaxed to the convex bounded-by-unit-modulus constraint

$$|\theta_n|^2 \leq 1, n = 1, \ldots, N. \tag{5.10}$$

The existing works use alternating optimization to address (5.8). Let $(\theta^{(\kappa)}, w^{(\kappa)})$ be a feasible point for (5.8) that is found from the $(k-1)$-th round. The n-th round aims to solve the following alternating optimization problem in $\boldsymbol{w}$ to generate the next iterative point $w^{(\kappa+1)}$:

$$\max_{\boldsymbol{w}} f(\theta^{(\kappa)},\boldsymbol{w}) \quad \text{s.t.} \quad (5.8b). \tag{5.11}$$

and then aims to solve the following alternating optimization problem in $\boldsymbol{\theta}$ to generate the next iterative point $\theta^{(\kappa+1)}$:

$$\max_{\boldsymbol{\theta}} f(\boldsymbol{\theta}, w^{(\kappa+1)}) \quad \text{s.t.} \quad (5.2), \tag{5.12}$$

It should be noted that the SINR ρ_k defined by (5.6) is a quotient of two functions, which are separately convex quadratic in $\boldsymbol{\theta}$ and $\boldsymbol{w}$, so both (5.11) and the unit-modulus-relaxed problem

$$\max_{\boldsymbol{\theta}} f(\boldsymbol{\theta}, w^{(\kappa)}) \quad \text{s.t.} \quad (5.10), \tag{5.13}$$

can be efficiently computed by the algorithms of [71, 70].

In [113], the objective is replaced by a surrogate function at each round so the alternating optimization in $\boldsymbol{w}$ is a convex problem, and by relaxing the UMC (5.2) by (5.10), the alternating optimization in $\boldsymbol{\theta}$ is also a convex problem.

The authors in [23] consider the following problem of power minimization subject to the SINR constraints

$$\min_{\boldsymbol{\theta},\boldsymbol{w}} \sum_{k=1}^{K} ||\boldsymbol{w}_k||^2 \quad \text{s.t.} \quad (5.2), \rho_k(\boldsymbol{\theta},\boldsymbol{w}) \geq \gamma, k \in \mathcal{K}, \tag{5.14}$$

for a given $\gamma > 0$. The alternating optimization in $\boldsymbol{w}$ to generate $w^{(\kappa+1)}$ is equivalent to a second-order cone problem of convex programming [122]. The alternating optimization in $\boldsymbol{\theta}$ to generate $\theta^{(\kappa+1)}$ is the feasibility problem

$$(5.2), \rho_k(\boldsymbol{\theta}, w^{(\kappa+1)}) \geq \gamma, k \in \mathcal{K}. \tag{5.15}$$

The authors use the auxiliary matrix variable $\widetilde{\Theta} \triangleq \begin{bmatrix} \Theta & \boldsymbol{\theta} \\ \boldsymbol{\theta}^H & 1 \end{bmatrix} \in \mathbb{C}^{(N+1)\times(N+1)}$, $\Theta \in \mathbb{C}^{N\times N}$, which must satisfy the semi-definite constraint $\widetilde{\Theta} \succeq 0$ and linear constraints $\widetilde{\Theta}(n,n) = 1$, $n \in \mathcal{N}$ and the matrix rank-one constraint

$$\text{rank}(\widetilde{\Theta}) = 1. \tag{5.16}$$

This matrix rank-one constraint is then dropped to have a convex relaxation for the feasibility problem (5.15). Obviously, $\theta^{(\kappa)}$ is already feasible for (5.15), so it is not clear for what one needs to consider (5.15) and how to judge which of feasible points for (5.15) is preferred. The number of decision variables in the convex relaxed problem is $N(2N+3)/2$, which is quickly grown in N. For instance, it is already 2575 for $N = 50$, hiking the computational complexity $\mathcal{O}((N(2N+2)/2)^3)$ of convex solvers. The reader is also referred to [112] for capacity of convex relaxation-based approaches in locating the needed matrix-rank one solution. After all, like [113], the convergence of the alternating procedure in [23] is not guaranteed.

We now propose a quite different approach for addressing the max-min SINR optimization problem (5.9). Note that the UMC (5.2) is equivalent to the convex

constraint (5.10) plus the constraint

$$N \leq \sum_{n=1}^{N} |\theta_n|^2, \tag{5.17}$$

which is reverse convex [30]. Indeed, (5.10) implies $\sum_{n=1}^{N} |\theta_n|^2 \leq N$, which together with (5.17) yield $\sum_{n=1}^{N} |\theta_n|^2 = N$ that is possible if and only if (5.2) is fulfilled. It is obvious that (5.17) is the same as

$$\frac{1}{N} - \frac{1}{\sum_{n=1}^{N} |\theta_n|^2} \geq 0, \tag{5.18}$$

and the equality sign in (5.18) forces the UMC (5.2). This means

$$\frac{1}{N} - \frac{1}{\sum_{n=1}^{N} |\theta_n|^2} \tag{5.19}$$

can be used a measure for satisfaction of the UCM (5.2). Like [123–125], instead of handling the nonconvex constraint (5.18) we minimize the measure (5.19) for its satisfaction by incorporating it in the optimization objective, leading to the following exactly penalized optimization problem

$$\max_{\boldsymbol{\theta},\boldsymbol{w}} \; g(\boldsymbol{\theta},\boldsymbol{w}) \triangleq \left[f(\boldsymbol{\theta},\boldsymbol{w}) + \mu \left(\frac{1}{N} - \frac{1}{\sum_{n=1}^{N} |\theta_n|^2} \right) \right] \quad \text{s.t.} \quad (5.8b), (5.10), \tag{5.20}$$

where $\mu > 0$ is the penalty parameter.[2] For μ sufficiently large, (5.9) and (5.20) have the same optimal solution [126]. Later, we will show how μ is chosen before hand.

Although all constraints in (5.20) are convex, (5.20) is still a difficult nonconvex problem as its objective remains to be nonconcave. We now develop iterative processes for its computation.

Let $(w^{(\kappa)}, \theta^{(\kappa)})$ be the feasible point for (5.20) that is found from the $(\kappa - 1)$-th round.

[2]Since the constraints (5.8b) and (5.8b) are already convex, there is no need to incorporate them in the optimization objective.

5.2.1 Alternating descent round

In alternating descent, we generate the next iterative point $w^{(\kappa+1)}$ with $\boldsymbol{\theta}$ held fixed at $w^{(\kappa)}$ and then the next iterative point $\theta^{(\kappa+1)}$ is generated with $\boldsymbol{w}$ held fixed at $w^{(\kappa+1)}$.

Beamforming descent iteration

To generate $w^{(\kappa+1)}$ we do not solve (5.11) but we seek $w^{(\kappa+1)}$ such that $f(\theta^{(\kappa)}, w^{(\kappa+1)}) > f(\theta^{(\kappa)}, w^{(\kappa)})$.

Using the inequality (A.21) in the appendix A yields

$$\begin{aligned}\rho_k(\theta^{(\kappa)}, \boldsymbol{w}) &\geq \rho_k^{(\kappa)}(\boldsymbol{w}) \\ &\triangleq 2\Re\{b_k^{(\kappa)}\boldsymbol{w}_k\} - c_k^{(\kappa)} \sum_{j\in\mathcal{K}\setminus\{k\}} |\mathcal{H}_k(\theta^{(\kappa)})\boldsymbol{w}_j|^2 - \sigma c_k^{(\kappa)},\end{aligned} \tag{5.21}$$

with

$$b_k^{(\kappa)} \triangleq \frac{(w_k^{(\kappa)})^H(\mathcal{H}_k(\theta^{(\kappa)}))^H\mathcal{H}_k(\theta^{(\kappa)})}{y_k^{(\kappa)}},\ 0 < c_k^{(\kappa)} \triangleq \frac{|\mathcal{H}_k(\theta^{(\kappa)})w_k^{(\kappa)}|^2}{(y_k^{(\kappa)})^2},$$
$$0 < y_k^{(\kappa)} \triangleq \sum_{j\in\mathcal{K}\setminus\{k\}} |\mathcal{H}_k(\theta^{(\kappa)})w_j^{(\kappa)}|^2 + \sigma.$$

The function $\rho_k^{(\kappa)}(\boldsymbol{w})$ is seen quadratic concave, which matches with $\rho_k(\theta^{(\kappa)}, \boldsymbol{w})$ at $w^{(\kappa)}$. The computational complexity of the problem is $\mathcal{O}\left((MK)^3\right)$ [98, p. 4]. To generate $w^{(\kappa+1)}$ at the κ-th iteration, we solve :

$$\max_{\boldsymbol{w}}\ f^{(\kappa)}(\boldsymbol{w}) \triangleq \min_{k=1,\ldots,K}\ \rho_k^{(\kappa)}(\boldsymbol{w}) \quad \text{s.t.} \quad (5.8b), \tag{5.22}$$

where $f^{(\kappa)}$ is concave [30]. Note that

$$f^{(\kappa)}(w^{(\kappa+1)}) > f^{(\kappa)}(w^{(\kappa)})$$

if $w^{(\kappa+1)} \neq w^{(\kappa)}$. Therefore,

$$f(\theta^{(\kappa)}, w^{(\kappa+1)}) \geq f^{(\kappa)}(w^{(\kappa+1)}) > f^{(\kappa)}(w^{(\kappa)}) = f(\theta^{(\kappa)}, w^{(\kappa)}). \tag{5.23}$$

Phase descent iteration

We seek the next iterative point $\theta^{(\kappa+1)}$ such that $g(\theta^{(\kappa+1)}, w^{(\kappa+1)}) > g(\theta^{(\kappa)}, w^{(\kappa+1)})$.

Using the inequality (A.21) in the appendix A yields

$$\begin{aligned}\rho_k(\boldsymbol{\theta}, w^{(\kappa+1)}) &\geq \tilde{\rho}_k^{(\kappa)}(\boldsymbol{\theta}) \\ &\triangleq 2\Re\{\tilde{b}_k^{(\kappa)}\mathcal{H}_k(\boldsymbol{\theta})w_k^{(\kappa+1)}\} - \tilde{c}_k^{(\kappa)}\sum_{j\in\mathcal{K}\setminus\{k\}}|\mathcal{H}_k(\boldsymbol{\theta})w_j^{(\kappa+1)}|^2 - \sigma\tilde{c}_k^{(\kappa)} \quad (5.24)\end{aligned}$$

with

$$\tilde{b}_k^{(\kappa)} \triangleq \frac{(w_k^{(\kappa+1)})^H(\mathcal{H}_k(\theta^{(\kappa)}))^H}{y_k^{(\kappa+1)}},\ 0 < \tilde{c}_k^{(\kappa)} \triangleq \frac{|\mathcal{H}_k(\theta^{(\kappa)})w_k^{(\kappa+1)}|^2}{(y_k^{(\kappa+1)})^2},$$
$$0 < y_k^{(\kappa+1)} \triangleq \sum_{j\in\mathcal{K}\setminus\{k\}}|\mathcal{H}_k(\theta^{(\kappa)})w_j^{(\kappa+1)}|^2 + \sigma,$$

and

$$\frac{1}{\sum_{n=1}^N|\theta_n|^2} \leq \iota^{(\kappa)}(\boldsymbol{\theta}) \triangleq \frac{1}{\sum_{n=1}^N(2\Re\{(\theta_n^{(\kappa)})^*\theta_n\} - |\theta_n^{(\kappa)}|^2)} \quad (5.25)$$

over the trust region

$$\sum_{n=1}^N(2\Re\{(\theta_n^{(\kappa)})^*\theta_n\} - |\theta_n^{(\kappa)}|^2) > 0. \quad (5.26)$$

The computational complexity of the optimization problem is $\mathcal{O}\left((N)^3(N+1)\right)$ [98, p. 4]. To generate $\theta^{(\kappa+1)}$ at the κ-th iteration, we solve:

$$\max_{\boldsymbol{\theta}}\ g^{(\kappa)}(\boldsymbol{\theta}) \triangleq \left[\min_{k=1,\ldots,K}\ \tilde{\rho}_k^{(\kappa)}(\boldsymbol{\theta}) + \mu\left(\frac{1}{N} - \iota^{(\kappa)}(\boldsymbol{\theta})\right)\right] \quad \text{s.t.} \quad (5.10), (5.26), \quad (5.27)$$

which is convex because its objective function is concave. Note that $g(\boldsymbol{\theta}, w^{(\kappa+1)}) \geq g^{(\kappa)}(\boldsymbol{\theta})$, and $g(\theta^{(\kappa)}, w^{(\kappa+1)}) = g^{(\kappa)}(\theta^{(\kappa)})$, so, by using a similar argument to that for proving (5.53), we can show that

$$g(\theta^{(\kappa+1)}, w^{(\kappa+1)}) > g(\theta^{(\kappa)}, w^{(\kappa+1)}), \quad (5.28)$$

as far as $\theta^{(\kappa+1)} \neq \theta^{(\kappa)}$.

Convergence

It follows from (5.24) and (5.28) that

$$g(\theta^{(\kappa+1)}, w^{(\kappa+1)}) > g(\theta^{(\kappa)}, w^{(\kappa)}), \tag{5.29}$$

and as such the sequence $\{(\theta^{(\kappa)}, w^{(\kappa)})\}$ converges to a point $(\bar{\theta}, \bar{w})$ such that $\bar{\theta}$ ($\bar{w}$, resp.) is a locally optimal solution of (5.20) with $\boldsymbol{w}$ ($\boldsymbol{\theta}$, resp.) held fixed at $\bar{w}$ ($\bar{\theta}$, resp.).

5.2.2 Path-following iteration

Using the inequality (A.20) in the appendix A yields

$$\rho_k(\boldsymbol{\theta}, \boldsymbol{w}) \geq a_k^{(\kappa)} - \frac{b_k^{(\kappa)}}{|\mathcal{H}_k(\boldsymbol{\theta})\boldsymbol{w}_k|^2} - c_k^{(\kappa)} \sum_{j \in \mathcal{K}\setminus\{k\}} |\mathcal{H}_k(\boldsymbol{\theta})\boldsymbol{w}_j|^2 \tag{5.30}$$

where

$$a_k^{(\kappa)} \triangleq \frac{3|\mathcal{H}_k(\theta^{(\kappa)})w_k^{(\kappa)}|^2}{y_k^{(\kappa)}}, 0 < b_k^{(\kappa)} \triangleq \frac{|\mathcal{H}_k(\theta^{(\kappa)})w_k^{(\kappa)}|^4}{y_k^{(\kappa)}}, 0 < c_k^{(\kappa)} \triangleq \frac{|\mathcal{H}_k(\theta^{(\kappa)})w_k^{(\kappa)}|^2}{(y_k^{(\kappa)})^2}$$
$$0 < y_k^{(\kappa)} \triangleq \sum_{j \in \mathcal{K}\setminus\{k\}} |\mathcal{H}_k(\theta^{(\kappa)})w_j^{(\kappa)}|^2 + \sigma.$$

We have

$$\sum_{j \in \mathcal{K}\setminus\{k\}} |\mathcal{H}_k(\boldsymbol{\theta})\boldsymbol{w}_j|^2 = \langle [\mathcal{H}_k^H(\boldsymbol{\theta})]^2, \sum_{j \in \mathcal{K}\setminus\{k\}} [\boldsymbol{w}_j]^2 \rangle \leq \langle \mathbf{X}_k, \sum_{j \in \mathcal{K}\setminus\{k\}} \mathbf{Y}_j \rangle, \tag{5.31}$$

for the Hermitian symmetric matrix variables $\mathbf{X}_k$, $k \in \mathcal{K}$ and $\mathbf{Y}_j$, $j \in \mathcal{K}$ of size $M \times M$ satisfying the semi-definite (convex) constraints

$$\mathbf{X}_k \succeq [\mathcal{H}_k^H(\boldsymbol{\theta})]^2 \Leftrightarrow \begin{bmatrix} \mathbf{X}_k & \mathcal{H}_k^H(\boldsymbol{\theta}) \\ \mathcal{H}_k(\boldsymbol{\theta}) & 1 \end{bmatrix} \succeq 0, \tag{5.32}$$

$$\mathbf{Y}_j \succeq [\boldsymbol{w}_j]^2, j \in \mathcal{K} \Leftrightarrow \begin{bmatrix} \mathbf{Y}_j & \boldsymbol{w}_j \\ \boldsymbol{w}_j^H & 1 \end{bmatrix} \succeq 0. \tag{5.33}$$

For $X_k^{(\kappa)}(t) \triangleq [\mathcal{H}_k^H(\theta^{(\kappa)})]^2 + tI_M$, and $Y_k^{(\kappa)}(t) = [w_k^{(\kappa)}]^2 + tI_M$, while $Y_{\backslash k}^{(\kappa)}(t) \triangleq \sum_{j\in\mathcal{K}\backslash\{k\}}[w_j^{(\kappa)}]^2 + tI_M$, for $k \in \mathcal{K}$, using the inequality (A.19) in the appendix A yields

$$\begin{aligned}
\langle \mathbf{X}_k, \sum_{j\in\mathcal{K}\backslash\{k\}} \mathbf{Y}_j\rangle &= \langle \mathbf{X}_k + \epsilon I_M, \sum_{j\in\mathcal{K}\backslash\{k\}} \mathbf{Y}_j + \epsilon I_M\rangle - \epsilon\langle \mathbf{X}_k + \sum_{j\in\mathcal{K}\backslash\{k\}} \mathbf{Y}_j\rangle - \epsilon^2 M \\
&\leq \frac{1}{2}\Big[||\left(X_k^{(\kappa)}(\epsilon)\right)^{-1/2}(\mathbf{X}_k + \epsilon I_M)\left(Y_{\backslash k}^{(\kappa)}(\epsilon)\right)^{1/2}||^2 \\
&\quad +||\left(X_k^{(\kappa)}(\epsilon)\right)^{1/2}\left(\sum_{j\in\mathcal{K}\backslash\{k\}} \mathbf{Y}_j + \epsilon I_M\right)\left(Y_{\backslash k}^{(\kappa)}(\epsilon)\right)^{-1/2}||^2\Big] \\
&\quad -\epsilon\langle \mathbf{X}_k + \sum_{j\in\mathcal{K}\backslash\{k\}} \mathbf{Y}_j\rangle - \epsilon^2 M \\
&\triangleq g_k^{(\kappa)}(\boldsymbol{w}, \mathbf{X}_k, \mathbf{Y}),
\end{aligned} \tag{5.34}$$

for $\mathbf{X} \triangleq \{\mathbf{X}_k, k \in \mathcal{K}\}$ and $\mathbf{Y} \triangleq \{\mathbf{Y}_j, j \in \mathcal{K}\}$, and $\epsilon > 0$.

Next, in the appendix B, we show that the nonconvex constraint

$$|\mathcal{H}_k(\boldsymbol{\theta})\boldsymbol{w}_k|^2 \geq \mathbf{z}_k, \tag{5.35}$$

is innerly approximated by the semi-definite constraint

$$\begin{bmatrix} \left(\mathcal{H}_k(\theta^{(\kappa)})Y_k^{(\kappa)}(\eta)\mathcal{H}_k^H(\boldsymbol{\theta}) + (*)^H\right) - \mathbf{z}_k - \eta\langle \mathbf{X}_k\rangle & * \\ Y_k^{(\kappa)}(\eta)\mathcal{H}_k^H(\theta^{(\kappa)}) & [w_k^{(\kappa)}(\boldsymbol{w}_k)^H + (*)^H] - [w_k^{(\kappa)}]^2 + \eta I_M \end{bmatrix} \succeq 0 \tag{5.36}$$

for $\eta > 0$, i.e. each feasible point for (5.36) is also feasible for (5.35).

It follows from (5.30), (5.34) and (5.36) that

$$\rho_k(\boldsymbol{\theta}, \boldsymbol{w}) \geq \rho_k^{(\kappa)}(\boldsymbol{\theta}, \boldsymbol{w}, \mathbf{z}_k, \mathbf{X}_k, \mathbf{Y}) \triangleq a_k^{(\kappa)} - \frac{b_k^{(\kappa)}}{\mathbf{z}_k} - c^{(\kappa)} g_k^{(\kappa)}(\boldsymbol{w}, \mathbf{X}_k, \mathbf{Y}). \tag{5.37}$$

for the scalar variable $\mathbf{z}_k$ satisfying the semi-definite constraint (5.36) and the linear constraint

$$\mathbf{z}_k > 0. \tag{5.38}$$

For $g_p^{(\kappa)}(\boldsymbol{\theta}, \boldsymbol{w}, \mathbf{z}, \mathbf{X}, \mathbf{Y}) \triangleq \min_{k=1,\ldots,K} \rho_k^{(\kappa)}(\boldsymbol{\theta}, \boldsymbol{w}, \mathbf{z}_k, \mathbf{X}_k, \mathbf{Y}) + \mu\left(\frac{1}{N} - \iota^{(\kappa)}(\boldsymbol{\theta})\right)$, at the κ-th iteration we solve the following convex problem of computational complexity $\mathcal{O}((2KM^2 + KM + K$

$+N)^3(4K+N+2))$ [98, p. 4] to generate $(\theta^{(\kappa+1)}, w^{(\kappa+1)}, z^{(\kappa+1)}, X^{(\kappa+1)}, Y^{(\kappa+1)})$:

$$\max_{\boldsymbol{\theta},\boldsymbol{w},\mathbf{z},\mathbf{X},\mathbf{Y}} g_p^{(\kappa)}(\boldsymbol{\theta},\boldsymbol{w},\mathbf{z},\mathbf{X},\mathbf{Y}) \quad \text{s.t.} \quad (5.8b),(5.10),(5.26),(5.32),(5.33),(5.38),(5.36)(5.39)$$

For $z_k^{(\kappa)} = [w_k^{(\kappa)}]^2$ and $z^{(\kappa)} = \{z_k^{(\kappa)}, k \in \mathcal{K}\}$, it is true that

$$g_p^{(\kappa)}(\theta^{(\kappa+1)}, w^{(\kappa+1)}, z^{(\kappa+1)}, X^{(\kappa+1)}, Y^{(\kappa+1)}) > g_p^{(\kappa)}(\theta^{(\kappa)}, w^{(\kappa)}, z^{(\kappa)}, X^{(\kappa)}, Y^{(\kappa)})$$

because $(\theta^{(\kappa+1)}, w^{(\kappa+1)}, z^{(\kappa+1)}, X^{(\kappa+1)}, Y^{(\kappa+1)})$ and $(\theta^{(\kappa)}, w^{(\kappa)}, z^{(\kappa)}, X^{(\kappa)}, Y^{(\kappa)})$ are respectively the optimal solution and a feasible point for (5.39). Also, under (5.26), (5.32), (5.33), (5.38), (5.36), $g(\boldsymbol{\theta},\boldsymbol{w}) \geq g_p^{(\kappa)}(\boldsymbol{\theta},\boldsymbol{w},\mathbf{z},\mathbf{X},\mathbf{Y})$, and $g(\theta^{(\kappa)}, w^{(\kappa)}) = g_p^{(\kappa)}(\theta^{(\kappa)}, w^{(\kappa)}, z^{(\kappa)}, X^{(\kappa)}, Y^{(\kappa)})$. Therefore, like (5.24), it is easy to show (5.29) but the sequence $\{(\theta^{(\kappa)}, w^{(\kappa)})\}$ of improved feasible points for the nonconvex problem (5.7) converges at least to a locally optimal solution of (5.7) [71].

5.2.3 Initialization and penalty parameter

We address the following optimization problem

$$\max_{\boldsymbol{\theta},\boldsymbol{w}} \ f(\boldsymbol{\theta},\boldsymbol{w}) \quad \text{s.t.} \quad (5.10),(5.8b) \tag{5.40}$$

by Algorithm 6, which is based on the above described alternating descent iterations.

Suppose that $(w^{(0)}, \theta^{(0)})$ is the found solution of (5.40) with the optimal value $\gamma^{(0)}$. Then determine μ by

$$\mu = \frac{\gamma^{(0)}}{\frac{1}{\sum_{n=1}^{N}|\theta_n^{(0)}|^2} - \frac{1}{N}}. \tag{5.41}$$

to make the values of the objective function and penalty term in (5.20) of similar magnitudes [127].

Algorithm 6 PGS initializing algorithm

1: **Initialization:** Randomly generate $(\theta^{(0)}, w^{(0)})$ satisfying the convex constraints (5.8b) and (5.47b). Set $\kappa = 0$.
2: **Repeat until convergence of the objective in** (5.40)**:** Solve the convex problem (5.22) to generate $w^{(\kappa+1)}$ and then solve the convex problem $\max_{\boldsymbol{\theta}} \min_{k=1,\ldots,K} \tilde{\rho}_k^{(\kappa)}(\boldsymbol{\theta})$ s.t. (5.10) to generate $\theta^{(\kappa+1)}$. Reset $\kappa := \kappa + 1$.
3: **Output** $(w^{(\kappa)}, \theta^{(\kappa)})$ and reset $(w^{(0)}, \theta^{(0)}) \leftarrow (w^{(\kappa)}, \theta^{(\kappa)})$.

5.2.4 Two-phase Algorithm

Observe from (5.22) and (5.27) for the proposed alternating descent procedure and (5.39) for the proposed path-following procedure that the latter is much more computationally costly than the latter. Therefore, we propose Algorithm 7 to exploit the computational efficiency of the alternating descent procedure and the solution optimality of the path-following procedure.

Algorithm 7 Two-phase PGS algorithm

1: **Alternating descent phase: repeat until** (5.20) **is reached:** Generate $w^{(\kappa+1)}$ by solving the convex problem (5.22) and then generate $\theta^{(\kappa+1)}$ by solving the convex problem (5.27); Reset $\kappa := \kappa + 1$.
2: **Path-following phase: repeat until** (5.20) **is reached:** Generate $(w^{(\kappa+1)}, \theta^{(\kappa+1)})$ by solving the convex problem (5.39); Reset $\kappa := \kappa + 1$.
3: **Output** $(w^{(\kappa)}, \theta^{(\kappa)})$.

5.3 Improper Gaussian signaling

In (5.3), the proper Gaussian sources s_k are linearly beamformed by the beamformer $\boldsymbol{w}_k$ so the transmit signal x is proper Gaussian too. In this section, the proper Gaussian sources s_k are widely linearly beamformed by a pair of two beamformers $\boldsymbol{w}_{1,k} \in \mathbb{C}^M$ and $\boldsymbol{w}_{2,k} \in \mathbb{C}^M$ as [75]

$$\begin{bmatrix} \boldsymbol{w}_{1,k} & \boldsymbol{w}_{2,k} \end{bmatrix} \begin{bmatrix} s_k \\ s_k^* \end{bmatrix}, \tag{5.42}$$

making the transmit signal

$$x = \sum_{k=1}^{K} (\boldsymbol{w}_{1,k} s_k + \boldsymbol{w}_{2,k} s_k^*), \tag{5.43}$$

improper Gaussian. The equation (5.1) is written by

$$y_k = \mathcal{H}_k(\boldsymbol{\theta}) \sum_{k=1}^{K} (\boldsymbol{w}_{1,k} s_k + \boldsymbol{w}_{2,k} s_k^*) + n_k. \tag{5.44}$$

Write the augmented equation for (5.44) as

$$\begin{aligned}\begin{bmatrix} y_k \\ y_k^* \end{bmatrix} &= \begin{bmatrix} \mathcal{H}(\boldsymbol{\theta}) & 0 \\ 0 & \mathcal{H}^*(\boldsymbol{\theta}) \end{bmatrix} \sum_{k=1}^{K} \begin{bmatrix} \boldsymbol{w}_{1,k} & \boldsymbol{w}_{2,k} \\ \boldsymbol{w}_{2,k}^* & \boldsymbol{w}_{1,k}^* \end{bmatrix} \begin{bmatrix} s_k \\ s_k^* \end{bmatrix} + \begin{bmatrix} n_k \\ n_k^* \end{bmatrix} \\ &= \Lambda_k(\boldsymbol{\theta}) \sum_{k=1}^{K} \mathbf{W}_k \bar{s}_k + \bar{n}_k, \end{aligned} \tag{5.45}$$

for $\Lambda_k(\boldsymbol{\theta}) \triangleq \begin{bmatrix} \mathcal{H}_k(\boldsymbol{\theta}) & 0 \\ 0 & \mathcal{H}_k^*(\boldsymbol{\theta}) \end{bmatrix} \in \mathbb{C}^{2\times(2M)}$, and $\mathbf{W}_k \triangleq \begin{bmatrix} \boldsymbol{w}_{1,k} & \boldsymbol{w}_{2,k} \\ \boldsymbol{w}_{2,k}^* & \boldsymbol{w}_{1,k}^* \end{bmatrix} \in \mathbb{C}^{2M\times 2}$, which are linear mappings, and $\bar{s}_k \triangleq \begin{bmatrix} s_k \\ s_k^* \end{bmatrix} \in \mathbb{C}^2$, $\bar{n}_k \triangleq \begin{bmatrix} n_k \\ n_k^* \end{bmatrix} \in \mathbb{C}^2$.

For $\boldsymbol{w} \triangleq \{(\boldsymbol{w}_{1,k}, \boldsymbol{w}_{2,k}) \;\; k \in \mathcal{K}\}$, the rate at UE k is calculated by $(1/2)r_k(\boldsymbol{\theta}, \boldsymbol{w})$ [74] with

$$r_k(\boldsymbol{\theta}, \boldsymbol{w}) = \ln \left| I_2 + [\Lambda_k(\boldsymbol{\theta})\mathbf{W}_k]^2 \left(\sum_{j\in\mathcal{K}\setminus\{k\}} [\Lambda_k(\boldsymbol{\theta})\mathbf{W}_j]^2 + \sigma I_2 \right)^{-1} \right| \tag{5.46}$$

For the particular class $\boldsymbol{w}_{2,k} \equiv 0$, i.e. x in (5.43) is proper Gaussian, a straight calculation yields

$$r_k(\boldsymbol{\theta}, \boldsymbol{w}) = 2\ln \left(1 + |\mathcal{H}_k(\boldsymbol{\theta})\boldsymbol{w}_{1,k}|^2 \left(\sum_{j\in\mathcal{K}\setminus\{k\}} |\mathcal{H}_k(\boldsymbol{\theta})\boldsymbol{w}_{1,j}|^2 + \sigma \right)^{-1} \right),$$

so $(1/2)r_k(\boldsymbol{\theta}, \boldsymbol{w})$ is the known PGS rate (5.7).

Given a power budget P, the max-min rate optimization problem under IGS is thus formulated as

$$\max_{\boldsymbol{\theta},\boldsymbol{w}} \; \min_{k=1,\ldots,K} \; \frac{1}{2} r_k(\boldsymbol{\theta}, \boldsymbol{w}) \quad \text{s.t.} \quad (5.2), \tag{5.47a}$$

$$\sum_{k=1}^{K} (||\boldsymbol{w}_{1,k}||^2 + ||\boldsymbol{w}_{2,k}||^2) \le P, \tag{5.47b}$$

which is equivalent to

$$\max_{\boldsymbol{\theta},\boldsymbol{w}} \; \Phi(\boldsymbol{\theta}, \boldsymbol{w}) \triangleq \min_{k=1,\ldots,K} \; r_k(\boldsymbol{\theta}, \boldsymbol{w}) \quad \text{s.t.} \quad (5.2), (5.47b). \tag{5.48}$$

Like (5.20), we address (5.48) via its exact penalized problem

$$\max_{\boldsymbol{\theta},\boldsymbol{w}} \; \Psi(\boldsymbol{\theta}, \boldsymbol{w}) \triangleq \left[\Phi(\boldsymbol{\theta}, \boldsymbol{w}) + \mu \left(\frac{1}{N} - \frac{1}{\sum_{n=1}^{N} |\theta_n|^2} \right) \right] \quad \text{s.t.} \quad (5.10), (5.47b), \tag{5.49}$$

where $\mu > 0$ is the penalty parameter. Unlike its PGS counterpart (5.20), which involves a single beamformer for each user, the problem (5.49) involves a pairs of correlated beamformers $\boldsymbol{w}_{1,k}$ and $\boldsymbol{w}_{2,k}$. More importantly, the problem (5.49) is an log-determinant function optimization and thus is much more computationally challenging than its PGS counterpart (5.20) of fractional function optimization. Particularly, the Algorithms 6 and 7 for PGS cannot be extended for the case of IGS. Nevertheless, we are still able to propose alternating descent and path-following iterations tailored for its computation.

5.3.1 Alternating descent round

Beamforming descent iteration

We seek $w^{(\kappa+1)}$ such that $\Phi(\theta^{(\kappa)}, w^{(\kappa+1)}) > \Phi(\theta^{(\kappa)}, w^{(\kappa)})$.

By using the inequality (A.15) in the appendix A, we obtain a concave quadratic lower bounding function approximation of $r_k(\theta^{(\kappa)}, \boldsymbol{w})$ as

$$r_k(\theta^{(\kappa)}, \boldsymbol{w}) \;\; \geq \;\; r_k^{(\kappa)}(\boldsymbol{w}) \triangleq a_k^{(\kappa)} + 2\Re\{\langle B_k^{(\kappa)} \mathbf{W}_k \rangle\} - \langle C_k^{(\kappa)}, \sum_{j \in \mathcal{K}} [\Lambda_k(\theta^{(\kappa)}) \mathbf{W}_j]^2 \rangle, \quad (5.50)$$

with

$$\begin{aligned} a_k^{(\kappa)} &\triangleq r_k(\theta^{(\kappa)}, w^{(\kappa)}) - \langle [\Lambda_k(\theta^{(\kappa)}) W_k^{(\kappa)}]^2 (Y_k^{(\kappa)})^{-1} \rangle - \sigma \langle C_k^{(\kappa)} \rangle, \\ B_k^{(\kappa)} &\triangleq (W_k^{(\kappa)})^H (\Lambda_k(\theta^{(\kappa)}))^H (Y_k^{(\kappa)})^{-1} \Lambda_k(\theta^{(\kappa)}), \\ 0 \prec C_k^{(\kappa)} &\triangleq (Y_k^{(\kappa)})^{-1} - \left(Y_k^{(\kappa)} + [\Lambda_k(\theta^{(\kappa)}) W_k^{(\kappa)}]^2 \right)^{-1}, \\ 0 \prec Y_k^{(\kappa)} &\triangleq \textstyle\sum_{j \in \mathcal{K} \setminus \{k\}} [\Lambda_k(\theta^{(\kappa)}) W_j^{(\kappa)}]^2 + \sigma I_2. \end{aligned}$$

The computational complexity of the optimization problem is$\mathcal{O}\left((2MK)^3\right)$ [98, p. 4]. To generate $w^{(\kappa+1)}$, we solve the following convex problem of at the κ-th iteration:

$$\max_{\boldsymbol{w}} \; \min_{k=1,\ldots,K} \; r_k^{(\kappa)}(\boldsymbol{w}) \quad \text{s.t.} \quad (5.47b), \quad (5.51)$$

which like (5.22) gives

$$\Phi(\theta^{(\kappa)}, w^{(\kappa+1)}) > \Phi(\theta^{(\kappa)}, w^{(\kappa)}) \quad (5.52)$$

as far as $w^{(\kappa+1)} \neq w^{(\kappa)}$.

Phase descent iteration

We seek $w^{(\kappa+1)}$ such that $\Psi(\theta^{(\kappa+1)}, w^{(\kappa+1)}) > \Psi(\theta^{(\kappa)}, w^{(\kappa+1)})$.

By using the inequality (A.15) in the appendix A, we obtain a concave quadratic lower bounding function approximation of $r_k(\boldsymbol{\theta}, w^{(\kappa+1)})$ as

$$\begin{aligned} r_k(\boldsymbol{\theta}, w^{(\kappa+1)}) &\geq \tilde{r}_k^{(\kappa)}(\boldsymbol{\theta}) \\ &\triangleq \tilde{a}_k^{(\kappa)} + 2\Re\{\langle \tilde{B}_k^{(\kappa)} \Lambda_k(\boldsymbol{\theta}) W_k^{(\kappa+1)} \rangle\} - \langle \tilde{C}_k^{(\kappa)}, \sum_{j\in\mathcal{K}} [\Lambda_k(\boldsymbol{\theta}) W_j^{(\kappa+1)}]^2 \rangle \quad (5.53) \end{aligned}$$

with

$$\begin{gathered} \tilde{a}_{\triangleq}^{(\kappa)} r_k(\theta^{(\kappa)}, w^{(\kappa+1)}) - \langle [\Lambda_k(\theta^{(\kappa)}) W_k^{(\kappa+1)}]^2 (Y_k^{(\kappa+1)})^{-1} \rangle - \sigma \langle \tilde{C}_k^{(\kappa)} \rangle, \\ \tilde{B}_k^{(\kappa)} \triangleq (W_k^{(\kappa+1)})^H (\Lambda_k(\theta^{(\kappa)}))^H (Y_k^{(\kappa+1)})^{-1}, \\ 0 \prec \tilde{C}_k^{(\kappa)} \triangleq (Y_k^{(\kappa+1)})^{-1} - \left(Y_k^{(\kappa+1)} + [\Lambda_k(\theta^{(\kappa)}) W_k^{(\kappa+1)}]^2 \right)^{-1}, \\ 0 \prec Y_k^{(\kappa+1)} \triangleq \textstyle\sum_{j\in\mathcal{K}\setminus\{k\}} [\Lambda_k(\theta^{(\kappa)}) W_j^{(\kappa+1)}]^2 + \sigma I_2. \end{gathered}$$

Accordingly, we solve the following convex problem has the computational complexity of $\mathcal{O}\left(N^3(N+1)\right)$ [98, p. 4]. To generate $\theta^{(\kappa+1)}$ at the κ-th iteration we solve:

$$\max_{\boldsymbol{\theta}} \left[\min_{k=1,\ldots,K} \tilde{r}_k^{(\kappa)}(\boldsymbol{\theta}) + \mu \left(\frac{1}{N} - \iota^{(\kappa)}(\boldsymbol{\theta}) \right) \right] \quad \text{s.t.} \quad (5.10), (5.26), \tag{5.54}$$

where $\iota^{(\kappa)}(\boldsymbol{\theta})$ is recalled from (5.25).

Like (5.28), we can easily show that

$$\Psi(\theta^{(\kappa+1)}, w^{(\kappa+1)}) > \Psi(\theta^{(\kappa)}, w^{(\kappa+1)}), \tag{5.55}$$

as far as $\theta^{(\kappa+1)} \neq \theta^{(\kappa)}$.

5.3.2 Path-following round

Decompose $r_k(\boldsymbol{\theta}, \boldsymbol{w}) = \psi_k(\boldsymbol{\theta}, \boldsymbol{w}) + \varphi_k(\boldsymbol{\theta}, \boldsymbol{w})$, for $\psi_k(\boldsymbol{\theta}, \boldsymbol{w}) \triangleq \ln \left| [\Lambda_k(\boldsymbol{\theta}) \mathbf{W}_k]^2 \right|$, and

$$\varphi_k(\boldsymbol{\theta}, \boldsymbol{w}) \triangleq \ln \left| [\Lambda_k(\boldsymbol{\theta}) \mathbf{W}_k]^{-2} + \left(\sum_{j\in\mathcal{K}\setminus\{k\}} [\Lambda_k(\boldsymbol{\theta}) \mathbf{W}_j]^2 + \sigma I_2 \right)^{-1} \right|.$$

Using the inequalities (A.17) in the appendix A yields

$$\begin{aligned}\varphi_k(\boldsymbol{\theta},\boldsymbol{w}) &\geq a_k^{(\kappa)} - \langle B_k^{(\kappa)}, [\Lambda_k(\boldsymbol{\theta})\mathbf{W}_k]^2\rangle - \langle C_k^{(\kappa)}, \sum_{j\in\mathcal{K}\setminus\{k\}} [\Lambda_k(\boldsymbol{\theta})\mathbf{W}_j]^2\rangle \\ &= a_k^{(\kappa)} - \langle \Lambda_k^H(\boldsymbol{\theta}) B_k^{(\kappa)} \Lambda_k(\boldsymbol{\theta}), [\mathbf{W}_k]^2\rangle - \langle \Lambda_k^H(\boldsymbol{\theta}) C_k^{(\kappa)} \Lambda_k(\boldsymbol{\theta}), \sum_{j\in\mathcal{K}\setminus\{k\}} [\mathbf{W}_j]^2\rangle \\ &\geq a_k^{(\kappa)} - \langle \mathbf{X}_{1k}, \mathbf{Y}_k\rangle - \langle \mathbf{X}_{2,k}, \sum_{j\in\mathcal{K}\setminus\{k\}} \mathbf{Y}_j\rangle \end{aligned} \tag{5.56}$$

for the newly introduced Hermitian symmetric matrix variables $\mathbf{X}_{1,k}$ and $\mathbf{X}_{2,k}$, $k \in \mathcal{K}$ and $\mathbf{Y}_j$, $j \in \mathcal{K}$ of size $(2M) \times (2M)$ satisfying the semi-definite constraints

$$\mathbf{X}_{1,k} \succeq \Lambda_k^H(\boldsymbol{\theta}) B_k^{(\kappa)} \Lambda_k(\boldsymbol{\theta}) \Leftrightarrow \begin{bmatrix} \mathbf{X}_{1,k} & \Lambda_k^H(\boldsymbol{\theta})(B_k^{(\kappa)})^{1/2} \\ (B_k^{(\kappa)})^{1/2}\Lambda_k(\boldsymbol{\theta}) & I_2 \end{bmatrix} \succeq 0, \tag{5.57}$$

and

$$\mathbf{X}_{2,k} \succeq \Lambda_k^H(\boldsymbol{\theta}) C_k^{(\kappa)} \Lambda_k(\boldsymbol{\theta}) \Leftrightarrow \begin{bmatrix} \mathbf{X}_{2,k} & \Lambda_k^H(\boldsymbol{\theta})(C_k^{(\kappa)})^{1/2} \\ (C_k^{(\kappa)})^{1/2}\Lambda_k(\boldsymbol{\theta}) & I_2 \end{bmatrix} \succeq 0, \tag{5.58}$$

and

$$\mathbf{Y}_j \succeq [\mathbf{W}_j]^2, \Leftrightarrow \begin{bmatrix} \mathbf{Y}_j & \mathbf{W}_j \\ \mathbf{W}_j^H & I_2 \end{bmatrix} \succeq 0, \tag{5.59}$$

under the definitions

$$\begin{aligned} a_k^{(\kappa)} &\triangleq \varphi_k(\theta^{(\kappa)}, w^{(\kappa)}) + 2 - \sigma\langle C_{kj}^{(\kappa)}\rangle \quad (j \neq k), \\ 0 \preceq B_k^{(\kappa)} &\triangleq \left([\Lambda_k(\theta^{(\kappa)})W_k^{(\kappa)}]^2\right)^{-1} - \left(\sum_{j\in\mathcal{K}} [\Lambda_k(\theta^{(\kappa)})W_j^{(\kappa)}]^2 + \sigma I_2\right)^{-1}, \\ 0 \preceq C_k^{(\kappa)} &\triangleq \left(\sum_{j\in\mathcal{K}\setminus\{k\}} [\Lambda_k(\theta^{(\kappa)})W_j^{(\kappa)}]^2 + \sigma I_2\right)^{-1} - \left(\sum_{j\in\mathcal{K}} [\Lambda_k(\theta^{(\kappa)})W_j^{(\kappa)}]^2 + \sigma I_2\right)^{-1}, \end{aligned}$$

and $X_{1,k}^{(\kappa)} \triangleq \Lambda_k^H(\theta^{(\kappa)}) B_k^{(\kappa)} \Lambda_k(\theta^{(\kappa)})$, and $X_{2,k}^{(\kappa)} \triangleq \Lambda_k^H(\theta^{(\kappa)}) C_k^{(\kappa)} \Lambda_k(\theta^{(\kappa)})$.

Furthermore, using the inequality (A.19) in the appendix A yields

$$\begin{aligned}
\text{RHS of (5.56)} &= a_k^{(\kappa)} - \langle \mathbf{X}_{1k} + \epsilon I_{2M}, \mathbf{Y}_k + \epsilon I_{2M} \rangle - \langle \mathbf{X}_{2,k} + \epsilon I_{2M}, \sum_{j \in \mathcal{K} \setminus \{k\}} \mathbf{Y}_j + \epsilon I_{2M} \rangle \\
&\quad + \epsilon \sum_{j \in \mathcal{K}} \langle \mathbf{Y}_j \rangle + \epsilon \langle \mathbf{X}_{1k} + \mathbf{X}_{2k} \rangle + 2M\epsilon^2 \\
&\geq a_k^{(\kappa)} - \frac{1}{2} || \left(X_{1,k}^{(\kappa)}(\epsilon) \right)^{-1/2} (\mathbf{X}_{1k} + \epsilon I_{2M}) \left(Y_k^{(\kappa)}(\epsilon) \right)^{1/2} ||^2 \\
&\quad - \frac{1}{2} || \left(X_{1,k}^{(\kappa)}(\epsilon) \right)^{1/2} (\mathbf{Y}_k + \epsilon I_{2M}) \left(Y_k^{(\kappa)}(\epsilon) \right)^{-1/2} ||^2 \\
&\quad - \frac{1}{2} || \left(X_{2,k}^{(\kappa)}(\epsilon) \right)^{-1/2} (\mathbf{X}_{2,k} + \epsilon I_{2M}) \left(Y_{\setminus k}^{(\kappa)}(\epsilon) \right)^{1/2} ||^2 \\
&\quad - \frac{1}{2} || \left(X_{2,k}^{(\kappa)}(\epsilon) \right)^{1/2} \left(\sum_{j \in \mathcal{K} \setminus \{k\}} \mathbf{Y}_j + \epsilon I_{2M} \right) \left(Y_{\setminus k}^{(\kappa)}(\epsilon) \right)^{-1/2} ||^2 \\
&\quad + \epsilon \sum_{j \in \mathcal{K}} \langle \mathbf{Y}_j \rangle + \epsilon \langle \mathbf{X}_{1k} + \mathbf{X}_{2k} \rangle + 2M\epsilon^2 \\
&\triangleq \varphi_k^{(\kappa)}(\boldsymbol{\theta}, \mathbf{X}_{1,k}, \mathbf{X}_{2,k}, \mathbf{Y}),
\end{aligned} \tag{5.60}$$

for $X_{i,k}^{(\kappa)}(t) \triangleq X_{i,k}^{(\kappa)} + tI_{2M}$, $i \in \{1,2\}$, $Y_k^{(\kappa)}(t) \triangleq [W_k^{(\kappa)}]^2 + tI_{2M}$, and $Y_{\setminus k}^{(\kappa)}(t) \triangleq \sum_{j \in \mathcal{K} \setminus \{k\}} [W_j^{(\kappa)}]^2 + tI_{2M}$.

Next, similarly to (5.36), the nonconvex constraint

$$[\Lambda_k(\boldsymbol{\theta}) \mathbf{W}_k]^2 \succeq \mathbf{Z}_k, \tag{5.61}$$

for the newly introduced Hermitian symmetric matrix variable $\mathbf{Z}_k$ of size $2\times$, is innerly approximated by the following semi-definite constraint

$$\begin{aligned}
&\begin{bmatrix} \Lambda_k(\theta^{(\kappa)}) Y_k^{(\kappa)}(\eta) \Lambda_k^H(\boldsymbol{\theta}) + (*)^H & * \\ Y_k^{(\kappa)}(\eta) \Lambda_k^H(\theta^{(\kappa)}) & [W_k^{(\kappa)} (\mathbf{W}_k)^H + (*)^H] + \eta I_{2M} \end{bmatrix} \succeq \\
&\qquad \begin{bmatrix} \mathbf{Z}_k + \eta \mathbf{Q}_k & 0_{2 \times (2M)} \\ 0_{(2M) \times 2} & [W_k^{(\kappa)}]^2 \end{bmatrix} \begin{bmatrix} \mathbf{Z}_k & \Lambda_k(\boldsymbol{\theta}) \\ \Lambda_k^H(\boldsymbol{\theta}) & I_{2M} \end{bmatrix} \succeq 0,
\end{aligned} \tag{5.62a}$$

for $\eta > 0$ and the slack Hermitian symmetric matrix variable $\mathbf{Q}_k$ of size 2×2.

The inequality (5.62) together with the inequality (A.18) in the appendix A yield

$$\begin{aligned}
\psi_k(\boldsymbol{\theta}, \boldsymbol{w}) &\geq \psi_k^{(\kappa)}(\boldsymbol{\theta}, \mathbf{Z}_k) \\
&\triangleq \psi_k(\theta^{(\kappa)}, w^{(\kappa)}) - \langle [\Lambda_k(\theta^{(\kappa)}) W_k^{(\kappa)}]^2, (\mathbf{Z}_k)^{-1} \rangle
\end{aligned} \tag{5.63}$$

under the trust region

$$\mathbf{Z}_k \succ 0. \tag{5.64}$$

Thus, we solve the following convex problem of inner approximation of (5.49) with computational complexity $\mathcal{O}\left((12KM^2 + 2KM + 4K + N)^3(5K + N + 2)\right)$ [98, p. 4] to generate $(\theta^{(\kappa+1)}, w^{(\kappa+1)})$ at the κ-th iteration:

$$\begin{aligned}\max_{\boldsymbol{\theta},\boldsymbol{w},\mathbf{X},\mathbf{Y},\mathbf{Z}} \left[\min_{k=1,\ldots,K}[\varphi_k^{(\kappa)}(\boldsymbol{\theta}, \mathbf{X}_{1,k}, \mathbf{X}_{2,k}, \mathbf{Y}) + \psi_k^{(\kappa)}(\boldsymbol{\theta}, \mathbf{Z}_k)] + \mu\left(\frac{1}{N} - \iota^{(\kappa)}(\boldsymbol{\theta})\right)\right] \\ \text{s.t.} \quad (5.10), (5.26), (5.47b), (5.57), (5.58), (5.59), (5.62), (5.64),\end{aligned} \tag{5.65}$$

where $\iota^{(\kappa)}(\boldsymbol{\theta})$ is recalled from (5.25).

5.3.3 Initialization and penalty parameter

We use Algorithm 8 for computing

$$\max_{\boldsymbol{\theta},\boldsymbol{w}} \ \Phi(\boldsymbol{\theta}, \boldsymbol{w}) \quad \text{s.t.} \quad (5.47b), (5.10) \tag{5.66}$$

Suppose that $(w^{(0)}, \theta^{(0)})$ is the found solution of (5.66) with the optimal value $\gamma^{(0)}$. Then determine μ by (5.41). It is noteworthy that the optimal solution $\boldsymbol{w}_{1,k}$ and $\boldsymbol{w}_{2,k}$ from Algorithm 8 are not the complex conjugate of each other.

Algorithm 8 IGS initializing algorithm

1: **Initialization:** Randomly generate $(\theta^{(0)}, w^{(0)})$ satisfying the convex constraints (5.8b) and (5.47b). Set $\kappa = 0$.
2: **Repeat until convergence of the objective in** (5.66)**:** Solve the convex problem (5.51) to generate $w^{(\kappa+1)}$ and then solve the convex problem $\max_{\boldsymbol{\theta}} \min_{k=1,\ldots,K} \tilde{r}_k^{(\kappa)}(\boldsymbol{\theta})$ s.t. (5.47b) to generate $\theta^{(\kappa+1)}$. Reset $\kappa := \kappa + 1$.
3: **Output** $(w^{(\kappa)}, \theta^{(\kappa)})$ and reset $(w^{(0)}, \theta^{(0)}) \leftarrow (w^{(\kappa)}, \theta^{(\kappa)})$.

5.3.4 Two-phase Algorithm

We propose 9, which like Algorithm 7 consists of two phases to exploit the computational efficiency of the alternating descent procedure and the solution optimality of the path-following procedure.

Algorithm 9 Two-phase IGS algorithm

1: **Alternating descent phase: repeat until** (5.49) **is reached:** Generate $w^{(\kappa+1)}$ by solving the convex problem (5.51) and then solve the convex problem (5.54) to generate $\theta^{(\kappa+1)}$; Reset $\kappa := \kappa + 1$.
2: **Path-following phase: repeat until** (5.49) **is reached:** Generate $(w^{(\kappa+1)}, \theta^{(\kappa+1)})$ by solving the convex problem (5.65); Reset $\kappa := \kappa + 1$.
3: **Output** $(w^{(\kappa)}, \theta^{(\kappa)})$.

5.4 Performance results

The performance of our proposed algorithms is examined in this section. The large scale fading coefficients, $\beta_{\text{AP-RIS}}$, $\beta_{\text{RIS-k}}$, and $\beta_{\text{AP-k}}$, in (5.5), are modeled as [121, 111]

$$\beta_{\text{AP-RIS}} = G_{\text{AP}} + G_{\text{RIS}} - 35.9 - 22\log_{10}(d_{\text{AP-RIS}}) \quad \text{(in dB)}, \tag{5.67a}$$

$$\beta_{\text{RIS-k}} = G_{\text{RIS}} - 33.05 - 30\log_{10}(d_{\text{RIS-k}}) \quad \text{(in dB)}, \tag{5.67b}$$

$$\beta_{\text{AP-k}} = G_{\text{AP}} - 33.05 - 36.7\log_{10}(d_{\text{AP-k}}) \quad \text{(in dB)}, \tag{5.67c}$$

where $G_{\text{AP}} = 5$ dBi and $G_{\text{RIS}} = 5$ dBi denote the antenna gain of the AP and the gain of the elements of RIS, respectively [121, 111], $d_{\text{AP-RIS}}$, $d_{\text{RIS-k}}$, and $d_{\text{AP-k}}$ are the distances between the AP and RIS, the RIS and UE k, and the AP and UE k, respectively. The full-rank AP-to-RIS LoS channel matrix is defined as $[H_{AR}]_{n,m} = e^{j\pi\left((n-1)\sin\bar{\theta}_n \sin\bar{\phi}_n + (m-1)\sin\theta_n \sin\phi_n\right)}$, where θ_n and ϕ_n are uniformly distributed as $\theta_n \sim \mathcal{U}(0,\pi)$ and $\phi_n \sim \mathcal{U}(0,2\pi)$, respectively, and $\bar{\theta}_n = \pi - \theta_n$ and $\bar{\phi}_n = \pi + \phi_n$ [111]. The normalized small-scale fading channel $h_{a,k}$ follows Rayleigh distribution while the small-scale fading channel gain $h_{r,k}$ follow Rician distribution with a Rician K-factor of 3. The spatial correlation matrix is given as $[\mathbf{R}_{\text{RIS-k}}]_{n,n'} = e^{j\pi(n-n')\sin\tilde{\phi}_k \sin\tilde{\theta}_k}$, where $\tilde{\phi}_k$ and $\tilde{\theta}$ represent the azimuth and elevation angle for UE k, respectively. The noise power is set to $\sigma = -114$ dBm, i.e., noise power spectral density $= -174$ dBm/Hz and transmission bandwidth $= 1$ MHz.

Considering the system model setup in Fig. 5.1 and let us use (x, y, z) to denote the coordinates (placement) of the AP, RIS and UEs, the AP is deployed at $(40, 0, 25)$, the RIS is deployed at $(0, 60, 40)$, and $K = 10$ UEs are randomly placed in $120m \times 120m$ right-hand-side of the obstacles and RIS. The following results have been plotted to analyze the performance of our proposed algorithms, where the tolerance level for the convergence of algorithms is set to 10^{-3}.

- *PSG-RIS*: This result simulates the performance of PGS algorithm. Particularly, the proposed Alg. 1 is simulated for initialization and proposed Alg. 2 is simulated during optimization phase.
- *IGS-RIS*: This result simulates the performance of IGS algorithm. Particularly, the proposed Alg. 3 is simulated for initialization and proposed Alg. 4 is simulated during optimization phase.
- *PGS-RIS with random* $\boldsymbol{\theta}$: This result simulates the performance of PGS algorithm without phase optimization, i.e., it assumes random phase coefficients $\boldsymbol{\theta}$ at the RIS. This result demonstrates the gain achieved by the proposed PGS-RIS algorithm, which assumes joint phase optimization with beamforming design.
- *IGS-RIS with random* $\boldsymbol{\theta}$: This result simulates the performance of IGS algorithm by assuming random phase coefficients $\boldsymbol{\theta}$ at the RIS. This result demonstrates the gain achieved by the proposed IGS-RIS algorithm, which assumes joint phase optimization with beamforming design.
- *PGS without RIS* This result simulates the performance of PGS algorithm in the absence of RIS. This result demonstrates the advantage of deploying RIS.
- *PGS without RIS* This result simulates the performance of IGS algorithm in the absence of RIS. This result demonstrates the advantage of deploying RIS.

Fig. 5.2 plots the convergence of the proposed algorithms with $P = 20$ dBm, $M = 9$ AP-antennas, and $N = 100$ RIS elements. Fig. 5.2 assumes the presence of the direct path between the AP and the UEs. It can be seen from Fig. 5.2 that all the algorithms converges rapidly within a few iterations (15-30). As expected, the PGS based algorithms converge faster than the IGS based algorithms because the latter need to handle more optimization variables. Fig. 5.3 plots the achievable max-min rate versus the number of antennas at the AP, M, with $P = 20$ dBm and $N = 100$ RIS elements. The results have been plotted for the side-range of AP-antennas $M = \{7, 8, 9, 10, 11\}$ to consider all three situations; (i) $M < K$, (ii) $M = K$, and (iii) $M > K$, where $K = 10$ is the number of UEs as described previously. Fig. 5.3 shows that the proposed IGS-RIS algorithm outperforms the "IGS without RIS" and "IGS-RIS with random $\boldsymbol{\theta}$". The performance margin increases when the value of M increases. Fig. 5.3 indicates that "IGS without RIS" and "IGS-RIS with random $\boldsymbol{\theta}$" yield similar performance which provides an important insight that there is no advantage of deploying RIS unless RIS reflection coefficients are optimized. Fig. 5.3 also plots the

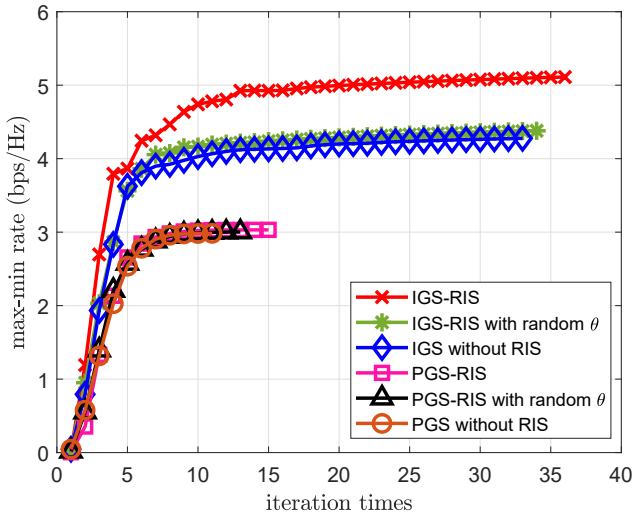

Fig. 5.2 Convergence with $P = 20$ dBm, $M = 9$ AP-antennas, and $N = 100$ RIS elements.

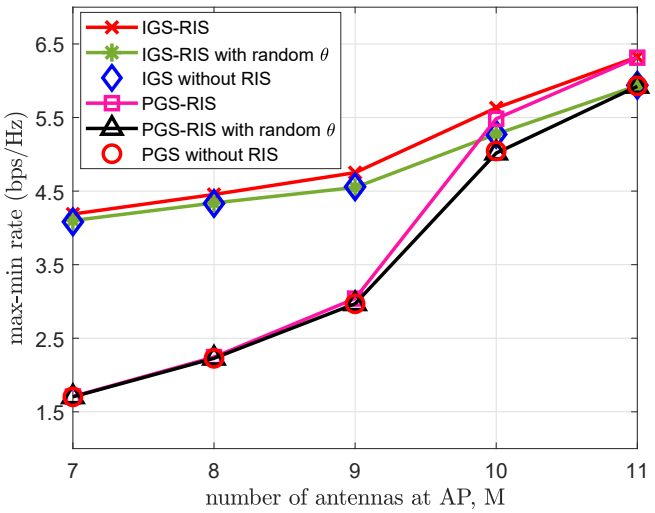

Fig. 5.3 Achievable max-min throughput versus the number of antennas at the AP, M, with $P = 20$ dBm and $N = 100$ RIS elements.

performance of the proposed PGS-RIS algorithm which outperforms the "PGS without RIS" and "PGS-RIS with random $\boldsymbol{\theta}$". Fig. 5.3 also shows that the performance of PGS-RIS performance gets closer to that of IGS-RIS for $M > K$, i.e., $M = 11$ AP-antennas.

Fig. 5.4 plots the achievable max-min rate versus the transmit power budget at the AP, P, with $M = 9$ AP-antennas and $N = 100$ RIS elements. As expected, the performance of the proposed IGS-RIS and PGS-RIS algorithms improve with the increase in the available

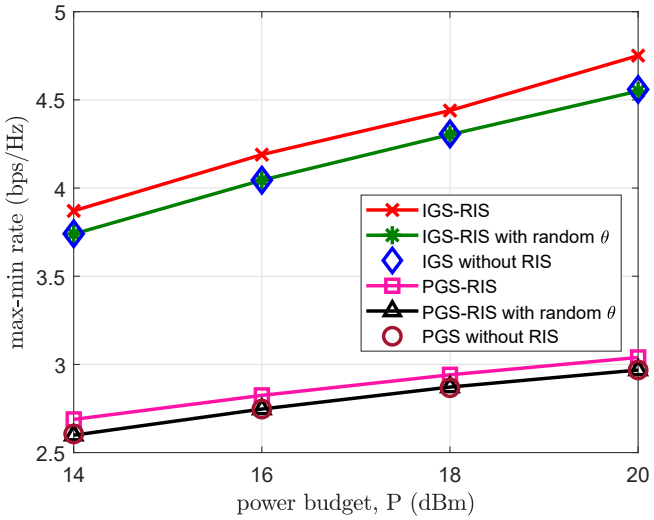

Fig. 5.4 Achievable max-min throughput versus the transmit power budget at the AP, P, with $M = 9$ AP-antennas and $N = 100$ RIS elements.

power budget. Fig. 5.4 also shows the advantage of the proposed IGS-RIS over "IGS without RIS" and "IGS-RIS with random $\boldsymbol{\theta}$" while the latter two yield similar performance. Similarly, Fig. 5.4 shows the performance gain of the proposed PGS-RIS over "PGS without RIS" and "PGS-RIS with random $\boldsymbol{\theta}$".

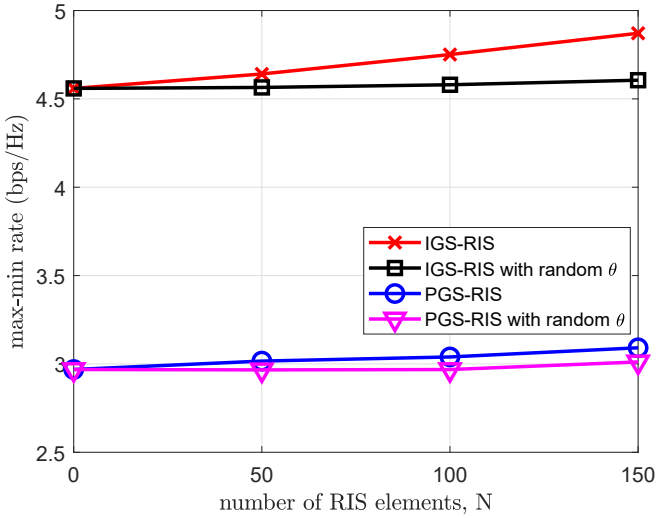

Fig. 5.5 Achievable max-min throughput versus the number of RIS elements, N, with $M = 9$ AP-antennas and $P = 20$ dBm.

Fig. 5.5 plots the achievable max-min rate versus the number of RIS elements, N, with $M = 9$ AP-antennas and $P = 20$ dBm. In Fig. 5.5, $N = 0$ implies IGS or PGS without RIS

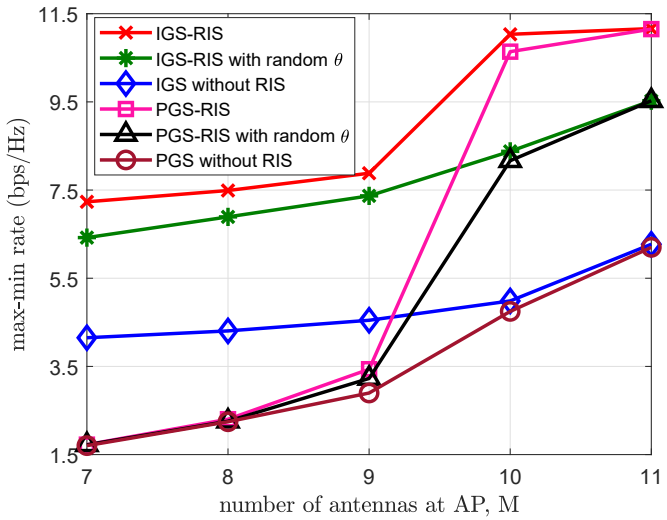

Fig. 5.6 Under the setup in Remark 1, achievable max-min throughput versus the number of antennas at the AP with $P = 20$ dBm and $N = 100$ RIS elements.

deployment. Fig. 5.5 shows that only the performance of the proposed algorithm IGS-RIS algorithm improves with the increase in the number of RIS elements. Fig. 5.5 shows that the proposed IGS-RIS algorithm clearly outperforms the "IGS-RIS with random $\boldsymbol{\theta}$" and the performance margin increases with the increase in N. Similarly, Fig. 5.5 shows the performance gain of the proposed PGS-RIS over "PGS-RIS with random $\boldsymbol{\theta}$". Fig. 5.5 clearly shows the advantage of employing IGS over PGS.

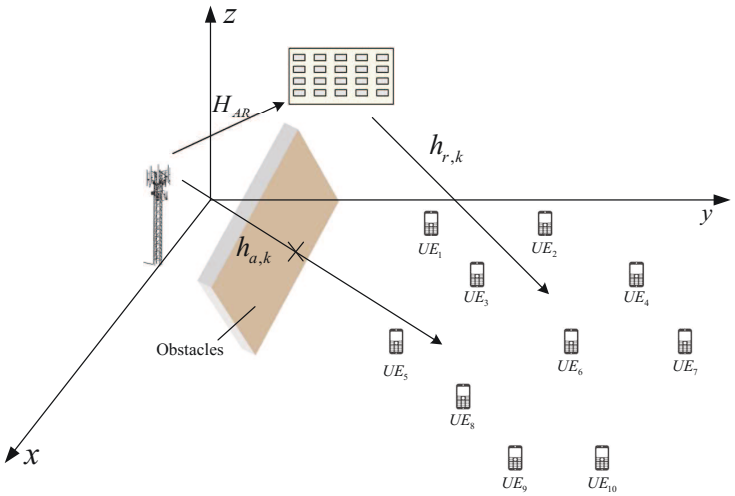

Fig. 5.7 A simulation setup with the blockage of the direct path between the AP and the UEs. The results for this setup are shown in Figs. 5.8-5.10.

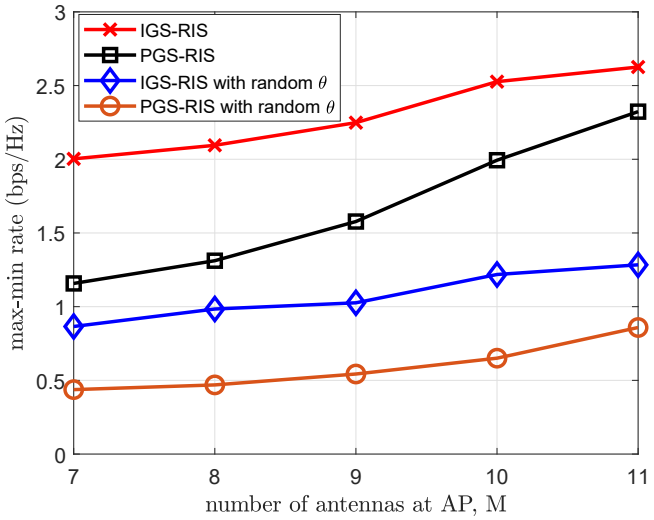

Fig. 5.8 Assuming blockage of direct path between AP and UEs $h_{a,k} \equiv 0$, achievable max-min throughput versus the number of antennas at the AP, M, with $P = 26$ dBm and $N = 60$ RIS elements.

Remark 1 *In this chapter, we consider more or less a practical RIS in the diffuse scattering regime with the size of each its meta-surface of the order of the radio wavelength [110]. The product of the two path-losses in the AP-RIS-UE reflected link (see* (5.1)*) attenuates it very much (see [121] for analysis in details). Both PGS-RIS and IGS-RIS can achieve much more significant gains in the anomalous reflection regime with the size of each RIS meta surface of ten times larger than the radio wavelength [110]. The path-loss of the reflected path then follows the model which is inversely proportional to sum of the two distances of AP-RIS and RIS-AP links [6], making the AP-RIS-UE reflected link in much better condition. For illustrative purpose, Fig. 5.6 plots the achievable max-min rate vs the number of antennas at AP for* $\beta_{AP\text{-}RIS}\beta_{RIS\text{-}k}$ *in* (5.1) *modelled by* $\beta_{AP\text{-}RIS\text{-}k} = G_{AP} - 33.05 - 30\log_{10}(d_{AP\text{-}RIS} + d_{RIS\text{-}k})$ *(in dB).*

Next, we consider another scenario of equally important practice as illustrated by Fig. 5.7, where there is the blockage of direct signal path between the AP and the multiple UEs, i.e. $h_{a,k} \equiv 0$ in (5.1) and (5.5). The path-loss $\beta_{\text{AP-RIS}}$ and $\beta_{\text{RIS-k}}$ are defined by (5.67a) and (5.67b). For simulation under this scenario, we can consider slightly smaller distances between AP and the UEs since there is no direct path availability. So under the scenario in Fig. 5.7, the AP is deployed at $(20, 0, 25)$, the RIS is deployed at $(0, 30, 40)$, and $K = 10$ UEs are randomly placed in $60m \times 60m$ right-hand-side of the obstacles and RIS.

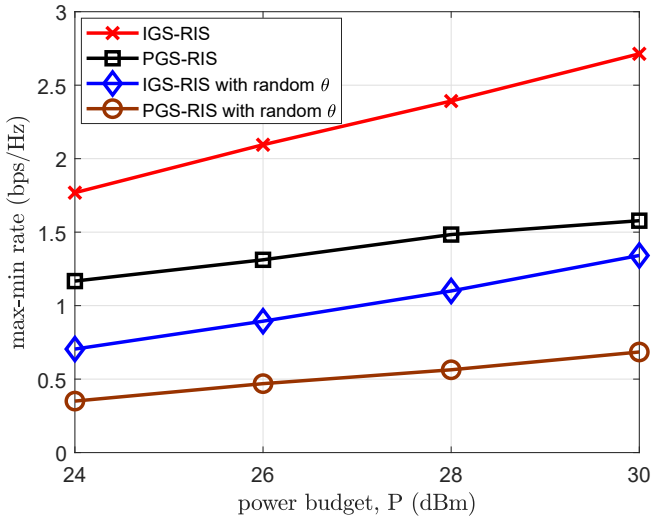

Fig. 5.9 Assuming blockage of direct path between AP and UEs $h_{a,k} \equiv 0$, achievable max-min throughput versus transmit power budget at the AP, P, with $M = 8$ AP-antennas and $N = 60$ RIS elements.

Fig. 5.8 plots the achievable max-min rate versus the number of antennas at the AP with $P = 26$ dBm and $N = 60$ RIS elements. Fig. 5.8 clearly shows that the proposed IGS-RIS algorithm outperforms the "IGS-RIS with random $\boldsymbol{\theta}$" and similarly the proposed PGS-RIS algorithm outperforms the "PGS-RIS with random $\boldsymbol{\theta}$". It clearly demonstrates the gain achieved by the proposed algorithms, which consider joint phase optimization with beamforming design over beamforming design alone (random phase selection). Fig. 5.8 also shows the advantage of employing IGS over PGS. Similar trend with superiority of the proposed IGS-RIS algorithm can be observed in Figs. 5.9 and 5.10, which plot achievable max-min rate versus the transmit power budget at the AP and the number of RIS elements, respectively. The above results also show that $\boldsymbol{w}_{1,k}$ and $\boldsymbol{w}_{2,k}$ are not one the complex conjugate of the other in IGS-RIS.

Computational experience

To speed up the convergence of Algorithms 7 and 9, at the κ-th round, define

$$\mathcal{N}^{(\kappa)} \triangleq \{n \in \mathcal{N} \triangleq \{1, \ldots, N\} \ : \ |\theta_n^{(\kappa)}|^2 \geq 1 - \epsilon_{tol}\} \tag{5.68}$$

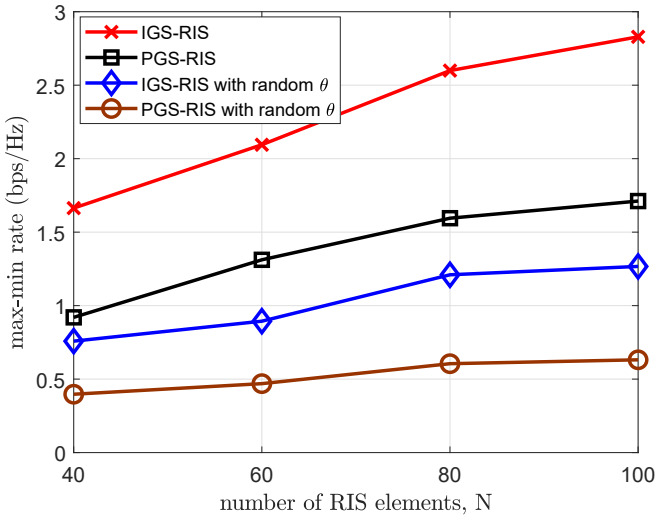

Fig. 5.10 Assuming blockage of direct path between AP and UEs $h_{a,k} \equiv 0$, achievable max-min throughput versus the number of RIS elements, N, with $M = 8$ AP-antennas and $P = 26$ dBm.

for a given tolerance ϵ_{tol}. Then, replace the trust region constraint (5.26) in (5.27), (5.39), (5.54), and (5.65) by the following constraints

$$\sum_{n \in \mathcal{N} \setminus \mathcal{N}^{(\kappa)}} (2\Re\{(\theta_n^{(\kappa)})^* \theta_n\} - |\theta_n^{(\kappa)}|^2) > 0, \tag{5.69}$$

$$2\Re\{(\theta_n^{(\kappa)})^* \theta_n\} - |\theta_n^{(\kappa)}|^2 \geq 1 - \epsilon_{tol}, n \in \mathcal{N}^{(\kappa)}, \tag{5.70}$$

to control the convergence of individual $|\theta_n|$, $n \in \mathcal{N}$ to one.

Table 5.1 and Table 5.2 provides the rounded average number of rounds in obtaining the numerical results in Fig. 5.3 (with the direct path between the AP and the UEs) and Fig. 5.8 (without direct path between the AP and the UEs). In most cases, the second phase of Algorithm 7 and Algorithm 9 takes a couple of iterations to confirm the optimality of the solution found from the first phase. In general, IGS Algorithms 8 and 9 need more rounds than that needed for PGS Algorithms 6 and 7 because optimization of logarithm-determinant functions with IGS is much more computationally challenging than that of logarithmic functions with PGS.

Table 5.1 The rounded average number of rounds for implementing Algorithms 6-9 in obtaining Fig. 5.3 (direct path between the AP and the UEs)

	$M = 7$	$M = 8$	$M = 9$	$M = 10$	$M = 11$
IGS-RIS	36	33	32	34	30
IGS-RIS with random $\boldsymbol{\theta}$	35	31	39	36	33
IGS without RIS	34	33	37	37	37
PGS-RIS	13	14	16	14	14
PGS-RIS with random $\boldsymbol{\theta}$	16	17	24	23	20
PGS without RIS	15	17	24	23	20

Table 5.2 The rounded average number of rounds for implementing Algorithms 6-9 in obtaining Fig.5.8 (without direct path between the AP and the UEs)

	$M = 7$	$M = 8$	$M = 9$	$M = 10$	$M = 11$
IGS-RIS	53	55	55	56	55
PGS-RIS	41	43	46	49	49
IGS-RIS with random $\boldsymbol{\theta}$	15	15	16	16	16
PGS-RIS with random $\boldsymbol{\theta}$	6	6	6	6	6

5.5 Conclusions

The chapter has considered a network of an multiple-antenna array acess points (AP) serving multiple single-antenna users (UEs) with the assistance of a reconfigured intelligent surface (RIS), under both proper Gaussian signaling (PGS) and improper Gaussian signaling (IGS) with and without direct channels from the AP to UEs. The problem of jointly designing the RIS's reflecting coefficients and transmit beamformers to maximize the users' worst rate subject to the transmit power constraint has been addressed. Namely, the chapter has developed algorithms of low computational complexity, which converge at least to a locally optimal solution. The provided simulations have shown the clear advantage of IGS over PGS, and of RIS-aided links over RIS-less links. Their extensions to similar problems for multiple-antenna users are under current study.

Chapter 6

Maximizing the Geometric Mean of User-Rates to Improve Rate-Fairness: Proper vs. Improper Gaussian Signaling

6.1 Introduction

The spectral efficiency optimization of wireless networks is often carried out by sum rate (SR) maximization, thanks to the computational tractability of the latter when relying on beamforming [39, 128]. However, by its nature, SR maximization has the deficiency of allocating a large fraction of the sum-rate to a few users having good channel conditions, while leaving the rest of the users with almost zero rates. Furthermore, the SR performance is typically improved with more users involved because there are more flexible choices for the users' channels [129]. The spectral efficiency is thus addressed more appropriately via either SR maximization under specific quality-of-service (QoS) constraints for users' minimum rate, or by max-min user-rate optimization, but their computation is quite demanding [39, 130–132, 128].

Reconfigurable intelligent surfaces (RISs) [103] are constructed by a planar array of programmable reflecting elements (PREs), which have recently been introduced for improving the energy and spectral efficiencies of future wireless networks (6G) [64, 102, 106, 133],

the coverage, reliability and the average achievable rate of UAV communication systems [134–136] and the outage probability and bit error rate (BER) of indoor mixed dual-hop VLC/RF systems [137]. Moreover, channel estimation and physical layer security for RIS-aided networks have been studied recently [138–141]. A typical RIS-aided system consists of a base station (BS) and a RIS for beneficially reflecting the incident electromagnetic waves from the BS to multi-target directions, where the spectral efficiency may be improved by the joint design of the transmit beamformer at the BS and RIS PREs [7]. The joint design is often based on alternating optimization between the beamformer and PREs. Thus, compared to the design of stand-alone transmit beamformers, the new challenge is the optimization of the PREs with the beamformer weights fixed, which is computationally challenging due to the nonconvex unit-modulus constraint (UMC) imposed on the PREs. In [64] and [111], general-purpose gradient/projected gradient algorithms were used, which do not necessarily converge. By contrast to either convex relaxation relying on dropping the matrix-rank of one constraint or on relaxing the UMC to the convex bounded-by-unit-modulus constraint were used in [23, 142–145] for mitigating the computational challenge. Except for the works [23] and [145], which particularly considered the problem of transmit power minimization subject to signal-to-interference-plus-noise ratio (SINR) constraints, all the following treatises [64, 111, 142–144] considered the problem of SR maximization. The authors of [142–144] applied convex relaxation not only to the UMC but also to the SR objective function. It should be noted that alternating optimization between two sets of decision variables is only efficient, when the optimization within each set with the other set held fixed is computationally tractable. However that is not the case for the problems considered in all these papers because both the optimization of the beamformers with the PREs held fixed and that of the PREs with the beamformer weights held fixed present difficult nonconvex problems. In the end, the convergence of alternating optimization-based algorithms to a locally optimal solution is not guaranteed. Our recent work [146] has been the first one that addressed the spectral efficiency of RIS-aided communication via max-min user-rate optimization. Instead of alternating optimization, we proposed an alternating descent at the first stage and then a joint descent at the second stage to confirm the optimality of the solutions computed. While the descent iterations in the beamformers generate a sequence of better feasible points, the descent iterations in the PREs generate a sequence of better infeasible points, which converges to a feasible point. Moreover, it has been also shown in [146] that using widely linear beamformers for facilitating improper Gaussian signaling (IGS) improves the users' max-min rate.

Against the above background, this chapter offers the following contributions:

- We consider the problem of maximizing the geometric mean (GM) of users' rates for allocating the rates to all users in an equitable manner. We use the users' rate deviation (RD) from their mean and the ratio of the users' maximal and minimal rates (RR) as the main criterion to judge the users' rate balance, which are 0 and 1, respectively, when all users are granted the same rate. The smaller these values are, the fairer the users' rate allocation becomes (more balanced).

- As this problem of GM maximization is computationally intractable, we address it via the min-max joint design of beamforming weights and RIS PREs. To eliminate the UMC of the RIS PREs, we use the polar form of unit-modulus complex numbers that allows each descent iteration of the RIS coefficient calculation to be based on the closed-form solution of an unconstrained nonconvex problem in the PREs' arguments. Each descent iteration of the beamformer weights and the PREs' arguments are also based on the closed-form solutions of convex problems. Thus, the proposed alternating descent method is purely based on closed forms and hence it is computationally efficient.

- Like in [146], here we also use improper Gaussian signaling (IGS) in the BS signal transmission, which has been shown to substantially improve the users' max-min rates (see e.g. [88, 92, 96, 116, 147]) thanks to its ability to mitigate the severe interferences in interference-limited systems. The performance gap between IGS and conventional proper Gaussian signaling (PGS) becomes substantially wider under more severe interference regimes. To elaborate a little further, IGS is not useful in interference-free regimes such as that of zero-forcing beamforming, which forces all interferences to zero. The interference scenario of SR maximization under PGS is unique in the sense that those users who were allocated zero-rate impose no interference on the other users. As a result, SR maximization under PGS exhibit a high RD and near-infinite RR. Our finding is that compared to PGS, IGS does not improve the system's SR but it results in much lower RD and RR as a benefit of having no users with zero rate. Hence SR maximization becomes a practically feasible option while providing the users with beneficial rate-fairness.

The chapter is organized as follows. The joint design of beamformer weights and PREs to maximize the GM of users' rates by tractable computation both under PGS and IGS is addressed in Section II and III, respectively. Their performances are evaluated by the simulations in Section IV, while Section V concludes the chapter.

6.2 Proper Gaussian signaling

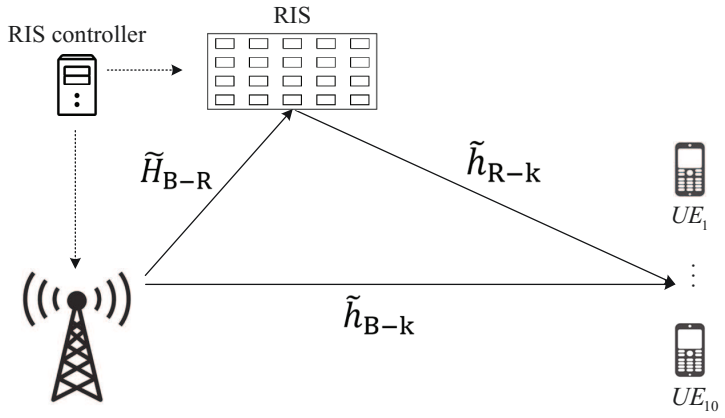

Fig. 6.1 System model

We consider the RIS-aided communication system illustrated by Fig. 6.1, where a RIS of N reflecting units supports the downlink spanning from an M-antenna array BS to K single-antenna users (UEs) $k \in \mathcal{K} \triangleq \{1, \ldots, K\}$. Since the RIS is typically deployed on the facade of high-rise buildings and the AP is also usually at a certain elevated height [106], it is justified to assume a LoS link between the AP and RIS, LoS communication between the RIS and UEs, and NLoS propagation between the AP and UEs. Accordingly, the channels spanning from the BS and the RIS to UE k and from the BS to the RIS are modelled by $\tilde{h}_{\text{B-k}} = \sqrt{\beta_{\text{B-k}}} h_{\text{B-k}} \in \mathbb{C}^{1\times M}$, $\tilde{h}_{\text{R-k}} = \sqrt{\beta_{\text{R-k}}} h_{\text{R-k}} \in \mathbb{C}^{1\times N}$, and $\tilde{H}_{\text{B-R}} = \sqrt{\beta_{\text{B-R}}} H_{\text{B-R}} \in \mathbb{C}^{N\times M}$, where $\sqrt{\beta_{\text{B-k}}}$, $\sqrt{\beta_{\text{R-k}}}$, and $\sqrt{\beta_{\text{B-R}}}$ model the path-loss and large-scale fading of the BS-to-UE k link, the RIS-to-UE k link, and the BS-to-RIS link, respectively [119, 111], while $h_{\text{R-k}}$ and $H_{\text{B-R}}$ are modelled by Rician fading for modeling the line-of-sight (LoS) channels between the RIS and the UEs as well as between the BS and the RIS [121]. Furthermore, $h_{\text{B-k}}$ is modelled by Rayleigh fading in the face of non-LoS (NLoS) channels between the BS and the UEs. Like many other papers on RIS-aided communication networks, we assume having perfect channel state information, which can be obtained from channel estimation [138, 64, 23].

Set $s_k \in \mathcal{C}(0,1)$ as the information symbol for UE k, which is beamformed by $\boldsymbol{w}_k \in \mathbb{C}^M$. The signal x transmited from the BS is

$$x = \sum_{k\in\mathcal{K}} \boldsymbol{w}_k s_k. \tag{6.1}$$

The signal received at UE k can be expressed as

$$y_k = \left(\tilde{h}_{\text{R-k}}\mathbf{R}_{\text{R-k}}^{1/2}\mathsf{diag}(e^{\jmath\boldsymbol{\theta}})\tilde{H}_{\text{B-R}} + \tilde{h}_{\text{B-k}}\right)x + n_k \tag{6.2}$$

$$= \mathcal{H}_k(\boldsymbol{\theta})\sum_{k\in\mathcal{K}}\boldsymbol{w}_k s_k + n_k, \tag{6.3}$$

for

$$\mathcal{H}_k(\boldsymbol{\theta}) \triangleq \tilde{h}_{\text{BR-k}}\mathsf{diag}(e^{\jmath\boldsymbol{\theta}})H_{\text{B-R}} + \tilde{h}_{\text{B-k}} \in \mathbb{C}^{1\times M}, \tag{6.4}$$

with

$$\tilde{h}_{\text{BR-k}} \triangleq \sqrt{\beta_{\text{B-R}}}\sqrt{\beta_{\text{R-k}}}h_{\text{R-k}}\mathbf{R}_{\text{R-k}}^{1/2} \in \mathbb{C}^{1\times N}, \tag{6.5}$$

where $\mathbf{R}_{\text{R-k}} \in \mathbb{C}^{N\times N}$ represents the spatial correlation matrix of the RIS elements with respect to user k [111, 120], $n_k \in \mathcal{C}(0,\sigma)$ is the background noise at UE k, and $\mathsf{diag}(e^{\jmath\boldsymbol{\theta}})$ in (6.2) for $\boldsymbol{\theta} = (\boldsymbol{\theta}_1,\ldots,\boldsymbol{\theta}_N)^T \in [0,2\pi]^N$ represents the matrix of PREs.

Let $\boldsymbol{w} \triangleq \{\boldsymbol{w}_k, k\in\mathcal{K}\}$. The rate in nats/sec at UE k is

$$r_k(\boldsymbol{w},\boldsymbol{\theta}) = \ln\left(1 + \frac{|\mathcal{H}_k(\boldsymbol{\theta})\boldsymbol{w}_k|^2}{\sum_{j\in\mathcal{K}\setminus\{k\}}|\mathcal{H}_k(\boldsymbol{\theta})\boldsymbol{w}_j|^2 + \sigma}\right). \tag{6.6}$$

We consider the following problem of jointly designing the beamformers' weight set $\boldsymbol{w}$ and the PREs $\boldsymbol{\theta}$ to maximize the GM of users' rates:

$$\max_{\boldsymbol{w},\boldsymbol{\theta}}\left(\prod_{k=1}^{K} r_k(\boldsymbol{w},\boldsymbol{\theta})\right)^{1/K} \quad \text{s.t.} \tag{6.7a}$$

$$\sum_{k=1}^{K}||\boldsymbol{w}_k||^2 \le P, \tag{6.7b}$$

where (6.7b) sets the transmit power constraint within a given power budget P. It is plausible that this problem is equivalent to the following one:

$$\min_{\boldsymbol{w},\boldsymbol{\theta}} f\left(r_1(\boldsymbol{w},\boldsymbol{\theta}),\ldots,r_K(\boldsymbol{w},\boldsymbol{\theta})\right) \triangleq \frac{1}{\left(\prod_{k=1}^{K} r_k(\boldsymbol{w},\boldsymbol{\theta})\right)^{1/K}} \quad \text{s.t.(6.7}b\text{)}. \tag{6.8}$$

The function $f(r_1(\boldsymbol{w},\boldsymbol{\theta}),\ldots,r_K(\boldsymbol{w},\boldsymbol{\theta}))$ is the composition of the convex function $f(r_1,\ldots,r_K) = 1/(\prod_{k=1}^{K} r_k)^{1/K}$ and the non-convex functions $r_k(\boldsymbol{w},\boldsymbol{\theta})$, $k=1,\ldots,K$.

Let $(w^{(\kappa)}, \theta^{(\kappa)})$ be a feasible point for (6.8) that is found from the $(\kappa-1)$-st round. We note that the linearized function of $f\left(r_1(\boldsymbol{w},\boldsymbol{\theta}),\ldots,r_K(\boldsymbol{w},\boldsymbol{\theta})\right)$ at $\left(r_1(w^{(\kappa)},\theta^{(\kappa)}),\ldots,r_K(w^{(\kappa)},\theta^{(\kappa)})\right)$ is

$$2f\left(r_1(w^{(\kappa)},\theta^{(\kappa)}),\ldots,r_K(w^{(\kappa)},\theta^{(\kappa)})\right) - f(r_1(w^{(\kappa)},\theta^{(\kappa)}) \\ ,\ldots,r_K(w^{(\kappa)},\theta^{(\kappa)}))\frac{1}{K}\sum_{k=1}^{K}\frac{r_k(\boldsymbol{w},\boldsymbol{\theta})}{r_k(w^{(\kappa)},\theta^{(\kappa)})}. \tag{6.9}$$

Since we have $f\left(r_1(w^{(\kappa)},\theta^{(\kappa)}),\ldots,r_K(w^{(\kappa)},\theta^{(\kappa)})\right) > 0$, we can use steepest descent optimization for the convex function $f(r_1,\ldots,r_K)$ for generating the next feasible point $(w^{(\kappa+1)},\theta^{(\kappa+1)})$:

$$\max_{\boldsymbol{w},\boldsymbol{\theta}} \frac{1}{K}\sum_{k=1}^{K}\frac{r_k(\boldsymbol{w},\boldsymbol{\theta})}{r_k(w^{(\kappa)},\theta^{(\kappa)})}f(r_1(w^{(\kappa)},\theta^{(\kappa)}),\ldots,r_K(w^{(\kappa)},\theta^{(\kappa)})) \quad \text{s.t.} \quad (6.7b), \tag{6.10}$$

which is equivalent to the following problem:

$$\max_{\boldsymbol{w},\boldsymbol{\theta}} f^{(\kappa)}(\boldsymbol{w},\boldsymbol{\theta}) \triangleq \sum_{k=1}^{K}\gamma_k^{(\kappa)} r_k(\boldsymbol{w},\boldsymbol{\theta}) \quad \text{s.t.} \quad (6.7b), \tag{6.11}$$

for

$$\gamma_k^{(\kappa)} \triangleq \frac{f\left(r_1(w^{(\kappa)},\theta^{(\kappa)}),\ldots,r_K(w^{(\kappa)},\theta^{(\kappa)})\right)}{r_k(w^{(\kappa)},\theta^{(\kappa)})}, k=1,\ldots,K. \tag{6.12}$$

6.2.1 Beamforming descent iteration

To generate $w^{(\kappa+1)}$ we seek $w^{(\kappa+1)}$, so that the following holds:

$$f^{(\kappa)}(w^{(\kappa+1)},\theta^{(\kappa)}) > f^{(\kappa)}(w^{(\kappa)},\theta^{(\kappa)}). \tag{6.13}$$

Using the inequality (A.15) for $\mathbf{V} = \mathcal{H}_k(\theta^{(\kappa)})\boldsymbol{w}_k$, $\mathbf{Y} = \sum_{j\in\mathcal{K}\setminus\{k\}}|\mathcal{H}_k(\theta^{(\kappa)})\boldsymbol{w}_j|^2+\sigma$, and $\bar{V} = \mathcal{H}_k(\theta^{(\kappa)})w_k^{(\kappa)}$, $\bar{Y} = y_k^{(\kappa)} \triangleq \sum_{j\in\mathcal{K}\setminus\{k\}}|\mathcal{H}_k(\theta^{(\kappa)})w_j^{(\kappa)}|^2+\sigma$, yields

$$\begin{aligned} r_k(\boldsymbol{w},\theta^{(\kappa)}) &\geq r_k^{(\kappa)}(\boldsymbol{w}) \\ &\triangleq a_k^{(\kappa)} + 2\Re\{\langle b_k^{(\kappa)},\boldsymbol{w}_k\rangle\} - c_k^{(\kappa)}\sum_{j=1}^{K}|\mathcal{H}_k(\theta^{(\kappa)})\boldsymbol{w}_j|^2, \end{aligned} \tag{6.14}$$

with

$$a_k^{(\kappa)} \triangleq r_k(w^{(\kappa)}, \theta^{(\kappa)}) - |\mathcal{H}_k(\theta^{(\kappa)})w_k^{(\kappa)}|^2/y_k^{(\kappa)} - \sigma c_k^{(\kappa)}, b_k^{(\kappa)} \triangleq \mathcal{H}_k^H(\theta^{(\kappa)})\mathcal{H}_k(\theta^{(\kappa)})w_k^{(\kappa)}/y_k^{(\kappa)},$$

and

$$0 < c_k^{(\kappa)} \triangleq |\mathcal{H}_k(\theta^{(\kappa)})w_k^{(\kappa)}|^2 / \left[y_k^{(\kappa)}\left(y_k^{(\kappa)} + |\mathcal{H}_k(\theta^{(\kappa)})w_k^{(\kappa)}|^2\right)\right].$$

The function $r_k^{(\kappa)}(\boldsymbol{w})$ is seen to be concave quadratic, which matches with $r_k^{(\kappa)}(\boldsymbol{w}, \theta^{(\kappa)})$ at $w^{(\kappa)}$. We solve the following convex problem at the κ-th iteration to generate $w^{(\kappa+1)}$:

$$\max_{\boldsymbol{w}} \; f_b^{(\kappa)}(\boldsymbol{w}) \quad \text{s.t.} \quad (6.7b), \tag{6.15}$$

where

$$\begin{aligned} f_b^{(\kappa)}(\boldsymbol{w}) &\triangleq \sum_{k=1}^{K} \gamma_k^{(\kappa)} r_k^{(\kappa)}(\boldsymbol{w}) \\ &= \sum_{k=1}^{K} \gamma_k^{(\kappa)} a_k^{(\kappa)} + 2\sum_{k=1}^{K} \Re\{\langle \gamma_k^{(\kappa)} b_k^{(\kappa)}, \boldsymbol{w}_k \rangle\} - \sum_{k=1}^{K} (\boldsymbol{w}_k)^H \Psi^{(\kappa)} \boldsymbol{w}_k \end{aligned} \tag{6.16}$$

with

$$0 \preceq \Psi^{(\kappa)} \triangleq \sum_{j=1}^{K} \gamma_j^{(\kappa)} c_j^{(\kappa)} \mathcal{H}_j^H(\theta^{(\kappa)}) \mathcal{H}_j(\theta^{(\kappa)}).$$

By using the Lagrangian multiplier method, we obtain the following closed-form solution of (6.15)[1]

$$w_k^{(\kappa+1)} = \begin{cases} (\Psi^{(\kappa)})^{-1} \gamma_k^{(\kappa)} b_k^{(\kappa)} & \text{if} \sum_{k=1}^{K} ||(\Psi^{(\kappa)})^{-1} \gamma_k^{(\kappa)} b_k^{(\kappa)}||^2 \le P \\ \left(\Psi^{(\kappa)} + \mu I_M\right)^{-1} \gamma_k^{(\kappa)} b_k^{(\kappa)} & \text{otherwise,} \end{cases} \tag{6.17}$$

where $\mu > 0$ is chosen by bisection such that

$$\sum_{k=1}^{K} || \left(\Psi^{(\kappa)} + \mu I_M\right)^{-1} \gamma_k^{(\kappa)} b_k^{(\kappa)}||^2 = P.$$

[1] $(\Psi^{(\kappa)})^{-1}$ is understood as the pseudo-inversion when $\Psi^{(\kappa)} \succeq 0$

6.2.2 Programmable reflecting elements' descent iteration

We seek the next iterative point $\theta^{(\kappa+1)}$ such that

$$f^{(\kappa)}(w^{(\kappa+1)},\theta^{(\kappa+1)}) > f^{(\kappa)}(w^{(\kappa+1)},\theta^{(\kappa)}). \tag{6.18}$$

Using the inequality (A.15) for

$$\mathbf{V} = \mathcal{H}_k(\boldsymbol{\theta})w_k^{(\kappa+1)}, \mathbf{Y} = \sum_{j\in\mathcal{K}\setminus\{k\}} |\mathcal{H}_k(\boldsymbol{\theta})w_j^{(\kappa+1)}|^2 + \sigma,$$

and

$$\bar{V} = \mathcal{H}_k(\theta^{(\kappa)})w_k^{(\kappa+1)}, \bar{Y} = y_k^{(\kappa+1)} \triangleq \sum_{j\in\mathcal{K}\setminus\{k\}} |\mathcal{H}_k(\theta^{(\kappa)})w_j^{(\kappa+1)}|^2 + \sigma,$$

yields

$$\begin{aligned} r_k(w^{(\kappa+1)},\boldsymbol{\theta}) &\geq \tilde{r}_k^{(\kappa)}(\boldsymbol{\theta}) \\ &\triangleq \frac{2\Re\{(w_k^{(\kappa+1)})^H\mathcal{H}_k^H(\theta^{(\kappa)})\mathcal{H}_k(\boldsymbol{\theta})w_k^{(\kappa+1)}\}}{y_k^{(\kappa+1)}} + \tilde{a}_k^{(\kappa)} - \tilde{c}_k^{(\kappa)}\sum_{j=1}^{K}|\mathcal{H}_k(\boldsymbol{\theta})w_j^{(\kappa+1)}|^2 \end{aligned} \tag{6.19}$$

with

$$\tilde{a}_k^{(\kappa)} \triangleq r_k(w^{(\kappa+1)},\theta^{(\kappa)}) - \rho_k(w^{(\kappa+1)},\theta^{(\kappa)}) - \sigma\tilde{c}_k^{(\kappa)},$$

and

$$0 < \tilde{c}_k^{(\kappa)} \triangleq |\mathcal{H}_k(\theta^{(\kappa)})w_k^{(\kappa+1)}|^2 / \left[y_k^{(\kappa+1)}\left(y_k^{(\kappa+1)} + |\mathcal{H}_k(\theta^{(\kappa)})w_k^{(\kappa+1)}|^2\right)\right].$$

Let us define Υ_n as the matrix of size $N\times N$ having only zero entries, except for its (n,n)-entry, which is 1, to express

$$\mathsf{diag}(e^{\jmath\boldsymbol{\theta}}) = \sum_{n=1}^{N} e^{\jmath\boldsymbol{\theta}_n}\Upsilon_n.$$

We then use (6.4) to arrive at:

$$\begin{aligned}
(w_k^{(\kappa+1)})^H \mathcal{H}_k^H(\theta^{(\kappa)})\mathcal{H}_k(\boldsymbol{\theta})w_k^{(\kappa+1)} &= \\
(w_k^{(\kappa+1)})^H \mathcal{H}_k^H(\theta^{(\kappa)})\left[\tilde{h}_{\text{BR-k}}\mathsf{diag}(e^{\jmath\boldsymbol{\theta}})H_{\text{B-R}}+\tilde{h}_{\text{B-k}}\right]w_k^{(\kappa+1)} &= \\
(w_k^{(\kappa+1)})^H \mathcal{H}_k^H(\theta^{(\kappa)})\tilde{h}_{\text{B-k}}w_k^{(\kappa+1)} + (w_k^{(\kappa+1)})^H \mathcal{H}_k^H(\theta^{(\kappa)})\tilde{h}_{\text{BR-k}}\mathsf{diag}(e^{\jmath\boldsymbol{\theta}})H_{\text{B-R}}w_k^{(\kappa+1)} &= \\
(w_k^{(\kappa+1)})^H \mathcal{H}_k^H(\theta^{(\kappa)})\tilde{h}_{\text{B-k}}w_k^{(\kappa+1)} + \sum_{n=1}^{N}(w_k^{(\kappa+1)})^H \mathcal{H}_k^H(\theta^{(\kappa)})\tilde{h}_{\text{BR-k}}\Upsilon_n H_{\text{B-R}}w_k^{(\kappa+1)}e^{\jmath\boldsymbol{\theta}_n} &= \\
\alpha_k^{(\kappa)} + \sum_{n=1}^{N}\tilde{b}_k^{(\kappa)}(n)e^{\jmath\theta_n}, \qquad (6.20)
\end{aligned}$$

with

$$\alpha_k^{(\kappa)} \triangleq (w_k^{(\kappa+1)})^H \mathcal{H}_k^H(\theta^{(\kappa)})\tilde{h}_{\text{B-k}}w_k^{(\kappa+1)},$$

and[2]

$$\tilde{b}_k^{(\kappa)}(n) = (w_k^{(\kappa+1)})^H \mathcal{H}_k^H(\theta^{(\kappa)})\tilde{h}_{\text{BR-k}}\Upsilon_n H_{\text{B-R}}w_k^{(\kappa+1)}, n = 1,\dots N.$$

To expound further, we have:

$$\begin{aligned}
|\mathcal{H}_k(\boldsymbol{\theta})w_j^{(\kappa+1)}|^2 &= \left|\left(\tilde{h}_{\text{BR-k}}\mathsf{diag}(e^{\jmath\boldsymbol{\theta}})H_{\text{B-R}}+\tilde{h}_{\text{B-k}}\right)w_j^{(\kappa+1)}\right|^2 \\
&= \left|\tilde{h}_{\text{BR-k}}\mathsf{diag}(e^{\jmath\boldsymbol{\theta}})H_{\text{B-R}}w_j^{(\kappa+1)}\right|^2 + |\tilde{h}_{\text{B-k}}w_j^{(\kappa+1)}|^2 \\
&\quad +2\Re\{(w_j^{(\kappa+1)})^H\left(\tilde{h}_{\text{B-k}}\right)^H\tilde{h}_{\text{BR-k}}\mathsf{diag}(e^{\jmath\boldsymbol{\theta}})H_{\text{B-R}}w_j^{(\kappa+1)}\} \\
&= \left|\tilde{h}_{\text{BR-k}}\mathsf{diag}(e^{\jmath\boldsymbol{\theta}})H_{\text{B-R}}w_j^{(\kappa+1)}\right|^2 + |\tilde{h}_{\text{B-k}}w_j^{(\kappa+1)}|^2 \\
&\quad +2\Re\{\sum_{n=1}^{N}(w_j^{(\kappa+1)})^H\left(\tilde{h}_{\text{B-k}}\right)^H\tilde{h}_{\text{BR-k}}\Upsilon_n H_{\text{B-R}}w_j^{(\kappa+1)}e^{\jmath\boldsymbol{\theta}_n}\}. \qquad (6.21)
\end{aligned}$$

Furthermore,

$$\tilde{h}_{\text{BR-k}}\mathsf{diag}(e^{\jmath\boldsymbol{\theta}})H_{\text{B-R}}w_j^{(\kappa+1)} = \tilde{h}_{\text{BR-k}}\left(\sum_{n=1}^{N}e^{\jmath\boldsymbol{\theta}_n}\Upsilon_n\right)H_{\text{B-R}}w_j^{(\kappa+1)} = \sum_{n=1}^{N}\alpha_{k,j}^{(\kappa+1)}(n)e^{\jmath\theta_n}, \quad (6.22)$$

for $\alpha_{k,j}^{(\kappa+1)}(n) = \tilde{h}_{\text{BR-k}}\Upsilon_n H_{\text{B-R}}w_j^{(\kappa+1)}, n = 1,\dots,N.$

[2]In what follows $b(i)$ is the i-th entry of b and $[A](i,i)$ is the i-th diagonal entry of A, and $[A]^*(i,i)$ is the complex conjugate of $[A](i,i)$

Based on (6.19), (6.20), (6.21), and (6.22), we obtain

$$\begin{aligned}\tilde{r}_k^{(\kappa)}(\boldsymbol{\theta}) &= \tilde{a}_k^{(\kappa+1)} + 2\Re\{\sum_{n=1}^{N}\tilde{b}_k^{(\kappa)}(n)e^{\jmath\theta_n}\} - \tilde{c}_k^{(\kappa)}\sum_{j=1}^{K}\left|\sum_{n=1}^{N}\alpha_{k,j}^{(\kappa+1)}(n)e^{\jmath\boldsymbol{\theta}_n}\right|^2 \\ &= \tilde{a}_k^{(\kappa+1)} + 2\Re\{\sum_{n=1}^{N}\tilde{b}_k^{(\kappa)}(n)e^{\jmath\theta_n}\} - \tilde{c}_k^{(\kappa)}\sum_{j=1}^{K}(e^{\jmath\boldsymbol{\theta}})^H\Phi_{k,j}^{(\kappa+1)}e^{\jmath\boldsymbol{\theta}}, \end{aligned} \tag{6.23}$$

where

$$\tilde{a}_k^{(\kappa+1)} \triangleq \tilde{a}_k^{(\kappa)} + 2\Re\{\alpha_k^{(\kappa)}\}/y_k^{(\kappa+1)} - \tilde{c}_k^{(\kappa)}\sum_{j=1}^{N}|\tilde{h}_{\text{B-k}}w_j^{(\kappa+1)}|^2,$$

$$\tilde{b}_k^{(\kappa+1)}(n) \triangleq \tilde{b}_k^{(\kappa)}(n)/y_k^{(\kappa+1)} - \tilde{c}_k^{(\kappa)}\sum_{j=1}^{K}(w_j^{(\kappa+1)})^H\left(\tilde{h}_{\text{B-k}}\right)^H\tilde{h}_{\text{BR-k}}\Upsilon_n H_{\text{B-R}}w_j^{(\kappa+1)},$$

and

$$\Phi_{k,j}^{(\kappa+1)}(n,m) = (\alpha_{k,j}^{(\kappa+1)}(n))^*\alpha_{k,j}^{(\kappa+1)}(m), n = 1,\ldots,N; m = 1,\ldots,N.$$

Note that $\Phi_{k,j}^{(\kappa+1)} \succeq 0$. Therefore,

$$\begin{aligned} f_c^{(\kappa)}(\boldsymbol{\theta}) &\triangleq \sum_{k=1}^{K}\gamma_k^{(\kappa)}\tilde{r}_k^{(\kappa)}(\boldsymbol{\theta}) \\ &= \tilde{a}^{(\kappa+1)} + 2\Re\{\sum_{n=1}^{N}\tilde{b}^{(\kappa+1)}(n)e^{\jmath\theta_n}\} - (e^{\jmath\boldsymbol{\theta}})^H\Phi^{(\kappa+1)}e^{\jmath\boldsymbol{\theta}}, \end{aligned} \tag{6.24}$$

for

$$\tilde{a}^{(\kappa+1)} \triangleq \sum_{k=1}^{K}\gamma_k^{(\kappa)}\tilde{a}_k^{(\kappa+1)}, \tilde{b}^{(\kappa+1)}(n) \triangleq \sum_{k=1}^{K}\gamma_k^{(\kappa)}\tilde{b}_k^{(\kappa+1)}(n), n = 1,\ldots,N,$$

and

$$0 \preceq \Phi^{(\kappa+1)} \triangleq \sum_{k=1}^{K}\sum_{j=1}^{N}\gamma_k^{(\kappa)}\tilde{c}_k^{(\kappa)}\Phi_{k,j}^{(\kappa+1)}.$$

We use the following problem at the κ-th iteration to generate $\theta^{(\kappa+1)}$:

$$\max_{\boldsymbol{\theta}} \; f_c^{(\kappa)}(\boldsymbol{\theta}). \tag{6.25}$$

Following [148], we have (6.26).

$$\begin{aligned}
f_c^{(\kappa)}(\boldsymbol{\theta}) &= \tilde{a}^{(\kappa+1)} + 2\Re\{\sum_{n=1}^{N} \tilde{b}^{(\kappa+1)}(n) e^{\jmath\theta_n}\} - (e^{\jmath\boldsymbol{\theta}})^H(\Phi^{(\kappa+1)} - \lambda_{\max}(\Phi^{(\kappa+1)})I_N)e^{\jmath\boldsymbol{\theta}} \\
&\quad -\lambda_{\max}(\Phi^{(\kappa+1)})(e^{\jmath\boldsymbol{\theta}})^H I_N e^{\jmath\boldsymbol{\theta}} \\
&= \tilde{a}^{(\kappa+1)} + 2\Re\{\sum_{n=1}^{N} \tilde{b}^{(\kappa+1)}(n) e^{\jmath\theta_n}\} - (e^{\jmath\boldsymbol{\theta}})^H(\Phi^{(\kappa+1)} - \lambda_{\max}(\Phi^{(\kappa+1)})I_N)e^{\jmath\boldsymbol{\theta}} \\
&\quad -\lambda_{\max}(\Phi^{(\kappa+1)})N \\
&\geq \tilde{f}_c^{(\kappa)}(\boldsymbol{\theta}) \\
&\triangleq \tilde{a}^{(\kappa+1)} + 2\Re\{\sum_{n=1}^{N} \tilde{b}^{(\kappa+1)}(n) e^{\jmath\theta_n}\} - [2\Re\{(e^{\jmath\theta^{(\kappa)}})^H(\Phi^{(\kappa+1)} - \lambda_{\max}(\Phi^{(\kappa+1)})I_N)e^{\jmath\boldsymbol{\theta}}\} \\
&\quad -(e^{\jmath\theta^{(\kappa)}})^H(\Phi^{(\kappa+1)} - \lambda_{\max}(\Phi^{(\kappa+1)})I_N)e^{\jmath\theta^{(\kappa)}}] - \lambda_{\max}(\Phi^{(\kappa+1)})N \\
&= \tilde{a}^{(\kappa+1)} + 2\Re\{\sum_{n=1}^{N} (\tilde{b}^{(\kappa+1)}(n) - \sum_{m=1}^{N} e^{-\jmath\theta_m^{(\kappa)}}\Phi^{(\kappa+1)}(m,n) + \lambda_{\max}(\Phi^{(\kappa+1)})e^{-\jmath\theta_n^{(\kappa)}})e^{\jmath\theta_n}\} \\
&\quad -(e^{\jmath\theta^{(\kappa)}})^H\Phi^{(\kappa+1)}e^{\jmath\theta^{(\kappa)}} - 2\lambda_{\max}(\Phi^{(\kappa+1)})N. \qquad (6.26)
\end{aligned}$$

We thus solve the following problem at the κ-th iteration to generate $\theta^{(\kappa+1)}$:

$$\max_{\boldsymbol{\theta}} \ \tilde{f}_c^{(\kappa)}(\boldsymbol{\theta}), \qquad (6.27)$$

where the function $\tilde{f}_c^{(\kappa)}(\boldsymbol{\theta})$ is an affine function of $e^{\jmath\boldsymbol{\theta}}$. By noting that $\Re\{ce^{\jmath\theta_n}\} = |c|\cos(\angle c + \theta_n)$ and thus it is maximized at $\theta_n = -\angle c$, we obtain the closed-form solution of (6.27) as[3]

$$\begin{aligned}
\theta_n^{(\kappa+1)} &= -\angle(\tilde{b}^{(\kappa+1)}(n) - \sum_{m=1}^{N} e^{-\jmath\theta_m^{(\kappa)}}\Phi^{(\kappa+1)}(m,n) \\
&\quad +\lambda_{\max}(\Phi^{(\kappa+1)})e^{-\jmath\theta_n^{(\kappa)}}), n = 1, \ldots, N. \qquad (6.28)
\end{aligned}$$

It follows from (6.26) that $f^{(\kappa)}(w^{(\kappa+1)}, \theta^{(\kappa+1)}) \geq f_c^{(\kappa)}(\theta^{(\kappa+1)}) \geq \tilde{f}_c^{(\kappa)}(\theta^{(\kappa+1)}) > \tilde{f}_c^{(\kappa)}(\theta^{(\kappa)}) = f_c^{(\kappa)}(\theta^{(\kappa)}) = f^{(\kappa)}(w^{(\kappa+1)}, \theta^{(\kappa)})$, confirming (6.18), so $\theta^{(\kappa+1)}$ is a better feasible point than $\theta^{(\kappa)}$.

[3] $[(\Phi^{(\kappa+1)} - \mu I_N)e^{\jmath\theta^{(\kappa)}}](n)$ is the n-th entry of $(\Phi^{(\kappa+1)} - \mu I_N)e^{\jmath\theta^{(\kappa)}}$

6.2.3 Proper Gaussian Signaling Geometric Mean Rate Optimization

Algorithm 10 provides the pseudo-code for the proposed computational procedure of steepest descent for computing (6.9) as the iterations (6.17) and (6.28) seek a descent direction by seeking a better feasible point for the nonconvex problem (6.10) instead of seeking its optimal solution for reducing the computational load with guaranteed convergence, as it is often done in the context of the Frank-and-Wolfe method [149]. Of course, one can still seek the optimal solution of (6.10) for the steepest descent by iterating (6.17) and (6.28) many times, because according to [146], this kind of alternating descent iterations often converge to at least a locally optimal solution of (6.10). The global optimality can not be proved theoretically, but we found that it is globally optimal in many cases.

To the best of our knowledge, there is no the conventional descent algorithm, because the conception of descent descent algorithms is a research branch in computational optimization and what make descent algorithms different is the specific way they choose their a descent directions. Hence, our descent directions are completely new and rather different from the popular steepest descent techniques. Furthermore, all other exiting algorithms, which solve convex problems and iteratively at a high complexity are very sensitive to the problem sizes. However, our algorithms iterate using closed- form expressions, hence their complexity is low.

Algorithm 10 PGS GM descent algorithm

1: **Initialization:** Set $\kappa = 0$. Randomly generate $(w^{(0)}, \theta^{(0)})$ satisfying the constraint (6.7b) and define $\gamma^{(0)}$ by (6.12).
2: **Repeat until** (5.8) **is reached:** Generate $w^{(\kappa+1)}$ by (6.17) and $\theta^{(\kappa+1)}$ by (6.28). Reset $\kappa \leftarrow \kappa + 1$.
3: **Output** $(w^{(\kappa)}, \theta^{(\kappa)})$ and rates $r_k(w^{(\kappa)}, \theta^{(\kappa)})$, $k = 1, \ldots, K$ with their GM $\left(\prod_{k=1}^{K} r_k(w^{(\kappa)}, \theta^{(\kappa)})\right)^{1/K}$.

6.3 Improper Gaussian signaling

In (6.1), the proper Gaussian sources s_k are linearly beamformed by the beamformers $\boldsymbol{w}_k$, hence the transmit signal x is also proper Gaussian, i.e. $\mathbb{E}(xx^T) = \sum_{k\in\mathcal{K}} \boldsymbol{w}_k(\boldsymbol{w}_k)^T\mathbb{E}[(s_k)^2]0$. In this section, the proper Gaussian sources s_k are widely linearly beamformed by the pairs

of beamformers $\boldsymbol{w}_{1,k} \in \mathbb{C}^M$ and $\boldsymbol{w}_{2,k} \in \mathbb{C}^M$ as in [75]

$$\begin{bmatrix} \boldsymbol{w}_{1,k} & \boldsymbol{w}_{2,k} \end{bmatrix} \begin{bmatrix} s_k \\ s_k^* \end{bmatrix}, \tag{6.29}$$

resulting in the transmit signal

$$x = \sum_{k=1}^{K} (\boldsymbol{w}_{1,k} s_k + \boldsymbol{w}_{2,k} s_k^*), \tag{6.30}$$

and for improper Gaussian, as

$$\mathbb{E}(xx^T) = \sum_{k=1}^{K} (\boldsymbol{w}_{1,k}\boldsymbol{w}_{2,k}^T + \boldsymbol{w}_{2,k}\boldsymbol{w}_{1,k}^T)\mathbb{E}(|s_k|^2) \neq 0.$$

The equation (6.2) of the received signal at UE k becomes:

$$y_k = \mathcal{H}_k(\boldsymbol{\theta}) \sum_{k=1}^{K} (\boldsymbol{w}_{1,k} s_k + \boldsymbol{w}_{2,k} s_k^*) + n_k. \tag{6.31}$$

We augment (6.31) as

$$\begin{aligned} \begin{bmatrix} y_k \\ y_k^* \end{bmatrix} &= \begin{bmatrix} \mathcal{H}_k(\boldsymbol{\theta}) & 0 \\ 0 & \mathcal{H}_k^*(\boldsymbol{\theta}) \end{bmatrix} \sum_{k=1}^{K} \begin{bmatrix} \boldsymbol{w}_{1,k} & \boldsymbol{w}_{2,k} \\ \boldsymbol{w}_{2,k}^* & \boldsymbol{w}_{1,k}^* \end{bmatrix} \begin{bmatrix} s_k \\ s_k^* \end{bmatrix} + \begin{bmatrix} n_k \\ n_k^* \end{bmatrix} \\ &= \Lambda_k(\boldsymbol{\theta}) \sum_{k=1}^{K} \mathbf{W}_k \bar{s}_k + \bar{n}_k, \end{aligned} \tag{6.32}$$

for the linear mappings

$$\Lambda_k(\boldsymbol{\theta}) \triangleq \begin{bmatrix} \mathcal{H}_k(\boldsymbol{\theta}) & 0 \\ 0 & \mathcal{H}_k^*(\boldsymbol{\theta}) \end{bmatrix} \in \mathbb{C}^{2\times(2M)}, \mathbf{W}_k \triangleq \begin{bmatrix} \boldsymbol{w}_{1,k} & \boldsymbol{w}_{2,k} \\ \boldsymbol{w}_{2,k}^* & \boldsymbol{w}_{1,k}^* \end{bmatrix} \in \mathbb{C}^{2M\times 2},$$

and

$$\bar{s}_k \triangleq \begin{bmatrix} s_k \\ s_k^* \end{bmatrix} \in \mathbb{C}^2, \bar{n}_k \triangleq \begin{bmatrix} n_k \\ n_k^* \end{bmatrix} \in \mathbb{C}^2.$$

For $\boldsymbol{w} \triangleq \{\boldsymbol{w}_k \triangleq \begin{bmatrix} \boldsymbol{w}_{1,k} \\ \boldsymbol{w}_{2,k} \end{bmatrix} \in \mathbb{C}^{2M} : \ k \in \mathcal{K}\}$, the rate at UE k is calculated by $(1/2)r_k(\boldsymbol{w}, \boldsymbol{\theta})$ [74] with

$$r_k(\boldsymbol{w}, \boldsymbol{\theta}) = \ln \left| I_2 + [\Lambda_k(\boldsymbol{\theta})\mathbf{W}_k]^2 \left(\sum_{j \in \mathcal{K} \setminus \{k\}} [\Lambda_k(\boldsymbol{\theta})\mathbf{W}_j]^2 + \sigma I_2 \right)^{-1} \right|. \tag{6.33}$$

For the particular class of $\boldsymbol{w}_{2,k} \equiv 0$, i.e. when x in (6.30) is proper Gaussian, it may be shown that

$$r_k(\boldsymbol{w}, \boldsymbol{\theta}) = 2 \ln \left(1 + |\mathcal{H}_k(\boldsymbol{\theta})\boldsymbol{w}_{1,k}|^2 / (\textstyle\sum_{j \in \mathcal{K} \setminus \{k\}} |\mathcal{H}_k(\boldsymbol{\theta})\boldsymbol{w}_{1,j}|^2 + \sigma) \right),$$

hence $(1/2)r_k(\boldsymbol{w}, \boldsymbol{\theta})$ is the known rate (6.6).

Like (6.8), the problem of maximizing the GM for users' rates corresponding IGS is thus formulated as

$$\min_{\boldsymbol{w}, \boldsymbol{\theta}} f\left(r_1(\boldsymbol{w}, \boldsymbol{\theta}), \ldots, r_K(\boldsymbol{w}, \boldsymbol{\theta})\right) \triangleq \frac{1}{\left(\prod_{k=1}^{K} r_k(\boldsymbol{w}, \boldsymbol{\theta}) \right)^{1/K}} \tag{6.34a}$$

$$\text{s.t.} \sum_{k=1}^{K} (||\boldsymbol{w}_{1,k}||^2 + ||\boldsymbol{w}_{2,k}||^2) \leq P. \tag{6.34b}$$

Let $(w^{(\kappa)}, \theta^{(\kappa)})$ be a feasible point for (6.34) that is found from the $(\kappa-1)$-st round. Like (6.11), we use the following steepest descent optimization for the convex function $f(r_1, \ldots, r_K) = 1/(\prod_{k=1}^{K} r_k)^{1/K}$ to generate the next feasible point $(w^{(\kappa+1)}, \theta^{(\kappa+1)})$:

$$\max_{\boldsymbol{w}, \boldsymbol{\theta}} \ F^{(\kappa)}(\boldsymbol{w}, \boldsymbol{\theta}) \triangleq \sum_{k=1}^{K} \gamma_k^{(\kappa)} r_k(\boldsymbol{w}, \boldsymbol{\theta}) \quad \text{s.t.} \quad (6.34b) \tag{6.35}$$

where

$$\gamma_k^{(\kappa)} \triangleq \frac{f\left(r_1(w^{(\kappa)}, \theta^{(\kappa)}), \ldots, r_K(w^{(\kappa)}, \theta^{(\kappa)}) \right)}{r_k(w^{(\kappa)}, \theta^{(\kappa)})}, k = 1, \ldots, K. \tag{6.36}$$

Another way of defining the UEs' rates is through the equivalent composite real system for (6.31):

$$\begin{aligned}
\tilde{y}_k &\triangleq \begin{bmatrix} \Re\{y_k\} \\ \Im\{y_k\} \end{bmatrix} \\
&= \begin{bmatrix} \Re\{\mathcal{H}_k(\boldsymbol{\theta})\} & -\Im\{\mathcal{H}_k(\boldsymbol{\theta})\} \\ \Im\{\mathcal{H}_k(\boldsymbol{\theta})\} & \Re\{\mathcal{H}_k(\boldsymbol{\theta})\} \end{bmatrix} \\
&\quad \times \sum_{j=1}^{K} \begin{bmatrix} \Re\{\boldsymbol{w}_{1,j}\} + \Re\{\boldsymbol{w}_{2,j}\} & -\Im\{\boldsymbol{w}_{1,j}\} + \Im\{\boldsymbol{w}_{2,j}\} \\ \Im\{\boldsymbol{w}_{1,j}\} + \Im\{\boldsymbol{w}_{2,j}\} & \Re\{\boldsymbol{w}_{1,j}\} - \Re\{\boldsymbol{w}_{2,j}\} \end{bmatrix} \begin{bmatrix} \Re\{s_j\} \\ \Im\{s_j\} \end{bmatrix} + \begin{bmatrix} \Re\{n_k\} \\ \Im\{n_k\} \end{bmatrix} \\
&= \bar{\mathcal{H}}_k(\boldsymbol{\theta}) \sum_{j=1}^{K} \mathbf{V}_j \tilde{s}_j + \tilde{n}_k, \qquad (6.37)
\end{aligned}$$

where we have:

$$\bar{\mathcal{H}}_k(\boldsymbol{\theta}) \triangleq \begin{bmatrix} \Re\{\mathcal{H}_k(\boldsymbol{\theta})\} & -\Im\{\mathcal{H}_k(\boldsymbol{\theta})\} \\ \Im\{\mathcal{H}_k(\boldsymbol{\theta})\} & \Re\{\mathcal{H}_k(\boldsymbol{\theta})\} \end{bmatrix}, \tilde{s}_j \triangleq \begin{bmatrix} \Re\{s_j\} \\ \Im\{s_j\} \end{bmatrix}, \qquad (6.38)$$

$$\mathbf{V}_j \triangleq \begin{bmatrix} \boldsymbol{v}_j^{11} & \boldsymbol{v}_j^{12} \\ \boldsymbol{v}_j^{21} & \boldsymbol{v}_j^{22} \end{bmatrix}, \tilde{n}_k = \begin{bmatrix} \Re\{n_k\} \\ \Im\{n_k\} \end{bmatrix}, \qquad (6.39)$$

under the following transformation:

$$\begin{bmatrix} \Re\{\boldsymbol{w}_{1,j}\} + \Re\{\boldsymbol{w}_{2,j}\} & -\Im\{\boldsymbol{w}_{1,j}\} + \Im\{\boldsymbol{w}_{2,j}\} \\ \Im\{\boldsymbol{w}_{1,j}\} + \Im\{\boldsymbol{w}_{2,j}\} & \Re\{\boldsymbol{w}_{1,j}\} - \Re\{\boldsymbol{w}_{2,j}\} \end{bmatrix} = \mathbf{V}_j. \qquad (6.40)$$

This transform is indeed legitimate, since its inverse is given by

$$\begin{bmatrix} \Re\{\boldsymbol{w}_{1,j}\} & \Im\{\boldsymbol{w}_{1,j}\} \\ \Re\{\boldsymbol{w}_{2,j}\} & \Im\{\boldsymbol{w}_{2,j}\} \end{bmatrix} = \frac{1}{2} \begin{bmatrix} \boldsymbol{v}_j^{11} + \boldsymbol{v}_j^{22} & \boldsymbol{v}_j^{21} - \boldsymbol{v}_j^{12} \\ \boldsymbol{v}_j^{11} - \boldsymbol{v}_j^{22} & \boldsymbol{v}_j^{21} + \boldsymbol{v}_j^{12} \end{bmatrix}. \qquad (6.41)$$

Furthermore, we have:

$$||\boldsymbol{w}_j||^2 = \frac{1}{2} \sum_{i=1}^{2} \sum_{\ell=1}^{2} ||\boldsymbol{v}_j^{i\ell}||^2, \qquad (6.42)$$

hence the power constraint (6.34b) for $\boldsymbol{w}$ is transferred to the following constraint

$$\sum_{j=1}^{K} ||\boldsymbol{v}_j||^2 \leq 2P \qquad (6.43)$$

for

$$\boldsymbol{v}_j \triangleq \mathsf{vec}(\mathbf{V}_j) = \begin{bmatrix} \boldsymbol{v}_j^{11} \\ \boldsymbol{v}_j^{21} \\ \boldsymbol{v}_j^{12} \\ \boldsymbol{v}_j^{22} \end{bmatrix}. \tag{6.44}$$

For $\boldsymbol{v} \triangleq \{\boldsymbol{v}_j, j \in \mathcal{K}\}$, the problem (6.35) is equivalent to the problem

$$\max_{\boldsymbol{v},\boldsymbol{\theta}} \tilde{F}^{(\kappa)}(\boldsymbol{v},\boldsymbol{\theta}) \triangleq \sum_{k=1}^{K} \gamma_k^{(\kappa)} \tilde{r}_k(\boldsymbol{v},\boldsymbol{\theta}) \quad \text{s.t.} \quad (6.43) \tag{6.45}$$

with

$$\tilde{r}_k(\boldsymbol{v},\boldsymbol{\theta}) = \ln \left| I_2 + [\bar{\mathcal{H}}_k(\boldsymbol{\theta})\mathbf{V}_k]^2 \left(\sum_{j \in \mathcal{K}\setminus\{k\}} [\bar{\mathcal{H}}_k(\boldsymbol{\theta})\mathbf{V}_j]^2 + \sigma I_2 \right)^{-1} \right|. \tag{6.46}$$

We propose the following alternating descent iterations at the κ-th round to generate a better feasible point $(w^{(\kappa+1)}, \theta^{(\kappa+1)})$.

6.3.1 Widely linear beamforming descent iteration

We seek $w^{(\kappa+1)}$ such that

$$F^{(\kappa)}(w^{(\kappa+1)}, \theta^{(\kappa)}) > F^{(\kappa)}(w^{(\kappa)}, \theta^{(\kappa)}). \tag{6.47}$$

Upon using (6.40) to define

$$V_j^{(\kappa)} \triangleq \begin{bmatrix} \Re\{w_{1,j}^{(\kappa)}\} + \Re\{w_{2,j}^{(\kappa)}\} & -\Im\{w_{1,j}^{(\kappa)}\} + \Im\{w_{2,j}^{(\kappa)}\} \\ \Im\{w_{1,j}^{(\kappa)}\} + \Im\{w_{2,j}^{(\kappa)}\} & \Re\{w_{1,j}^{(\kappa)}\} - \Re\{w_{2,j}^{(\kappa)}\} \end{bmatrix} \tag{6.48}$$

we have $v_j^{(\kappa)} \triangleq \mathsf{vec}(V_j^{(\kappa)})$.

By using the inequality (A.15) for

$$\mathbf{V} = \bar{\mathcal{H}}_k(\theta^{(\kappa)})\mathbf{V}_k,$$
$$\mathbf{Y} = \sum_{j \in \mathcal{K}\setminus\{k\}} [\bar{\mathcal{H}}_k(\theta^{(\kappa)})\mathbf{V}_j]^2 + \sigma I_2,$$

and

$$\bar{V} = \bar{\mathcal{H}}_k(\theta^{(\kappa)})V_k^{(\kappa)},$$
$$\bar{Y} = Y_k^{(\kappa)} \triangleq \sum_{j\in\mathcal{K}\setminus\{k\}} [\bar{\mathcal{H}}_k(\theta^{(\kappa)})V_j^{(\kappa)}]^2 + \sigma I_2 \succeq 0,$$

we obtain the following concave quadratic lower bounding function approximation of $\tilde{r}_k(\theta^{(\kappa)}, \boldsymbol{v})$:

$$\tilde{r}_k(\boldsymbol{v}, \theta^{(\kappa)}) \geq \tilde{r}_k^{(\kappa)}(\boldsymbol{v}) \triangleq a_k^{(\kappa)} + 2\langle B_k^{(\kappa)}\mathbf{V}_k\rangle - \langle C_k^{(\kappa)}, \sum_{j\in\mathcal{K}}[\bar{\mathcal{H}}_k(\theta^{(\kappa)})\mathbf{V}_j]^2\rangle, \tag{6.49}$$

with

$$a_k^{(\kappa)} \triangleq \tilde{r}_k(v^{(\kappa)}, \theta^{(\kappa)}) - \langle [\bar{\mathcal{H}}_k(\theta^{(\kappa)})V_k^{(\kappa)}]^2 (Y_k^{(\kappa)})^{-1}\rangle - \sigma\langle C_k^{(\kappa)}\rangle,$$
$$B_k^{(\kappa)} \triangleq (V_k^{(\kappa)})^H (\bar{\mathcal{H}}_k(\theta^{(\kappa)}))^t (Y_k^{(\kappa)})^{-1} \times \bar{\mathcal{H}}_k(\theta^{(\kappa)},$$

and

$$0 \prec C_k^{(\kappa)} \triangleq (Y_k^{(\kappa)})^{-1} - \left(Y_k^{(\kappa)} + [\bar{\mathcal{H}}_k(\theta^{(\kappa)})V_k^{(\kappa)}]^2\right)^{-1}.$$

Note that $\langle B_k^{(\kappa)}\mathbf{V}_k\rangle = \langle \mathsf{vec}((B_k^{(\kappa)})^T), \boldsymbol{v}_k\rangle$, and

$$\begin{aligned}
\langle C_k^{(\kappa)}, [\bar{\mathcal{H}}_k(\theta^{(\kappa)})\mathbf{V}_j]^2\rangle &= ||\mathsf{vec}\left((C_k^{(\kappa)})^{1/2}\bar{\mathcal{H}}_k(\theta^{(\kappa)})\mathbf{V}_j\right)||^2 \\
&= ||\left(I_2 \otimes ((C_k^{(\kappa)})^{1/2}\bar{\mathcal{H}}_k(\theta^{(\kappa)}))\right)\mathsf{vec}(\mathbf{V}_j)||^2 \\
&= \mathsf{vec}^T(\mathbf{V}_j)\left[I_2 \otimes \left(\bar{\mathcal{H}}_k^T(\theta^{(\kappa)})C_k^{(\kappa)}\bar{\mathcal{H}}_k(\theta^{(\kappa)})\right)\right]\mathsf{vec}(\mathbf{V}_j) \\
&= \boldsymbol{v}_j^T\mathcal{Q}_k^{(\kappa)}\boldsymbol{v}_j
\end{aligned}$$

for $\mathcal{Q}_k^{(\kappa)} \triangleq I_2 \otimes \left(\bar{\mathcal{H}}_k^T(\theta^{(\kappa)})C_k^{(\kappa)}\bar{\mathcal{H}}_k(\theta^{(\kappa)})\right)$.

Thus,we have

$$\begin{aligned}
\sum_{k=1}^K \gamma_k^{(\kappa)}\tilde{r}_k^{(\kappa)}(\boldsymbol{w}) &= \sum_{k=1}^K \gamma_k^{(\kappa)}a_k^{(\kappa)} + 2\sum_{k=1}^K \langle \gamma_k^{(\kappa)}\mathsf{vec}((B_k^{(\kappa)})^T), \boldsymbol{v}_k\rangle + \sum_{k=1}^K\sum_{j=1}^K \boldsymbol{v}_j^T(\gamma_k^{(\kappa)}\mathcal{Q}_k^{(\kappa)})\boldsymbol{v}_j \\
&= \sum_{k=1}^K \gamma_k^{(\kappa)}a_k^{(\kappa)} + 2\sum_{k=1}^K \langle \gamma_k^{(\kappa)}\mathsf{vec}((B_k^{(\kappa)})^T), \boldsymbol{v}_k\rangle + \sum_{k=1}^K \boldsymbol{v}_k^T\left(\sum_{j=1}^K \gamma_j^{(\kappa)}\mathcal{Q}_j^{(\kappa)}\right)\boldsymbol{v}_k
\end{aligned} \tag{6.50}$$

We solve the following convex problem at the κ-th iteration to generate $v^{(\kappa+1)}$:

$$\max_{\boldsymbol{w}} \sum_{k=1}^{K} \gamma_k^{(\kappa)} \tilde{r}_k^{(\kappa)}(\boldsymbol{w}) \quad \text{s.t.} \quad (6.43), \tag{6.51}$$

which similarly to (6.15) gives

$$\tilde{F}^{(\kappa)}(v^{(\kappa+1)}, \theta^{(\kappa)}) > \tilde{F}^{(\kappa)}(v^{(\kappa)}, \theta^{(\kappa)}) \tag{6.52}$$

as far as $v^{(\kappa+1)} \neq v^{(\kappa)}$.

Like (6.15), the problem (6.51) admits the following closed-form solution

$$v_k^{(\kappa+1)} = \begin{cases} \left(\sum_{j=1}^{K} \gamma_j^{(\kappa)} \mathcal{Q}_j^{(\kappa)}\right)^{-1} \gamma_k^{(\kappa)} \mathsf{vec}((B_k^{(\kappa)})^T) \\ \text{if } \sum_{k=1}^{K} || \left(\sum_{j=1}^{K} \gamma_j^{(\kappa)} \mathcal{Q}_j^{(\kappa)}\right)^{-1} \gamma_k^{(\kappa)} \mathsf{vec}((B_k^{(\kappa)})^T)||^2 \leq 2P \\ \left(\sum_{j=1}^{K} \gamma_j^{(\kappa)} \mathcal{Q}_j^{(\kappa)} + \mu I_M\right)^{-1} \gamma_k^{(\kappa)} \mathsf{vec}((B_k^{(\kappa)})^T) \quad \text{otherwise,} \end{cases} \tag{6.53}$$

where $\mu > 0$ is found by bisection such that

$$\sum_{k=1}^{K} || \left(\sum_{j=1}^{K} \gamma_j^{(\kappa)} \mathcal{Q}_j^{(\kappa)} + \mu I_M\right)^{-1} \gamma_k^{(\kappa)} \mathsf{vec}((B_k^{(\kappa)})^T)||^2 = 2P.$$

By reconstructing $v_j^{i\ell,(\kappa+1)}$, $i = 1, 2$ and $\ell = 1, 2$, from $v_j^{(\kappa+1)}$ we use (6.41) to determine $w_{1,j}^{(\kappa+1)}$ and $w_{2,j}^{(\kappa+1)}$:

$$\begin{bmatrix} \Re\{w_{1,j}^{(\kappa+1)}\} & \Im\{w_{1,j}^{(\kappa+1)}\} \\ \Re\{w_{1,j}^{(\kappa+1)}\} & \Im\{w_{1,j}^{(\kappa+1)}\} \end{bmatrix} = \frac{1}{2} \begin{bmatrix} v_j^{11,(\kappa+1)} + v_j^{22,(\kappa+1)} & v_j^{21,(\kappa+1)} - v_j^{12,(\kappa+1)} \\ v_j^{11,(\kappa+1)} - v_j^{22,(\kappa+1)} & v_j^{21,(\kappa+1)} + v_j^{12,(\kappa+1)} \end{bmatrix}, \tag{6.54}$$

which results in (6.47).

6.3.2 Programmable reflecting elements' descent iteration

We seek $\theta^{(\kappa+1)}$ such that

$$F^{(\kappa)}(w^{(\kappa+1)}, \theta^{(\kappa+1)}) > F^{(\kappa)}(w^{(\kappa+1)}, \theta^{(\kappa)}). \tag{6.55}$$

By using the inequality (A.15) for

$$\mathbf{V} = \Lambda_k(\boldsymbol{\theta})W_k^{(\kappa+1)}, \mathbf{Y} = \sum_{j\in\mathcal{K}\setminus\{k\}} [\Lambda_k(\boldsymbol{\theta})W_j^{(\kappa+1)}]^2 + \sigma I_2,$$

and

$$\bar{V} = \Lambda_k(\theta^{(\kappa)})W_k^{(\kappa+1)}, \bar{Y} = Y_k^{(\kappa+1)} \triangleq \sum_{j\in\mathcal{K}\setminus\{k\}} [\Lambda_k(\theta^{(\kappa)})W_j^{(\kappa+1)}]^2 + \sigma I_2 \succeq 0,$$

we obtain the following concave quadratic lower bounding function approximation of $r_k(w^{(\kappa+1)}, \boldsymbol{\theta})$:

$$\begin{aligned} r_k(w^{(\kappa+1)}, \boldsymbol{\theta}) &\geq \tilde{r}_k^{(\kappa)}(\boldsymbol{\theta}) \\ &\triangleq \tilde{a}_{1k}^{(\kappa)} + 2\Re\{\langle \tilde{B}_k^{(\kappa)}\Lambda_k(\boldsymbol{\theta})W_k^{(\kappa+1)}\rangle\} - \langle \tilde{C}_k^{(\kappa)}, \sum_{j\in\mathcal{K}}[\Lambda_k(\boldsymbol{\theta})W_j^{(\kappa+1)}]^2\rangle \\ &= \tilde{a}_{1k}^{(\kappa)} + 2\Re\{\langle \tilde{B}_k^{(\kappa)}\Lambda_k(\boldsymbol{\theta})W_k^{(\kappa+1)}\rangle\} - \langle \tilde{C}_k^{(\kappa)}, \Lambda_k(\boldsymbol{\theta})\mathcal{W}_k^{(\kappa+1)}(\Lambda_k(\boldsymbol{\theta}))^H\rangle, \end{aligned} \tag{6.56}$$

with

$$\begin{aligned} \tilde{a}_{1k}^{(\kappa)} &\triangleq r_k(w^{(\kappa+1)}, \theta^{(\kappa)}) - \langle [\Lambda_k(\theta^{(\kappa)})W_k^{(\kappa+1)}]^2 (Y_k^{(\kappa+1)})^{-1}\rangle - \sigma\langle \tilde{C}_k^{(\kappa)}\rangle, \\ \tilde{B}_k^{(\kappa)} &\triangleq (W_k^{(\kappa+1)})^H(\Lambda_k(\theta^{(\kappa)}))^H(Y_k^{(\kappa+1)})^{-1} \in \mathbb{C}^{2\times 2}, \\ 0 \prec \tilde{C}_k^{(\kappa)} &\triangleq (Y_k^{(\kappa+1)})^{-1} - \left(Y_k^{(\kappa+1)} + [\Lambda_k(\theta^{(\kappa)})W_k^{(\kappa+1)}]^2\right)^{-1} \in \mathbb{C}^{2\times 2}, \end{aligned}$$

and

$$0 \prec \mathcal{W}_k^{(\kappa+1)} \triangleq \sum_{j\in\mathcal{K}} [W_j^{(\kappa+1)}]^2.$$

For

$$\mathcal{H}_{\text{B-k}} \triangleq \begin{bmatrix} \tilde{h}_{\text{B-k}} & 0_{1\times M} \\ 0_{1\times M} & \tilde{h}_{\text{B-k}}^* \end{bmatrix},$$

we can write

$$\begin{aligned}\Lambda_k(\boldsymbol{\theta}) &= \\ \mathcal{H}_{\text{B-k}} + \begin{bmatrix} \tilde{h}_{\text{BR-k}}\mathsf{diag}(e^{\jmath\boldsymbol{\theta}})H_{\text{B-R}} & 0_{1\times M} \\ 0_{1\times M} & \tilde{h}^*_{\text{R-k}}\mathsf{diag}(e^{-\jmath\boldsymbol{\theta}})H^*_{\text{B-R}} \end{bmatrix} &= \\ \mathcal{H}_{\text{B-k}} + \sum_{n=1}^{N}\left[\begin{bmatrix} \tilde{h}_{\text{BR-k}}\Psi_n H_{\text{B-R}} & 0_{1\times M} \\ 0_{1\times M} & 0_{1\times M} \end{bmatrix} e^{\jmath\theta_n} + \begin{bmatrix} 0_{1\times M} & 0_{1\times M} \\ 0_{1\times M} & \tilde{h}^*_{\text{R-k}}\Psi_n H^*_{\text{B-R}} \end{bmatrix} e^{-\jmath\theta_n}\right] &= \\ \mathcal{H}_{\text{B-k}} + \sum_{n=1}^{N}\left[\Gamma_n e^{\jmath\theta_n} + \Xi_n e^{-\jmath\theta_n}\right], \qquad (6.57)\end{aligned}$$

with

$$\begin{aligned}\Gamma_n &\triangleq \begin{bmatrix} \tilde{h}_{\text{BR-k}}\Psi_n H_{\text{B-R}} & 0_{1\times M} \\ 0_{1\times M} & 0_{1\times M} \end{bmatrix}, n = 1,\ldots,N, \\ \Xi_n &\triangleq \begin{bmatrix} 0_{1\times M} & 0_{1\times M} \\ 0_{1\times M} & \tilde{h}^*_{\text{R-k}}\Psi_n H^*_{\text{B-R}} \end{bmatrix}, n = 1,\ldots,N. \qquad (6.58)\end{aligned}$$

By using the identity

$$\Re\{ab^*\} = \Re\{a^*b\} \quad \forall\ a \in \mathbb{C}, b \in \mathbb{C}, \qquad (6.59)$$

we arrive at:

$$\begin{aligned}\Re\{\langle \tilde{B}_k^{(\kappa)}\Lambda_k(\boldsymbol{\theta})W_k^{(\kappa+1)}\rangle\} &= \tilde{a}_{2k}^{(\kappa)} + \Re\{\sum_{n=1}^{N}(\hat{b}_{1k}^{(\kappa)}(n)e^{\jmath\theta_n} + \hat{b}_{2k}^{(\kappa)}(n)e^{-\jmath\theta_n})\} \\ &= \tilde{a}_{2k}^{(\kappa)} + \Re\{\sum_{n=1}^{N}\tilde{b}_{2k}^{(\kappa)}(n)e^{\jmath\theta_n}\}, \qquad (6.60)\end{aligned}$$

for

$$\begin{aligned}\tilde{a}_{2k}^{(\kappa)} &\triangleq \Re\{\langle \tilde{B}_k^{(\kappa)}\mathcal{H}_{\text{B-k}}W_k^{(\kappa+1)}\rangle\}, \\ \hat{b}_{1k}^{(\kappa)}(n) &\triangleq \langle \tilde{B}_k^{(\kappa)}\Gamma_n W_k^{(\kappa+1)}\rangle, \\ \hat{b}_{2k}^{(\kappa)}(n) &\triangleq \langle \tilde{B}_k^{(\kappa)}\Xi_n W_k^{(\kappa+1)}\rangle,\end{aligned}$$

and

$$\tilde{b}_{2k}^{(\kappa)}(n) = \hat{b}_{1k}^{(\kappa)}(n) + (\hat{b}_{2k}^{(\kappa)})^*(n), n = 1,\ldots,N.$$

Furthermore,

$$\begin{aligned}
\langle \tilde{C}_k^{(\kappa)}, \Lambda_k(\boldsymbol{\theta}) \mathcal{W}_k^{(\kappa+1)} \Lambda_k^H(\boldsymbol{\theta}) \rangle &= \\
\langle \tilde{C}_k^{(\kappa)}, \left[\sum_{n=1}^{N} \left(\Gamma_n e^{\jmath\theta_n} + \Xi_n e^{-\jmath e^{\jmath\theta_n}} \right) + \mathcal{H}_{\text{B-k}} \right] \mathcal{W}_k^{(\kappa+1)} \left[\sum_{n=1}^{N} \left(\Gamma_n^H e^{-\jmath\theta_n} + \Xi_n^H e^{\jmath\theta_n} \right) + \mathcal{H}_{\text{B-k}}^H \right] \rangle &= \\
\langle \tilde{C}_k^{(\kappa)}, \mathcal{H}_{\text{B-k}} \mathcal{W}_k^{(\kappa+1)} \mathcal{H}_{\text{B-k}}^H \rangle + 2\Re\{ \langle \tilde{C}_k^{(\kappa)}, \mathcal{H}_{\text{B-k}} \mathcal{W}_k^{(\kappa+1)} \sum_{n=1}^{N} \left(\Gamma_n^H e^{-\jmath\theta_n} + \Xi_n^H e^{\jmath\theta_n} \right) \} & \\
+ \langle \tilde{C}_k^{(\kappa)}, \left[\sum_{n=1}^{N} \left(\Gamma_n e^{\jmath\theta_n} + \Xi_n e^{-\jmath\theta_n} \right) \right] \mathcal{W}_k^{(\kappa+1)} \left[\sum_{n=1}^{N} \left(\Gamma_n^H e^{-\jmath\theta_n} + \Xi_n^H e^{\jmath\theta_n} \right) \right] \rangle &= \\
\langle \tilde{C}_k^{(\kappa)}, \mathcal{H}_{\text{B-k}} \mathcal{W}_k^{(\kappa+1)} \mathcal{H}_{\text{B-k}}^H \rangle & \\
+ 2\Re\{ \sum_{n=1}^{N} \left(\langle \tilde{C}_k^{(\kappa)}, \mathcal{H}_{\text{B-k}} \mathcal{W}_k^{(\kappa+1)} \Gamma_n^H \rangle^* + \langle \tilde{C}_k^{(\kappa)}, \mathcal{H}_{\text{B-k}} \mathcal{W}_k^{(\kappa+1)} \Xi_n^H \rangle \right) e^{\jmath\theta_n} \} & \\
+ \sum_{n=1}^{N} \sum_{m=1}^{N} \langle \tilde{C}_k^{(\kappa)}, \Gamma_n \mathcal{W}_k^{(\kappa+1)} \Gamma_m^H \rangle e^{\jmath\theta_n} e^{-\jmath\theta_m} + \sum_{n=1}^{N} \sum_{m=1}^{N} \langle \tilde{C}_k^{(\kappa)}, \Gamma_n \mathcal{W}_k^{(\kappa+1)} \Xi_m^H \rangle e^{\jmath\theta_n} e^{-\jmath\theta_m} & \\
+ \sum_{n=1}^{N} \sum_{m=1}^{N} \langle \tilde{C}_k^{(\kappa)}, \Xi_n \mathcal{W}_k^{(\kappa+1)} \Gamma_m^H \rangle e^{-\jmath\theta_n} e^{-\jmath\theta_m} + \sum_{n=1}^{N} \sum_{m=1}^{N} \langle \tilde{C}_k^{(\kappa)}, \Xi_n \mathcal{W}_k^{(\kappa+1)} \Xi_m^H \rangle e^{-\jmath\theta_n} e^{-\jmath\theta_m} &= \\
\tilde{a}_{3k}^{(\kappa)} + 2\Re\{ \sum_{n=1}^{N} \tilde{b}_{3k}^{(\kappa)}(n) e^{\jmath\theta_n} \rangle \} + (e^{\jmath\boldsymbol{\theta}})^H \mathcal{Q}_{22,k}^{(\kappa)} e^{\jmath\boldsymbol{\theta}} + (e^{\jmath\boldsymbol{\theta}})^T \mathcal{Q}_{12,k}^{(\kappa)} e^{\jmath\boldsymbol{\theta}} + (e^{\jmath\boldsymbol{\theta}})^H (\mathcal{Q}_{12,k}^{(\kappa)})^* e^{-\jmath\boldsymbol{\theta}} & \\
+ (e^{\jmath\boldsymbol{\theta}})^H \mathcal{Q}_{11,k}^{(\kappa)} e^{\jmath\boldsymbol{\theta}}, \quad (6.61) &
\end{aligned}$$

where

$$\begin{aligned}
\tilde{a}_{3k}^{(\kappa)} &\triangleq \langle \tilde{C}_k^{(\kappa)}, \mathcal{H}_{\text{B-k}} \mathcal{W}_k^{(\kappa+1)} \mathcal{H}_{\text{B-k}}^H \rangle, \\
\tilde{b}_{3k}^{(\kappa)}(n) &\triangleq \langle \tilde{C}_k^{(\kappa)}, \mathcal{H}_{\text{B-k}} \mathcal{W}_k^{(\kappa+1)} \Gamma_n^H \rangle^* + \langle \tilde{C}_k^{(\kappa)}, \mathcal{H}_{\text{B-k}} \mathcal{W}_k^{(\kappa+1)} \Xi_n^H \rangle, \\
\mathcal{Q}_{11,k}^{(\kappa)}(n,m) &= \langle \tilde{C}_k^{(\kappa)}, \Xi_n \mathcal{W}_k^{(\kappa+1)} \Xi_m^H \rangle, \\
\mathcal{Q}_{22,k}^{(\kappa)}(n,m) &= \langle \tilde{C}_k^{(\kappa)}, \Gamma_m \mathcal{W}_k^{(\kappa+1)} \Gamma_n^H \rangle, \\
\mathcal{Q}_{12,k}^{(\kappa)}(n,m) &= \langle \tilde{C}_k^{(\kappa)}, \Gamma_n \mathcal{W}_k^{(\kappa+1)} \Xi_m^H \rangle, n = 1, \ldots, N; m = 1, \ldots, N.
\end{aligned}$$

Let us define

$$\begin{aligned}
\mathcal{Q}_{22,k}^{(\kappa)} + \mathcal{Q}_{11,k}^{(\kappa)} &= \mathcal{Q}_{2,k}^{R,(\kappa)} + \jmath \mathcal{Q}_{2,k}^{I,(\kappa)}, \\
\mathcal{Q}_{2,k}^{R,(\kappa)} &\in \mathbb{R}^{N \times N}, \mathcal{Q}_{2,k}^{I,(\kappa)} \in \mathbb{R}^{N \times N},
\end{aligned}$$

$$(e^{\jmath\boldsymbol{\theta}})^H(\mathcal{Q}_{22,k}^{(\kappa)}+\mathcal{Q}_{11,k}^{(\kappa)})e^{\jmath\boldsymbol{\theta}}=\begin{bmatrix}\cos\boldsymbol{\theta}\\ \sin\boldsymbol{\theta}\end{bmatrix}^T\begin{bmatrix}\mathcal{Q}_{2,k}^{R,(\kappa)} & -\mathcal{Q}_{2,k}^{I,(\kappa)}\\ \mathcal{Q}_{2,k}^{I,(\kappa)} & \mathcal{Q}_{2,k}^{R,(\kappa)}\end{bmatrix}\begin{bmatrix}\cos\boldsymbol{\theta}\\ \sin\boldsymbol{\theta}\end{bmatrix}, \tag{6.62}$$

$$\begin{aligned}(e^{\jmath\boldsymbol{\theta}})^T\mathcal{Q}_{12,k}^{(\kappa)}e^{\jmath\boldsymbol{\theta}}+(e^{\jmath\boldsymbol{\theta}})^H(\mathcal{Q}_{12,k}^{(\kappa)})^*e^{-\jmath\boldsymbol{\theta}} &= \\ \begin{bmatrix}\cos\boldsymbol{\theta}\\ \sin\boldsymbol{\theta}\end{bmatrix}^T\begin{bmatrix}\mathcal{Q}_{1,k}^{R,(\kappa)}+(\mathcal{Q}_{1,k}^{R,(\kappa)})^T & -\mathcal{Q}_{1,k}^{I,(\kappa)}-(\mathcal{Q}_{1,k}^{I,(\kappa)})^T\\ -\mathcal{Q}_{1,k}^{I,(\kappa)}-(\mathcal{Q}_{1,k}^{I,(\kappa)})^T & -\mathcal{Q}_{1,k}^{R,(\kappa)}-(\mathcal{Q}_{1,k}^{R,(\kappa)})^T\end{bmatrix}\begin{bmatrix}\cos\boldsymbol{\theta}\\ \sin\boldsymbol{\theta}\end{bmatrix}, &\end{aligned} \tag{6.63}$$

where the matrix $\mathcal{Q}_{2,k}^{R,(\kappa)}$ is symmetric, while the matrix $\mathcal{Q}_{2,k}^{I,(\kappa)}$ is skew-symmetric because the matrix $\mathcal{Q}_{22,k}^{(\kappa)}+\mathcal{Q}_{11,k}^{(\kappa)}$ is Hermitian symmetric, and

$$\mathcal{Q}_{12,k}^{(\kappa)}=\mathcal{Q}_{1,k}^{R,(\kappa)}+\jmath\mathcal{Q}_{1,k}^{I,(\kappa)},\mathcal{Q}_{1,k}^{R,(\kappa)}\in\mathbb{R}^{N\times N},\mathcal{Q}_{1,k}^{I,(\kappa)}\in\mathbb{R}^{N\times N}.$$

Upon recalling that $e^{\jmath\boldsymbol{\theta}}=\cos\boldsymbol{\theta}+\jmath\sin\boldsymbol{\theta}$, we have (6.62) and (6.63), whose proof is given in the Appendix.

Therefore, we have (6.64) for

$$\begin{aligned}\mathcal{Q}_{k,R}^{(\kappa)}&\triangleq\mathcal{Q}_{2,k}^{R,(\kappa)}+\mathcal{Q}_{1,k}^{R,(\kappa)}+(\mathcal{Q}_{1,k}^{R,(\kappa)})^T,\\ \mathcal{Q}_{k,C}^{(\kappa)}&\triangleq-\mathcal{Q}_{2,k}^{I,(\kappa)}-\mathcal{Q}_{1,k}^{I,(\kappa)}-(\mathcal{Q}_{1,k}^{I,(\kappa)})^T,\\ \mathcal{Q}_{k,I}^{(\kappa)}&\triangleq\mathcal{Q}_{2,k}^{R,(\kappa)}-\mathcal{Q}_{1,k}^{R,(\kappa)}-(\mathcal{Q}_{1,k}^{R,(\kappa)})^T.\end{aligned}$$

Combining (6.56), (6.60), (6.61), and (6.64) yields

$$\gamma_k^{(\kappa)}\tilde{r}^{(\kappa)}(w^{(\kappa+1)},\boldsymbol{\theta}) = \tilde{a}_k^{(\kappa)}+2\Re\{\sum_{n=1}^{N}\tilde{b}_k^{(\kappa)}(n)e^{\jmath\theta_n}\}-\begin{bmatrix}\cos\boldsymbol{\theta}\\ \sin\boldsymbol{\theta}\end{bmatrix}^T\mathcal{Q}_k^{(\kappa)}\begin{bmatrix}\cos\boldsymbol{\theta}\\ \sin\boldsymbol{\theta}\end{bmatrix} \tag{6.65}$$

with

$$\begin{aligned}\tilde{a}_k^{(\kappa)}&=\gamma_k^{(\kappa)}\left(\tilde{a}_{1k}^{(\kappa)}+2\tilde{a}_{2k}^{(\kappa)}-\tilde{a}_{3k}^{(\kappa)}\right),\\ \tilde{b}_k^{(\kappa)}(n)&=\gamma_k^{(\kappa)}\left(\tilde{b}_{2k}^{(\kappa)}(n)-\tilde{b}_{3k}^{(\kappa)}(n)\right),n=1,\ldots,N,\\ \mathcal{Q}_k^{(\kappa)}&=\gamma_k^{(\kappa)}\begin{bmatrix}\mathcal{Q}_{k,R}^{(\kappa)} & \mathcal{Q}_{k,C}^{(\kappa)}\\ (\mathcal{Q}_{k,C}^{(\kappa)})^T & \mathcal{Q}_{k,I}^{(\kappa)}\end{bmatrix}.\end{aligned}$$

$$(e^{\jmath\boldsymbol{\theta}})^H(\mathcal{Q}_{22,k}^{(\kappa)}+\mathcal{Q}_{11,k}^{(\kappa)})e^{\jmath\boldsymbol{\theta}}+(e^{\jmath\boldsymbol{\theta}})^T\mathcal{Q}_{12,k}^{(\kappa)}e^{\jmath\boldsymbol{\theta}}+(e^{\jmath\boldsymbol{\theta}})^H(\mathcal{Q}_{12,k}^{(\kappa)})^*e^{-\jmath\boldsymbol{\theta}} = \begin{bmatrix}\cos\boldsymbol{\theta}\\ \sin\boldsymbol{\theta}\end{bmatrix}^T\begin{bmatrix}\mathcal{Q}_{k,R}^{(\kappa)} & \mathcal{Q}_{k,C}^{(\kappa)}\\ (\mathcal{Q}_{k,C}^{(\kappa)})^T & \mathcal{Q}_{k,I}^{(\kappa)}\end{bmatrix}\begin{bmatrix}\cos\boldsymbol{\theta}\\ \sin\boldsymbol{\theta}\end{bmatrix} \tag{6.64}$$

Therefore, we have:

$$\begin{aligned}F^{(\kappa)}(w^{(\kappa+1)},\boldsymbol{\theta},\gamma^{(\kappa)}) &\geq F_c^{(\kappa)}(\boldsymbol{\theta})\\ &\triangleq \tilde{a}^{(\kappa)}+2\Re\{\sum_{n=1}^{N}\tilde{b}^{(\kappa)}(n)e^{\jmath\theta_n}\}-\begin{bmatrix}\cos\boldsymbol{\theta}\\ \sin\boldsymbol{\theta}\end{bmatrix}^T\mathcal{Q}^{(\kappa)}\begin{bmatrix}\cos\boldsymbol{\theta}\\ \sin\boldsymbol{\theta}\end{bmatrix}\end{aligned} \tag{6.66}$$

for

$$\tilde{a}^{(\kappa)}=\sum_{k=1}^{K}\tilde{a}_k^{(\kappa)},$$
$$\tilde{b}^{(\kappa)}(n)=\sum_{k=1}^{K}\tilde{b}_k^{(\kappa)}(n), n=1,\ldots,N,$$

and

$$\mathcal{Q}^{(\kappa)}=\sum_{k=1}^{K}\mathcal{Q}_k^{(\kappa)}=\begin{bmatrix}\mathcal{Q}_R^{(\kappa)} & \mathcal{Q}_C^{(\kappa)}\\ (\mathcal{Q}_C^{(\kappa)})^T & \mathcal{Q}_I^{(\kappa)}\end{bmatrix},$$

with

$$\mathcal{Q}_R^{(\kappa)}=\sum_{k=1}^{K}\mathcal{Q}_{k,R}^{(\kappa)},\mathcal{Q}_C^{(\kappa)}=\sum_{k=1}^{K}\mathcal{Q}_{k,C}^{(\kappa)},\mathcal{Q}_I^{(\kappa)}=\sum_{k=1}^{K}\mathcal{Q}_{k,I}^{(\kappa)}.$$

Furthermore, we have (6.67). Now, using the formula

$$\alpha^{R,(\kappa)}(n)\cos\boldsymbol{\theta}_n+\alpha^{I,(\kappa)}(n)\sin\boldsymbol{\theta}_n=\Re\{\beta(n)e^{\jmath\boldsymbol{\theta}_n}\}$$

$$
\begin{aligned}
F_c^{(\kappa)}(\boldsymbol{\theta}) &= \tilde{a}^{(\kappa)} + 2\Re\{\sum_{n=1}^{N} \tilde{b}^{(\kappa)}(n) e^{\jmath\theta_n}\rangle\} - \begin{bmatrix}\cos\boldsymbol{\theta}\\ \sin\boldsymbol{\theta}\end{bmatrix}^T \left(\mathcal{Q}^{(\kappa)} - \lambda_{\max}(\mathcal{Q}^{(\kappa)}) I_{2N}\right) \begin{bmatrix}\cos\boldsymbol{\theta}\\ \sin\boldsymbol{\theta}\end{bmatrix} \\
&\quad -\lambda_{\max}(\mathcal{Q}^{(\kappa)}) N \\
&\geq \tilde{a}^{(\kappa)} + 2\Re\{\sum_{n=1}^{N} \tilde{b}^{(\kappa)}(n) e^{\jmath\theta_n}\rangle\} - 2\begin{bmatrix}\cos\theta^{(\kappa)}\\ \sin\theta^{(\kappa)}\end{bmatrix}^T \left(\mathcal{Q}^{(\kappa)} - \lambda_{\max}(\mathcal{Q}^{(\kappa)}) I_{2N}\right) \begin{bmatrix}\cos\boldsymbol{\theta}\\ \sin\boldsymbol{\theta}\end{bmatrix} \\
&\quad + \begin{bmatrix}\cos\theta^{(\kappa)}\\ \sin\theta^{(\kappa)}\end{bmatrix}^T \left(\mathcal{Q}^{(\kappa)} - \lambda_{\max}(\mathcal{Q}^{(\kappa)}) I_{2N}\right) \begin{bmatrix}\cos\theta^{(\kappa)}\\ \sin\theta^{(\kappa)}\end{bmatrix} - \lambda_{\max}(\mathcal{Q}^{(\kappa)}) N \\
&= \tilde{\tilde{a}}^{(\kappa)} + 2\Re\{\sum_{n=1}^{N} \tilde{b}^{(\kappa)}(n) e^{\jmath\theta_n}\rangle\} - 2\sum_{n=1}^{N} \left(\alpha^{R,(\kappa)}(n)\cos\boldsymbol{\theta}_n + \alpha^{I,(\kappa)}(n)\sin\boldsymbol{\theta}_n\right) \\
&\triangleq \tilde{F}_c^{(\kappa)}(\boldsymbol{\theta}),
\end{aligned} \tag{6.67}
$$

with

$$
\begin{aligned}
\tilde{\tilde{a}}^{(\kappa)} &= \tilde{a}^{(\kappa)} - \begin{bmatrix}\cos\theta^{(\kappa)}\\ \sin\theta^{(\kappa)}\end{bmatrix}^T \mathcal{Q}^{(\kappa)} \begin{bmatrix}\cos\theta^{(\kappa)}\\ \sin\theta^{(\kappa)}\end{bmatrix} - 2\lambda_{\max}(\mathcal{Q}^{(\kappa)}) N, \\
\alpha^{R,(\kappa)} &= (\theta^{R,(\kappa)})^T \left(\mathcal{Q}_R^{(\kappa)} - \lambda_{\max}(\mathcal{Q}^{(\kappa)}) I_N\right) + (\theta^{I,(\kappa)})^T (\mathcal{Q}_C^{(\kappa)})^T \in \mathbb{R}^{1\times N}, \\
\alpha^{I,(\kappa)} &= (\theta^{R,(\kappa)})^T (\mathcal{Q}_C^{(\kappa)}) + (\theta^{I,(\kappa)})^T \left(\mathcal{Q}_I^{(\kappa)} - \lambda_{\max}(\mathcal{Q}^{(\kappa)}) I_N\right) \in \mathbb{R}^{1\times N}.
\end{aligned}
$$

for $\beta(n) = \sqrt{(\alpha^{R,(\kappa)}(n))^2 + (\alpha^{I,(\kappa)}(n))^2} e^{-\jmath\gamma(n)}$, where $\gamma(n)$ is such that $[\cos\gamma(n), \sin\gamma(n)] = [\alpha^{R,(\kappa)}(n), \alpha^{I,(\kappa)}(n)]/\sqrt{[\alpha^{R,(\kappa)}(n)]^2 + [\alpha^{I,(\kappa)}(n)]^2}$, we can rewrite (6.67) by

$$
\begin{aligned}
\tilde{F}_c^{(\kappa)}(\boldsymbol{\theta}) &= \tilde{\tilde{a}}^{(\kappa)} + 2\Re\{\sum_{n=1}^{N} \tilde{b}^{(\kappa)}(n) e^{\jmath\theta_n}\rangle\} - 2\sum_{n=1}^{N} \Re\{\beta(n) e^{\jmath\boldsymbol{\theta}_n}\} \\
&= \tilde{\tilde{a}}^{(\kappa)} + 2\sum_{n=1}^{N} \Re\{\left(\tilde{b}^{(\kappa)}(n) - \beta(n)\right) e^{\jmath\boldsymbol{\theta}_n}\}.
\end{aligned} \tag{6.68}
$$

Accordingly, we solve the following convex problem at the κ-th iteration to generate $\theta^{(\kappa+1)}$:

$$
\max_{\boldsymbol{\theta}} \ \tilde{F}_c^{(\kappa)}(\boldsymbol{\theta}). \tag{6.69}
$$

Like (6.28), its optimal solution is given in closed-form by

$$
\theta_n^{(\kappa+1)} = -\angle\left(\tilde{b}^{(\kappa)}(n) - \beta(n)\right), n = 1, \ldots, N. \tag{6.70}
$$

It follows from (6.67) that $F^{(\kappa)}(w^{(\kappa+1)},\theta^{(\kappa+1)}) \geq F_c^{(\kappa)}(\theta^{(\kappa+1)}) \geq \tilde{F}_c^{(\kappa)}(\theta^{(\kappa+1)}) > \tilde{F}_c^{(\kappa)}(\theta^{(\kappa)}) = F_c^{(\kappa)}(\theta^{(\kappa)}) = F^{(\kappa)}(w^{(\kappa+1)},\theta^{(\kappa)})$, confirming (6.55), so $\theta^{(\kappa+1)}$ is a better feasible point than $\theta^{(\kappa)}$.

6.3.3 Improper Gaussian Signaling Geometric Mean Rate Optimization

All other exiting algorithms, which solve convex problems and iteratively at a high complexity are very sensitive to the problem sizes. However, our algorithms iterate using closed-form expressions, hence their complexity is low. Algorithm 11 provides the pseudo-code for the proposed computational procedure for the solution of (6.35).

Algorithm 11 IGS GM descent algorithm

1: **Initialization:** Set $\kappa = 0$. Randomly generate $(\theta^{(0)}, w^{(0)})$ satisfying the constraint (6.34b) and then define $\gamma^{(0)}$ by (6.12).
2: **Repeat until** (5.48) **is reached:** Generate $w^{(\kappa+1)}$ by (6.53)- (6.54) and $\theta^{(\kappa+1)}$ by (6.70). Reset $\kappa \leftarrow \kappa + 1$.
3: **Output** $(w^{(\kappa)}, \theta^{(\kappa)})$ and the rates $r_k(w^{(\kappa)}, \theta^{(\kappa)})$, $k = 1, \ldots, K$ with their GM $(\prod_{k=1}^{K} r_k(w^{(\kappa)}, \theta^{(\kappa)}))^{1/K}$.

6.4 Numerical examples

This section evaluates the efficiency of the proposed algorithms by numerical examples. Table 6.1 provides the numerical values of the main parameters taken from [121, 111] for numerical characterization. Furthermore, the elements of the BS-to-RIS LoS channel matrix are generated by $[H_{\text{B-R}}]_{n,m} = e^{j\pi\left((n-1)\sin\bar{\theta}_n \sin\bar{\phi}_n + (m-1)\sin e^{\jmath\theta_n}\sin\phi_n\right)}$, where $e^{\jmath\theta_n}$ and ϕ_n are uniformly distributed as $e^{\jmath\theta_n} \sim \mathcal{U}(0,\pi)$ and $\phi_n \sim \mathcal{U}(0,2\pi)$, respectively, and $\bar{\theta}_n = \pi - \theta_n$ and $\bar{\phi}_n = \pi + \phi_n$ [111]. The normalized small-scale fading channel $h_{\text{B-k}}$ spanning from the BS to UE k follows the classic Rayleigh distribution, while the small-scale fading channel gain $h_{\text{R-k}}$ of the RIS to UE k obeys Rician distribution with a K-factor of 3. The spatial correlation matrix is given by $[\mathbf{R}_{\text{R-k}}]_{n,n'} = e^{j\pi(n-n')\sin\tilde{\phi}_k \sin\tilde{\theta}_k}$, where $\tilde{\phi}_k$ and $\tilde{\theta}$ are the azimuth and elevation angle for UE k, respectively. Unless otherwise stated, $P = 20$dBm and $N = 100$ are used. The results are multiplied by $\log_2 e$ to convert the unit nats/sec into the unit bps/Hz. The convergence tolerance of the proposed algorithms is set to 10^{-3}. For computational

stability, $\gamma_k^{(\kappa)}$ in (6.12) is scaled as

$$\gamma_k^{(\kappa)} \to \frac{\gamma_k^{(\kappa)}}{\min_{j=1,\ldots,K} \gamma_j^{(\kappa)}}, k = 1, \ldots, K. \tag{6.71}$$

Table 6.1 Major parameters setup

Parameter	Numerical value
BS-to-RIS path-loss in (5.5)	$G_{\text{BS}} + G_{\text{RIS}} - 35.9 - 22\log_{10}(d_{\text{B-R}})$ (in dB)
RIS-to-UE path-loss in (5.5)	$G_{\text{RIS}} - 33.05 - 30\log_{10}(d_{\text{R-k}})$ (in dB)
BS-to-UE Path-loss in (5.5)	$G_{\text{BS}} - 33.05 - 36.7\log_{10}(d_{\text{B-k}})$ (in dB)
Antenna gain G_{BS} and G_{RIS}	5 dBi
Bandwidth	1MHz
Noise power density	-174 dBm/Hz

For the setup of Fig. 6.1 the BS and the RIS are deployed at the coordinates of $(40, 0, 25)$ and $(0, 60, 40)$ in the three-dimensional (3D) space, while $K = 10$ UEs are randomly placed in a $(120m \times 120m)$ area right of the BS and RIS. In what follows, we refer to SR-PGS and SR-IGS as the SR under PGS and IGS, which are achieved by iterating (6.17) and (6.28), and (6.53) and (6.54) with $\gamma_k^{(\kappa)} \equiv 1$. Their stand-alone counter-parts dispensing with the RIS are referred by SR-PGS w/t RIS and SR-IGS w/t RIS, which are achieved by iterating (6.17) and and (6.53) with $\gamma_k^{(\kappa)} \equiv 1$ in the corresponding stand-alone models. Another pair of counter-parts labelled by SR-PGS-RIS w. random $\boldsymbol{\theta}$ and SR-IGS-RIS w. random $\boldsymbol{\theta}$ represent the SR with the PREs randomly selected, which correspond to iterating (6.17) and (6.53) under a fixed $\theta^{(\kappa)} = \bar{\theta}$ with $\gamma_k^{(\kappa)} \equiv 1$. Finally, GM-PGS-RIS and GM-IGS-RIS represent to the achievable GMs under PGS and IGS, which are computed by Algorithm 10 and 11.

Fig. 6.2 plots the SR performance versus the number M of antennas at the BS. The SR-PGS and SR-IGS are only slightly better than their counter-parts SR-IGS w/t RIS and SR-PGS, because the direct channel $\tilde{h}_{\text{B-k}}$ spanning from the BS to UE k is much stronger than the reflected channel $\tilde{h}_{\text{R-k}}\mathbf{R}_{\text{R-k}}^{1/2}(e^{\jmath\boldsymbol{\theta}})\tilde{H}_{\text{B-R}}$. The performance margin becomes wider with M increased. Furthermore, SR-PGS approaches SR-IGS for $M \geq K$ in Fig. 6.2.

Next, Fig. 6.3 portrays a rate distribution pattern for $(M, N, P) = (9, 100, P = 20\text{dBm})$. Observe in the figure that only GM-IGS and GM-PGS are capable of avoiding the assignment of zero rate, hence demonstrating its superiority.

To substantiate this fact, Table 6.2 provides the average number of zero-rate users (ZR-UEs) for the optimization schemes considered under different number of antennas M. For

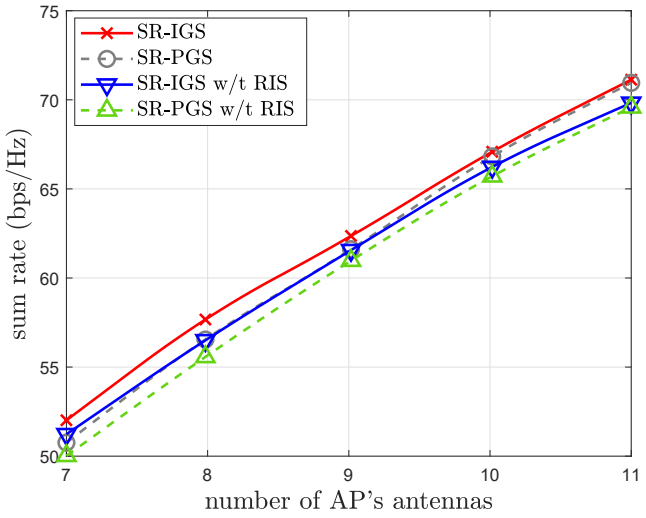

Fig. 6.2 SR for different the number of antennas M.

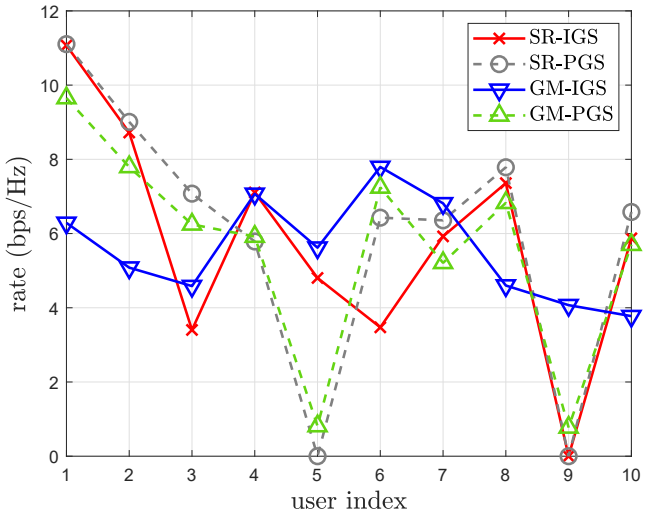

Fig. 6.3 Rate distribution for $M = 9$.

SR-IGS and SR-PGS, the number of ZR-UEs increases when M is reduced. SR-PGS results in more ZR-UEs than SR-IGS, while there are no ZR-UEs in GM-IGS and GM-PGS, confirming that both of them are beneficial in providing the adequate rates to all users.

Furthermore, we also examine the resultant ratio of the minimum rate and maximum rate (min-rate/max-rate) and the resultant rate-variance of these schemes versus the number of antennas, M. Fig. 6.4 shows that both GM-PGS and GM-IGS produce min-rate/max-rates that are substantially higher than that of SR-PGS and SR-IGS. SR-IGS produces higher

Table 6.2 The average number of ZR-UEs versus M

Number of antennas	SR-IGS	SR-PGS	GM-IGS	GM-PGS
M = 7	0.33	3.13	0	0
M = 8	0.23	2.37	0	0
M = 9	0.17	1.64	0	0
M = 10	0	1.10	0	0
M = 11	0	0.72	0	0

min-rate/max-rates than SR-PGS does. Fig. 6.4 also shows the min-rate/max-rate of SR-PGS remains zero for $M < K$ since there are always some ZR-UEs. Furthermore, upon increasing the number of AP antennas, both the min-rate and the max-rate both are improved due to the increased benefit of spatial diversity, but the value of min-rate /max-rate is not necessary a monotonic function of the number of AP antennas. In Fig. 6.5, the rate variance of SR-PGS is seen to be twice of that by its IGS counter SR-IGS at $M = 7$. The discrepancy becomes narrower upon increasing M and it is closer to zero for $M = 11$. The rate-variances are beneficially reduced by the GM-maximization based schemes GM-IGS and GM-PGS. Both Fig. 6.4 and Fig. 6.5 indicate the advantages of IGS over PGS both in terms of SR and GM maximization. Fig. 6.6 shows the GM rates. As expected, GM-IGS and GM-PGS produce

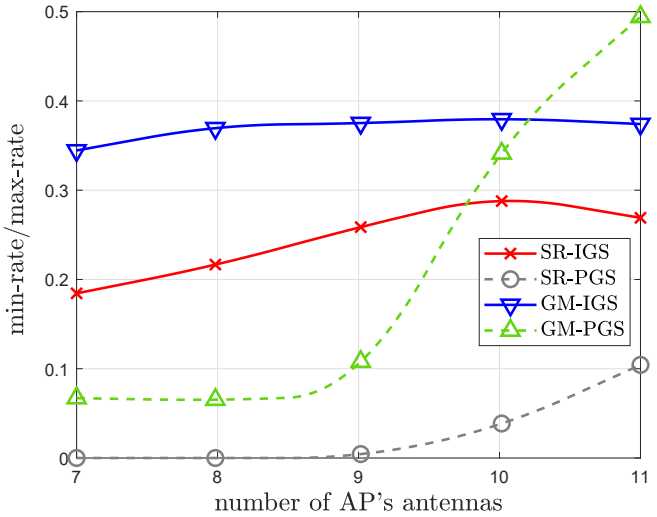

Fig. 6.4 Min-rate/max-rate for the different number of antennas M.

much better GM rate than that of SR-IGS and SR-PGS. Note that GM-PGS has better GM rates than GM-IGS for $M > K$ due to the well-known capability of PGS to mitigate the

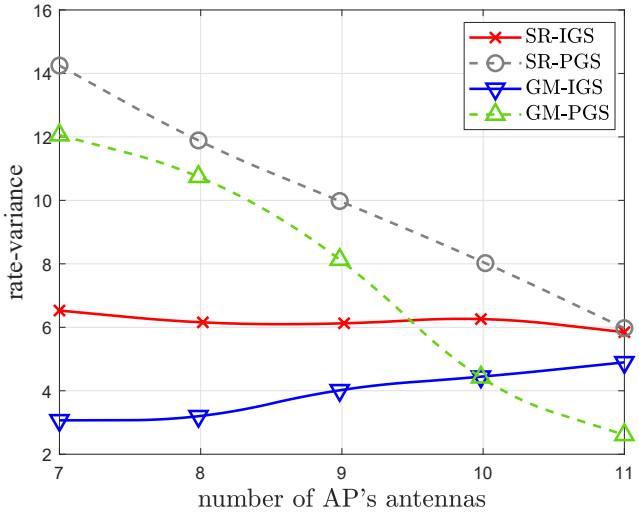

Fig. 6.5 Rate-variance for the different of antennas M.

multi-user interference, when the number of transmit antennas is higher than the number of users.

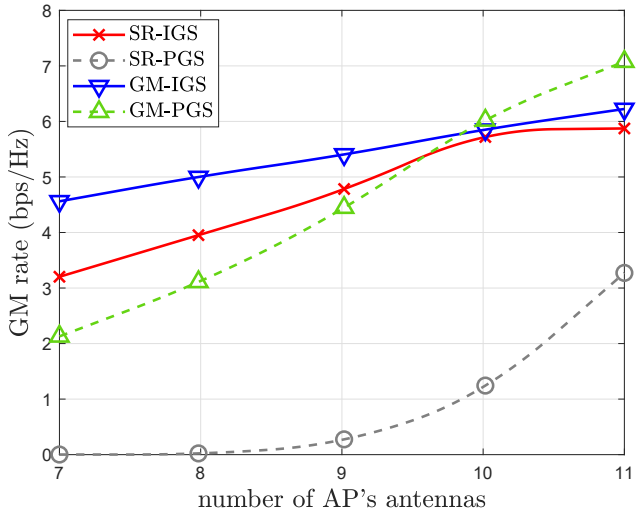

Fig. 6.6 GM for the different number of antennas M.

We also consider another scenario as illustrated by Fig. 6.7, where the direct signal path between the BS and users is blocked, i.e. we have $h_{\text{B-k}} \equiv 0$ in (6.2) and (6.4). The distances between the BS and users becomes slightly smaller upon deploying the BS at the coordinates $(20, 0, 25)$ and the RIS at the coordinates $(0, 30, 40)$. In this scenario, $K = 10$ UEs are randomly placed in a $(60m \times 60m)$ area right of the BS and RIS.

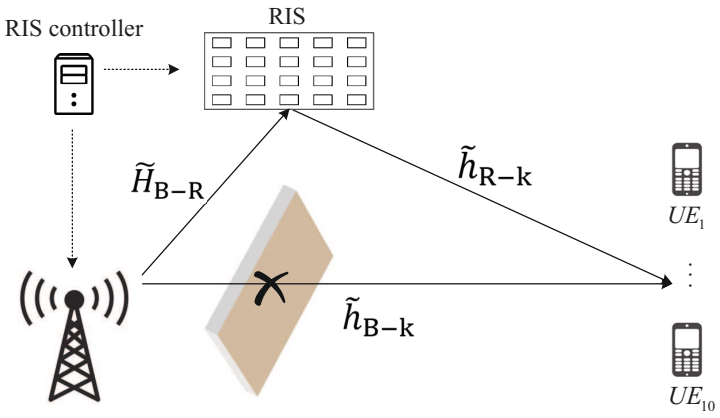

Fig. 6.7 System model

Fig. 6.8 portrays the SR versus M, where SR-IGS outperforms SR-PGS. Furthermore, both the former and the latter substantially outperform their counter-parts SR-IGS w. random θ and SR-PGS w. random θ operating without an RIS.

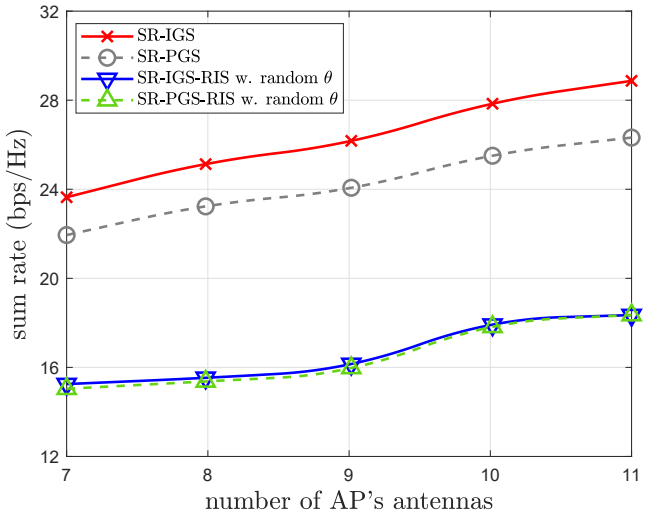

Fig. 6.8 SR for the different number of antennas M.

Similarly to Fig. 6.3, Fig. 6.9 shows a typical user rate distribution, where both the GM maximization based GM-IGS and GM-PGS schemes assign more transmit power to the users having worse channel conditions for achieving fair rate distributions.

Table 6.3 shows the average number of ZR-UEs versus M, demonstrating that the number of ZR-UEs for both SR-IGS and SR-PGS is higher than 3, with that of SR-PGS having higher than that of SR-IGS. As expected, there are no ZR-UEs for GM-IGS and GM-PGS.

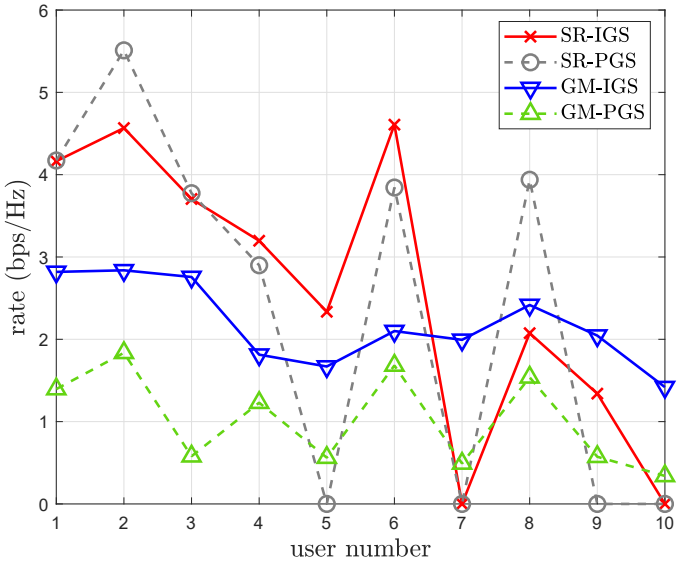

Fig. 6.9 User rate distribution for $M = 9$.

Table 6.3 The average number of ZR-UEs versus the number of antennas M

Number of antennas	SR-IGS	SR-PGS	GM-IGS	GM-PGS
M = 7	3.97	5.40	0	0
M = 8	3.63	4.79	0	0
M = 9	3.20	5.61	0	0
M = 10	3.30	4.13	0	0
M = 11	3.11	3.82	0	0

Fig. 6.10 and Fig. 6.11 plot the min-rate/max-rate and rate-variance versus M, respectively. The min-rate/max-rate of SR-IGS and SR-PGS remains zero for the practical range of $M \in \{7, \ldots, 11\}$. Furthermore, GM-IGS has a better performance than GM-PGS . Fig. 6.11 shows that the rate variance is substantially improved by the GM-based maximization, where GM-IGS results in much better rate variance than GM-PGS. The advantage of GM rate maximization based IGS becomes quite convincing.

Finally, Fig. 6.12 plots the GM rate versus M, which remains zero for both SR-IGS and SR-PGS for $M \in \{7, \ldots, 11\}$, because there are ZR-UEs. The performance of GM-PGS gets closer to that of GM-IGS for $M \geq K$. The advantage of rates GM maximization based IGS is well justified in above results.

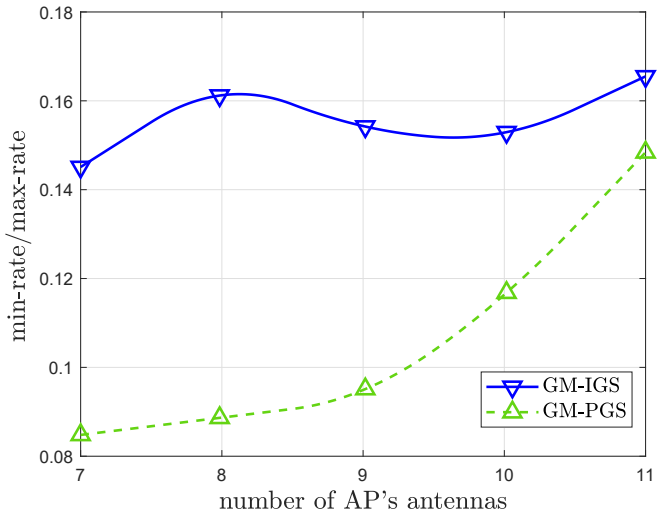

Fig. 6.10 Min-rate/max-rate for the different number of antennas M.

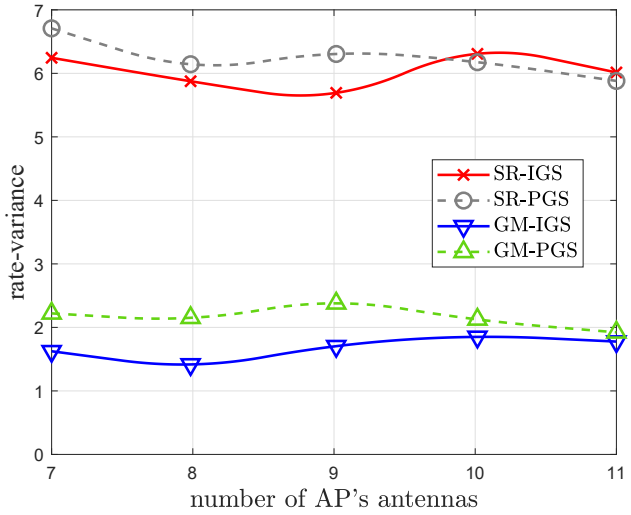

Fig. 6.11 Rate-variance for the different number of antennas M.

6.5 Conclusions

We proposed to maximize the geometric mean (GM) of the users' rates for the sake of maintaining a uniform quality-of-service for the downlink users of an RIS-aid communication network. The computationally intractable unit modulus constraint imposed on the programmable reflecting coefficients has been eliminated by directly optimizing their argument. The problem of maximizing the users' GM rate has been solved by the proposed alternating descent iterations leading to a closed-form solution for the associated convex problems

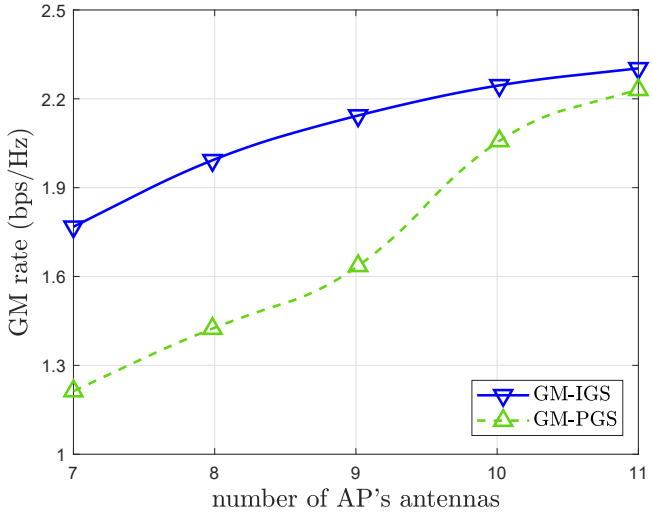

Fig. 6.12 GM rate for the different number of antennas M.

and thus it is computationally efficient. The numerical examples provided have shown a substantially improved rate-fairness amongst the users.

Chapter 7

RIS-aided Zero-Forcing and Regularized Zero-Forcing Beamfoming in Integrated Information and Energy Delivery

7.1 Introduction

Jointly supporting both wireless information and power transfer networking poses challenging problems in signal processing for communication (see e.g. [150] and references therein). For information and energy delivery over a single time slot, simultaneous wireless information and power transfer (SWIPT) apportions the power of the signals received by the users for energy-harvesting (EH) and information detection (ID). In the context, the EH performance is dependent on the power of the received signal, by contrast, the ID performance is critically dependent on the signal-to-interference-plus-noise ratio (SINR). The popular SWIPT systems have primarily used conjugate beamforming (CB) to deliver sufficient energy for EH [5], even though this limits the ID performance due to the multi-user interference (MUI) imposed. By contrast, zero-forcing beamforming (ZFB)completely eliminates the MUI, but it is less efficient for SWIPT. To circumvent these drawbacks, it has been proposed to convey information and energy over the same time slot by transmitting information and energy in separate fractions of the time-slot. Termed as transmit time-switching (transmit-TS), it has been

shown to outperform SWIPT due to its ability to support individual energy beamforming for EH and information beamforming for ID (see e.g. [14, 151, 152, 147]). As a benefit, transmit-TS enables CB for EH and ZFB or regularized zero-forcing beamforming (RZFB) for ID [153, 131][147].

A reconfigurable intelligent surface (RIS) is a planar array of "nearly-passive" reflecting elements, which can beneficially manipulate the reflected signals by programming its reflection coefficients [103]. By strategically installing a RIS in places such as building facades so that it can have a line-of-sight (LoS) path from both the users and a base station (BS), the RIS facilitates reliable communication when there are no direct links between them [64, 102, 106, 133]. A challenging problem in signal processing for these RIS-aided networks is to jointly design the BS's transmit beamformers and the RIS's programmable reflecting coefficients (PRCs) to maximizing the sum throughput [64, 154, 142, 143] or the users' minimum throughput [146]. The joint design of power allocation for ZFB and PRCs to maximize the sum throughput subject to individual user throughput constraints has been considered in [64]. While the alternating power allocation optimization with the PRCs held fixed is simple, the alternating optimization in PRCs with the power allocation held fixed is very challenging since the user throughput becomes a complex function due to the matrix inversion involved in ZFB. As a result, the convergence behavior of the general purpose gradient descent algorithm used in [64] is unknown. Thus, the expected computational tractability of the ZFB design could not be achieved. The authors of [115] and [13] considered some RIS-aided SWIPT scenarios which require that the BS, the RIS and the energy users (EUs) must be located within a small cell radius of about 10m, however the reflected signal by the RIS after undergoing the associated double path-loss becomes quite weak compared to that coming directly from the BS to the EUs, which erodes the benefit of the RIS in EH.

Against the above background, this chapter offers the following contributions.

- We reveal that as a benefit of the transmit-TS technique, the joint optimization of power allocations (for ZFB) and PRCs may be simplified to optimizing the PRCs only, because the power allocation for ZFB can be easily determined. Instead of iterating by relying on convex problems or using deep Q-learning methods to handle the unit-modulus constraint on the PRCs which incur much higher computational complexity [7, 146, 155], we use the polar form of unit-modulus complex numbers that allows each descent iteration of the RIS coefficient calculation to be based on computational efficient closed-form expressions for the solution of concave trigonometric function

optimization [30]. Accordingly, we develop efficient computational procedures, which are based on closed-form expressions for its computation;

- Similarly, we also show that the joint optimization of power allocations (for RZFB) and PRCs can be decomposed into the separate optimization of power allocations (for RZFB) and optimization of PRCs. Accordingly, we develop efficient computational procedures for PRC optimization, which are still based on closed-form expressions. A computational procedure is also proposed for power allocations optimization, which involves a convex quadratic problem at each iteration;

- Furthermore, we develop a new RZFB for improving the throughput of IUs. Our simulations show that the IUs' throughput using the new RZFB is 15% - 25% higher than that obtained by the existing RZFB in the challenging rank-deficient scenario, when the BS only has a few antennas for serving more IUs;

- We consider a practical scenario of RIS-aided integrated information and energy deliveries to both information users (IUs) and energy users (EUs). By adopting the aforementioned transmit-TS approach, we harness CB for delivering energy to EUs, and RIS-aided ZFB/RZFB/new RZFB for delivering information to IUs. Naturally, the PRCs are still separately optimized in this joint design problem. We then develop efficient computational procedures for solving the problem of maximizing the IUs' minimum throughput subject to a constraint on the quality-of-energy-service (QoES) in terms of the EUs' harvested energy thresholds.

The rest of the chapter is organized as follows. Section II and Section III are respectively devoted to PRC optimization for ZFB and RZFB with its applications to RIS-aided information and energy delivery studied in Section IV and V. A new RZFB is also introduced in Section V. Section VI provides simulations to support the technical developments of the previous sections. Section VII concludes the chapter. The Appendix provides several inequalities that are frequently used in the technical sections. The flow chart of chapter organization can be seen in Fig. 7.1.

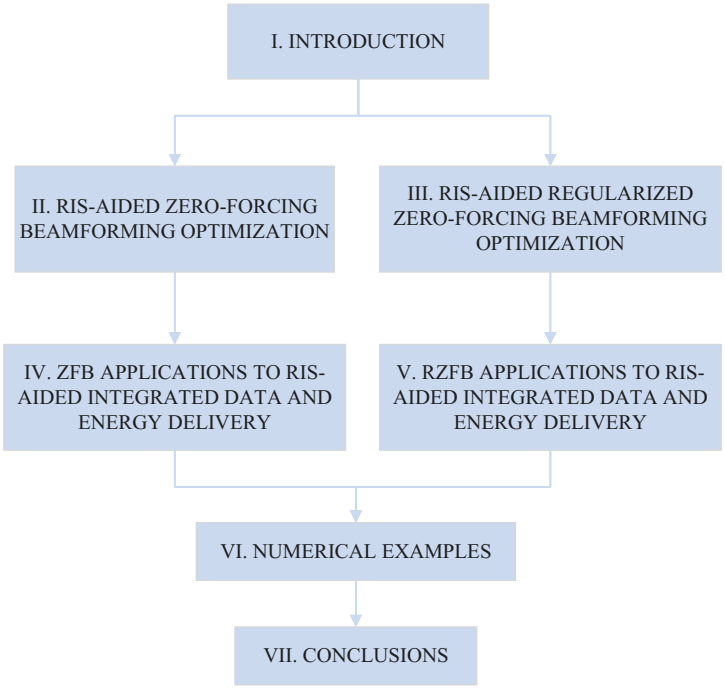

Fig. 7.1 Chapter organization.

7.2 RIS-aided zero-forcing beamforming optimization

Consider a RIS-aided network, which is illustrated by Fig. 7.2 with a RIS of N reflecting units to assist the downlink from an M-antenna base station (BS) to K single-antenna information users (IUs) $k \in \mathcal{K} \triangleq \{1, \ldots, K\}$ because there is no direct signal path between the former and the latter.[1] The channel spanning from the BS to the RIS is $\tilde{H}_{B-R} \triangleq \sqrt{\beta_{B-R}} H_{B-R} \in \mathbb{C}^{N \times M}$, where $\sqrt{\beta_{B-R}}$ models the path-loss and large-scale fading of LoS and the entries of H_{B-R} are $\mathcal{C}(0,1)$, modelling small-scale fading. Analogously, the channel spanning from the RIS to IU k is $\tilde{h}_{R-k} = \sqrt{\beta_{R-k}} \bar{h}_{R-k} \in \mathbb{C}^{1 \times N}$, where $\sqrt{\beta_{R-k}}$ represents the large-scale fading, while $\bar{h}_{R-k}$ denotes the small-scale fading having elements of $\mathcal{C}(0,1)$. Like in many other papers on RIS-aided communication networks, we assume perfect channel state information, which can be obtained by channel estimation [138, 13, 7].

[1] According to [146, 156], the networks throughput is hardly improved by RIS's, when there are direct paths from the BS to the IUs.

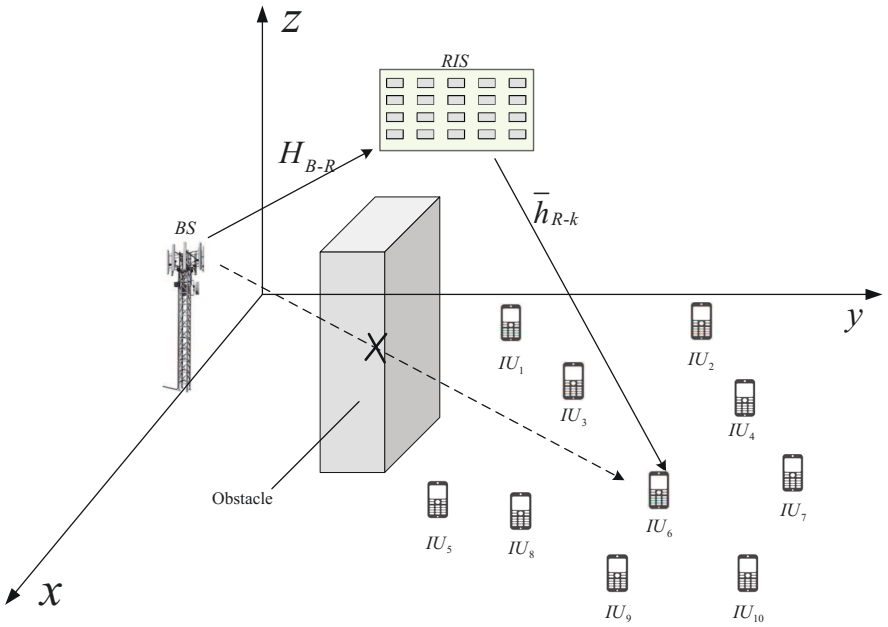

Fig. 7.2 Scenario setup with the blockage of the direct path between the BS and the IUs.

Let $\boldsymbol{\theta} \triangleq (\boldsymbol{\theta}_1, \ldots, \boldsymbol{\theta}_N) \in [0, 2\pi]^N$ and

$$e^{\jmath\boldsymbol{\theta}} \triangleq (e^{\jmath\boldsymbol{\theta}_1}, \ldots, e^{\jmath\boldsymbol{\theta}_N})^T \in \mathbb{C}^N,$$

which is a complex-vector function of the variable $\boldsymbol{\theta}$. We also define the diagonal complex-matrix function of the variable $e^{\jmath\boldsymbol{\theta}}$ as

$$\mathsf{diag}[e^{\jmath\boldsymbol{\theta}}] = \mathsf{diag}\{e^{\jmath\boldsymbol{\theta}_1}, \ldots, e^{\jmath\boldsymbol{\theta}_N}\} \in \mathbb{C}^{N\times N}$$

representing the matrix of RIS reflection-coefficients.

The received signal at IU k is

$$y_k \quad = \quad h_{B-k}(e^{\jmath\boldsymbol{\theta}})x_I + n_k, \tag{7.1}$$

where $n_k \in \mathcal{C}(0, \sigma)$ is the background noise, and

$$h_{B-k}(\boldsymbol{\theta}) \triangleq \tilde{h}_{R-k} R_{RIS-k}^{1/2} \mathsf{diag}[e^{\jmath\boldsymbol{\theta}}] \tilde{H}_{B-R} \in \mathbb{C}^{1\times M}, \tag{7.2}$$

which is the composite channel spanning from the BS to IU k.

In (7.2), $R_{RIS-k} \in \mathbb{C}^{N\times N}$ represents the spatial correlation matrix of the RIS elements with respect to IU k [154]. For

$$y \triangleq \begin{bmatrix} y_1 \\ \dots \\ y_K \end{bmatrix} \in \mathbb{C}^K, \bar{n} \triangleq \begin{bmatrix} n_1 \\ \dots \\ n_K \end{bmatrix} \in \mathbb{C}^K,$$

and

$$\mathcal{H}(e^{\jmath\boldsymbol{\theta}}) \triangleq \begin{bmatrix} h_{B-1}(e^{\jmath\boldsymbol{\theta}}) \\ \dots \\ h_{B-K}(e^{\jmath\boldsymbol{\theta}}) \end{bmatrix} = H_R \mathsf{diag}[e^{\jmath\boldsymbol{\theta}}]\tilde{H}_{B-R} = \sum_{n=1}^{N} e^{\jmath\theta_n}\mathcal{H}_n \in \mathbb{C}^{K\times M}$$

with

$$\mathcal{H}_n \triangleq H_R\Psi_n\tilde{H}_{B-R} \in \mathbb{C}^{K\times M}, H_R \triangleq \begin{bmatrix} \tilde{h}_{R-1}R_{RIS-1}^{1/2} \\ \dots \\ \tilde{h}_{R-K}R_{RIS-K}^{1/2} \end{bmatrix} \in \mathbb{C}^{K\times N},$$

where Ψ_n is a matrix of size $N \times N$ with all-zero entries, excepts $\Psi_n(n,n) = 1$.

We can write

$$y = \mathcal{H}(e^{\jmath\boldsymbol{\theta}})x_I + \bar{n}. \tag{7.3}$$

Now, for $K \leq M$ we consider the ZFB, under which the BS transmits

$$x_I = \mathcal{H}^H(e^{\jmath\boldsymbol{\theta}}) \left([\mathcal{H}(e^{\jmath\boldsymbol{\theta}})]^2\right)^{-1} \mathrm{diag}[\boldsymbol{p}_k]_{k=1,\dots,K}s, \tag{7.4}$$

where $s = (s_1, \dots, s_K)^T$, $s_k \in \mathcal{C}(0,1)$ is the information intended for the IUs having the power of $\boldsymbol{p} = (\boldsymbol{p}_1, \dots, \boldsymbol{p}_K)^T$. Then Equation (7.3) becomes

$$\begin{aligned} y &= \mathcal{H}(e^{\jmath\boldsymbol{\theta}})\mathcal{H}^H(e^{\jmath\boldsymbol{\theta}}) \left([\mathcal{H}(e^{\jmath\boldsymbol{\theta}})]^2\right)^{-1} \mathrm{diag}[\boldsymbol{p}_k]_{k=1,\dots,K}s + \bar{n} \\ &= [\mathcal{H}(e^{\jmath\boldsymbol{\theta}})]^2 \left([\mathcal{H}(e^{\jmath\boldsymbol{\theta}})]^2\right)^{-1} \mathrm{diag}[\boldsymbol{p}_k]_{k=1,\dots,K}s + \bar{n} \\ &= \mathrm{diag}[\boldsymbol{p}_k]_{k=1,\dots,K}s + \bar{n} \end{aligned} \tag{7.5}$$

simplifying (7.1) to

$$y_k = \boldsymbol{p}_k s_k + \bar{n}_k. \tag{7.6}$$

The throughput for s_k is

$$\ln(1+\boldsymbol{p}_k^2/\sigma), \tag{7.7}$$

and the transmit power is

$$\begin{aligned}\mathbb{E}(||x_I||^2) &= \langle \mathcal{H}^H(e^{\jmath\boldsymbol{\theta}}) \left([\mathcal{H}(e^{\jmath\boldsymbol{\theta}})]^2\right)^{-1} \mathrm{diag}[\boldsymbol{p}_k^2]_{k=1,\ldots,K} \left([\mathcal{H}(e^{\jmath\boldsymbol{\theta}})]^2\right)^{-1} \mathcal{H}(e^{\jmath\boldsymbol{\theta}})\rangle &(7.8)\\ &= \langle \mathrm{diag}[\boldsymbol{p}_k^2]_{k=1,\ldots,K} \left([\mathcal{H}(e^{\jmath\boldsymbol{\theta}})]^2\right)^{-1}\rangle. &(7.9)\end{aligned}$$

For the IUs' max-min throughput optimization is employed, which aims for maximizing the users' worst-case (minimal) throughput, where we have $\boldsymbol{p}_k \equiv \boldsymbol{p}_0$ [2]$(\ln(1+\boldsymbol{p}_k^2/\sigma) \equiv \ln(1+\boldsymbol{p}_0^2/\sigma)$. Then by (7.9), the transmit power is $\boldsymbol{p}_0^2\langle\left([\mathcal{H}(e^{\jmath\boldsymbol{\theta}})]^2\right)^{-1}\rangle$, and the max-min IU throughput optimization under transmit power budget P can be expressed as

$$\begin{aligned}&\max_{\boldsymbol{p}_0,\boldsymbol{\theta}} \ \ln(1+\boldsymbol{p}_0^2/\sigma) \quad \text{s.t.} \quad \boldsymbol{p}_0^2\langle\left([\mathcal{H}(e^{\jmath\boldsymbol{\theta}})]^2\right)^{-1}\rangle \le P &(7.10)\\ \Leftrightarrow\ &\max_{\boldsymbol{\theta}} \ P/\langle\left([\mathcal{H}(e^{\jmath\boldsymbol{\theta}})]^2\right)^{-1}\rangle &(7.11)\\ \Leftrightarrow\ &\min_{\boldsymbol{\theta}} f(e^{\jmath\boldsymbol{\theta}}) \triangleq \langle\left(\mathcal{H}(e^{\jmath\boldsymbol{\theta}})\mathcal{H}^H(e^{\jmath\boldsymbol{\theta}})\right)^{-1}\rangle. &(7.12)\end{aligned}$$

In fact, it follows from the power constraint in (7.10) that $\boldsymbol{p}_0^2 \le P/\langle\left([\mathcal{H}(e^{\jmath\boldsymbol{\theta}})]^2\right)^{-1}\rangle$. Hence the problem (7.10) is actually $\max \ln(1+P/(\sigma\langle\left([\mathcal{H}(e^{\jmath\boldsymbol{\theta}})]^2\right)^{-1}\rangle))$, which is the same as (7.11). Since only the denominator of the fractional objective function in (7.11) is dependent on $\boldsymbol{\theta}$, its maximization is equivalent to the minimization of its denominator, which is (7.12).

The rest of this section is devoted to the detailed portrayal of our algorithms conceived for computing (7.12), which is very challenging because its objective function is highly nonlinear and computationally intractable.

[2]From (7.7), the users' worst-case throughput is $\min_{k=1,\ldots,K} \ln(1+\boldsymbol{p}_k^2/\sigma)$, which is maximized at $\ln(1+\boldsymbol{p}_1^2/\sigma) = \ln(1+\boldsymbol{p}_2^2/\sigma) = \cdots = \ln(1+\boldsymbol{p}_K^2/\sigma) \Leftrightarrow \boldsymbol{p}_k \equiv \boldsymbol{p}_0$

7.2.1 Step descent algorithm

Let $\theta^{(\kappa)}$ be a point found during the $(\kappa-1)$-st iteration. The linearized function of f at $e^{\jmath\theta^{(\kappa)}}$ is

$$\begin{aligned} 3f(e^{\jmath\theta^{(\kappa)}}) - 2\Re\{\langle[\mathcal{H}^H(e^{\jmath\theta^{(\kappa)}})\left([\mathcal{H}(e^{\jmath\theta^{(\kappa)}})]^2\right)^{-2}\mathcal{H}(e^{\jmath\boldsymbol{\theta}})\rangle\} \quad = \\ 3f(e^{\jmath\theta^{(\kappa)}}) - 2\sum_{n=1}^{N}\Re\{e^{\jmath\theta_n}\langle\mathcal{H}^H(e^{\jmath\theta^{(\kappa)}})\mathcal{A}^{(\kappa)}\mathcal{H}_n\rangle\}, \end{aligned} \tag{7.13}$$

for

$$\mathcal{A}^{(\kappa)} \triangleq \left([\mathcal{H}(e^{\jmath\theta^{(\kappa)}})]^2\right)^{-2}. \tag{7.14}$$

We seek a step descent by addressing the following problem

$$\max_{\boldsymbol{\theta}} \sum_{n=1}^{N}\Re\{e^{\jmath\theta_n}\langle\mathcal{H}^H(e^{\jmath\theta^{(\kappa)}})\mathcal{A}^{(\kappa)}\mathcal{H}_n\rangle\}, \tag{7.15}$$

which is decomposed into N independent problems:

$$\max_{\boldsymbol{\theta}_n} \Re\{e^{\jmath\theta_n}\langle\mathcal{H}^H(e^{\jmath\theta^{(\kappa)}})\mathcal{A}^{(\kappa)}\mathcal{H}_n\rangle\}, n = 1,\ldots,N,$$

each of which admits the closed-form solution

$$\tilde{\theta}_n^{(\kappa+1)} = -\angle\langle\mathcal{H}^H(e^{\jmath\theta^{(\kappa)}})\mathcal{A}^{(\kappa)}\mathcal{H}_n\rangle, n = 1,\ldots,N. \tag{7.16}$$

We may then choose $\theta^{(\kappa+1)}$ according to one of the following rules:

- The simplest one
$$\theta^{(\kappa+1)} = \tilde{\theta}^{(\kappa+1)}. \tag{7.17}$$

- Considering $\psi^{(\kappa)} \triangleq \tilde{\theta}^{(\kappa+1)} - \theta^{(\kappa)}$ as a step descent, we update $\theta^{(\kappa+1)}$ according to the so-called Barzilai-Borwein (BB) step size of [157] in (7.18) and (7.19):

$$\theta^{(\kappa+1)} = \theta^{(\kappa)} + \frac{|\langle\psi^{(\kappa)}, \psi^{(\kappa)} - \psi^{(\kappa-1)}\rangle|}{||\psi^{(\kappa)} - \psi^{(\kappa-1)}||^2}\psi^{(\kappa)} \tag{7.18}$$

$$= \theta^{(\kappa)} + \frac{|\langle\tilde{\theta}^{(\kappa+1)} - \theta^{(\kappa)}, \tilde{\theta}^{(\kappa+1)} - \theta^{(\kappa)} - \tilde{\theta}^{(\kappa)} + \theta^{(\kappa-1)}\rangle|}{||\tilde{\theta}^{(\kappa+1)} - \theta^{(\kappa)} - \tilde{\theta}^{(\kappa)} + \theta^{(\kappa-1)}||^2}(\tilde{\theta}^{(\kappa+1)} - \theta^{(\kappa)}). \tag{7.19}$$

- Considering $\psi^{(\kappa)} \triangleq e^{\jmath\tilde{\theta}^{(\kappa+1)}} - e^{\jmath\theta^{(\kappa)}}$ we update $\theta^{(\kappa+1)}$ according to (7.20) and (7.21):

$$\begin{aligned}\theta^{(\kappa+1)} &= \angle\left(e^{\jmath\theta^{(\kappa)}} + \frac{|\langle\psi^{(\kappa)}, \psi^{(\kappa)} - \psi^{(\kappa-1)}\rangle|}{||\psi^{(\kappa)} - \psi^{(\kappa-1)}||^2}\psi^{(\kappa)}\right) &(7.20)\\ &= \angle\left(e^{\jmath\theta^{(\kappa)}} + \frac{|\langle e^{\jmath\tilde{\theta}^{(\kappa+1)}} - e^{\jmath\theta^{(\kappa)}}, e^{\jmath\tilde{\theta}^{(\kappa+1)}} - e^{\jmath\tilde{\theta}^{(\kappa)}} - e^{\jmath\tilde{\theta}^{(\kappa)}} + e^{\jmath\theta^{(\kappa-1)}}\rangle|}{||e^{\jmath\tilde{\theta}^{(\kappa+1)}} - e^{\jmath\tilde{\theta}^{(\kappa)}} - e^{\jmath\tilde{\theta}^{(\kappa)}} + e^{\jmath\theta^{(\kappa-1)}}||^2}\right.\\ &\quad \left.(e^{\jmath\tilde{\theta}^{(\kappa+1)}} - e^{\jmath\theta^{(\kappa)}})\right). &(7.21)\end{aligned}$$

  We will refer this as the projective Barzilai-Borwein (PBB) step size.

Algorithm 12 provides the pseudo-code for the procedure iterating (7.17) or (7.19), or (7.21) in order to arrive at the computational solution of (7.12). The reader is referred to [157] for the rationale behind them in locating better feasible points, which are suitable for unconstrained optimization only. There is an explicit update of the incumbent point in Algorithm 12 because the updating rules (7.17)-(7.21) do not enhance that $\theta^{(\kappa)}$ is the incumbent. Somewhat surprisingly, the performance of Algorithm 12 was found to be indifferent with using any of three aforementioned rules.

Algorithm 12 ZFB step descent algorithm for (7.12)

1: **Initialization:** Initial $\theta^{(0)}$ and set $\theta^{opt} = \theta^{(0)}$ and $\gamma^{opt} = f(\theta^{opt})$ as the incumbent RIS and value.
2: **Repeat until convergence of $\theta^{(\kappa)}$:** Generate $\tilde{\theta}^{(\kappa+1)}$ by (7.16). Then generate $\theta^{(\kappa+1)}$ either by (7.17) or (7.19), or (7.21). If $f(\theta^{(\kappa+1)}) < \gamma^{opt}$, set $\theta^{opt} = \theta^{(\kappa+1)}$ and $\gamma^{opt} = f(\theta^{(\kappa+1)})$. Set $\kappa := \kappa + 1$.
3: **Output** θ^{opt} and γ^{opt}.

7.2.2 Full step descent algorithms

We express f in (7.12) as:

$$\begin{aligned}f(e^{\jmath\boldsymbol{\theta}}) &= \alpha||e^{\jmath\boldsymbol{\theta}}||^2 - \left(\alpha||e^{\jmath\boldsymbol{\theta}}||^2 - \langle\left([\mathcal{H}(e^{\jmath\boldsymbol{\theta}})]^2\right)^{-1}\rangle\right) &(7.22)\\ &= \alpha N - g(e^{\jmath\boldsymbol{\theta}}), &(7.23)\end{aligned}$$

where $\alpha > 0$ is chosen for ensuring that the function

$$g(e^{\jmath\boldsymbol{\theta}}) \triangleq \alpha||e^{\jmath\boldsymbol{\theta}}||^2 - \langle\left([\mathcal{H}(e^{\jmath\boldsymbol{\theta}})]^2\right)^{-1}\rangle$$

is convex in $e^{\jmath\boldsymbol{\theta}}$. The problem (7.12) is equivalent to the following problem of unconstrained concave optimization [30][3]

$$\max_{\boldsymbol{\theta}} \; g(e^{\jmath\boldsymbol{\theta}}). \tag{7.24}$$

Following [158–160] we will develop a local Frank-and-Wolf (FW) feasible direction algorithm for solving this problem as it bypasses the line search to give as a full step size of length 1. Moreover, this kind of FW algorithm has proved to be very efficient in practice [161]. To this end, let $\theta^{(\kappa)}$ be a point found during the $(\kappa-1)$-st iteration. Note that as g is convex, its linearized function provides its lower bound formulated as:

$$\begin{aligned} g(e^{\jmath\boldsymbol{\theta}}) \;&\geq\; \alpha\left(2\Re\{\sum_{n=1}^{N} e^{\jmath\theta_n}e^{-\jmath\theta_n^{(\kappa)}}\} - N\right) - 3\langle\left([\mathcal{H}(e^{\jmath\theta^{(\kappa)}})]^2\right)^{-1}\rangle \\ &\quad +2\Re\{\sum_{n=1}^{N} e^{\jmath\theta_n}\langle\mathcal{H}^H(e^{\jmath\theta^{(\kappa)}})\mathcal{A}^{(\kappa)}\mathcal{H}_n\rangle\} \qquad (7.25) \\ &=\; -\alpha N - 3\langle\left([\mathcal{H}(e^{\jmath\theta^{(\kappa)}})]^2\right)^{-1}\rangle + 2\sum_{n=1}^{N}\Re\{e^{\jmath\theta_n}\left(\alpha e^{-\jmath\theta_n^{(\kappa)}} + \langle\mathcal{H}^H(e^{\jmath\theta^{(\kappa)}})\mathcal{A}^{(\kappa)}\mathcal{H}_n\rangle\right)\} \\ &\triangleq\; g^{(\kappa)}(e^{\jmath\boldsymbol{\theta}}), \qquad (7.26) \end{aligned}$$

where $\mathcal{A}^{(\kappa)}$ is defined in (7.14). For finding the FW feasible direction, we solve the following problem at the κ-th iteration to generate $\theta^{(\kappa+1)}$

$$\max_{\boldsymbol{\theta}} \; 2\sum_{n=1}^{N}\Re\{e^{\jmath\theta_n}\left(\alpha e^{-\jmath\theta_n^{(\kappa)}} + \langle\mathcal{H}^H(e^{\jmath\theta^{(\kappa)}})\mathcal{A}^{(\kappa)}\mathcal{H}_n\rangle\right)\}, \tag{7.27}$$

which admits the following closed-form solution similar to (7.16):

$$\theta_n^{(\kappa+1)} = -\angle\left(\alpha e^{-\jmath\theta_n^{(\kappa)}} + \langle\mathcal{H}^H(e^{\jmath\theta^{(\kappa)}})\mathcal{A}^{(\kappa)}\mathcal{H}_n\rangle\right), n = 1,\ldots,N. \tag{7.28}$$

We can readily show that

$$g(e^{\jmath\theta^{(\kappa+1)}}) \geq g^{(\kappa)}(e^{\jmath\theta^{(\kappa+1)}}) > g^{(\kappa)}(e^{\jmath\theta^{(\kappa)}}) = g(e^{\jmath\theta^{(\kappa)}}), \tag{7.29}$$

so $\theta^{(\kappa+1)}$ is a better point than $\theta^{(\kappa)}$, i.e. $1 = \arg\max_{0\leq\boldsymbol{\nu}\leq 1} g(e^{\jmath(\theta^{(\kappa)}+\boldsymbol{\nu}(\theta^{(\kappa+1)}-\theta^{(\kappa)}))})$, so the full step size of length one is achieved. [4] The associated pseudo-code is provided by Algorithm 13, which iterates incumbent points bypassing any line search. In contrast to Algorithm 12,

[3] (7.24) is equivalent to $\min_{\boldsymbol{\theta}}(-g(e^{\jmath\boldsymbol{\theta}})$, where $-g(e^{\jmath\boldsymbol{\theta}})$ is a concave function

[4] Obviously, the step size is not full whenever $\arg\max_{0\leq\boldsymbol{\nu}\leq 1} g(e^{\jmath(\theta^{(\kappa)}+\boldsymbol{\nu}(\theta^{(\kappa+1)}-\theta^{(\kappa)}))}) < 1$

the convergence of Algorithm 13 to at least a locally optimal solution of (7.24) can be readily proved [161].

Remark. To efficiently find a reasonable α in (7.22), we rely on the following procedure. Initialize the procedure by using a sufficiently large $\alpha^{(0)}$, solve (7.27) and update $\alpha^{(\kappa+1)} = \alpha^{(\kappa)}/10$ until not arrive at $g(e^{\jmath\theta^{(\kappa+1)}}) \leq g(e^{\jmath\theta^{(\kappa)}})$.

We also propose an alternative full step descent procedure for (7.12) by addressing the following problem of perturbed optimization:

$$\min_{\boldsymbol{\theta}} f_\alpha(e^{\jmath\boldsymbol{\theta}}) \triangleq \langle \Big([\mathcal{H}(e^{\jmath\boldsymbol{\theta}})]^2 + \alpha I_K \Big)^{-1} \rangle \tag{7.30}$$

for a sufficient small $\alpha > 0$. Using the matrix inverse formula (7.31) of (see e.g. [162]):

$$\begin{aligned} \Big([\mathcal{H}(e^{\jmath\boldsymbol{\theta}})]^2 + \alpha I_K \Big)^{-1} &= \alpha^{-1} I_K - \alpha^{-2} \mathcal{H}(e^{\jmath\boldsymbol{\theta}}) \Big(I_M + \alpha^{-1} [\mathcal{H}^H(e^{\jmath\boldsymbol{\theta}})]^2 \Big)^{-1} \mathcal{H}^H(e^{\jmath\boldsymbol{\theta}}) \\ &= \alpha^{-1} I_K - \alpha^{-1} \mathcal{H}(e^{\jmath\boldsymbol{\theta}}) \Big(\alpha I_M + \mathcal{H}^H(e^{\jmath\boldsymbol{\theta}}) \mathcal{H}(e^{\jmath\boldsymbol{\theta}}) \Big)^{-1} \mathcal{H}^H(e^{\jmath\boldsymbol{\theta}}), \end{aligned} \tag{7.31}$$

the problem in (7.30) may be shown to be equivalent to

$$\max_{\boldsymbol{\theta}} \; g_\alpha(e^{\jmath\boldsymbol{\theta}}) \triangleq \langle \mathcal{H}(e^{\jmath\boldsymbol{\theta}}) \Big(\alpha I_M + [\mathcal{H}^H(e^{\jmath\boldsymbol{\theta}})]^2 \Big)^{-1} \mathcal{H}^H(e^{\jmath\boldsymbol{\theta}}) \rangle. \tag{7.32}$$

Again, let $\theta^{(\kappa)}$ be a point found during the $(\kappa-1)$-st iteration. Exploiting the inequality (A.25) in the Appendix yields (7.33):

$$\begin{aligned} g_\alpha(e^{\jmath\boldsymbol{\theta}}) &\geq -\alpha \langle [\mathcal{H}^H(e^{\jmath\theta^{(\kappa)}})]^2 [\Psi^{(\kappa)}]^2 \rangle + 2\Re\{ \langle \mathcal{H}(e^{\jmath\boldsymbol{\theta}}) \Psi^{(\kappa)} \mathcal{H}^H(e^{\jmath\theta^{(\kappa)}}) \rangle \} \\ &\quad - \langle [\mathcal{H}^H(e^{\jmath\boldsymbol{\theta}})]^2 [\Psi^{(\kappa)} \mathcal{H}^H(e^{\jmath\theta^{(\kappa)}})]^2 \rangle \\ &= a^{(\kappa)} + 2\Re\{ \sum_{n=1}^N e^{\jmath\theta_n} b^{(\kappa)}(n) \} + (e^{\jmath\boldsymbol{\theta}})^H \mathcal{C}^{(\kappa)} e^{\jmath\boldsymbol{\theta}} \\ &\geq a^{(\kappa)} + 2\Re \left\{ \sum_{n=1}^N e^{\jmath\theta_n} \left(b^{(\kappa)}(n) - \sum_{m=1}^N e^{-\jmath\theta_m^{(\kappa)}} \mathcal{C}^{(\kappa)}(m,n) + \lambda_{\max}(\mathcal{C}^{(\kappa)}) e^{-\jmath\theta_n^{(\kappa)}} \right) \right\} \\ &\quad - (e^{\jmath\theta^{(\kappa)}})^H \mathcal{C}^{(\kappa)} e^{\jmath\theta^{(\kappa)}} - 2\lambda_{\max}(\mathcal{C}^{(\kappa)}) N \\ &\triangleq g_\alpha^{(\kappa)}(e^{\jmath\boldsymbol{\theta}}), \end{aligned} \tag{7.33}$$

for

$$\Psi^{(\kappa)} = \left(\alpha I_M + [\mathcal{H}^H(e^{\jmath\theta^{(\kappa)}})]^2\right)^{-1},$$
$$a^{(\kappa)} \triangleq -\alpha\langle[\mathcal{H}^H(e^{\jmath\theta^{(\kappa)}})]^2[\Psi^{(\kappa)}]^2\rangle,$$
$$b^{(\kappa)}(n) \triangleq \langle\mathcal{H}_n\Psi^{(\kappa)}\mathcal{H}^H(e^{\jmath\theta^{(\kappa)}})\rangle, n \in \mathcal{N},$$

and

$$\mathcal{C}^{(\kappa)}(n,m) \triangleq \langle\mathcal{H}_n^H\mathcal{H}_m[\Psi^{(\kappa)}\mathcal{H}^H(e^{\jmath\theta^{(\kappa)}})]^2\rangle, (n,m) \in \mathcal{N}\times\mathcal{N},$$

while $\lambda_{\max}(\mathcal{C}^{(\kappa)})$ is the maximum eigenvalue of $\mathcal{C}^{(\kappa)}$, which is positive because the matrix $\mathcal{C}^{(\kappa)}$ is positive definite.

We thus solve the following problem to generate $\theta^{(\kappa+1)}$

$$\max_{\boldsymbol{\theta}} g_\alpha^{(\kappa)}(e^{\jmath\boldsymbol{\theta}}), \tag{7.34}$$

which admits the following closed-form solution similar to (7.16):

$$\theta_n^{(\kappa+1)} = -\angle\left(b^{(\kappa)}(n) - \sum_{m=1}^{N} e^{-\jmath\theta_m^{(\kappa)}}\mathcal{C}^{(\kappa)}(m,n) + \lambda_{\max}(\mathcal{C}^{(\kappa)})e^{-\jmath\theta_n^{(\kappa)}}\right), n \in \mathcal{N}. \tag{7.35}$$

Similarly to (7.29), we can readily show that $g_\alpha(e^{\jmath\theta^{(\kappa+1)}}) > g_\alpha(e^{\jmath\theta^{(\kappa)}})$ as far as $\theta^{(\kappa+1)} \neq \theta^{(\kappa)}$, so (7.35) provides full step size update. A compact presentation of (7.34) is also included in Algorithm 13.

Before concluding this section, observe that after designing θ^{opt}, the throughput of all IUs is defined with the aid of (7.7) and (7.9) as

$$\ln\left(1 + \frac{P}{\sigma\langle([\mathcal{H}(e^{\jmath\theta^{opt}})]^2)^{-1}\rangle}\right). \tag{7.36}$$

Algorithm 13 ZFB full step descent algorithm

1: **Initialization:** Initial $\theta^{(0)}$.
2: **Repeat until convergence of** $\theta^{(\kappa)}$**:** Generate $\theta^{(\kappa+1)}$ by (7.28) or (7.35). Set $\kappa := \kappa + 1$.
3: **Output** $\theta^{opt} = \theta^{(\kappa)}$.

7.3 RIS-aided regularized zero-forcing beamforming optimization

Now, whenever we have $K > M$, the matrix $\mathcal{H}(e^{\jmath\boldsymbol{\theta}})\mathcal{H}^H(e^{\jmath\boldsymbol{\theta}})$ becomes singular and it cannot be inverted. Hence we cannot use the ZFB of (7.4). Instead, we consider RZFB, under which the BS transmits

$$\begin{aligned} x_I &= \mathcal{H}^H(e^{\jmath\boldsymbol{\theta}}) \left([\mathcal{H}(e^{\jmath\boldsymbol{\theta}})]^2 + \alpha I_K\right)^{-1} \text{diag}[\boldsymbol{p}_k]_{k=1,\ldots,K} s \\ &= \left([\mathcal{H}^H(e^{\jmath\boldsymbol{\theta}})]^2 + \alpha I_M\right)^{-1} \mathcal{H}^H(e^{\jmath\boldsymbol{\theta}}) \text{diag}[\boldsymbol{p}_k]_{k=1,\ldots,K} s. \end{aligned} \tag{7.37}$$

The Equation (7.3) may be rewritten as

$$y = \mathcal{H}(e^{\jmath\boldsymbol{\theta}}) \left([\mathcal{H}^H(e^{\jmath\boldsymbol{\theta}})]^2 + \alpha I_M\right)^{-1} \mathcal{H}^H(e^{\jmath\boldsymbol{\theta}}) \text{diag}[\boldsymbol{p}_k]_{k=1}^K s + \bar{n}. \tag{7.38}$$

Thanks to the regularization of the ill-posed part only, we can design $\boldsymbol{\theta}$ separately, because the capability of RZFB actually depends on the matrix $\mathcal{H}(e^{\jmath\boldsymbol{\theta}}) \left([\mathcal{H}^H(e^{\jmath\boldsymbol{\theta}})]^2 + \alpha I_M\right)^{-1} \mathcal{H}^H(e^{\jmath\boldsymbol{\theta}})$ in (7.38). Note that we have:

$$\begin{aligned} \begin{bmatrix} I_K & \mathcal{H}(e^{\jmath\boldsymbol{\theta}}) \\ \mathcal{H}^H(e^{\jmath\boldsymbol{\theta}}) & [\mathcal{H}^H(e^{\jmath\boldsymbol{\theta}})]^2 + \alpha I_M \end{bmatrix} &\succeq \begin{bmatrix} I_K & \mathcal{H}(e^{\jmath\boldsymbol{\theta}}) \\ \mathcal{H}^H(e^{\jmath\boldsymbol{\theta}}) & [\mathcal{H}^H(e^{\jmath\boldsymbol{\theta}})]^2 \end{bmatrix} \\ &= \begin{bmatrix} I_K \\ \mathcal{H}^H(e^{\jmath\boldsymbol{\theta}}) \end{bmatrix} \begin{bmatrix} I_K & \mathcal{H}(e^{\jmath\boldsymbol{\theta}}) \end{bmatrix} \\ &\succeq 0. \end{aligned}$$

Upon using the Shur complement (see e.g. [162]), we arrive at:

$$I_K \succeq \mathcal{H}(e^{\jmath\boldsymbol{\theta}}) \left([\mathcal{H}^H(e^{\jmath\boldsymbol{\theta}})]^2 + \alpha I_M\right)^{-1} \mathcal{H}^H(e^{\jmath\boldsymbol{\theta}}). \tag{7.39}$$

It is plausible that the more similar the matrix in the right hand side (RHS) to the identity matrix in the left hand side (LHS), the better RZFB performs. Define an ellipsoid in $\mathbb{C}^K$:

$$\mathcal{E}(\boldsymbol{\theta}) \triangleq \{x \in \mathbb{C}^K : x^H \mathcal{H}(e^{\jmath\boldsymbol{\theta}}) \left([\mathcal{H}^H(e^{\jmath\boldsymbol{\theta}})]^2 + \alpha I_M\right)^{-1} \mathcal{H}^H(e^{\jmath\boldsymbol{\theta}}) x \leq 1\}. \tag{7.40}$$

The matrix inequality (7.39) shows that $\mathcal{E}(\boldsymbol{\theta})$ always contains the unit sphere:

$$\mathcal{E}(\boldsymbol{\theta}) \supset \mathcal{U} \triangleq \{x \in \mathbb{C}^K : \ ||x||^2 \leq 1\}. \tag{7.41}$$

The rest of this section is devoted to the optimization of $\boldsymbol{\theta}$ based on optimizing the shape of $\mathcal{E}(\boldsymbol{\theta})$.

7.3.1 Trace-maximization based algorithm

We aim to minimize the surface of $\mathcal{E}(\boldsymbol{\theta})$, i.e. we aim to maximize the trace of the right hand size (RHS) of (7.39) [163]. As such, the problem is the same as (7.32), thus it may be solved by Alg. 13. We repeat it here as Algorithm 14 to emphasize that it is specifically tailored for RZFB.

Algorithm 14 RZF full step descent algorithm for trace maximization (7.32)

1: **Initialization:** Initial $\theta^{(0)}$.
2: **Repeat until convergence of** $\theta^{(\kappa)}$**:** Generate $\theta^{(\kappa+1)}$ by (7.35). Set $\kappa := \kappa + 1$.
3: **Output** θ^{opt}.

7.3.2 Determinant-maximization algorithms

We aim to minimize the volume of the set $\mathcal{E}(\boldsymbol{\theta}) \setminus \mathcal{U}$, which is equivalent to the problem [163]:

$$\min_{\boldsymbol{\theta}} |I_K - \mathcal{H}(e^{\jmath\boldsymbol{\theta}}) \left([\mathcal{H}^H(e^{\jmath\boldsymbol{\theta}})]^2 + \alpha I_M\right)^{-1} \mathcal{H}^H(e^{\jmath\boldsymbol{\theta}})| \tag{7.42}$$

$$\Leftrightarrow \quad \max_{\boldsymbol{\theta}} \ \phi(e^{\jmath\boldsymbol{\theta}}) \triangleq \ln|I_K + \frac{1}{\alpha}[\mathcal{H}(e^{\jmath\boldsymbol{\theta}})]^2|, \tag{7.43}$$

because according to the matrix inversion formula, we have

$$I_K - \mathcal{H}(e^{\jmath\boldsymbol{\theta}}) \left([\mathcal{H}^H(e^{\jmath\boldsymbol{\theta}})]^2 + \alpha I_M\right)^{-1} \mathcal{H}^H(e^{\jmath\boldsymbol{\theta}}) = \left(I_K + \frac{1}{\alpha}[\mathcal{H}(e^{\jmath\boldsymbol{\theta}})]^2\right)^{-1}.$$

The problem (7.43) is equivalent to

$$\max_{\boldsymbol{\theta}} \varphi(e^{\jmath\boldsymbol{\theta}}) \triangleq \ln|\alpha I_K + [\mathcal{H}(e^{\jmath\boldsymbol{\theta}})]^2|. \tag{7.44}$$

As always, let $\theta^{(\kappa)}$ be a point found during the $(\kappa-1)$-st iteration.

Step descent algorithm

The linearization of the function φ at $\theta^{(\kappa)}$ is formulated as:

$$\varphi(e^{\jmath\theta^{(\kappa)}}) - \langle \mathcal{A}^{(\kappa)}[\mathcal{H}(e^{\jmath\theta^{(\kappa)}})]^2\rangle + \langle \mathcal{A}^{(\kappa)}[\mathcal{H}(e^{\jmath\boldsymbol{\theta}})]^2\rangle, \tag{7.45}$$

for

$$\mathcal{A}^{(\kappa)} \triangleq \left(\alpha I_K + [\mathcal{H}(e^{\jmath\theta^{(\kappa)}})]^2\right)^{-1}. \tag{7.46}$$

Thus, for $\mathcal{A}^{(\kappa)}$ defined by (7.46) we address the problem (7.13) and then (7.15) to generate the descent direction $\theta^{(\kappa+1)}$ given by (7.16) as per Algorithm 15, which has to update the incumbent point with the convergence not granted.

Algorithm 15 RZFB step descent algorithm for maximizing the log determinant (7.44)

1: **Initialization:** Initial $\theta^{(0)}$ and set $\theta^{opt} = \theta^{(0)}$ and $\eta^{opt} = \varphi(\theta^{opt})$ as the incumbent RIS and value.
2: **Repeat:** For $\mathcal{A}^{(\kappa)}$ in (7.46), generate $\theta^{(\kappa+1)}$ by (7.16). If $\varphi(\theta^{(\kappa+1)}) < \eta^{opt}$, set $\theta^{opt} = \theta^{(\kappa+1)}$ and $\eta^{opt} = \varphi(\theta^{(\kappa+1)})$. Set $\kappa := \kappa + 1$.
3: **Output** θ^{opt} and η^{opt}.

Full step descent algorithm

We also can use the inequality (A.15) to address (7.43) as (7.47):

$$\begin{aligned}
\phi(e^{\jmath\boldsymbol{\theta}}) &\geq \phi(e^{\jmath\theta^{(\kappa)}}) - ||\mathcal{H}(e^{\jmath\theta^{(\kappa)}})||^2 + \frac{1}{\alpha}\Big[2\Re\{\mathcal{H}(e^{\jmath\boldsymbol{\theta}})\mathcal{H}^H(e^{\jmath\theta^{(\kappa)}})\} \\
&\quad -\langle \mathcal{H}(e^{\jmath\theta^{(\kappa)}})(\alpha I_m + [\mathcal{H}^H(e^{\jmath\theta^{(\kappa)}})]^2)^{-1}\mathcal{H}^H(e^{\jmath\theta^{(\kappa)}}), [\mathcal{H}(e^{\jmath\boldsymbol{\theta}})]^2\rangle\Big] \\
&= a^{(\kappa)} + \frac{1}{\alpha}\Big[2\Re\{\mathcal{H}(e^{\jmath\boldsymbol{\theta}})\mathcal{H}^H(e^{\jmath\theta^{(\kappa)}})\} - \langle [\Psi^{(\kappa)}\mathcal{H}(e^{\jmath\boldsymbol{\theta}})]^2\rangle\Big] \\
&= a^{(\kappa)} + \frac{1}{\alpha}\left[2\Re\{\sum_{n=1}^{N} e^{\jmath\theta_n} b^{(\kappa)}(n)\} - (e^{\jmath\boldsymbol{\theta}})^H \mathcal{C}^{(\kappa)} e^{\jmath\boldsymbol{\theta}}\right] \\
&\geq a^{(\kappa)} + \frac{1}{\alpha}\left[2\Re\left\{\sum_{n=1}^{N} e^{\jmath\theta_n}\left(b^{(\kappa)}(n) - \sum_{m=1}^{N} e^{-\jmath\theta_m^{(\kappa)}}\mathcal{C}^{(\kappa)}(m,n) + \lambda_{\max}(\mathcal{C}^{(\kappa)})e^{-\jmath\theta_n^{(\kappa)}}\right)\right\}\right. \\
&\quad \left. -(e^{\jmath\theta^{(\kappa)}})^H\mathcal{C}^{(\kappa)}e^{\jmath\theta^{(\kappa)}} - 2\lambda_{\max}(\mathcal{C}^{(\kappa)})N\right] \\
&\triangleq \phi^{(\kappa)}(e^{\jmath\boldsymbol{\theta}}),
\end{aligned}$$

for

$$a^{(\kappa)} \triangleq \phi(e^{\jmath\theta^{(\kappa)}}) - ||\mathcal{H}(e^{\jmath\theta^{(\kappa)}})||^2,$$
$$\Psi^{(\kappa)} \triangleq (\alpha I_m + [\mathcal{H}^H(e^{\jmath\theta^{(\kappa)}})]^2)^{-1/2}\mathcal{H}^H(e^{\jmath\theta^{(\kappa)}}),$$
$$b^{(\kappa)}(n) \triangleq \langle \mathcal{H}_n\mathcal{H}^H(e^{\jmath\theta^{(\kappa)}})\rangle, n \in \mathcal{N},$$
$$\mathcal{C}^{(\kappa)}(n,m) \triangleq \langle \mathcal{H}_m\mathcal{H}_n^H[(\Psi^{(\kappa)})^H]^2\rangle, (n,m) \in \mathcal{N}\times\mathcal{N},$$

and $\lambda_{\max}(\mathcal{C}^{(\kappa)})$ is the maximum eigenvalue of $\mathcal{C}^{(\kappa)}$, which is positive because the matrix $\mathcal{C}^{(\kappa)}$ is positive definite.

To generate a better point $\theta^{(\kappa+1)}$, we thus solve the following problem:

$$\max_{\boldsymbol{\theta}} \phi^{(\kappa)}(e^{\jmath\boldsymbol{\theta}}), \tag{7.47}$$

which admits the following closed-form solution similar to (7.16):

$$\theta_n^{(\kappa+1)} = -\angle\left(b^{(\kappa)}(n) - \sum_{m=1}^{N} e^{-\jmath\theta_m^{(\kappa)}}\mathcal{C}^{(\kappa)}(m,n) + \lambda_{\max}(\mathcal{C}^{(\kappa)})e^{-\jmath\theta_n^{(\kappa)}}\right), n \in \mathcal{N}. \tag{7.48}$$

Algorithm 16 RZF full step descent algorithm for maximizing the log determinant (7.44)

1: **Initialization:** Initial $\theta^{(0)}$.
2: **Repeat:** Generate a better point $\theta^{(\kappa+1)}$ by (7.48). Set $\kappa := \kappa + 1$.
3: **Output** $\theta^{opt} = \theta^{(\kappa)}$.

Before concluding this section, let us mention that after designing θ^{opt}, we insert it into (7.38) to consider the problem of power allocation $\boldsymbol{p}_k$, $k = 1, \ldots, K$ for max-min users rate optimization. However, we will treat it as a particular case of the problems in the next section.

7.4 ZFB Applications to RIS-aided integrated data and energy delivery

Now, in addition to IUs we consider a scenario with the BS serving also K_E EUs e_ℓ, $\ell \in \mathcal{K}_E \triangleq \{1, \ldots, K_E\}$, which are located near the BS to harvest energy from the BS. We

employ the transmit-TS technique, under which the first time-slot fraction $1/t_1$ is used for energy delivery and the second time-slot fraction $1/t_2$ is used for information delivery.

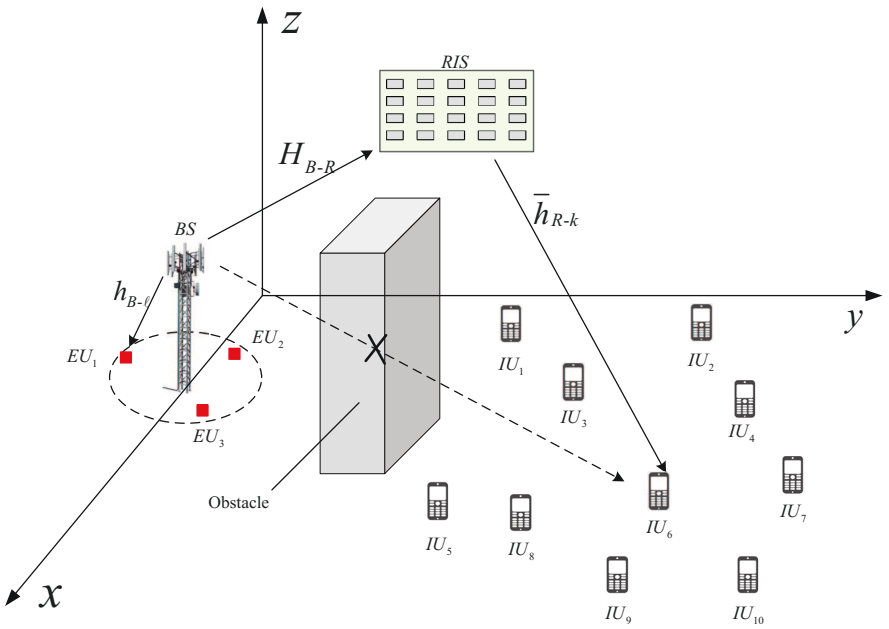

Fig. 7.3 Scenario setup for integrated data and energy networking.

7.4.1 Energy delivery during $1/t_1$

Let us assume that the LoS channel spanning from the BS to EU e_ℓ is $\tilde{h}_{B-e_\ell} \triangleq \sqrt{\beta^E_{B-e_\ell}} h_{B-e_\ell} \in \mathbb{C}^{1\times M}$, where $\sqrt{\beta^E_{B-e_\ell}}$ models both the path-loss and the large-scale fading of the LoS component, where the entries of h_{B-e_ℓ} are $\mathcal{C}(0,1)$, to modelling the small-scale fading.

The signal received at EU e_ℓ is

$$y_{e_\ell} = \tilde{h}_{B-e_\ell} x_E, \tag{7.49}$$

where $x_E \in \mathbb{C}^M$ is the transmitted signal carrying the energy. Note that in (7.49) we ignore the background noise, as its power is negligible for EH. Inspired by [147], conjugate energy beamforming is used, so we have

$$x_E = \sum_{\ell=1}^{K_E} \tilde{h}^H_{B-e_\ell} \sqrt{\boldsymbol{x}_\ell} \delta_\ell,$$

where $\delta_\ell \in \mathcal{C}(0,1)$, which is the energy symbol. The power of the transmit energy signal is

$$\pi_E(\boldsymbol{x}) = \sum_{\ell=1}^{K_E} ||\tilde{h}_{B-e_\ell}||^2 \boldsymbol{x}_\ell.$$

The energy harvested by EU e_ℓ during $1/t_1$ is $\zeta\pi_\ell(\boldsymbol{x})$ with

$$\pi_\ell(\boldsymbol{x}) \triangleq \frac{\sum_{\ell'=1}^{K_E} |\langle \tilde{h}_{B-e_\ell}, \tilde{h}_{B-e_{\ell'}} \rangle|^2 \boldsymbol{x}_{\ell'}}{t_1}, \tag{7.50}$$

while ζ is the efficiency of energy conversion, which is set to 0.5 in this chapter.

7.4.2 Information transmission during $1/t_2$

The information transmission is implemented during the time-slot fraction $1/t_2$, with the signal received at IU k given by Equation (7.1), while the corresponding multi-input multi-output (MIMO) equation is given by (7.3). Since the specific design of PRCs has no impact on the EH performance, we insert θ^{opt} found in the previous sections into the equation (7.1) and (7.3) and also into (7.4) and (7.37) for ZFB or RZF beamforming, respectively. When the ZF beamformer of(7.4) is used in conjunction with $\boldsymbol{p}_k \equiv \boldsymbol{p}_0$, the throughput at IU k is expressed according to (7.7) as

$$r_0(\boldsymbol{p}_0) = \ln\left(1 + \boldsymbol{p}_0^2/\sigma\right), \tag{7.51}$$

and the power used for information transmission according to (7.9) is given by

$$a_{zf}\boldsymbol{p}_0^2 \tag{7.52}$$

for

$$a_{zf} \triangleq \langle \left([\mathcal{H}(e^{\jmath\theta^{opt}})]^2 \right)^{-1} \rangle. \tag{7.53}$$

7.4.3 Optimal energy and ZF information beamforming

Here we consider the IUs' max-min throughput optimization problem subject to the QoES in terms of the EUs' harvested energy rate formulated as:

$$\max_{\boldsymbol{p}_0,\boldsymbol{x}\in\mathbb{R}_+^{K_E},\gamma,\mathbf{t}=(t_1,t_2)^T\in\mathbb{R}_+^2} \quad \gamma \quad \text{s.t.} \tag{7.54a}$$

$$\frac{\pi_E(\boldsymbol{x})}{t_1}+\frac{a_{zf}\boldsymbol{p}_0^2}{t_2}\le P, \tag{7.54b}$$

$$\pi_E(\boldsymbol{x})\le 3P, a_{zf}\boldsymbol{p}_0^2\le 3P, \tag{7.54c}$$

$$\frac{1}{t_1}+\frac{1}{t_2}\le 1, \tag{7.54d}$$

$$\sum_{\ell'=1}^{K_E}|\langle\tilde{h}_{B-e_\ell}\tilde{h}_{B-e_{\ell'}}^H\rangle|^2\boldsymbol{x}_{\ell'}\ge t_1 e_{\min}/\zeta, \ell\in\mathcal{K}_E, \tag{7.54e}$$

$$r_0(\boldsymbol{p}_0)\ge\gamma t_2, \tag{7.54f}$$

where $e_{\min}$ is the harvested energy threshold. The slack variable γ is introduced in (7.54a) and (7.54f) to reflect the IUs' minimal throughput; (7.54b) is the total transmit power constraint under a given budget P and (7.54c) is a physical transmission constraint; (7.54d) restricts the energy and information transfer to a specific time slot, and (7.54e) represents the energy constraint of EUs in terms of their minimal required energy, which in fact reflects the following constraint:

$$\pi_\ell(\boldsymbol{x})\ge e_{\min}/\zeta, \ell\in\mathcal{K}_E, \tag{7.55}$$

with $\pi_\ell(\boldsymbol{x})$ defined in (7.50).

In the problem (7.54), the constraints (7.54c)-(7.54e) are convex but the constraints (7.54b) and (7.54f) are not, making (7.54) a nonconvex problem. We now develop inner convex approximations for these nonconvex constraints to propose a path-following algorithm for computing (7.54).

Let the feasible point for (7.54) $(p_0^{(\kappa)}, x^{(\kappa)}, t^{(\kappa)}, \gamma^{(\kappa)})$ is found from the $(\kappa-1)$-st iteration. Then upon the following inequality

$$\pi_E(\boldsymbol{x})\le\pi_E^{(\kappa)}(\boldsymbol{x})\triangleq\frac{1}{2}\left(\frac{\pi_E^2(\boldsymbol{x})}{\pi_E(x^{(\kappa)})}+\pi_E(x^{(\kappa)})\right), \tag{7.56}$$

the nonconvex constraint (7.54b) is innerly approximated by

$$\frac{\pi_E^{(\kappa)}(\boldsymbol{x})}{t_1} + \frac{a_{zf}\boldsymbol{p}_0^2}{t_2} \leq P. \tag{7.57}$$

Using the inequality (A.26) yields the following concave quadratic minorant of $r_0(\boldsymbol{p}_0)$ in the LHS of (7.54f):[5]

$$r_0^{(\kappa)}(\boldsymbol{p}_0) \triangleq r_0^{(\kappa)}(p_0^{(\kappa)}) - \frac{(p_0^{(\kappa)})^2}{\sigma} + 2\frac{p_0^{(\kappa)}}{\sigma}\boldsymbol{p}_0 - \frac{(p_0^{(\kappa)})^2}{\sigma\left((p_0^{(\kappa)})^2+\sigma\right)}\left(\boldsymbol{p}_0^2+\sigma\right). \tag{7.58}$$

Meanwhile, the RHS of (7.54f) is upper bounded as follows:

$$\gamma t_2 \leq \frac{\gamma^{(\kappa)} t_2^{(\kappa)}}{4}\left(\frac{\gamma}{\gamma^{(\kappa)}} + \frac{t_2}{t_2^{(\kappa)}}\right)^2. \tag{7.59}$$

The nonconvex constraint (7.54f) is thus innerly approximated by the following convex quadratic constraint

$$r_0^{(\kappa)}(\boldsymbol{p}_0) \geq \frac{\gamma^{(\kappa)} t_2^{(\kappa)}}{4}\left(\frac{\gamma}{\gamma^{(\kappa)}} + \frac{t_2}{t_2^{(\kappa)}}\right)^2. \tag{7.60}$$

To generate the next feasible point $(p_0^{(\kappa+1)}, x^{(\kappa+1)}, t^{(\kappa+1)}, \gamma^{(\kappa+1)})$ for (7.54), we then solve the following convex optimization problem:

$$\max_{\boldsymbol{p}_0,\boldsymbol{x},\gamma,\mathbf{t}=(t_1,t_2)^T\in\mathbb{R}_+^2} \quad \gamma \quad \text{s.t.} \quad (7.54c), (7.54d), (7.54e), (7.57), (7.60). \tag{7.61}$$

As this convex problem involves $m_c = K_E + 3$ decision variables and $n_v = 5$ quadratic constraints, its computational complexity is on the order of [98]

$$\mathcal{O}[m_c^{2.5}(n_v^2 + m_c)]. \tag{7.62}$$

As $(p_0^{(\kappa+1)}, x^{(\kappa+1)}, t^{(\kappa+1)}, \gamma^{(\kappa+1)})$ is the optimal solution of (7.61), while $(p_0^{(\kappa+1)}, x^{(\kappa)}, t^{(\kappa)}, \gamma^{(\kappa)})$ is its feasible point, it follows that

$$\gamma^{(\kappa+1)} > \gamma^{(\kappa)}, \tag{7.63}$$

provided that $(p_0^{(\kappa+1)}, x^{(\kappa+1)}, t^{(\kappa+1)}, \gamma^{(\kappa+1)}) \neq (p_0^{(\kappa)}, x^{(\kappa)}, t^{(\kappa)}, \gamma^{(\kappa)})$, i.e. $(p_0^{(\kappa+1)}, x^{(\kappa+1)}, t^{(\kappa+1)}, \gamma^{(\kappa+1)})$ is a better feasible point than $(p_0^{(\kappa)}, x^{(\kappa)}, t^{(\kappa)}, \gamma^{(\kappa)})$. The sequence $\{(p_0^{(\kappa)}, x^{(\kappa)}, t^{(\kappa)}, \gamma^{(\kappa)})\}$ of improved feasible points for (7.54) converges at least to a locally optimal solution of (7.54).

[5] $r_0(\boldsymbol{p}_0) \geq r_0^{(\kappa)}(\boldsymbol{p}_0)$

As analyzed in [14], this locally optimal solution often turns out to be the globally optimal one. Algorithm 17 provides the pseudo-code for the procedure iterating (7.61).

Algorithm 17 ZF Path-following algorithm for (7.54)

1: **Initialization:** Randomly generate a feasible point $(p_0^{(0)}, x^{(0)}, t^{(0)}, \gamma^{(0)})$ for (7.54). Set $\kappa = 0$.
2: **Repeat:** Generate $(p_0^{(\kappa+1)}, x^{(\kappa+1)}, t^{(\kappa+1)}, \gamma^{(\kappa+1)})$ by solving the convex problem (7.61). Set $\kappa := \kappa + 1$.
3: **Output** $(p_0^{(\kappa)}, x^{(\kappa)}, t^{(\kappa)}, \gamma^{(\kappa)})$.

7.5 RZFB applications to RIS-aided integrated data and energy delivery

7.5.1 The conventional RZFB

When the RZFB (7.37) is used, Equation (7.38) becomes

$$y_k = \bar{h}_{B-k}\bar{\mathcal{H}}^{rz}\sum_{j=1}^{K}\bar{h}_{B-j}^{H}\boldsymbol{p}_j s_j + \bar{n}_k \tag{7.64}$$

$$= \sum_{j=1}^{K}\bar{h}_{kj}\boldsymbol{p}_j s_j + \bar{n}_k, \tag{7.65}$$

for

$$\begin{aligned}\bar{\mathcal{H}}^{rz} &\triangleq \left(\mathcal{H}^H(\theta^{opt})\mathcal{H}(\theta^{opt}) + \alpha I_M\right)^{-1}\\ \bar{h}_{B-j} &\triangleq h_{B-j}(\theta^{opt}), j = 1, \ldots, K.\end{aligned} \tag{7.66}$$

and

$$\bar{h}_{kj} \triangleq \bar{h}_{B-k}\bar{\mathcal{H}}^{rz}\bar{h}_{B-j}^{H}. \tag{7.67}$$

The throughput at IU k is expressed as:

$$r_k(\boldsymbol{p}) = \ln\left(1 + |\bar{h}_{kk}|^2\boldsymbol{p}_k^2\left(\sum_{j\neq k}^{K}|\bar{h}_{kj}|^2\boldsymbol{p}_j^2 + \sigma\right)^{-1}\right). \tag{7.68}$$

The transmit power apportioned for information delivery is

$$\pi_I(\boldsymbol{p}) \triangleq \sum_{j=1}^{K} ||\bar{\mathcal{H}}^{rz}\bar{h}_{B-j}^H||^2 \boldsymbol{p}_j^2. \tag{7.69}$$

Thus we consider the following problem of the IUs' max-min throughput optimization subject to the QoES in terms of the EUs' harvested energy thresholds:

$$\max_{\boldsymbol{p},\boldsymbol{x},\gamma,\mathbf{t}=(t_1,t_2)^T\in\mathbb{R}_+^2} \quad \gamma \quad \text{s.t.} \quad (7.54d), (7.54e), \tag{7.70a}$$

$$\frac{\pi_E(\boldsymbol{x})}{t_1} + \frac{\pi_I(\boldsymbol{p})}{t_2} \leq P, \tag{7.70b}$$

$$\pi_E(\boldsymbol{x}) \leq 3P, \pi_I(\boldsymbol{p}) \leq 3P, \tag{7.70c}$$

$$r_k(\boldsymbol{p}) \geq \gamma t_2, k \in \mathcal{K}, \tag{7.70d}$$

where like their counterparts in (7.54), γ in (7.70a) and (7.70d) is a slack variable to express the IUs minimal throughput, (7.70b) and (7.70c) are respectively the total power transmit constraint under the budget P and a physical transmission constraint, while as before, (7.54d) restricts the energy and information transfer within a time slot, and (7.54e) is the energy constraint of EUs in terms of their minimal required energy.

To propose a path-following algorithm for computing (7.70), we have to develop inner approximations for its nonconvex constraints (7.70b) and (7.70d).

Let $(p^{(\kappa)}, x^{(\kappa)}, t^{(\kappa)}, \gamma^{(\kappa)})$ be the feasible point found from the $(\kappa-1)$-st iteration for (7.70). Based on the inequality (7.56), the nonconvex constraint (7.70b) is innerly approximated by

$$\frac{\pi_E^{(\kappa)}(\boldsymbol{x})}{t_1} + \frac{\pi_I(\boldsymbol{p})}{t_2} \leq P. \tag{7.71}$$

Using the inequality (A.26) yields the following concave quadratic minorant of $r_k(\mathbf{P})$ in the LHS of (7.70d):

$$r_k^{(k)}(\mathbf{P}) \triangleq \tilde{\tilde{a}}^{(\kappa)} + 2\tilde{\tilde{b}}^{(\kappa)}\boldsymbol{p}_k - \tilde{\tilde{c}}^{(\kappa)} \sum_{j=1}^{K} |\bar{h}_{kj}|^2 \boldsymbol{p}_j^2, \tag{7.72}$$

where

$$\begin{aligned}
\tilde{\tilde{a}}_k^{(\kappa)} &= r_k(p^{(\kappa)}) - |\bar{h}_{kk}|^2 (p_k^{(\kappa)})^2 \left(\textstyle\sum_{j\neq k} |\bar{h}_{kj}|^2 (p_j^{(\kappa)})^2 + \sigma\right)^{-1} - \sigma\tilde{\tilde{c}}_k^{(\kappa)}, \\
\tilde{\tilde{b}}_k^{(\kappa)} &= |\bar{h}_{kk}|^2 p_k^{(\kappa)} \left(\textstyle\sum_{j\neq k} |\bar{h}_{kj}|^2 (p_j^{(\kappa)})^2 + \sigma\right)^{-1}, \\
\tilde{\tilde{c}}_k^{(\kappa)} &= \left(\textstyle\sum_{j\neq k} |\bar{h}_{kj}|^2 (p_j^{(\kappa)})^2 + \sigma\right)^{-1} - \left(\textstyle\sum_{j=1}^{K} |\bar{h}_{kj}|^2 (p_j^{(\kappa)})^2 + \sigma\right)^{-1}.
\end{aligned}$$

By (7.59) and (7.72), the nonconvex constraint (7.70d) is innerly approximated by the following convex quadratic constraint

$$r_k^{(k)}(\boldsymbol{p}) \geq \frac{\gamma^{(\kappa)} t_2^{(\kappa)}}{4} \left(\frac{\gamma}{\gamma^{(\kappa)}} + \frac{t_2}{t_2^{(\kappa)}} \right)^2, k \in \mathcal{K}. \tag{7.73}$$

To generate the next feasible point $(p^{(\kappa+1)}, x^{(\kappa+1)}, t^{(\kappa+1)}, \gamma^{(\kappa+1)})$ for (7.70), we then solve the following convex optimization problem :

$$\max_{\boldsymbol{p},\boldsymbol{x},\gamma,\mathbf{t}=(t_1,t_2)^T \in \mathbb{R}_+^2} \quad \gamma \quad \text{s.t.} \quad (7.54d), (7.54e), (7.70c), (7.71), (7.73). \tag{7.74}$$

The computational complexity order of this convex problem is given by (7.62) where we have $n_v = K + K_E + 3$ and $m_c = K + 4$. As $(p^{(\kappa+1)}, x^{(\kappa+1)}, t^{(\kappa+1)}, \gamma^{(\kappa+1)})$ is the optimal solution of (7.74) while $(p^{(\kappa+1)}, x^{(\kappa)}, t^{(\kappa)}, \gamma^{(\kappa)})$ is its feasible point, (7.63) is satisfied, provided that $(p^{(\kappa+1)}, x^{(\kappa+1)}, t^{(\kappa+1)}, \gamma^{(\kappa+1)}) \neq (p^{(\kappa)}, x^{(\kappa)}, t^{(\kappa)}, \gamma^{(\kappa)})$, i.e. $(p^{(\kappa+1)}, x^{(\kappa+1)}, t^{(\kappa+1)}, \gamma^{(\kappa+1)})$ is a better feasible point than $(p^{(\kappa)}, x^{(\kappa)}, t^{(\kappa)}, \gamma^{(\kappa)})$. Algorithm 18 provides the pseudo-code for solving (7.70) by iterating the convex problem (7.74).

Algorithm 18 Conventional RZF Path-following algorithm for (7.70)

1: **Initialization:** Randomly generate a feasible point $(p^{(0)}, x^{(0)}, t^{(0)}, \gamma^{(0)})$ for (7.70). Set $\kappa = 0$.
2: **Repeat:** Generate $(p^{(\kappa+1)}, x^{(\kappa+1)}, t^{(\kappa+1)}, \gamma^{(\kappa+1)})$ by solving the convex problem (7.74). Set $\kappa := \kappa + 1$.
3: **Output** $(p^{(\kappa)}, x^{(\kappa)}, t^{(\kappa)}, \gamma^{(\kappa)})$.

7.5.2 New RZFB

Instead of (7.37), let us now design the transmit signal as

$$x_I \quad = \quad \bar{\mathcal{H}}^{rz} \sum_{j=1}^{K} \bar{h}_{B-j}^H [\boldsymbol{p}_{1,j} s_j + \boldsymbol{p}_{2,j} s_j^*] \tag{7.75}$$

with $\boldsymbol{p}_{1,j} \in \mathbb{C}$ and $\boldsymbol{p}_{2,j} \in \mathbb{C}$, so instead of (7.65) the received signal by IU k is

$$y_k = \sum_{j=1}^{K} \bar{h}_{kj} [\boldsymbol{p}_{1,j} s_j + \boldsymbol{p}_{2,j} s_j^*] + \bar{n}_k. \tag{7.76}$$

While x_I defined by (7.37) is a proper Gaussian random variable with $\mathbb{E}((x_I)^2) = 0$, that defined by (7.75) is an improper Gaussian random variable [75] with $\mathbb{E}((x_I)^2) \neq 0$. The augmented form of (7.76) is

$$\bar{y}_k = \sum_{k=1}^{K} \bar{H}_{kj} V(\boldsymbol{p}_j) \bar{s}_j + \bar{n}_k^A, \tag{7.77}$$

where

$$\bar{y}_k \triangleq \begin{bmatrix} y_k \\ y_k^* \end{bmatrix}, \bar{H}_{kj} = \begin{bmatrix} \bar{h}_{kj} & 0 \\ 0 & \bar{h}_{kj}^* \end{bmatrix}, \bar{s}_j \triangleq \begin{bmatrix} s_j \\ s_j^* \end{bmatrix}, \bar{n}_k^A \triangleq \begin{bmatrix} \bar{n}_k \\ \bar{n}_k^* \end{bmatrix},$$

and

$$V(\boldsymbol{p}_j) \triangleq \begin{bmatrix} \boldsymbol{p}_{1,j} & \boldsymbol{p}_{2,j} \\ \boldsymbol{p}_{2,j}^* & \boldsymbol{p}_{1,j}^* \end{bmatrix}, \boldsymbol{p}_j \triangleq (\boldsymbol{p}_{1,j}, \boldsymbol{p}_{2,j}).$$

The throughput of IU k is $\frac{1}{2}\rho_k(\boldsymbol{p})$ [97] with

$$\rho_k(\boldsymbol{p}) \triangleq \ln \left| I_2 + [\bar{H}_{kk} V(\boldsymbol{p}_k)]^2 \left(\sum_{j \neq k}^{K} [\bar{H}_{kj} V(\boldsymbol{p}_j)]^2 + \sigma I_2 \right)^{-1} \right|.$$

The transmit power apportioned for information delivery is

$$\tilde{\pi}_I(\boldsymbol{p}) \triangleq \sum_{j=1}^{K} ||\bar{\mathcal{H}}^{rz} \bar{h}_{B-j}^H \begin{bmatrix} \boldsymbol{p}_{1,j} & \boldsymbol{p}_{2,j} \end{bmatrix}||^2. \tag{7.78}$$

Thus we consider the following problem of the IUs' max-min rate optimization subject to the QoES in terms of the EUs' harvested energy thresholds corresponding to (7.70):

$$\max_{\boldsymbol{p}, \boldsymbol{x}, \gamma, \mathbf{t}=(t_1,t_2)^T \in \mathbb{R}_+^2} \quad \gamma \quad \text{s.t.} \quad (7.54d), (7.54e), \tag{7.79a}$$

$$\frac{\pi_E(\boldsymbol{x})}{t_1} + \frac{\tilde{\pi}_I(\boldsymbol{p})}{t_2} \leq P, \tag{7.79b}$$

$$\pi_E(\boldsymbol{x}) \leq 3P, \tilde{\pi}_I(\boldsymbol{p}) \leq 3P, \tag{7.79c}$$

$$\rho_k(\boldsymbol{p}) \geq 2\gamma t_2, k \in \mathcal{K}. \tag{7.79d}$$

where like their counterparts in (7.70), the slack variable γ is introduced in (7.79a) and (7.79d) to express the IUs' minimal throughput, (7.79b) and (7.79c) are respectively the total power transmit constraint under the budget P and a physical transmission constraint, while as before, (7.54d) restricts the energy and information transfer within a time slot, and (7.54e) is the energy constraint of EUs in terms of their minimal required energy. To propose

a path-following algorithm for computing (7.79), we have to develop inner approximations for its nonconvex constraints (7.79b) and (7.79d).

Let $(p^{(\kappa)}, x^{(\kappa)}, t^{(\kappa)}, \gamma^{(\kappa)})$ be a feasible point for (7.70) that is found from the $(\kappa-1)$-st iteration.

Using inequality (A.26) yields

$$\begin{aligned}\rho_k(\boldsymbol{p}) &\geq a_k^{(\kappa)} + 2\Re\{\langle V^H(p_k^{(\kappa)})\bar{H}_{kk}^H(B_k^{(\kappa)})^{-1}\bar{H}_{kk}V(\boldsymbol{p}_k)\rangle\} - \sum_{j=1}^{K}||(C^{(\kappa)})^{1/2}\bar{H}_{kj}V(\boldsymbol{p}_j)||^2 \\ &\triangleq \rho_k^{(k)}(\mathbf{P}),\end{aligned} \tag{7.80}$$

where

$$\begin{gathered}a_k^{(\kappa)} \triangleq r_k(p^{(\kappa)}) - \langle[\bar{H}_{kk}V(p_k^{(\kappa)})]^2(B_k^{(\kappa)})^{-1}\rangle - \sigma\langle C_k^{(\kappa)}\rangle, \\ B_k^{(\kappa)} \triangleq \textstyle\sum_{j\neq k}^{K}[\bar{H}_{kj}V(p_j^{(\kappa)})]^2 + \sigma I_2, \\ C_k^{(\kappa)} \triangleq (B_k^{(\kappa)})^{-1} - \left(B_k^{(\kappa)} + [\bar{H}_{kk}V(p_k^{(\kappa)})]^2\right)^{-1}.\end{gathered}$$

To generate the next better feasible point $\left(p^{(\kappa+1)}, x^{(\kappa+1)}\right)$ for (7.79), we then solve the following convex problem:

$$\max_{\boldsymbol{p},\boldsymbol{x},\gamma,\mathbf{t}=(t_1,t_2)^T\in\mathbb{R}_+^2} \quad \gamma \quad \text{s.t.} \quad (7.54d), (7.54e), (7.71), (7.79b), (7.79c), \tag{7.81a}$$

$$\rho_k^{(k)}(\boldsymbol{p}) \geq \frac{\gamma^{(\kappa)}t_2^{(\kappa)}}{2}\left(\frac{\gamma}{\gamma^{(\kappa)}} + \frac{t_2}{t_2^{(\kappa)}}\right)^2. \tag{7.81b}$$

The computational complexity order of this convex problem is given by (7.62) for $n_v = 2K + K_E + 3$ and $m_c = K + 4$. The pseudo-code for iterating (7.81) for computing (7.79) is provided by Algorithm 19.

Algorithm 19 New RZF Path-following algorithm for (7.79)

1: **Initialization:** Randomly generate a feasible point $(p^{(0)}, x^{(0)}, t^{(0)}, \gamma^{(0)})$ for (7.79). Set $\kappa = 0$.
2: **Repeat until convergence of** $\gamma^{(\kappa)}$**:** Generate $(p^{(\kappa+1)}, x^{(\kappa+1)}, t^{(\kappa+1)}, \gamma^{(\kappa+1)})$ by solving the convex problem (7.81). Set $\kappa := \kappa + 1$.
3: **Output** $(p^{(\kappa)}, x^{(\kappa)}, t^{(\kappa)}, \gamma^{(\kappa)})$.

7.5.3 Notices on RZFB for information delivery only

When $K_E = 0$, i.e. there are no EUs, we use the whole time-slot for information transfer. Hence we have $t_2 = 1$, i.e. the problems (7.70) and (7.79) are respectively reduced to

$$\max_{\boldsymbol{p}} \min_{k=1,\ldots,K} r_k(\boldsymbol{p}) \quad \text{s.t.} \quad \pi_I(\boldsymbol{p}) \leq P, \tag{7.82}$$

and

$$\max_{\boldsymbol{p}} \min_{k=1,\ldots,K} \rho_k(\boldsymbol{p}) \quad \text{s.t.} \quad \tilde{\pi}_I(\boldsymbol{p}) \leq P. \tag{7.83}$$

Algorithms 18 and 19 are directly adjusted for their computation. The pseudo-code is provided by Algorithm 20.

Algorithm 20 Path-following algorithm for (7.82)/(7.83)

1: **Initialization:** Randomly generate a initial point for the optimization problem. $p^{(0)}$ for (7.82)/(7.83). Set $\kappa = 0$.
2: **Repeat:** Generate $p^{(\kappa+1)}$ by solving the convex problem $\max_{\boldsymbol{p}} \min_{k=1,\ldots,K} r_k^{(\kappa)}(\boldsymbol{p})$ s.t. $\pi_I(\boldsymbol{p}) \leq P$ (for computing (7.82)) and $\max_{\boldsymbol{p}} \min_{k=1,\ldots,K} \rho_k^{(\kappa)}(\boldsymbol{p})$ s.t. $\tilde{\pi}_I(\boldsymbol{p}) \leq P$ (for computing (7.83)) Set $\kappa := \kappa + 1$.
3: **Output** $p^{(\kappa)}$.

7.6 Numerical examples

In this section, the performance of our proposed algorithms is investigated . The elements of the BS-to-RIS LoS channel matrix are generated by $[H_{B-R}]_{n,m} = e^{j\pi\left((n-1)\sin\bar{\theta}_n \sin\bar{\phi}_n + (m-1)\sin e^{j\theta_n}\sin\phi_n\right)}$, where $e^{j\theta_n}$ and ϕ_n are uniformly distributed as $e^{j\theta_n} \sim \mathcal{U}(0,\pi)$ and $\phi_n \sim \mathcal{U}(0,2\pi)$, respectively, and $\bar{\theta}_n = \pi - \theta_n$ and $\bar{\phi}_n = \pi + \phi_n$ [154]. The normalized small-scale fading channel h_{B-e^ℓ} spanning from the BS to EU ℓ and $\bar{h}_{R-k}$ of the RIS to IU k obeys Rician distribution with a K-factor of 3 for modeling the LoS channels. The large scale fading coefficients, β_{B-R}, β_{R-k}, and $\beta^E_{B-e_\ell}$, are modeled as [154, 147]

$$\beta_{B-R} = G_{\text{BS}} + G_{\text{RIS}} - 35.9 - 22\log_{10}(d_{B-R}) \text{ (in dB)}, \tag{7.84a}$$

$$\beta_{R-k} = G_{\text{RIS}} - 33.05 - 30\log_{10}(d_{RIS-k}) \text{ (in dB)}, \tag{7.84b}$$

$$\beta^E_{B-e_\ell} = G_{\text{BS}} - 30 - 20\log_{10}(d_{B-e^\ell}) \text{ (in dB)}, \tag{7.84c}$$

where $G_{\text{BS}} = 5$ dBi and $G_{\text{RIS}} = 5$ dBi denote the antenna gain of the BS and the RIS gain, respectively, while d_{B-R}, d_{RIS-k}, and d_{B-e^ℓ} are the distances between the BS and RIS, the RIS and IU k, and the BS and EU ℓ, respectively. The signal reflected by the RIS can be ignored for EUs, since $\beta_{B-R}\beta_{R-k} \ll \beta^E_{B-e_\ell}$. The spatial correlation matrix is given by $[\mathbf{R}_{RIS-k}]_{n,n'} = e^{j\pi(n-n')\sin\tilde{\phi}_k \sin\tilde{\theta}_k}$, where $\tilde{\phi}_k$ and $\tilde{\theta}$ are the azimuth and elevation angle for IU k, respectively. Unless otherwise stated, $K = 10$, $K_E = 3$, $e_0 = -20$ dBm and $N = 100$ are used. The results are multiplied by $\log_2 e$ to convert units of nats/sec into units of bps/Hz. The convergence tolerance of the proposed algorithms is set to 10^{-3}. All simulations implemented on a Core i7-10875H 2.30GHz processor.

We use the 3D coordinates (x, y, z) to locate all the objects concerned . The BS is at $(20, 0, 10)$, the RIS is at $(0, 30, 40)$.

7.6.1 RIS-aided information delivery

There are $K = 10$ IUs, which are randomly placed in a $60m \times 60m$ area RHS of the obstacle and the RIS. Unless stated otherwise, the transmit power of $P = 25$ dBm is used. The performance of Algorithm 12 is not sensitive to which step size from Eqaution (7.17), (7.19) and (7.21) is used. In the simulated figures, Alg 2A and Alg 2B refer to the performance of the full step descent algorithm 13 based on iterating (7.28) and (7.35), respectively. Alg 3, Alg 4 and Alg 5 respectively refer to the performance of Algorithm 14 for the trace-maximization (7.32), Algorithm 15 and Algorithm 16 for the log determinant maximization (7.44). ZFB random θ and RZFB random θ respectively refer to the performance of ZFB and RZFB under random PRCs.

Fig. 7.4 and Fig. 7.5 plot the achievable minimum throughput versus the number of BS antennas, M under ZFB and RZFB, respectively.

Regarding ZFB for $M > K$, Fig. 7.4 reveals that Algorithm 13A outperforms Algorithm 13B, and the latter outperforms Algorithm 12, showing that the concave optimization reformulation (7.23) is the best option for computing (7.12), while Algorithm 12 of common purpose step descent is inefficient. Furthermore, the average running time for Algorithm 12, Algorithm 13A and Algorithm 13B are 0.24s, 0.06s and 7.96s under $N = 100$, respectively.

Regarding RZFB for $M > K$, Fig. 7.5 shows that Algorithm 14 achieves the best performance, i.e. the trace-maximization (7.32) has a more beneficial impact on the IUs' throughput than the log determinant maximization (7.44). It is not surprising to see that

Algorithm 16 outperforms Algorithm 15 because the former iterates the incumbent points, while the latter simply provides a way to locate a beneficial direction.

The worst performance is attained by ZFB random θ and RZFB random θ in all figures which is a clear indication that the PRC optimization is absolutely necessary upon using RIS.

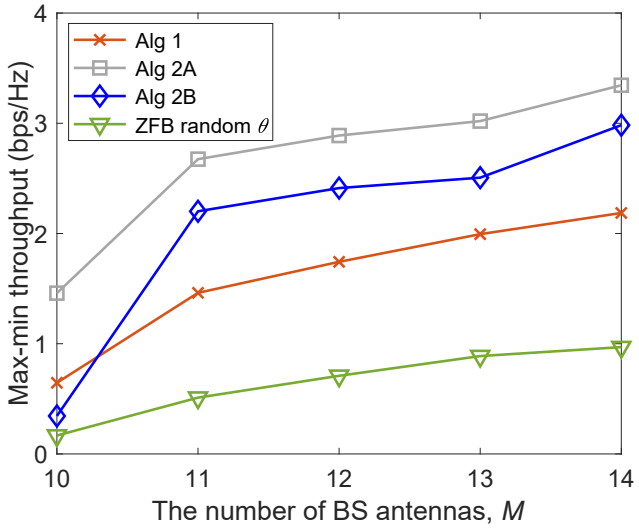

Fig. 7.4 Achievable minimum throughput vs the number of BS antennas M under ZF.

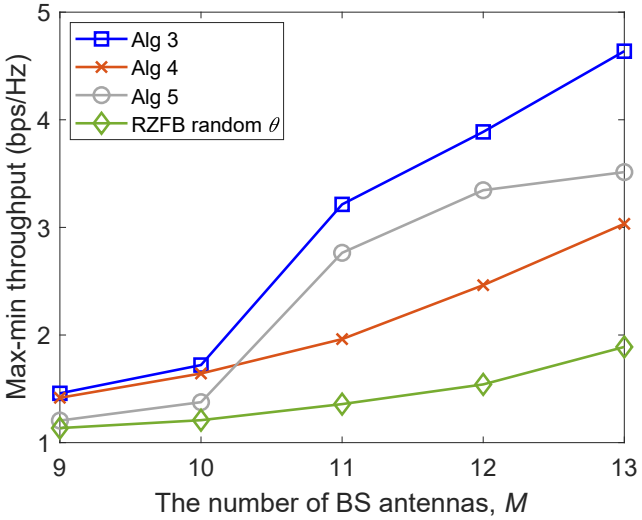

Fig. 7.5 Achievable minimum throughput vs the number of BS antenna M under RZF.

7.6.2 RIS-aided information and energy delivery

Next, we consider the problem of RIS-aided information and energy delivery by the network of Fig. 7.3 with $K_E = 3$ EUs randomly placed within a radius of 10m from the BS.

Alg 1-PGS, Alg 2A-PGS, Alg 2B-PGS and ZFB random θ-PGS refer to the performance of Algorithm 12, Algorithm 13A, Algorithm 13B, and ZFB random θ. Alg 3-PGS, Alg 4-PGS, Alg 5-PGS, and RZFB random θ-PGS refer to the performance of Algorithm 14, Algorithm 15, Algorithm 16, and RZFB random θ under RZFB (7.37), while Alg 3-IGS, Alg 4-IGS and Alg 5-IGS refer to the performance of Algorithm 14, Algorithm 15, Algorithm 16 under the new RZFB (7.75).

The transmit power of $P = 31$ dBm is set in Fig. 7.7-Fig. 7.9 and Fig. 7.11, but $P = 35$ dBm is set in Fig. 7.10 due to the relative small numbers of BS antennas.

Fig. 7.6 and Fig. 7.7 plot the minimum achievable IU throughput versus the number M of BS antennas under ZFB and RZFB, respectively. In Fig. 7.6, Alg 2A-PGS outperforms Alg 1-PGS and Alg 2B-PGS, Alg 2B-PGS outperforms Alg 1-PGS. Furthermore, all the proposed algorithms outperform ZFB random θ-PGS. As expected, Figures 7.5 and 7.7 exhibit similar trend. Fig. 7.6 and Fig. 7.7 also confirm the gain achieved by optimizing the PRCs. Furthermore, all algorithms in Fig. 7.4, Fig. 7.5, Fig. 7.6 and Fig. 7.7 benefit from the spatial diversity, which is commensurate with the number BS antennas.

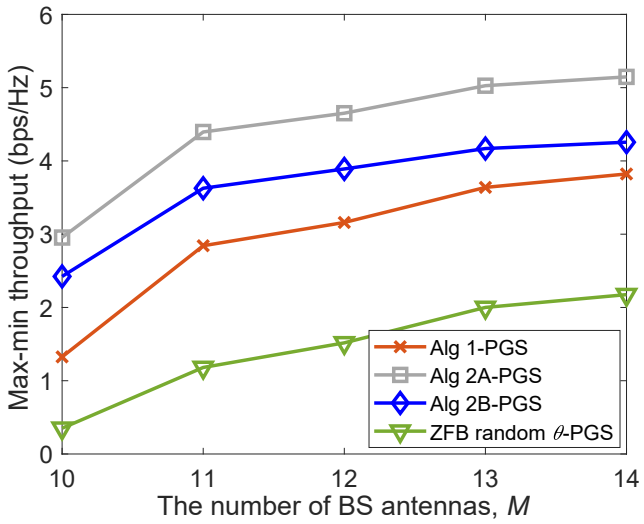

Fig. 7.6 Achievable minimum throughput vs the number of BS antennas M under ZF.

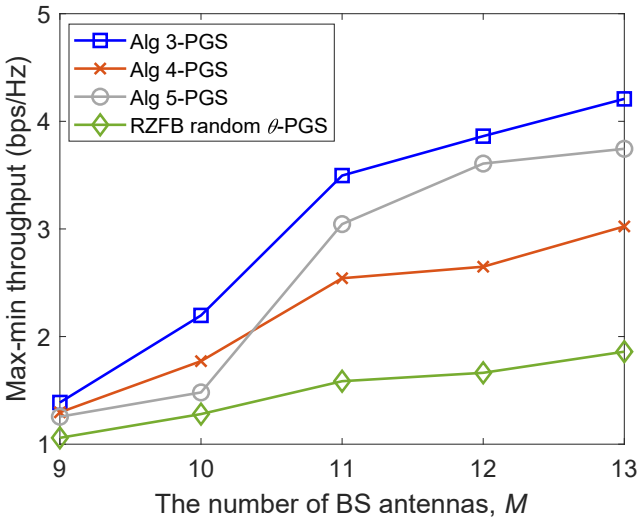

Fig. 7.7 Achievable minimum throughput vs the number of BS antennas M under RZF.

In Fig. 7.8, we now examine the minimum achievable IU throughput upon varying the BS transmit power budget P under RZFB for $M = 10$. As excepted, the IUs' minimum throughput increases upon increasing the available power budget because more power can be used for information delivery. Naturally, beyond a certain threshold, namely $P = 40$ dBm in Fig. 7.8, Alg 3's performance becomes saturated because the network is interference-limited. Fig. 7.8 also shows the gap between Algorithm 16 and RZFB under random θ, which is quite narrow for $P \geq 34$ dBm because the beneficial impact of the RIS is reduced, when the power budget is increased.

Fig. 7.9 plots the achievable minimum IU throughput for $M = 10$ under RZF versus the number N of RIS reflecting elements, showing that the performance is improved upon increasing N.

Fig. 7.10 and Fig. 7.11 allow us to compare the performance achieved by the RZFB (7.75) and the new RZFB (7.81). Fig. 7.10 plots the achievable minimum IU throughput versus the number M of BS antennas, clearly showing that Alg 3-IGS outperforms its counterpart Alg 3-PGS. Similarly, Alg 4-IGS and Alg 5-IGS outperform their counterparts Alg 4-PGS and Alg 5-PGS. Fig. 7.11, which plots the achievable minimum IU throughput for $K = M + 1$, follow the same trend as Fig. 7.10: Alg 3-IGS , Alg 4-IGS and Alg 5-IGS outperform their counterparts Alg 3-PGS, Alg 4-PGS and Alg 5-PGS, respectively. The advantage of the new

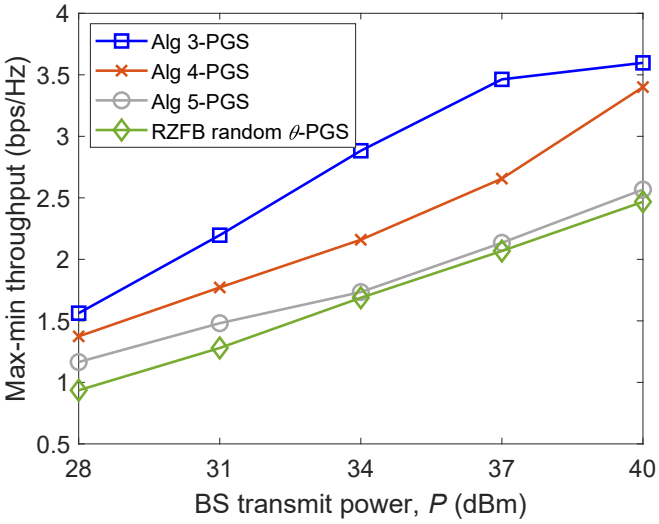

Fig. 7.8 Achievable minimum throughput for $M = 10$ under RZF vs the BS transmit power P.

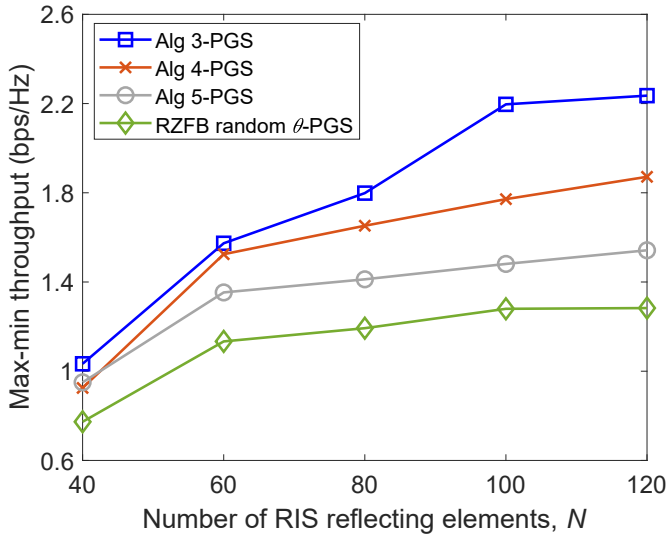

Fig. 7.9 Achievable minimum throughput for $M = 10$ with energy harvesting under RZF vs RIS for N reflecting elements.

RZFB over the conventional RZFB is also confirmed. Furthermore, Algorithm 15 benefits to a lesser extent from the new RZFB than Algorithm 14 and Algorithm 16.

Finally, Table 7.1 provides the average number of required iterations for the convex optimization part of the algorithms' convergence in simulating Fig. 9. The average single iteration time is 3.02s and 4.83s for the PGS based and IGS based algorithms, respectively.

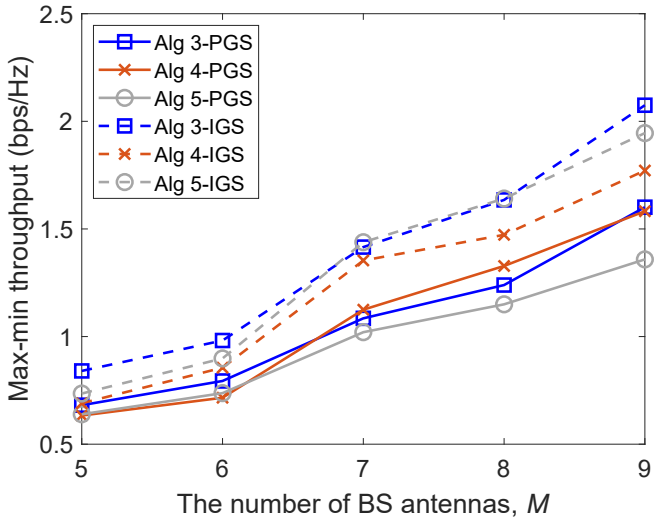

Fig. 7.10 Achievable minimum throughput under RZF vs the number of BS antennas M.

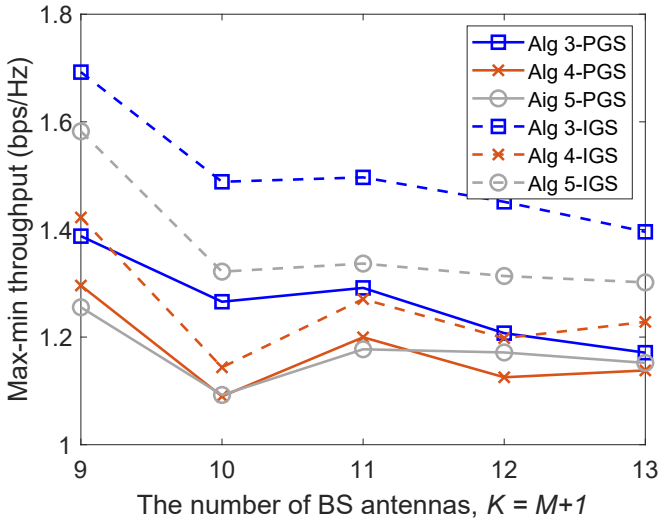

Fig. 7.11 Achievable minimum throughput under RZF for $K = M + 1$ BS antennas.

All the algorithms only need 30% of the maximum number of iterations to reach 80% of their optimal values.

Table 7.1 The average number of iterations required for the algorithm's convergence

	$M = 5$	$M = 6$	$M = 7$	$M = 8$	$M = 9$
Alg 3-PGS	15	14	14	10	9
Alg 4-PGS	10	9	8	8	8
Alg 5-PGS	17	16	17	14	11
Alg 3-IGS	17	16	17	14	13
Alg 4-IGS	17	15	15	15	11
Alg 5-IGS	23	21	23	17	12

7.7 Conclusions

We have considered a network in which a multi-antenna aided BS and an RIS support multiple IUs and EUs. To facilitate computational tractability while aiming for the maximum possible information and energy throughput, conjugate beamforming has been used for delivering energy, while zero-forcing or regularized zero-forcing beamforming has been used for delivering information under the transmit-TS framework, where energy and information are separately delivered during different time-slot fractions. The problem of jointly designing the RIS PRCs and the power allocation of the beamformers for maximizing the minimum IU throughput subject to QoES in terms of the harvested energy thresholds at the EUs end has been addressed. It has been shown that this joint design can be decomposed into separate designs of the RIS PRCs and of the power allocation of the IUs' beamforming. We have developed several efficient algorithms for these designs. A new regularized zero-forcing beamforming method has also been conceived for improving the IUs' throughput, which can improve the IUs' throughput significantly, especially in the regime of low numbers of BS antennas.

Chapter 8

Conclusions and Future Work

8.1 Conclusions

At present, the global revolution in industry is accelerating, internet of things (IoT) , artificial Intelligence (AI), virtual reality/enhanced reality (VR/AR), three-dimensional media and other new-generation technologies are widely used, which puts forward higher requirements in wireless communication. In the thesis, aiming at the quality of service, we developed low complexity optimization algorithms on STR, EH and RIS-aided communication network. The work of this dissertation is summarized as follows:

1) In uplink and downlink transmission communication, beamforming optimizations based on time-fraction-based allocation and bandwidth allocation are proposed in Chapter 3. By joint optimization of the beamforming and time fraction (bandwithd allocation), the self-interference in full-duplex communication can be eliminated, and the energy efficiency and specturm efficiency can be improved compared with traditional full-duplex and half-duplex communication.

2) For the multi-cell and multi-user energy harvesting scenarios, we developed IGS based beamforming optimization algorithms in Chapter 4. Aiming at the problem of more variables and higher complexity in the algorithm of IGS, a s-IGS algorithm is proposed, and the corresponding optimization algorithm is developed, has lower complexity. Compared with the traditional PGS based optimization algorithms, the proposed algorithm can obtain higher users' maximum throughput, and the security of the information can be protected.

3) In Chapter 5, PGS and IGS based joint optimization algorithms of the beamforming and RIS elements' phase in RIS-aided communication scenario are developed, and the algorithm complexity is analyzed. A new method to represent the unit-modulus constraint is proposed. The simulation results demonstrate the superior of IGS and the proposed algorithms.

4) In order to overcome the problem of high algorithm complexity in the RIS-aided communication, closed-form solution based algorithms are developed in Chapter 6. Furthermore, to ensure the users' achievable minimum throughput, the GM rate is used as the object function which takes the edge users' throughput and the sum rate into account. PGS based algorithms and IGS based algorithms are compared in the simulation section, the simulation results show IGS based algorithms have better GM rate while the PGS based algorithms have better time cost.

5) Finally, in Chapter 7, EH networks and RIS-aided communication are considered at the same time. By time-fraction-based allocation, the interference cause by EH users to IU users is eliminated. A joint optimization for information beamforming, energy transfer beamforming and time allocation is developed. In the simulation section, the conclusion that RIS cannot help energy harvesting is confirmed, however, RIS still can improve the IUs' throughput in the RIS-aided EH network.

8.2 Future work

Interesting directions for future work are presented in the following.

- In Chapter 3, the communication system is under proper Gaussian signaling, in the future, we think it is possible to use improper Gaussian signaling instead of the conventional proper Gaussian signaling in STR which might achieve better performance.
- In Chapter 4, the exploitation of IGS in massive multi-input multi-output energy-harvesting enabled networks is under current study.
- In Chapter 5, the future research direction is to consider channel estimation and solve the joint design of RIS's reflecting coefficients and transmit beamformers in the presence of channel estimation errors.

- In Chapter 6, extension of the GM maximization-based approach to multi-carrier communication is under our current study. Its extension to the quantized RIS-aided communication is also interesting and deserves a separate study in our future research.
- In Chapter 7, indoor scenarios for RIS-aided EH network is an interesting direction for future research.

Appendix A

Fundamental Inequalities

The following result [48] is used.

Theorem 1 *The following inequality holds true*

$$\frac{\ln(1+1/\boldsymbol{xy})}{\boldsymbol{t}} \geq 2\frac{\ln(1+1/\bar{x}\bar{y})}{\bar{t}} + \frac{1}{(\bar{x}\bar{y}+1)\bar{t}}(2-\frac{\boldsymbol{x}}{\bar{x}}-\frac{\boldsymbol{y}}{\bar{y}}) - \frac{\ln(1+1/\bar{x}\bar{y})}{\bar{t}^2}\boldsymbol{t}$$
$$\forall\ (\boldsymbol{x},\boldsymbol{y},\boldsymbol{t}) \in \mathbb{R}^3_+,\ (\bar{x},\bar{y},\bar{t}) \in \mathbb{R}^3_+. \tag{A.1}$$

The right-hand-side (RHS) of (A.1) agrees with the left-hand-side (LHS) at $(\bar{x},\bar{y},\bar{t})$.

A particular case of (A.1) is

$$\ln(1+1/\boldsymbol{xy}) \geq \ln(1+1/\bar{x}\bar{y}) + \frac{1}{(\bar{x}\bar{y}+1)}(2-\frac{\boldsymbol{x}}{\bar{x}}-\frac{\boldsymbol{y}}{\bar{y}})\forall\ (\boldsymbol{x},\boldsymbol{y}) \in \mathbb{R}^2_+,\ (\bar{x},\bar{y}) \in \mathbb{R}^2_+, \tag{A.2}$$

and

$$\frac{\ln(1+1/\boldsymbol{x})}{\boldsymbol{t}} \geq 2\frac{\ln(1+1/\bar{x})}{\bar{t}} + \frac{1}{(\bar{x}+1)\bar{t}}(1-\frac{\boldsymbol{x}}{\bar{x}}) - \frac{\ln(1+1/\bar{x})}{\bar{t}^2}\boldsymbol{t}\forall\ (\boldsymbol{x},\boldsymbol{t}) \in \mathbb{R}^2_+,\ (\bar{x},\bar{t}) \in \mathbb{R}^2_+ \tag{A.3}$$

and

$$\ln(1+1/\boldsymbol{x}) \geq \ln(1+1/\bar{x}) + \frac{1}{(\bar{x}+1)}(1-\frac{\boldsymbol{x}}{\bar{x}})\forall\ \boldsymbol{x} \in \mathbb{R}^2_+,\ \bar{x} \in \mathbb{R}^2_+. \tag{A.4}$$

Another inequality

$$\frac{\boldsymbol{x}}{\boldsymbol{t}} \geq 2\frac{\sqrt{\bar{x}}\sqrt{\boldsymbol{x}}}{\bar{t}} - \frac{\bar{x}}{\bar{t}^2}\boldsymbol{t} \quad \forall \boldsymbol{x} > 0,\ \boldsymbol{t} > 0,\ \bar{x} > 0,\ \bar{t} > 0 \tag{A.5}$$

follows from the convexity of the function $\boldsymbol{x}/\boldsymbol{t} = \sqrt{\boldsymbol{x}}^2/\boldsymbol{t}$ *on* $\sqrt{\boldsymbol{x}}$ *and* $\boldsymbol{t}$.

Substituting $\boldsymbol{x} \to 1/\boldsymbol{x}$ and $\bar{x} \to 1/\bar{x}$ in (A.1) and (A.2) lead to

$$\frac{\ln(1+\boldsymbol{x}/\boldsymbol{y})}{\boldsymbol{t}} \geq 2\frac{\ln(1+\bar{x}/\bar{y})}{\bar{t}} + -\frac{\bar{x}}{(\bar{y}+\bar{x})\bar{t}}(2-\frac{\bar{x}}{\boldsymbol{x}}-\frac{\boldsymbol{y}}{\bar{y}}) - \frac{\ln(1+\bar{x}/\bar{y})}{\bar{t}^2}\boldsymbol{t}$$
$$\forall\ (\boldsymbol{x},\boldsymbol{y},\boldsymbol{t}) \in \mathbb{R}^3_+,\ (\bar{x},\bar{y},\bar{t}) \in \mathbb{R}^3_+, \tag{A.6}$$

and

$$\ln(1+\boldsymbol{x}/\boldsymbol{y}) \geq \ln(1+\bar{x}/\bar{y}) + \frac{\bar{x}}{\bar{y}+\bar{x}}(2-\frac{\bar{x}}{\boldsymbol{x}}-\frac{\boldsymbol{y}}{\bar{y}})\forall\ (\boldsymbol{x},\boldsymbol{y}) \in \mathbb{R}^2_+,\ (\bar{x},\bar{y}) \in \mathbb{R}^2_+. \tag{A.7}$$

As a particular case of (A.6) and (A.7) it is

$$\frac{\ln(1+\boldsymbol{x})}{\boldsymbol{t}} \geq 2\frac{\ln(1+\bar{x})}{\bar{t}} + \frac{\bar{x}}{(\bar{x}+1)\bar{t}}(1-\frac{\bar{x}}{\boldsymbol{x}}) - \frac{\ln(1+\bar{x})}{\bar{t}^2}\boldsymbol{t} \quad \forall\ (\boldsymbol{x},\boldsymbol{t}) \in \mathbb{R}^2_+,\ (\bar{x},\bar{t}) \in \mathbb{R}^2_+, \tag{A.8}$$

and

$$\ln(1+\boldsymbol{x}) \geq \ln(1+\bar{x}) + \frac{\bar{x}}{\bar{x}+1}(1-\frac{\bar{x}}{\boldsymbol{x}})\forall\ \boldsymbol{x} \in \mathbb{R}_+,\ \bar{x} \in \mathbb{R}_+. \tag{A.9}$$

Substituting $\boldsymbol{t} \to 1/\boldsymbol{t}$ and $\bar{t} \to 1/\bar{t}$ in (A.6) leads to

$$\boldsymbol{t}\ln(1+\boldsymbol{x}/\boldsymbol{y}) \geq 2\bar{t}\ln(1+\bar{x}/\bar{y}) + \frac{\bar{t}\bar{x}}{\bar{y}+\bar{x}}(2-\frac{\bar{x}}{\boldsymbol{x}}-\frac{\boldsymbol{y}}{\bar{y}}) - \frac{\bar{t}^2\ln(1+\bar{x}/\bar{y})}{\boldsymbol{t}}$$
$$\forall\ (\boldsymbol{x},\boldsymbol{y},\boldsymbol{t}) \in \mathbb{R}^3_+,\ (\bar{x},\bar{y},\bar{t}) \in \mathbb{R}^3_+, \tag{A.10}$$

By substituting $\boldsymbol{x} \to ||\boldsymbol{x}||^2$ and $\bar{x} \to ||\bar{x}||^2$ with $\boldsymbol{x} \in \mathbb{C}^n$ and $\bar{x} \in \mathbb{C}^n$ in (A.6), (A.7), and (A.10) and using the inequality

$$||\boldsymbol{x}||^2 \geq 2\Re\{\bar{x}^H\boldsymbol{x}\} - ||\bar{x}||^2 \quad \forall\ \boldsymbol{x} \in \mathbb{C}^n,\ \bar{x} \in \mathbb{C}^n$$

we obtain

$$\frac{\ln(1+||\boldsymbol{x}||^2/\boldsymbol{y})}{\boldsymbol{t}} \geq 2\frac{\ln(1+||\bar{x}||^2/\bar{y})}{\bar{t}} + \frac{||\bar{x}||^2}{(\bar{y}+||\bar{x}||^2)\bar{t}}(2-\frac{||\bar{x}||^2}{2\Re\{\bar{x}^H\boldsymbol{x}\}-||\bar{x}||^2}-\frac{\boldsymbol{y}}{\bar{y}})$$
$$-\frac{\ln(1+||\bar{x}||^2/\bar{y})}{\bar{t}^2}\boldsymbol{t}\forall\ (\boldsymbol{x},\boldsymbol{y},\boldsymbol{t}) \in \mathbb{C}^n \times \mathbb{R}^2_+,\ (\bar{x},\bar{y},\bar{t}) \in \mathbb{C}^n \times \mathbb{R}^2_+, \tag{A.11}$$

and

$$\ln(1+||\boldsymbol{x}||^2/\boldsymbol{y}) \geq \ln(1+||\bar{x}||^2/\bar{y}) + \frac{||\bar{x}||^2}{\bar{y}+||\bar{x}||^2}(2 - \frac{||\bar{x}||^2}{2\Re\{\bar{x}^H\boldsymbol{x}\}-||\bar{x}||^2} - \frac{\boldsymbol{y}}{\bar{y}}) \\ \forall\ (\boldsymbol{x},\boldsymbol{y}) \in \mathbb{C}^n \times \mathbb{R}_+,\ (\bar{x},\bar{y}) \in \mathbb{C}^n \times \mathbb{R}_+. \tag{A.12}$$

and

$$\boldsymbol{t}\ln(1+||\boldsymbol{x}||^2/\boldsymbol{y}) \geq 2\bar{t}\ln(1+||\bar{x}||^2/\bar{y}) + \frac{\bar{t}||\bar{x}||^2}{\bar{y}+||\bar{x}||^2}\left(2 - \frac{||\bar{x}||^2}{2\Re\{\bar{x}^H\boldsymbol{x}\}-||\bar{x}||^2} - \frac{\boldsymbol{y}}{\bar{y}}\right) \\ -\frac{\bar{t}^2\ln(1+||\bar{x}||^2/\bar{y})}{\boldsymbol{t}} \forall\ (\boldsymbol{x},\boldsymbol{y},\boldsymbol{t}) \in \mathbb{C}^n \times \mathbb{R}_+^2,\ (\bar{x},\bar{y},\bar{t}) \in \mathbb{C}^n \times \mathbb{R}_+^2, \tag{A.13}$$

over the trust region

$$2\Re\{\bar{x}^H\boldsymbol{x}\} - ||\bar{x}||^2 > 0. \tag{A.14}$$

The following inequalities hold true for matrices of dimension 2×2 [39] and [164]:

$$\ln\left|\mathbf{I}_2 + [\mathbf{V}]^2(\mathbf{Y})^{-1}\right| \geq \\ \ln\left|\mathbf{I}_2 + [\bar{\mathbf{V}}]^2(\bar{\mathbf{Y}})^{-1}\right| - \langle[\bar{\mathbf{V}}]^2(\bar{\mathbf{Y}})^{-1}\rangle + 2\Re\{\langle\bar{\mathbf{V}}^H(\bar{\mathbf{Y}})^{-1}\mathbf{V}\rangle\} \\ -\langle(\bar{\mathbf{Y}})^{-1} - (\bar{\mathbf{Y}}+[\bar{\mathbf{V}}]^2)^{-1}, [\mathbf{V}]^2+\mathbf{Y}\rangle, \\ \forall\ \mathbf{V},\mathbf{X} \succeq 0, \mathbf{Y} \succ 0 \quad \& \quad \bar{\mathbf{V}},\bar{\mathbf{X}} \succeq 0, \bar{\mathbf{Y}} \succ 0, \tag{A.15}$$

and

$$\ln\left|\mathbf{I}_2 + \mathbf{X}(\mathbf{Y})^{-1}\right| \geq \\ \ln\left|\mathbf{I}_2 + \bar{\mathbf{X}}(\bar{\mathbf{Y}})^{-1}\right| + 4 - \langle\bar{\mathbf{X}}+\bar{\mathbf{Y}}, (\mathbf{X}+\mathbf{Y})^{-1}\rangle - \langle(\bar{\mathbf{Y}})^{-1}, \mathbf{Y}\rangle \\ \forall\ \mathbf{V},\mathbf{X} \succeq 0, \mathbf{Y} \succ 0 \quad \& \quad \bar{\mathbf{V}},\bar{\mathbf{X}} \succeq 0, \bar{\mathbf{Y}} \succ 0, \tag{A.16}$$

and

$$\ln|\mathbf{X}^{-1}+\mathbf{Y}^{-1}| \geq \\ \log|\bar{\mathbf{X}}^{-1}+\bar{\mathbf{Y}}^{-1}| + 2 \\ -\langle\left(\bar{\mathbf{X}}\right)^{-1} - \left(\bar{\mathbf{X}}+\bar{\mathbf{Y}}\right)^{-1}, \mathbf{X}\rangle - \langle\left(\bar{\mathbf{Y}}\right)^{-1} - \left(\bar{\mathbf{X}}+\bar{\mathbf{Y}}\right)^{-1}, \mathbf{Y}\rangle \\ \forall\ \mathbf{X} \succ 0, \mathbf{Y} \succ 0 \quad \& \quad \bar{\mathbf{X}} \succ 0, \bar{\mathbf{Y}} \succ 0, \tag{A.17}$$

and

$$\log|\mathbf{X}| \geq \log|\bar{\mathbf{X}}| + 2 - \langle\bar{\mathbf{X}}, (\mathbf{X})^{-1}\rangle \forall\ \mathbf{X} \succ 0 \quad \& \quad \bar{\mathbf{X}} \succ 0.$$

Theorem 2 *The following inequalities hold true for all* $\mathbf{X} \succ 0$, $\mathbf{Y} \succ 0$ *and* $\bar{\mathbf{X}} \succ 0$, $\bar{\mathbf{Y}} \succ 0$

$$\langle\mathbf{X}, \mathbf{Y}\rangle \leq \frac{1}{4}||\bar{\mathbf{X}}^{-1/2}\mathbf{X}\bar{\mathbf{Y}}^{1/2} + \bar{\mathbf{X}}^{1/2}\mathbf{Y}\bar{\mathbf{Y}}^{-1/2}||^2 \tag{A.18}$$

and

$$\langle\mathbf{X}, \mathbf{Y}\rangle \leq \frac{1}{2}\left(||\bar{\mathbf{X}}^{-1/2}\mathbf{X}\bar{\mathbf{Y}}^{1/2}||^2 + ||\bar{\mathbf{X}}^{1/2}\mathbf{Y}\bar{\mathbf{Y}}^{-1/2}||^2\right) \tag{A.19}$$

Proof It follows from the matrix inequality

$$\begin{aligned}
0 \ &\preceq\ \left(\bar{\mathbf{X}}^{-1/2}\mathbf{X}\bar{\mathbf{Y}}^{1/2} - \bar{\mathbf{X}}^{1/2}\mathbf{Y}\bar{\mathbf{Y}}^{-1/2}\right) \times \left(\bar{\mathbf{X}}^{-1/2}\mathbf{X}\bar{\mathbf{Y}}^{1/2} - \bar{\mathbf{X}}^{1/2}\mathbf{Y}\bar{\mathbf{Y}}^{-1/2}\right)^H \\
&=\ \left(\bar{\mathbf{X}}^{-1/2}\mathbf{X}\bar{\mathbf{Y}}^{1/2} + \bar{\mathbf{X}}^{1/2}\mathbf{Y}\bar{\mathbf{Y}}^{-1/2}\right) \times \left(\bar{\mathbf{X}}^{-1/2}\mathbf{X}\bar{\mathbf{Y}}^{1/2} + \bar{\mathbf{X}}^{1/2}\mathbf{Y}\bar{\mathbf{Y}}^{-1/2}\right)^H \\
&\quad -2\left(\bar{\mathbf{X}}^{-1/2}\mathbf{X}\bar{\mathbf{Y}}^{1/2}\bar{\mathbf{Y}}^{-1/2}\mathbf{Y}\bar{\mathbf{X}}^{1/2} + \bar{\mathbf{X}}^{1/2}\mathbf{Y}\bar{\mathbf{Y}}^{-1/2}\bar{\mathbf{Y}}^{1/2}\mathbf{X}\bar{\mathbf{X}}^{-1/2}\right) \\
&=\ \left(\bar{\mathbf{X}}^{-1/2}\mathbf{X}\bar{\mathbf{Y}}^{1/2} + \bar{\mathbf{X}}^{1/2}\mathbf{Y}\bar{\mathbf{Y}}^{-1/2}\right) \times \left(\bar{\mathbf{X}}^{-1/2}\mathbf{X}\bar{\mathbf{Y}}^{1/2} + \bar{\mathbf{X}}^{1/2}\mathbf{Y}\bar{\mathbf{Y}}^{-1/2}\right)^H \\
&\quad -2\left(\bar{\mathbf{X}}^{-1/2}\mathbf{X}\mathbf{Y}\bar{\mathbf{X}}^{1/2} + \bar{\mathbf{X}}^{1/2}\mathbf{Y}\mathbf{X}\bar{\mathbf{X}}^{-1/2}\right)
\end{aligned}$$

that

$$\begin{aligned}
&\bar{\mathbf{X}}^{-1/2}\mathbf{X}\mathbf{Y}\bar{\mathbf{X}}^{1/2} + \bar{\mathbf{X}}^{1/2}\mathbf{Y}\mathbf{X}\bar{\mathbf{X}}^{-1/2} \\
&\frac{1}{2}\left(\bar{\mathbf{X}}^{-1/2}\mathbf{X}\bar{\mathbf{Y}}^{1/2} + \bar{\mathbf{X}}^{1/2}\mathbf{Y}\bar{\mathbf{Y}}^{-1/2}\right) \times \left(\bar{\mathbf{X}}^{-1/2}\mathbf{X}\bar{\mathbf{Y}}^{1/2} + \bar{\mathbf{X}}^{1/2}\mathbf{Y}\bar{\mathbf{Y}}^{-1/2}\right)^H.
\end{aligned} \quad \preceq$$

Therefore

$$\begin{aligned}
2\langle\mathbf{X}\mathbf{Y}\rangle \ &=\ \langle\bar{\mathbf{X}}^{-1/2}\mathbf{X}\mathbf{Y}\bar{\mathbf{X}}^{1/2}\rangle + \langle\bar{\mathbf{X}}^{1/2}\mathbf{Y}\mathbf{X}\bar{\mathbf{X}}^{-1/2}\rangle \\
&\leq\ \frac{1}{2}||\bar{\mathbf{X}}^{-1/2}\mathbf{X}\bar{\mathbf{Y}}^{1/2} + \bar{\mathbf{X}}^{1/2}\mathbf{Y}\bar{\mathbf{Y}}^{-1/2}||^2,
\end{aligned}$$

which is (A.18).

Furthermore, we use

$$\left(\bar{\mathbf{X}}^{-1/2}\mathbf{X}\bar{\mathbf{Y}}^{1/2} - \bar{\mathbf{X}}^{1/2}\mathbf{Y}\bar{\mathbf{Y}}^{-1/2}\right) \times \left(\bar{\mathbf{X}}^{-1/2}\mathbf{X}\bar{\mathbf{Y}}^{1/2} - \bar{\mathbf{X}}^{1/2}\mathbf{Y}\bar{\mathbf{Y}}^{-1/2}\right)^H \quad \succeq 0$$

that yields

$$\begin{aligned}&\bar{\mathbf{X}}^{-1/2}\mathbf{X}\bar{\mathbf{Y}}^{1/2}\bar{\mathbf{Y}}^{-1/2}\mathbf{Y}\bar{\mathbf{X}}^{1/2}+\bar{\mathbf{X}}^{1/2}\mathbf{Y}\bar{\mathbf{Y}}^{-1/2}\bar{\mathbf{Y}}^{1/2}\mathbf{X}\bar{\mathbf{X}}^{-1/2}\\&\preceq\bar{\mathbf{X}}^{-1/2}\mathbf{X}\bar{\mathbf{Y}}^{1/2}(\bar{\mathbf{X}}^{-1/2}\mathbf{X}\bar{\mathbf{Y}}^{1/2})^H+\bar{\mathbf{X}}^{1/2}\mathbf{Y}\bar{\mathbf{Y}}^{-1/2}(\bar{\mathbf{X}}^{1/2}\mathbf{Y}\bar{\mathbf{Y}}^{-1/2})^H.\end{aligned}$$

Therefore,

$$\begin{aligned}2\langle\mathbf{XY}\rangle&=\langle\bar{\mathbf{X}}^{-1/2}\mathbf{X}\bar{\mathbf{Y}}^{1/2}\bar{\mathbf{Y}}^{-1/2}\mathbf{Y}\bar{\mathbf{X}}^{1/2}\rangle+\langle\bar{\mathbf{X}}^{1/2}\mathbf{Y}\bar{\mathbf{Y}}^{-1/2}\bar{\mathbf{Y}}^{1/2}\mathbf{X}\bar{\mathbf{X}}^{-1/2}\rangle\\&\leq||\bar{\mathbf{X}}^{-1/2}\mathbf{X}\bar{\mathbf{Y}}^{1/2}||^2+||\bar{\mathbf{X}}^{1/2}\mathbf{Y}\bar{\mathbf{Y}}^{-1/2}||^2,\end{aligned}$$

which is (A.19).

The following results of [48] are used

$$\frac{\boldsymbol{x}}{\boldsymbol{y}}\geq\frac{3\bar{x}}{\bar{y}}-\frac{\bar{x}^2}{\bar{y}}\frac{1}{\boldsymbol{x}}-\frac{\bar{x}}{\bar{y}^2}\boldsymbol{y}\quad\forall\,(\boldsymbol{x},\boldsymbol{y})\in\mathbb{R}_+^2\;\&\;(\bar{x},\bar{y})\in\mathbb{R}_+^2,\tag{A.20}$$

and

$$\frac{|\boldsymbol{x}|^2}{\mathbf{y}}\geq\frac{2\Re\{\bar{x}^*\boldsymbol{x}\}}{\bar{y}}-\frac{|\bar{x}|^2}{\bar{y}^2}\mathbf{y}\quad\forall\,(\boldsymbol{x},\mathbf{y})\in\mathbb{C}\times\mathbb{R}_+\;\&\;(\bar{x},\bar{y})\in\mathbb{C}\times\mathbb{R}_+,\tag{A.21}$$

where $\mathbb{R}_+^m\triangleq\{(x_1,\ldots,x_m)\;:\;x_i>0,i=1,\ldots,m\}$.

The following matrix inequality holds true for all matrices $\mathbf{Y}\succ 0$, $\bar{Y}\succ 0$ and $\mathbf{X}$ and $\bar{X}$ of appropriate dimension [165, Appendix C]

$$\mathbf{XYX}^H\succeq\bar{X}\bar{Y}\mathbf{X}^H+\mathbf{X}\bar{Y}\bar{X}^H-\bar{X}\bar{Y}\mathbf{Y}^{-1}\bar{Y}\bar{X}^H.\tag{A.22}$$

Using the inequality (A.22) in the appendix A yields (A.23).

$$\begin{aligned}|\mathcal{H}_k(\boldsymbol{\theta})\boldsymbol{w}_k|^2&=\mathcal{H}_k(\boldsymbol{\theta})[\boldsymbol{w}_k]^2\mathcal{H}_k^H(\boldsymbol{\theta})\\&=\mathcal{H}_k(\boldsymbol{\theta})\left([\boldsymbol{w}_k]^2+\eta I_M\right)\mathcal{H}_k^H(\boldsymbol{\theta})-\eta[\mathcal{H}_k(\boldsymbol{\theta})]^2\\&\geq\mathcal{H}_k(\theta^{(\kappa)})Y_k^{(\kappa)}(\eta)\mathcal{H}_k^H(\boldsymbol{\theta})+\mathcal{H}_k(\boldsymbol{\theta})Y_k^{(\kappa)}(\eta)(\mathcal{H}_k^H(\theta^{(\kappa)})\\&\quad-\mathcal{H}_k(\theta^{(\kappa)})Y_k^{(\kappa)}(\eta)\left([\boldsymbol{w}_k]^2+\eta I_M\right)^{-1}Y_k^{(\kappa)}(\eta)\mathcal{H}_k^H(\theta^{(\kappa)})-\eta[\mathcal{H}_k(\boldsymbol{\theta})]^2\\&\geq\mathcal{H}_k(\theta^{(\kappa)})Y_k^{(\kappa)}(\eta)\mathcal{H}_k^H(\boldsymbol{\theta})+\mathcal{H}_k(\boldsymbol{\theta})Y_k^{(\kappa)}(\eta)\mathcal{H}_k^H(\theta^{(\kappa)})\\&\quad-\mathcal{H}_k(\theta^{(\kappa)})Y_k^{(\kappa)}(\eta)\left(w_k^{(\kappa)}\boldsymbol{w}_k^H+\boldsymbol{w}_k(w_k^{(\kappa)})^H-[w_k^{(\kappa)}]^2+\eta I_M\right)^{-1}\\&\quad\times Y_k^{(\kappa)}(\eta)\mathcal{H}_k^H(\theta^{(\kappa)})-\eta\langle\mathbf{X}_k\rangle.\end{aligned}\tag{A.23}$$

Therefore, the nonconvex constraint (5.35) is innerly approximated by the constraint

$$\text{RHS of (A.23)} \geq \mathbf{z}_k, \tag{A.24}$$

which is

$$\begin{aligned}\Big(\mathcal{H}_k(\theta^{(\kappa)})Y_k^{(\kappa)}(\eta)\mathcal{H}_k^H(\boldsymbol{\theta}) + (*)^H\Big) - \mathbf{z}_k - \eta\langle\mathbf{X}_k\rangle \\ -\mathcal{H}_k(\theta^{(\kappa)})Y_k^{(\kappa)}(\eta)\left[\Big(w_k^{(\kappa)}\boldsymbol{w}_k^H + (*)^H\Big) - [w_k^{(\kappa)}]^2 + \eta I_M\right]^{-1} Y_k^{(\kappa)}(\eta)\mathcal{H}_k^H(\theta^{(\kappa)}) \quad \geq \quad 0.\end{aligned}$$

The latest inequality is equivalent to (5.36) by the Shur's complement.

The following inequality follows from the fact that the function $\langle[\mathbf{V}]^2\mathbf{Y}^{-1}\rangle$ is convex for the the matrix variable $\mathbf{V}$ and positive matrix variable $\mathbf{Y}$ [165]:

$$\langle[\mathbf{V}]^2\mathbf{Y}^{-1}\rangle \geq 2\Re\{\langle\bar{V}^H\bar{Y}^{-1}\mathbf{V}\} - \langle[\bar{V}]^2\bar{Y}^{-1}\mathbf{Y}\bar{Y}^{-1}\rangle, \tag{A.25}$$

for all $\mathbf{V}$, $\bar{V}$, and positive definite $\mathbf{Y}$ and $\bar{Y}$ of an appropriate dimension.

The following inequalities were obtained in [39]:

$$\ln\left(1 + \frac{\boldsymbol{v}^2}{\mathbf{y}}\right) \geq \ln\left(1 + \frac{\bar{v}^2}{\bar{y}}\right) - \frac{\bar{v}^2}{\bar{y}} + 2\frac{\bar{v}\boldsymbol{v}}{\bar{y}} - \frac{\bar{v}^2\left(\mathbf{y} + \boldsymbol{v}^2\right)}{\bar{y}(\bar{y} + \bar{v}^2)}, \tag{A.26}$$

Particularly,

$$\ln\left(1 + \frac{\boldsymbol{v}^2}{\sigma}\right) \geq \ln\left(1 + \frac{\bar{v}^2}{\sigma}\right) - \frac{\bar{v}^2}{\sigma} + 2\frac{\bar{v}\boldsymbol{v}}{\sigma} - \frac{\bar{v}^2\left(\sigma + \boldsymbol{v}^2\right)}{\sigma(\sigma + \bar{v}^2)} \tag{A.27}$$

for $\sigma > 0$ and $\boldsymbol{v} \in \mathbb{R}$, $\bar{v} \in \mathbb{R}$.

Appendix B

Proof of (6.62) and (6.63)

Note that

$$\mathcal{Q}_{22,k}^{(\kappa)} + \mathcal{Q}_{11,k}^{(\kappa)} = \mathcal{Q}_{2,k}^{R,(\kappa)} + \jmath \mathcal{Q}_{2,k}^{I,(\kappa)}$$

and $\mathcal{Q}_{2,k}^{R,(\kappa)}$ is symmetric, while $\mathcal{Q}_{2,k}^{I,(\kappa)}$ is anti-symmetric ($\mathcal{Q}_{2,k}^{I,(\kappa)} = -(\mathcal{Q}_{2,k}^{I,(\kappa)})^T$, hence we have $x^T \mathcal{Q}_{2,k}^{I,(\kappa)} x = 0 \ \forall \ x \in \mathbb{R}^N$).

Then the

$$\begin{aligned}
& \text{LHS of (6.62)} \\
= \ & (\cos\boldsymbol{\theta} - \jmath \sin\boldsymbol{\theta})^T \left(\mathcal{Q}_{2,k}^{R,(\kappa)} + \jmath \mathcal{Q}_{2,k}^{I,(\kappa)} \right) (\cos\boldsymbol{\theta} + \jmath \sin\boldsymbol{\theta}) \\
= \ & \left((\cos\boldsymbol{\theta})^T \mathcal{Q}_{2,k}^{R,(\kappa)} - \jmath (\sin\boldsymbol{\theta})^T \mathcal{Q}_{2,k}^{R,(\kappa)} + \jmath (\cos\boldsymbol{\theta})^T \mathcal{Q}_{2,k}^{I,(\kappa)} \ - (\sin\boldsymbol{\theta})^T \mathcal{Q}_{2,k}^{I,(\kappa)} \right) (\cos\boldsymbol{\theta} + \jmath \sin\boldsymbol{\theta}) \\
= \ & (\cos\boldsymbol{\theta})^T \mathcal{Q}_{2,k}^{R,(\kappa)} \cos\boldsymbol{\theta} - \jmath (\sin\boldsymbol{\theta})^T \mathcal{Q}_{2,k}^{R,(\kappa)} \cos\boldsymbol{\theta} + \jmath (\cos\boldsymbol{\theta})^T \mathcal{Q}_{2,k}^{I,(\kappa)} \cos\boldsymbol{\theta} - (\sin\boldsymbol{\theta})^T \mathcal{Q}_{2,k}^{I,(\kappa)} \cos\boldsymbol{\theta} \\
& + \jmath (\cos\boldsymbol{\theta})^T \mathcal{Q}_{2,k}^{R,(\kappa)} \sin\boldsymbol{\theta} + (\sin\boldsymbol{\theta})^T \mathcal{Q}_{2,k}^{R,(\kappa)} \sin\boldsymbol{\theta} - (\cos\boldsymbol{\theta})^T \mathcal{Q}_{2,k}^{I,(\kappa)} \sin\boldsymbol{\theta} - \jmath (\sin\boldsymbol{\theta})^T \mathcal{Q}_{2,k}^{I,(\kappa)} \sin\boldsymbol{\theta} \\
= \ & (\cos\boldsymbol{\theta})^T \mathcal{Q}_{2,k}^{R,(\kappa)} \cos\boldsymbol{\theta} - (\sin\boldsymbol{\theta})^T \mathcal{Q}_{2,k}^{I,(\kappa)} \cos\boldsymbol{\theta} + (\sin\boldsymbol{\theta})^T \mathcal{Q}_{2,k}^{R,(\kappa)} \sin\boldsymbol{\theta} - (\cos\boldsymbol{\theta})^T \mathcal{Q}_{2,k}^{I,(\kappa)} \sin\boldsymbol{\theta} \\
= \ & \text{RHS of (6.62)},
\end{aligned}$$

proving (6.62). Furthermore,

$$\begin{aligned}
& \text{LHS of (6.63)} \\
= \ & 2\Re\{(e^{\jmath\boldsymbol{\theta}})^T \mathcal{Q}_{12,k}^{(\kappa)} e^{\jmath\boldsymbol{\theta}}\} \\
= \ & 2\Re\left\{ (\cos\boldsymbol{\theta} + \jmath \sin\boldsymbol{\theta})^T \left(\mathcal{Q}_{1,k}^{R,(\kappa)} + \jmath \mathcal{Q}_{1,k}^{I,(\kappa)} \right) \ (\cos\boldsymbol{\theta} + \jmath \sin\boldsymbol{\theta}) \right\} \\
= \ & 2\left((\cos\boldsymbol{\theta})^T \mathcal{Q}_{1,k}^{R,(\kappa)} \cos\boldsymbol{\theta} - (\cos\boldsymbol{\theta})^T \mathcal{Q}_{1,k}^{I,(\kappa)} \sin\boldsymbol{\theta} \ - (\sin\boldsymbol{\theta})^T \mathcal{Q}_{1,k}^{R,(\kappa)} \sin\boldsymbol{\theta} - (\sin\boldsymbol{\theta})^T \mathcal{Q}_{1,k}^{I,(\kappa)} \cos\boldsymbol{\theta} \right) \\
= \ & \text{RHS of (6.63)},
\end{aligned}$$

proving (6.63).

References

[1] K. David and H. Berndt, "6g vision and requirements: Is there any need for beyond 5g?," *IEEE Vehicular Technology Magazine*, vol. 13, no. 3, pp. 72–80, 2018.

[2] A. Mourad, R. Yang, P. H. Lehne, and A. de la Oliva, "Towards 6g: Evolution of key performance indicators and technology trends," in *2020 2nd 6G Wireless Summit (6G SUMMIT)*, pp. 1–5, 2020.

[3] S. Zhang, C. Xiang, and S. Xu, "6g: Connecting everything by 1000 times price reduction," *IEEE Open Journal of Vehicular Technology*, vol. 1, pp. 107–115, 2020.

[4] R. Zhang and C. K. Ho, "Mimo broadcasting for simultaneous wireless information and power transfer," *IEEE Transactions on Wireless Communications*, vol. 12, no. 5, pp. 1989–2001, 2013.

[5] L. Zhao, X. Wang, and K. Zheng, "Downlink hybrid information and energy transfer with massive MIMO," *IEEE Trans. Wirel. Commun.*, vol. 15, pp. 1309–1322, Feb. 2016.

[6] E. Basar, M. Di Renzo, J. De Rosny, M. Debbah, M.-S. Alouini, and R. Zhang, "Wireless communications through reconfigurable intelligent surfaces," *Access IEEE*, vol. 7, pp. 116753–116773, 2019.

[7] C. Huang, R. Mo, and C. Yuen, "Reconfigurable intelligent surface assisted multiuser MISO systems exploiting deep reinforcement learning," *IEEE J. Select. Areas Commun.*, vol. 38, no. 8, pp. 1839–1850, 2020.

[8] N. H. Mahmood, H. Alves, O. A. López, M. Shehab, D. P. M. Osorio, and M. Latva-Aho, "Six key features of machine type communication in 6g," in *2020 2nd 6G Wireless Summit (6G SUMMIT)*, pp. 1–5, 2020.

[9] A. Sabharwal, P. Schniter, D. Guo, D. Bliss, S. Rangarajan, and R. Wichman, "In-band full-duplex wireless: Challenges and opportunities," *IEEE J. Sel. Areas Commun.*, vol. 32, pp. 1637–1652, Sept 2014.

[10] A. Sabharwal et al, "In-band full-duplex wireless: challenges and opportunities," *IEEE J. Selected Areas in Commun.*, vol. 32, pp. 1637–1652, Sep 2014.

[11] R. Ghaffar and R. Knopp, "Interference suppression strategy for cell-edge users in the downlink," *IEEE Trans. Wireless Commun.*, vol. 11, pp. 154–165, January 2012.

[12] A. A. Nasir, H. D. Tuan, and T. Q. Duong, "Fractional time exploitation for serving IoT users with guaranteed QoS by 5G spectrum," *IEEE Commun. Mag.*, vol. 56, pp. 128–133, Oct. 2018.

[13] Q. Wu and R. Zhang, "Joint active and passive beamforming optimization for intelligent reflecting surface assisted SWIPT under QoS constraints," *IEEE J. Select. Areas Commun.*, vol. 38, pp. 1735–1748, Aug. 2020.

[14] A. A. Nasir, H. D. Tuan, D. T. Ngo, T. Q. Duong, and H. V. Poor, "Beamforming design for wireless information and power transfer systems: Receive power-splitting versus transmit time-switching," *IEEE Trans. Commun.*, vol. 65, pp. 876–889, Feb. 2017.

[15] L. R. Varshney, "Transporting information and energy simultaneously," in *2008 IEEE International Symposium on Information Theory*, pp. 1612–1616, 2008.

[16] P. Grover and A. Sahai, "Shannon meets tesla: Wireless information and power transfer," in *2010 IEEE International Symposium on Information Theory*, pp. 2363–2367, 2010.

[17] L. Liu, R. Zhang, and K.-C. Chua, "Wireless information transfer with opportunistic energy harvesting," in *2012 IEEE International Symposium on Information Theory Proceedings*, pp. 950–954, 2012.

[18] Z. Wang, V. Aggarwal, and X. Wang, "Joint energy-bandwidth allocation in multiple broadcast channels with energy harvesting," *IEEE Transactions on Communications*, vol. 63, no. 10, pp. 3842–3855, 2015.

[19] J. Park and B. Clerckx, "Joint wireless information and energy transfer in a two-user mimo interference channel," *IEEE Transactions on Wireless Communications*, vol. 12, no. 8, pp. 4210–4221, 2013.

[20] B. K. Chalise, Y. D. Zhang, and M. G. Amin, "Energy harvesting in an ostbc based amplify-and-forward mimo relay system," in *2012 IEEE International Conference on Acoustics, Speech and Signal Processing (ICASSP)*, pp. 3201–3204, 2012.

[21] F. Boccardi, R. W. Heath, A. Lozano, T. L. Marzetta, and P. Popovski, "Five disruptive technology directions for 5G," *IEEE Communications Magazine*, vol. 52, pp. 74–80, February 2014.

[22] S. Buzzi, C.-L. I, T. E. Klein, H. V. Poor, C. Yang, and A. Zappone, "A survey of energy-efficient techniques for 5G networks and challenges ahead," *IEEE J. Select. Areas Commun.*, vol. 34, pp. 697–709, Apr. 2016.

[23] Q. Wu and R. Zhang, "Intelligent reflecting surface enhanced wireless network via joint active and passive beamforming," *https://arxiv.org/abs/1810.03961*, 2018.

[24] T. J. Cui, M. Q. Qi, X. Wan, J. Zhao, and Q. Cheng, "Coding metamaterials, digital metamaterials and programmable metamaterials," *Light: Science & Applications*, vol. 3, no. 10, pp. e218–e218, 2014.

[25] Q. Wu and R. Zhang, "Intelligent reflecting surface enhanced wireless network: Joint active and passive beamforming design," *IEEE Trans. Wireless Commun.*, vol. 18, p. 5394–5409, Nov. 2019.

[26] H. Phan, T. Q. Duong, M. Elkashlan, and H.-J. Zepernick, "Beamforming amplify-and-forward relay networks with feedback delay and interference," *IEEE Signal Processing Letters*, vol. 19, no. 1, pp. 16–19, 2012.

[27] B. Lyu, D. T. Hoang, S. Gong, D. Niyato, and D. I. Kim, "Irs-based wireless jamming attacks: When jammers can attack without power," *IEEE Wireless Communications Letters*, vol. 9, no. 10, pp. 1663–1667, 2020.

[28] P. J. Schreier and L. L. Scharf, *Statistical signal processing of complex-valued data: the theory of improper and noncircular signals*. Cambridge university press, 2010.

[29] S. Boyd, S. P. Boyd, and L. Vandenberghe, *Convex optimization*. Cambridge university press, 2004.

[30] H. Tuy, *Convex Analysis and Global Optimization (second edition)*. Springer International, 2017.

[31] M. Bennis, M. Debbah, and H. V. Poor, "Ultra reliable and low-latency wireless communication: Tail, risk, and scale," *Proc. IEEE*, vol. 106, pp. 1834–1853, Oct. 2018.

[32] S. Hong, J. Brand, J. I. Choi, J. Mehlman, S. Katti, and P. Levis, "Application of self-interference cancellation in 5G and beyond," *IEEE Commun. Mag.*, vol. 52, pp. 114–21, Feb. 2014.

[33] Z. Zhang, X. Chai, K. Long, A. V. Vasilakos, and L. Hanzo, "Full duplex techniques for 5G networks: self-interference cancellation, protocol design, and relay selection," *IEEE Commun. Mag.*, vol. 53, no. 5, pp. 128–136, 2015.

[34] Z. Zhang, K. Long, A. V. Vasilakos, and L. Hanzo, "Full-duplex wireless communications: Challenges, solutions, and future research directions," *Proc. IEEE*, vol. 104, no. 7, pp. 1369–1409, 2016.

[35] M. Heino et al, "Recent advances in antenna design and interference cancelllation algorithms for in-band full duplex relays," *IEEE Commun. Magazine*, pp. 91–101, May 2015.

[36] D. W. K. Ng, E. S. Lo, and R. Schober, "Dynamic resource allocation in MIMO-OFDMA systems with full-duplex and hybrid relaying," *IEEE Trans. Commun.*, vol. 60, pp. 1291–1303, May 2012.

[37] H. Q. Ngo, H. A. Suraweera, M. Matthaiou, and E. G. Larsson, "Multipair full-duplex relaying with massive arrays and linear processing," *IEEE J. Sel. Areas Commun.*, vol. 32, pp. 1721–1737, 2014.

[38] S. Huberman and T. Le-Ngoc, "MIMO full-duplex precoding: A joint beamforming and self-interference cancellation structure," *IEEE Trans. Wirel. Commun.*, vol. 14, pp. 2205–2217, Apr. 2015.

[39] H. H. M. Tam, H. D. Tuan, and D. T. Ngo, "Successive convex quadratic programming for quality-of-service management in full-duplex MU-MIMO multicell networks," *IEEE Trans. Commun.*, vol. 64, pp. 2340–2353, Jun. 2016.

[40] H. H. M. Tam, H. D. Tuan, A. A. Nasir, T. Q. Duong, and H. V. Poor, "MIMO energy harvesting in full-duplex multi-user networks," *IEEE Trans. Wirel. Commun.*, vol. 16, pp. 3282–3297, May 2017.

[41] H. D. Tuan, D. T. Ngo, and H. H. M. Tam, "Joint power allocation for MIMO-OFDM full-duplex relaying communications," *Eurasip J. Wirel. Commun. Networ.*, 2017, DOI 10.1186/s13638-016-0800-4.

[42] D. Wen, G. Yu, R. Li, Y. Chen, and G. Y. Li, "Results on energy- and spectral-efficiency tradeoff in cellular networks with full-duplex enabled base stations," *IEEE Trans. Wirel. Commun.*, vol. 16, no. 3, pp. 1494–1507, 2017.

[43] Z. Sheng, H. D. Tuan, H. H. M. Tam, H. H. Nguyen, and Y. Fang, "Energy-efficient precoding in multicell networks with full-duplex base stations," *Eurasip J. Wirel. Commun. Network.*, 2017, DOI 10.1186/s13638-017-0831-5.

[44] B. K. Chalise, H. A. Suraweera, G. Zheng, and G. K. Karagiannidis, "Beamforming optimization for full-duplex wireless-powered MIMO systems," *IEEE Trans. Commun.*, vol. 65, no. 9, pp. 3750–3764, 2017.

[45] X. Quan, Y. Liu, S. Shao, C. Huang, and Y. Tang, "Impacts of phase noise on digital self-interference cancellation in full-duplex communications," *IEEE Trans. Signal Process.*, vol. 65, no. 7, pp. 1881–1893, 2017.

[46] E. Sharma, R. Budhiraja, K. Vasudevan, and L. Hanzo, "Full-duplex massive MIMO multi-pair two-way AF relaying: Energy efficiency optimization," *IEEE Trans. Commun.*, vol. 66, no. 8, pp. 3322–3340, 2018.

[47] T.-H. Chang, Y.-F. Liu, and S.-C. Lin, "QoS-based linear transceiver optimization for full-duplex multiuser communications," *IEEE Trans. Signal Process.*, vol. 66, no. 9, pp. 2300–2313, 2018.

[48] Z. Sheng, H. D. Tuan, T. Q. Duong, H. V. Poor, and Y. Fang, "Low-latency multiuser two-way wireless relaying for spectral and energy efficiencies," *IEEE Trans. Signal Process.*, vol. 66, no. 16, pp. 4362–4376, 2018.

[49] Z. Sheng, H. D. Tuan, T. Q. Duong, and L. Hanzo, "UAV-aided two-way multi-user relaying," *under submission to IEEE Trans. Commun.*

[50] L. Wang and L. Hanzo, "Optimum time resource allocation for TDMA-based differential decode-and-forward cooperative systems: a capacity perspective," *IEEE Commun. Lett.*, vol. 14, pp. 506–508, Jun. 2010.

[51] L. Wang, L. Li, C. Xu, D. Liang, S. X. Ng, and L. Hanzo, "Multiple-symbol joint signal processing for differentially encoded single- and multi-carrier communications: Principles, designs and applications," *IEEE Commun. Surveys & Tuts.*, vol. 16, pp. 689–712, 2nd quarter 2014.

[52] A. Zappone, L. Sanguinetti, G. Bacci, E. A. Jorswieck, and M. Debbah, "Energy-efficient power control: A look at 5G wirel. technologies," *IEEE Trans. Signal Process.*, vol. 64, pp. 1668–1683, Apr. 2016.

[53] M. Duarte, C. Dick, and A. Sabharwal, "Experiment-driven characterization of full-duplex wireless systems," *IEEE Trans. Wireless Commun.*, vol. 11, pp. 4296–4307, Dec. 2012.

[54] M. Duarte, A. Sabharwal, V. Aggarwal, R. Jana, K. Ramakrishnan, C. Rice, and N. Shankaranarayanan, "Design and characterization of a full-duplex multiantenna system for WiFi networks," *IEEE Trans. Veh. Technol.*, vol. 63, pp. 1160–1177, Mar. 2014.

[55] Y. Kim et al, "Full-dimension MIMO (FD-MIMO): The next evolution of MIMO in LTE systems," *IEEE Wireless Commun.*, vol. 21, no. Jun., pp. 26–33, 2014.

[56] L. Anttila et al, "Modeling and efficient cancelation of nonlinear self-interference in MIMO full-duplex transceivers," in *Proc. of Globecom*, pp. 777–783, Dec. 2014.

[57] C. Xiong, G. Y. Li, S. Zhang, Y. Chen, and S. Xu, "Energy-efficient resource allocation in OFDMA networks," *IEEE Trans. Commun.*, vol. 60, pp. 3767–3778, Dec. 2012.

[58] W. Dinkelbach, "On nonlinear fractional programming," *Management Science*, vol. 13, pp. 492–498, Jul. 1967.

[59] L. D. Nguyen, H. D. Tuan, T. Q. Duong, O. A. Dobre, and H. V. Poor, "Downlink beamforming for energy-efficient heterogeneous networks with massive MIMO and small cells," *IEEE Trans. Wirel. Commun.*, vol. 17, no. 5, pp. 3386–3400, 2018.

[60] B. R. Marks and G. P. Wright, "A general inner approximation algorithm for nonconvex mathematical programs," *Operations Research*, vol. 26, no. 4, pp. 681–683, 1978.

[61] "3GPP technical specification group radio access network evolved universal terrestrial radio access (E-UTRA): Further advancements for E-UTRA physical layer aspects (release 9)," 2010.

[62] "Channels, physical. "mapping of transport channels onto physical channels (fdd)." gpp technical specification (2003)," 2010.

[63] O. Arnold, F. Richter, G. Fettweis, and O. Blume, "Power consumption modeling of different base station types in heterogeneous cellular networks," in *2010 Future Network & Mobile Summit*, pp. 1–8, IEEE, 2010.

[64] C. Huang, A. Zappone, G. C. Alexandropoulos, M. Debbah, and C. Yuen, "Reconfigurable intelligent surfaces for energy efficiency in wireless communication," *IEEE Trans. Wirel. Commun.*, vol. 18, pp. 4157–4170, Aug. 2019.

[65] I. Krikidis et al., "Simultaneous wireless information and power transfer in modern communications systems," *IEEE Commun. Mag.*, vol. 52, pp. 104–110, Nov. 2014.

[66] R. Zhang, R. G. Maunder, and L. Hanzo, "Wireless information and power transfer: from scientific hypothesis to engineering practice," *IEEE Commun. Mag.*, vol. 2015, pp. 99–105, Aug. 2015.

[67] X. Lu, P. Wang, D. Niyato, D. I. Kim, and Z. Han, "Wireless networks with RF energy harvesting: A contemporary survey," *IEEE Commun. Surveys Tuts.*, vol. 17, pp. 757–789, 2015.

[68] A. A. Nasir, X. Zhou, S. Durrani, and R. A. Kennedy, "Relaying protocols for wireless energy harvesting and information process.," *IEEE Trans. Wirel. Commun.*, vol. 12, pp. 3622–3636, Jul. 2013.

[69] L. Zhao and X. Wang, "Massive MIMO downlink for wireless information and energy transfer with energy harvesting receivers," *IEEE Trans. Commun.*, vol. 67, pp. 3309–3322, May 2019.

[70] A. A. Nasir, H. D. Tuan, T. Q. Duong, and H. V. Poor, "Secrecy rate beamforming for multicell networks with information and energy harvesting," *IEEE Trans, Signal Process.*, vol. 65, pp. 677–689, Feb. 2017.

[71] A. A. Nasir, H. D. Tuan, D. T. Ngo, T. Q. Duong, and H. V. Poor, "Beamforming design for wireless information and power transfer systems: Receive power-splitting versus transmit time-switching," *IEEE Trans. Commun.*, vol. 65, pp. 876–889, Feb. 2017.

[72] H. Sun, F. Zhou, R. Q. Hu, and L. Hanzo, "Robust beamforming design in a NOMA cognitive radio network relying on SWIPT," *IEEE J. Sel. Areas Commun.*, vol. 37, pp. 142–155, Jan 2019.

[73] A. A. Nasir, H. D. Tuan, T. Q. Duong, and M. Debbah, "NOMA throughput and energy efficiency in energy harvesting enabled networks," *IEEE Trans. Commun.*, vol. 67, pp. 6499–6511, Sept. 2019.

[74] I. E. Telatar, "Capacity of multi-antenna Gaussian channels," *Eur. Trans. Telecommun.*, vol. 10, pp. 585–595, Nov./Dec. 1999.

[75] P. J. Schrerier and L. L. Scharf, *Statistical Signal Processing of Complex-Valued Data: The Theory of Improper and Noncircular Signals.* Cambridge University Press, 2010.

[76] S. Javed, O. Amin, B. Shihada, and M.-S. Alouini, "A journey from improper Gaussian signaling to asymmetric signaling," 2019.

[77] Y. Zeng, R. Zhang, E. Gunawan, and Y. L. Guan, "Optimized transmission with improper Gaussian signaling in the k-user MISO interference channel," *IEEE Trans. Wirel. Commun.*, vol. 12, pp. 6303–6313, Dec. 2013.

[78] Y. Zeng, C. M. Yetis, E. Gunawan, Y. L. Guan, and R. Zhang, "Transmit optimization with improper Gaussian signaling for interference channels," *IEEE Trans. Signal Process.*, vol. 61, pp. 2899–2913, Jun. 2013.

[79] Z. K. M. Ho and E. Jorswieck, "Improper Gaussian signaling on the two-user SISO interference channel," *IEEE Trans. Wireless Commun.*, vol. 11, pp. 3194–3203, Sep. 2012.

[80] C. Lameiro and I. Santamaría, "Degrees-of-freedom for the 4-user SISO interference channel with improper signaling," in *Proc IEEE Inter. Conf. Commun. (ICC)*, pp. 3053–3057, Jun. 2013.

[81] H. D. Nguyen, R. Zhang, and S. Sun, "Improper signaling for symbol error rate minimization in k-user interference channel," *IEEE Trans. Commun.*, vol. 63, pp. 857–869, Mar. 2015.

[82] C. Hellings and W. Utschick, "Improper signaling versus time-sharing in the SISO Z-interference channel," *IEEE Communications Letters*, vol. 21, pp. 2432–2435, Nov 2017.

[83] E. Kurniawan and S. Sun, "Improper Gaussian signaling scheme for the z-interference channel," *IEEE Trans. Wirel. Commun.*, vol. 14, pp. 3912–3923, Jul. 2015.

[84] C. Lameiro, I. Santamaría, and P. J. Schreier, "Rate region boundary of the SISO Z-interference channel with improper signaling," *IEEE Trans. on Commun.*, vol. 65, pp. 1022–1034, Mar. 2017.

[85] V. R. Cadambe, S. A. Jafar, and C. Wang, "Interference alignment with asymmetric complex signaling—settling the Host-Madsen-Nosratinia conjecture," *IEEE Trans. Inf. Theory*, vol. 56, pp. 4552–4565, Sept 2010.

[86] S. A. Jafar, "Interference alignment — a new look at signal dimensions in a communication network," *Foundations and Trends® in Communications and Information Theory*, vol. 7, no. 1, pp. 1–134, 2011.

[87] L. Yang and W. Zhang, "Interference alignment with asymmetric complex signaling on MIMO X channels," *IEEE Trans. Commun.*, vol. 62, pp. 3560–3570, Oct 2014.

[88] S. Lagen, A. Agustin, and J. Vidal, "Coexisting linear and widely linear transceivers in the MIMO interference channel," *IEEE Trans. Signal Process.*, vol. 64, pp. 652–664, Feb 2016.

[89] S. Lagen, A. Agustin, and J. Vidal, "On the superiority of improper Gaussian signaling in wireless interference MIMO scenarios," *IEEE Trans. Commun.*, vol. 64, pp. 3350–3368, Aug. 2016.

[90] H. Shin, S. Park, H. Park, and I. Lee, "A new approach of interference alignment through asymmetric complex signaling and multiuser diversity," *IEEE Trans. on Wirel. Commun.*, vol. 11, pp. 880–884, Mar. 2012.

[91] C. Hellings, M. Joham, and W. Utschick, "QoS feasibility in MIMO broadcast channels with widely linear transceivers," *IEEE Signal Process. Letts.*, vol. 20, pp. 1134–1137, Nov. 2013.

[92] A. A. Nasir, H. D. Tuan, T. Q. Duong, and H. V. Poor, "Improper Gaussian signaling for broadcast interference networks," *IEEE Signal Process. Lett.*, vol. 26, pp. 808–812, Jun. 2019.

[93] C. Lameiro, I. Santamaria, and P. J. Schreier, "Benefits of improper signaling for underlay cognitive radio," *IEEE Commun. Letts.*, vol. 4, pp. 22–25, Feb. 2015.

[94] O. Amin, W. Abediseid, and M.-S. Alouini, "Underlay cognitive radio systems with improper Gaussian signaling: outage performance analysis," *IEEE Trans. Wirel. Commun.*, vol. 15, pp. 4875–4887, Jul. 2016.

[95] C. Lameiro, I. Santamaria, and P. J. Schreier, "Improper Gaussian signaling for multiple-access channels in underlay cognitive radio," *IEEE Trans. Commun.*, vol. 67, pp. 1817–1830, Mar. 2019.

[96] H. D. Tuan, A. A. Nasir, H. H. Nguyen, T. Q. Duong, and H. V. Poor, "Non-orthogonal multiple access with improper Gaussian signaling," *IEEE J. Selec. Topics Signal Process.*, vol. 13, pp. 496–507, Mar. 2019.

[97] T. M. Cover and J. A. Thomas, *Elements of Information Theory (second edition)*. John Wileys & Sons, 2006.

[98] D. Peaucelle, D. Henrion, and Y. Labit, "Users guide for SeDuMi interface 1.03," 2002.

[99] J. G. Andrews, S. Buzzi, W. Choi, S. V. Hanly, A. Lozano, A. C. K. Soong, and J. C. Zhang, "What will 5G be?," *IEEE J. Sel. Areas Commun.*, vol. 32, pp. 1065–1082, June 2014.

[100] S. Zhang, Q. Wu, S. Xu, and G. Y. Li, "Fundamental green tradeoffs: Progresses, challenges, and impacts on 5G networks," *IEEE Commun. Surveys Tuts.*, vol. 19, pp. 33–56, Firstquarter 2017.

[101] Q. Wu, G. Y. Li, W. Chen, D. W. K. Ng, and R. Schober, "An overview of sustainable green 5G networks," *IEEE Wireless Communications*, vol. 24, pp. 72–80, Aug 2017.

[102] Q. Wu and R. Zhang, "Towards smart and reconfigurable environment: Intelligent reflecting surface aided wireless network," *IEEE Commun. Mag.*, pp. 1–7, 2019.

[103] S. Tretyakov, V. Asadchy, and A. Diaz-Rubio, "Chapter 6: Metasurfaces for general control of reflection and transmission," in *World Scientific Handbook of Metamaterials and Plasmonics*, pp. 249–293, 2017.

[104] F. Liu et al., "Intelligent metasurfaces with continuously tunable local surface impedance for multiple reconfigurable functions," *Physical Review Applied*, vol. 11, no. 4, p. 044024, 2019.

[105] Z. Li, Y. Xie, L. Shangguan, R. I. Zelaya, J. Gummeson, W. Hu, and K. Jamieson, "Towards programming the radio environment with large arrays of inexpensive antennas," in *16th USENIX Symposium on Networked Systems Design and Implementation (NSDI 19)*, pp. 285–300, Feb. 2019.

[106] M. Di Renzo, M. Debbah, D.-T. Phan-Huy, A. Zappone, M.-S. Alouini, C. Yuen, V. Sciancalepore, G. C. Alexandropoulos, J. Hoydis, H. Gacanin, J. de Rosny, A. Bounceu, G. Lerosey, and M. Fink, "Smart radio environments empowered by AI reconfigurable meta-surfaces: An idea whose time has come," *EURASIP J. Wirel. Commun. Network.*, no. 1, p. 129, 2019.

[107] S. Gong, J. Xu, D. Niyato, X. Huang, and Z. Han, "Backscatter-aided cooperative relay communications in wireless-powered hybrid radio networks," *IEEE Network*, vol. 33, pp. 234–241, Sept. 2019.

[108] D. Ciuonzo, G. Gelli, A. Pescapé, and F. Verde, "Decision fusion rules in ambient backscatter wireless sensor networks," in *Proc. 2019 IEEE 30th Ann. Inter. Symp. Pers. Ind. Mob. Radio Commun. (PIMRC)*, pp. 1–6, IEEE, 2019.

[109] S. Hu, F. Rusek, and O. Edfors, "Beyond massive MIMO: The potential of data transmission with large intelligent surfaces," *IEEE Trans. Signal Process.*, vol. 66, pp. 2746–2758, May. 2018.

[110] K. Ntontin, M. Di Renzo, J. Song, F. Lazarakis, J. de Rosny, D.-T. Phan-Huy, O. Simeone, R. Zhang, M. Debbah, G. Lerosey, M. Fink, S. Tretyakov, and S. Shama, "Reconfigurable intelligent surfaces vs. relaying: Differences, similarities, and performance comparison," *https://arxiv.org/abs/1908.08747*.

[111] Q. U. A. Nadeem, A. Kammoun, A. Chaaban, M. Debbah, and M. S. Alouini, "Asymptotic max-min SINR analysis of reconfigurable intelligent surface assisted MISO systems," *IEEE Trans. Wirel. Commun.*, vol. 19, no. 12, pp. 7748–7764, 2020.

[112] A. H. Phan, H. D. Tuan, H. H. Kha, and D. T. Ngo, "Nonsmooth optimization for efficient beamforming in cognitive radio multicast transmission," *IEEE Trans. Signal Process.*, vol. 60, pp. 2941–2951, Jun. 2012.

[113] G. Zhou, C. Pan, H. Ren, K. Wang, W. Xu, and A. Nallanathan, "Intelligent reflecting surface aided multigroup multicast MISO communication systems," *https://arxiv.org/abs/1909.04606*.

[114] C. Pan, H. Ren, K. Wang, W. Xu, M. Elkashlan, A. Nallanathan, and L. Hanzo, "Multicell MIMO communications relying on intelligent reflecting surface," *https://arxiv.org/abs/1907.10864*.

[115] C. Pan, H. Ren, K. Wang, M. Elkashlan, A. Nallanathan, J. Wang, and L. Hanzo, "Intelligent reflecting surface aided mimo broadcasting for simultaneous wireless information and power transfer," *IEEE J. Select. Areas Commun.*, vol. 38, pp. 1719–1734, Aug. 2020.

[116] H. Yu, H. D. Tuan, T. Q. Duong, and L. Hanzo, "Improper Gaussian signaling for integrated data and energy networking," *IEEE Trans. Commun.*, vol. 68, pp. 3922–3934, Jun. 2020.

[117] G. Gelli, L. Paura, and A. R. Ragozini, "Blind widely linear multiuser detection," *IEEE Commun. Lett.*, vol. 4, pp. 187–189, Jun. 2000.

[118] S. Buzzi, M. Lops, and S. Sardellitti, "Widely linear reception strategies for layered space-time wireless communications," *IEEE Trans. Signal Process.*, vol. 54, pp. 2252–2262, Jun. 2006.

[119] O. Ozdogan, E. Bjornson, and E. G. Larsson, "Intelligent reflecting surfaces: Physics, propagation, and pathloss modeling," *https://arxiv.org/abs/1911.03359*.

[120] Q.-U.-A. Nadeem, A. Kammoun, M. Debbah, and M.-S. Alouini, "A generalized spatial correlation model for 3D MIMO channels based on the Fourier coefficients of power spectrums," *IEEE Trans. Signal Process.*, vol. 63, pp. 3671–3686, Jul. 2015.

[121] E. Bjornson, O. Ozdogan, and E. G. Larsson, "Intelligent reflecting surface versus decode-and-forward: How large surfaces are needed to beat relaying?," *IEEE Wirel. Commun. Lett.*, vol. 9, no. 2, pp. 244–248, 2020.

[122] A. Wiesel, Y. C. Eldar, and S. Shamai, "Linear precoding via conic optimization for fixed MIMO receivers," *IEEE Trans. Signal Process.*, vol. 54, pp. 161–176, Jan. 2006.

[123] E. Che, H. D. Tuan, and H. H. Nguyen, "Joint optimization of cooperative beamforming and relay assignment in multi-user wireless relay networks," *IEEE Trans. Wirel. Commun.*, vol. 13, pp. 5481–5495, Oct. 2014.

[124] H. H. M. Tam, H. D. Tuan, D. T. Ngo, T. Q. Duong, and H. V. Poor, "Joint load balancing and interference management for small-cell heterogeneous networks with limited backhaul capacity," *IEEE Trans. Wirel. Commun.*, vol. 16, pp. 872–884, Feb. 2017.

[125] Y. Shi, H. D. Tuan, T. Q. Duong, H. V. Poor, and A. V. Savkin, "Pmu placement optimization for efficient state estimation in smart grid," *IEEE Journal on Selected Areas in Communications*, vol. 38, no. 1, pp. 71–83, 2020.

[126] J. F. Bonnans, J. C. Gilbert, C. Lemarechal, and C. Sagastizabal, *Numerical Optimization – Theoretical and Practical Aspects (second edition).* Springer, 2006.

[127] Y. Shi, H. D. Tuan, S. Su, and H. Tuy, "Global optimization for optimal power flow over transmission networks," *J. of Glob. Optim.*, vol. 69, pp. 745–760, 2017.

[128] L. D. Nguyen, H. D. Tuan, T. Q. Duong, H. V. Poor, and L. Hanzo, "Energy-efficient multi-cell massive mimo subject to minimum user-rate constraints," *IEEE Transactions on Communications*, vol. 69, no. 2, pp. 914–928, 2021.

[129] T. Yoo and A. Goldsmith, "On the optimality of multiantenna broadcast scheduling using zero-forcing beamforming," *IEEE J. Sel. Areas Commun.*, vol. 54, pp. 528–541, Mar. 2006.

[130] L. D. Nguyen, H. D. Tuan, T. Q. Duong, O. A. Dobre, and H. V. Poor, "Downlink beamforming for energy-efficient heterogeneous networks with massive MIMO and small cells," *IEEE Trans. Wirel. Commun.*, vol. PP, no. 99, 2018.

[131] L. D. Nguyen, H. D. Tuan, T. Q. Duong, and H. V. Poor, "Multi-user regularized zero forcing beamforming," *IEEE Trans. Signal Process.*, vol. 67, pp. 2839–2853, Jun. 2019.

[132] A. A. Nasir, H. D. Tuan, T. Q. Duong, H. V. Poor, and L. Hanzo, "Hybrid beamforming for multi-user millimeter-wave networks," *IEEE Trans. Vehic. Techn.*, vol. 69, pp. 2943–2956, Mar. 2020.

[133] C. Huang, S. Hu, G. C. Alexandropoulos, A. Zappone, C. Yuen, R. Zhang, M. D. Renzo, and M. Debbah, "Holographic MIMO surfaces for 6G wireless networks: Opportunities, challenges, and trends," *IEEE Wirel. Commun.*, vol. 27, pp. 118–125, Oct. 2020.

[134] L. Yang, F. Meng, J. Zhang, M. O. Hasna, and M. D. Renzo, "On the performance of ris-assisted dual-hop uav communication systems," *IEEE Trans. Vehic. Techn.*, vol. 69, no. 9, pp. 10385–10390, 2020.

[135] X. Liu, Y. Liu, and Y. Chen, "Machine learning empowered trajectory and passive beamforming design in uav-ris wireless networks," *IEEE J. Selec. Areas Commun.*, pp. 1–1, 2020.

[136] S. Li, B. Duo, X. Yuan, Y. Liang, and M. Di Renzo, "Reconfigurable intelligent surface assisted uav communication: Joint trajectory design and passive beamforming," *IEEE Wireless Commun. Lett.*, vol. 9, no. 5, pp. 716–720, 2020.

[137] L. Yang, X. Yan, D. B. da Costa, T. A. Tsiftsis, H. C. Yang, and M. S. Alouini, "Indoor mixed dual-hop vlc/rf systems through reconfigurable intelligent surfaces," *IEEE Wirel. Commun. Lett.*, vol. 9, no. 11, pp. 1995–1999, 2020.

[138] L. Wei, C. Huang, G. C. Alexandropoulos, C. Yuen, Z. Zhang, and M. Debbah, "Channel estimation for RIS-empowered multi-user MISO wireless communications," *IEEE Tran. Commun.*, vol. 69, no. 6, pp. 4144–4157, 2021.

[139] J. He, H. Wymeersch, and M. Juntti, "Channel estimation for ris-aided mmwave mimo systems via atomic norm minimization," *IEEE Transactions on Wireless Communications*, pp. 1–1, 2021.

[140] Z. Zhang, C. Zhang, C. Jiang, F. Jia, J. Ge, and F. Gong, "Improving physical layer security for reconfigurable intelligent surface aided noma 6g networks," *IEEE Transactions on Vehicular Technology*, pp. 1–1, 2021.

[141] M. H. Khoshafa, T. M. N. Ngatched, and M. H. Ahmed, "Reconfigurable intelligent surfaces-aided physical layer security enhancement in d2d underlay communications," *IEEE Commun. Lett.*, pp. 1–1, 2020.

[142] G. Zhou, C. Pan, H. Ren, K. Wang, W. Xu, and A. Nallanathan, "Intelligent reflecting surface aided multigroup multicast MISO communication systems," *IEEE Trans. Signal Process.*, vol. 68, pp. 3236–3251, 2020.

[143] C. Pan, H. Ren, K. Wang, W. Xu, M. Elkashlan, A. Nallanathan, and L. Hanzo, "Multicell MIMO communications relying on intelligent reflecting surface," *IEEE Trans. Wirel. Commun.*, vol. 19, pp. 5218–5233, Aug. 2020.

[144] C. Pan, H. Ren, K. Wang, M. Elkashlan, A. Nallanathan, J. Wang, and L. Hanzo, "Intelligent reflecting surface aided MIMO broadcasting for simultaneous wireless information and power transfer," *IEEE J. Sel. Areas Commun.*, vol. 38, pp. 1719–1734, Aug. 2020.

[145] M. M. Zhao, Q. Wu, M. J. Zhao, and R. Zhang, "Intelligent reflecting surface enhanced wireless networks: Two-timescale beamforming optimization," *IEEE Trans. Wirel. Commun.*, vol. 20, no. 1, pp. 2–17, 2021.

[146] H. Yu, H. D. Tuan, A. A. Nasir, T. Q. Duong, and H. V. Poor, "Joint design of reconfigurable intelligent surfaces and transmit beamforming under proper and improper Gaussian signaling," *IEEE J. Sel. Areas Commun.*, vol. 38, pp. 2589–2603, Nov. 2020.

[147] H. Yu, H. D. Tuan, A. A. Nasir, T. Q. Duong, and L. Hanzo, "Improper Gaussian signaling for computationally tractable energy and information beamforming," *IEEE Trans. Vehic. Techn.*, vol. 69, no. 11, pp. 13990–13995, 2020.

[148] P. D. Tao and L. T. H. An, "A d. c. optimization algorithm for solving the trust-region subproblem," *SIAM J. Optimiz.*, vol. 8, no. 2, pp. 476–505, 1998.

[149] A. Migdalas, "A regularization of the Frank-and-Wolfe method and unification of certain nonlinear programming methods," *Math. Program.*, vol. 65, pp. 331–346, 1994.

[150] J. Hu, K. Yang, G. Wen, and L. Hanzo, "Integrated data and energy communication network: A comprehensive survey," *IEEE Commun. Surveys Tuts.*, vol. 20, pp. 3169–3219, Fourthquarter 2018.

[151] H. H. M. Tam, H. D. Tuan, A. A. Nasir, T. Q. Duong, and H. V. Poor, "MIMO energy harvesting in full-duplex multi-user networks," *IEEE Trans. Wirel. Commun.*, vol. 16, pp. 3282–3297, May 2017.

[152] H. Yu, H. D. Tuan, T. Q. Duong, Y. Fang, and L. Hanzo, "Improper Gaussian signaling for integrated data and energy networking," *IEEE Trans. Commun.*, vol. 68, pp. 3922–3934, Jun. 2020.

[153] C. B. Peel, B. M. Hochwald, and A. L. Swindlerhurst, "A vector-perturbation technique for near capacity multiantenna multiuser communication-Part I: channel inversion and regularization," *IEEE Trans. Commun.*, vol. 53, pp. 195–202, Jan. 2005.

[154] Q.-U.-A. Nadeem, A. Kammoun, A. Chaaban, M. Debbah, and M.-S. Alouini, "Asymptotic max-min SINR analysis of reconfigurable intelligent surface assisted MISO systems," *IEEE Trans. Wirel. Commun.*, vol. 19, pp. 7748–7764, Dec. 2020.

[155] C. Huang, Z. Yang, G. C. Alexandropoulos, K. Xiong, L. Wei, C. Yuen, Z. Zhang, and M. Debbah, "Multi-hop ris-empowered terahertz communications: A drl-based hybrid beamforming design," *IEEE J. Select. Areas Commun.*, vol. 39, no. 6, pp. 1663–1677, 2021.

[156] H. Yu, H. D. Tuan, E. Dutkiewicz, H. V. Poor, and L. Hanzo, "Maximizing the geometric mean of user-rates to improve rate-fairness: Proper vs. improper gaussian signaling," *IEEE Trans. Wirel. Commun.*, pp. 1–1, 2021.

[157] J. Barzilai and J. M. Borwein, "Two-point step size gradient methods," *IMA J. Numerical Analysis*, vol. 8, no. 1, pp. 141–148, 1988.

[158] P. Apkarian and H. D. Tuan, "Robust control via concave minimization local and global algorithms," in *Proc. of the 37th IEEE Conf. Decision Control*, pp. 3855–3860, 1998.

[159] P. Apkarian and H. D. Tuan, "Concave programming in control theory," *J. of Glob. Optim.*, vol. 15, pp. 243–270, Apr. 1999.

[160] P. Apkarian and H. D. Tuan, "Robust control via concave optimization: local and global algorithms," *IEEE Trans. Autom. Control*, vol. 45, pp. 299–305, Feb. 2000.

[161] K. P. Bennett and O. L. Mangasarian, "Bilinear separation of two sets in n-space," *Computat. Optim. Applicat.*, vol. 2, pp. 207–227, 1993.

[162] K. Zhou and J. Doyle, *Essentials of Robust Control*. Prentice Hall, 1999.

[163] R. Schneider, *Convex Bodies: The Brunn-Minkowski Theory,*. Cambridge University Press, Cambridge, 1993.

[164] L. D. Nguyen, H. D. Tuan, T. Q. Duong, and H. V. Poor, "Multi-user regularized zero-forcing beamforming," *IEEE Trans. Signal Process.*, vol. 67, pp. 2839–2853, Jun. 2019.

[165] U. Rashid, H. D. Tuan, H. H. Kha, and H. H. Nguyen, "Joint optimization of source precoding and relay beamforming in wireless MIMO relay networks," *IEEE Trans. Commun.*, vol. 62, pp. 488–499, Feb. 2014.